UNIVERSITÀ DEGLI STUDI DI MILANO

UNIVERSITÀ DEGLI STUDI DI MILANO

CORSO DI DOTTORATO:
The Human Mind and its Explanation: Language, Brain, and Reasoning

DIPARTIMENTO DI AFFERENZA DEL CORSO:
Department of Philosophy "Piero Martinetti"

TESI DI DOTTORATO DI RICERCA:
Exploring brain complexity and its mechanisms: from theory to practice and back

BIOS-06/A

Gianluca Gaglioti
Matr. R13746
ORCID n. 0009-0004-7420-7968

TUTOR: prof. Marcello Massimini

CO-TUTOR: prof. Simone Sarasso

COORDINATORE DEL DOTTORATO: prof. Andrea Sereni

A.A. 2024-2025

Abstract

This thesis explores brain complexity and its structural and functional substrates, linking theoretical principles, empirical TMS–EEG recordings, and multi-scale computational modeling. The central question it addresses is how brain networks sustain complex dynamics and how these dynamics break down in pathology. Across five interconnected studies, it standardizes experimental TMS–EEG data analysis and whole-brain computational pipelines to investigate how structural connectivity, network topology, and dynamical regimes jointly shape brain complexity.

First, a standardized analysis framework (TEPpy) is developed to map the temporal and spectral signatures of TMS-evoked potentials, operationalizing local circuit differentiation by characterizing peak-based features and natural frequencies. Second, an integrated whole-brain modeling workflow (TVB–Cobrawap) is introduced to tune connectome-based neural mass models toward biologically realistic regimes that jointly reproduce spontaneous rhythms, features of criticality, and high perturbational complexity in evoked responses, thereby unifying expectations for spontaneous and evoked activity within a single tuned model. Third, local virtual manipulations in a whole-brain computational model show that silencing highly central posterior hubs produces the largest reductions in perturbational complexity, indicating a central role of posterior network hubs in sustaining complex dynamics. Fourth, a multiscale computational model demonstrates that structural disconnection alone is sufficient to generate cortical bistability and slow waves via neuronal disfacilitation, and further shows that their propagation depends on hierarchical topology and the temporal coherence of afferent slow wave activity, providing a mechanistic account of perilesional sleep-like dynamics and large-scale slow wave propagation after focal lesions. Fifth, a computational analysis across rewired networks indicates that perturbational complexity peaks in small-world regimes and remains robust to common-driver confounds, whereas observational measures exhibit systematic biases toward segregation or integration. This clarifies complexity metric sensitivities and provides a principled basis for interpreting complexity markers.

Collectively, these contributions provide standardized empirical and computational tools, establish a mechanistic link between criticality and perturbational complexity, and bridge abstract information-theoretic constructs with the neurobiology of brain structure and dynamics. They further delineate translational avenues for assessing brain complexity and modeling slow wave dynamics following brain injury.

Keywords

brain complexity; integration–differentiation balance; criticality; TMS–EEG; PCI; whole-brain modeling; cortical bistability; brain injury; slow waves; standardized pipelines

Contents

1

Introduction

1.1 Brain Complexity: the Integration-Differentiation Framework

The concept of brain complexity addresses a fundamental dilemma in brain organization: how does the brain achieve both global coordination (integration) and local specialization (differentiation) within large-scale distributed networks? This dialectical tension underpins the brain's capacity for cognition, adaptive behavior, and consciousness. Differentiation refers to the ability of specialized groups of neurons to extract relevant information from diverse multisensory inputs, thereby supporting rich information content. Integration, by contrast, emphasizes the need for these specialized and segregated neurons to interact dynamically in order to combine this wealth of information and generate unique, coherent cognitive states that enable appropriate behavior (Sporns et al., 2000). The coexistence and dynamic balance of these properties is considered a hallmark of healthy brain function and conscious awareness (Tononi et al., 1994; Sporns, 2013). In the following sections I outline the conceptual and structural foundations of this framework, its mechanistic relationship to critical dynamics, and recent empirical and methodological advances.

1.1.1 Conceptual Foundations of Brain complexity

The conceptual foundations of brain complexity can be traced to converging insights from neuroscience, information theory, and dynamical systems. Early proposals by Tononi and colleagues formalized the idea that conscious experience is both highly integrated (irreducible as a whole) and highly differentiated (rich in informational content). They argued that the brain's capacity for consciousness depends on the repertoire of causal states it can generate (Tononi et al., 1994; Tononi and Edelman, 1998). This framework gave rise to the Dynamic Core Hypothesis, which posits that conscious experience emerges from distributed,

interacting thalamocortical regions that transiently form a unified, complex functional cluster (Edelman and Tononi, 2000). The hypothesis emphasized that consciousness is not localized in a single region but arises from dynamic patterns of large-scale integration, continuously reconfiguring as neural activity unfolds.

This line of thought was later developed into Integrated Information Theory (IIT), which seeks to capture both the quantity (Φ) and quality of experience by formalizing how information is integrated across a system (Tononi, 2004; Oizumi et al., 2014; Tononi et al., 2016). IIT provided a principled attempt to link the phenomenology of consciousness to measurable properties of causal networks. More recently, a "weak" form of IIT has been proposed, emphasizing empirical measures of information dynamics that are tractable for neuroscience without committing to the full ontological claims of the original theory (Mediano et al., 2022). In this framework, integrated information is treated as a family of practical markers that can be applied to neural data to predict conscious states and contents, sidestepping the computational intractability and metaphysical commitments of "strong" IIT. Weak IIT thus operationalizes the core notions of integration and differentiation in terms of implementable measures that remain faithful to the spirit, if not the letter, of the original theory.

Crucially, these complex dynamics are both enabled and constrained by the brain's structural architecture. Several studies have highlighted how the connectome (i.e., the network of anatomical connections) provides the substrate for balancing integration and differentiation (Sporns et al., 2005; Hagmann et al., 2008). Differentiation is grounded in the heterogeneity of local microcircuits, including variations in cytoarchitecture, gene expression, and neurotransmitter receptor profiles across cortical and subcortical regions (Economo et al., 2008; Burt et al., 2018; Hansen et al., 2022). Integration, by contrast, is supported by the dense web of long-range white-matter tracts that enable efficient communication between specialized areas, with hub regions rich in connections (e.g., nodes of the default mode networks) playing a disproportionately important role in large-scale coordination (Heuvel and Sporns, 2013; Crossley et al., 2014). The architectural requirements underlying complex dynamics will be further discussed in section 1.3.1.1.

The articles presented in Chapter 2 provide a comprehensive validation and operationalization of these theoretical principles across multiple scales. Article 1 (section 2.1) introduces *TEPpy*, a standardized computational framework that can be used to quantify the differentiation of stimulated neuronal circuits by analyzing TMS-evoked potential (TEP) features, such as natural frequencies and early components, establishing systematic and reproducible methods for probing the mesoscale substrates of brain complexity. Article 2 (section 2.2) advances computational modeling by showing that whole-brain models, when tuned to critical regimes, naturally exhibit the integration–differentiation balance in their evoked dynamics. Article 3 (section 2.3) investigates the global impact of local alterations, demonstrating that disruptions to posterior hub regions produce the largest declines in perturbational complexity, revealing the architectural dependencies of this balance. Article 4

(section 2.4) employs a multiscale modeling approach to explore mechanisms underlying the loss of brain complexity. Finally, Article 5 (section 2.5) systematically evaluates how different complexity measures capture the theoretical integration–differentiation balance.

Together, these five studies establish a comprehensive framework for understanding brain complexity as a measurable, mechanistically grounded phenomenon that bridges theory, empirical observation, and clinical application.

1.1.2 Complexity and Critical Dynamics

An influential idea for explaining how the brain generates complex activity is the hypothesis that neural systems operate close to a state of criticality (Fig 1.1), a dynamical regime poised between order and disorder (Chialvo, 2010; Shew and Plenz, 2013). At this boundary, the system achieves a delicate balance: it is ordered enough to sustain coherent communication across networks, yet sufficiently variable to explore a rich repertoire of states. This is precisely the balance between integration and differentiation that defines complex neural dynamics.

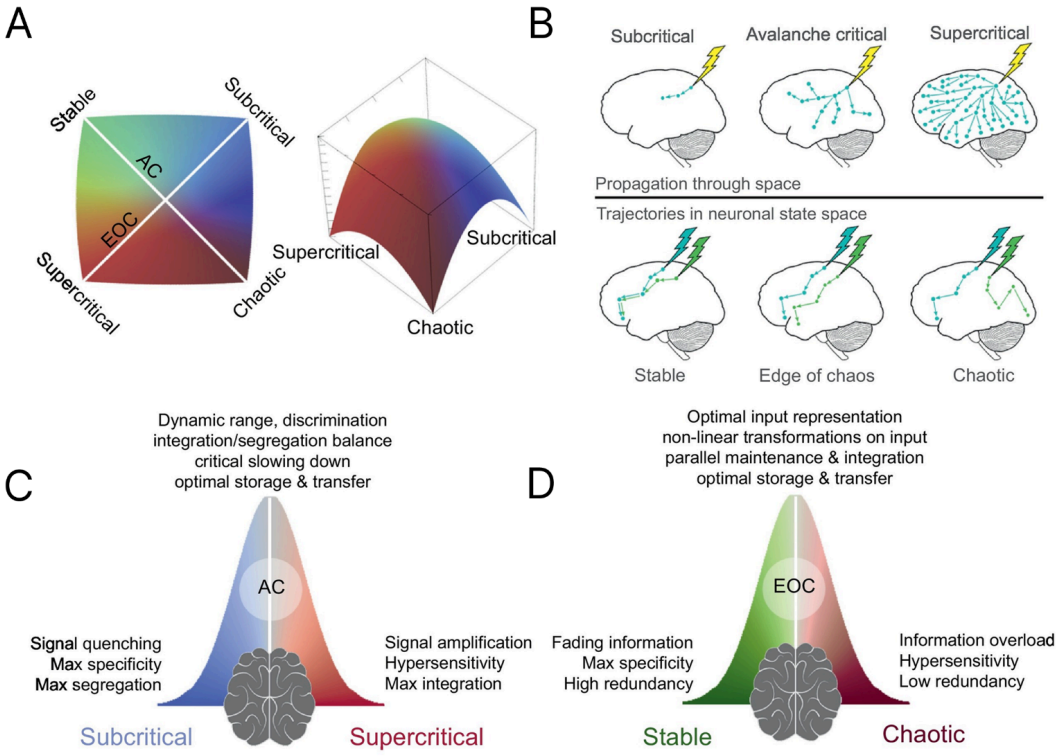

Figure 1.1 Computational Regimes at the Edge of Criticality. (A) High-dimensional landscape of brain dynamics, demarcated by two principal phase transitions: the classical avalanche criticality (AC) boundary and the edge-of-chaos (EOC) boundary. The AC transition separates regimes where small perturbations either diminish (subcritical) or amplify uncontrollably (supercritical), while the EOC transition marks the onset of sensitivity to minute input differences (chaotic) versus convergence of

trajectories (stable). **(B)** Schematic illustrating responses to a brief perturbation under each phase. *Subcritical*: Activity rapidly decays, yielding quenched, low-diversity responses. *Avalanche critical* (AC): Perturbations propagate broadly without runaway growth, balancing signal spread and containment. *Supercritical*: Inputs trigger explosive, high-gain activity. *Stable*: Trajectories converge, minimizing variability and encoding specificity. *Edge-of-chaos* (EOC): Input distinctions are sustained over time, maximizing both representation fidelity and richness of dynamics. *Chaotic*: Nearby trajectories diverge exponentially, creating hypersensitivity to noise. **(C–D)** Trade-off curves for AC **(C)** and EOC **(D)** showing how computational metrics vary with distance from each critical point. For AC, moving toward criticality enhances dynamic range, integration-segregation balance, and information transfer at the expense of specificity and rapid quenching. For EOC, proximity maximizes nonlinear transformation and storage capacity but risks redundancy or overload in stable and chaotic extremes, respectively. Figure adapted from O'Byrne and Jerbi (2022).

Critical dynamics are characterized by a number of distinctive signatures. Neuronal activity unfolds in scale-free cascades, or avalanches, whose size distributions follow power laws (Beggs and Plenz, 2003). In such a regime, the branching parameter approaches unity, ensuring that perturbations neither die out too quickly nor grow without bound, but instead propagate efficiently through the network (Haldeman and Beggs, 2005; Kinouchi and Copelli, 2006). This poised state has profound computational consequences: it maximizes the system's dynamic range, information transmission, and responsiveness to inputs of varying amplitude (Kinouchi and Copelli, 2006; Shew et al., 2009).

A central functional hallmark of criticality is critical slowing down, the tendency of systems near a phase transition to recover more slowly from perturbations (Meisel et al., 2015). Far from being a limitation, this slowing enables activity to persist and evolve over time, enriching the temporal structure of neural dynamics. Theoretically, such a regime confers the twin advantages of robustness and flexibility: local events can spread widely without destabilizing the system, while global coherence is preserved. This dual property maps directly onto the requirements for sustaining integration and differentiation in neural processing (Chialvo, 2010).

The relationship between criticality and complexity is supported by both theoretical models and empirical observations. Theoretically, scale-free correlations allow local perturbations to influence activity across multiple spatial scales, creating conditions that optimize the integration–differentiation balance. Empirically, measures grounded in information theory demonstrate that neural complexity is maximized near criticality, when the system explores the broadest repertoire of spatiotemporal activity patterns (Shew and Plenz, 2013; Timme et al., 2016). Studies of altered states of consciousness further reinforce this connection: anesthetics such as propofol and xenon push neural networks away from criticality, concomitantly reducing measures of brain complexity, whereas ketamine, despite altering perception, preserves near-critical dynamics and maintains high complexity (Maschke et al., 2024).

This mechanistic relationship is a central theme of this thesis. In Article 2 (section 2.2), systematic tuning of whole-brain models reveals that networks exhibiting critical features (including scale-free dynamics and critical slowing down) naturally generate the complex evoked activity patterns characteristic of conscious states. Article 5 (section 2.5) provides complementary evidence, showing that the structural transition toward optimal integration–differentiation balance coincides with the emergence of critical slowing down in evoked responses, establishing that the network bases of complexity and criticality are fundamentally intertwined.

1.1.3 Measuring Brain Complexity

Quantifying the integration–differentiation balance poses a major empirical challenge. By definition, it requires capturing both the diversity of accessible brain states (differentiation) and their causal interdependence (integration) (Tononi et al., 1994). Over the past two decades, a consistent body of evidence has shown that measures linked to brain complexity serve as robust markers of consciousness across physiological states such as sleep, pharmacological manipulations with anesthesia, and clinical conditions involving disorders of consciousness. Remarkably, this convergence has occurred despite the fact that these measures were derived from diverse analysis approaches (Sarasso et al., 2021).

A wide range of metrics has been developed, which can be roughly grouped according to their strategy for estimating the state repertoire (differentiation) and integration. Spatial approaches reconstruct functional brain networks directly from empirical recordings, using correlations, coherence, or phase synchrony to define edges between regions. Graph-theoretic analyses of these networks then probe the balance between segregation and integration through indices such as modularity, clustering coefficient, global efficiency, or characteristic path length. These analyses consistently reveal a small-world organization, a hallmark of complex systems that simultaneously supports localized specialization and long-range integration (Bullmore and Sporns, 2009; Sporns, 2013; Cohen and D'Esposito, 2016).

In contrast, temporal approaches bypass explicit network reconstruction and quantify complexity directly from the unfolding dynamics of neural signals. Here, activity patterns are extracted from time series (through binarization, symbolization, or microstate analysis) and their unpredictability or information content is captured using entropy-based measures, fractal indices, or empirical approximations of integrated information (Schartner et al., 2015; Andrillon et al., 2016; Mateos et al., 2018; Nilsen et al., 2024). These measures foreground the richness of the temporal repertoire itself, rather than the topological structure of interactions.

Both strategies have yielded valuable insights, but they face important limitations. Measures of spontaneous activity can be confounded by common drivers (e.g., shared sensory inputs or global neuromodulatory fluctuations) which inflate apparent interactions and lead to overestimates of integration. Entropy-based metrics, on the other hand, may be

disproportionately sensitive to local variability and often rest on implicit assumptions about causal dependencies rather than testing them directly (Sarasso et al., 2021).

Perturbational approaches address these limitations by actively probing causal interactions through controlled stimuli and measuring the resulting spatiotemporal propagation of activity. The Perturbational Complexity Index (PCI) exemplifies this strategy, combining TMS with source-projected EEG responses compressed via the Lempel-Ziv algorithm to quantify the algorithmic complexity of the brain's causal repertoire: when a perturbation evokes an integrated yet highly differentiated response, the resulting spatiotemporal pattern is hard to compress and PCI is high, whereas responses that lack integration or are stereotyped yield easily compressible signals and low PCI (Casali et al., 2013; Sarasso et al., 2015; Casarotto et al., 2016). Despite these advances, important gaps remain. Different measures capture different structural and dynamical features of neural activity, and it is often unclear whether they are biased toward integration or differentiation. Bridging these gaps, by clarifying the scope, assumptions, and complementary strengths of each approach, is essential for a mechanistic understanding of how complexity supports consciousness.

In chapter 2, particularly in Article 5 (section 2.5), I address these gaps using large-scale neural mass simulations to systematically relate observational and perturbational complexity measures to underlying network topology, ranging from lattice-like to random to modular architectures. By examining spontaneous and evoked dynamics and assessing robustness to confounds such as common drivers, we disentangle the structural and dynamical determinants captured by each measure, clarify their complementarity, and provide a principled basis for interpreting complexity estimates as markers of conscious brain function. The results indicate that, while observational metrics are often confounded, PCI robustly identifies the optimal integration–differentiation balance of the underlying network, establishing it as a rigorous operationalization of brain complexity.

1.2 TMS-EEG as a Causal Perturbational Approach

A major advance in the empirical study of brain complexity has been the development of TMS combined with EEG (TMS-EEG). Unlike purely observational approaches, TMS-EEG provides a causal probe of cortical dynamics: a brief magnetic pulse locally excites neuronal populations, and the subsequent propagation of activity can be tracked across the brain with millisecond temporal precision. This capacity to actively perturb the system and then observe its spatiotemporal unfolding makes TMS-EEG suited to assess the brain's ability to generate responses that are both integrated and differentiated (Massimini et al., 2005; Casali et al., 2013). In doing so, it bypasses many confounds of spontaneous activity measures and directly tests the causal interactions that underlie complex neural dynamics. The following sections detail the principles of this approach and illustrate how it can be used to probe circuit- and network-level mechanisms of brain complexity.

1.2.1 Principles of TMS-EEG

TMS operates through the principle of electromagnetic induction: a very brief (~100 μs) and high-intensity current (~5 kA) in the coil generates a strong but transient magnetic field (~1–3 T). This field passes largely unattenuated through the scalp and skull, inducing an electric field in the underlying cortex. Neuronal elements aligned with this field, most effectively the axons of pyramidal neurons in superficial layers, can become depolarized. When the induced current is sufficiently strong, it triggers action potentials that propagate both orthodromically and antidromically, thereby recruiting local microcircuits as well as connected regions (Ilmoniemi et al., 1997; Ruohonen and Karhu, 2010; Hernandez-Pavon et al., 2023).

The downstream consequence of this perturbation is measurable with EEG. The scalp signal does not directly reflect action potentials but rather the summed postsynaptic potentials of large neuronal populations acting in synchrony (Nunez et al., 2006; Hernandez-Pavon et al., 2023). Averaging the EEG response across many stimulations yields the TMS-evoked potential (TEP), a characteristic sequence of deflections that capture the temporal evolution of cortical activation. The early components of the TEP are typically interpreted as indices of local excitability near the stimulation site, while the later components reflect trans-synaptic propagation and the recruitment of distributed networks. Thus, the TEP provides a reproducible physiological signature that encompasses both local cortical reactivity and large-scale effective connectivity. By combining a controlled external perturbation (TMS) with whole-scalp recording (EEG), this approach uniquely allows researchers to causally probe the dynamics of brain networks.

Over the past two decades, methodological refinements have progressively transformed TMS-EEG from an initial proof-of-concept into a robust and standardized research tool. A major challenge has been the removal of stimulation-related artifacts while preserving genuine neural responses. Advanced approaches such as signal-space projection, source-informed reconstruction, and independent component analysis now allow for effective suppression of these artifacts (Mutanen et al., 2016; Bertazzoli et al., 2021). In parallel, advances in source modeling enable increasingly precise localization of TMS-evoked activity (Gramfort et al., 2014), while the integration of TMS-EEG with structural and functional imaging provides essential anatomical context for interpreting propagation patterns (Casali et al., 2010; Casarotto et al., 2010; Atalay et al., 2025).

More recently, real-time visualization tools have further improved experimental control by allowing researchers to monitor TEP quality during acquisition and optimize stimulation parameters online (Casarotto et al., 2022). In addition, brain-state–dependent stimulation protocols, in which TMS pulses are triggered by specific EEG-defined patterns, have opened new avenues for investigating how cortical reactivity depends on ongoing brain dynamics (Zrenner et al., 2018; Wischnewski et al., 2024). Together, these methodological advances have

consolidated TMS-EEG as a reproducible, versatile, and uniquely causal approach for probing brain dynamics (Fig. 1.2).

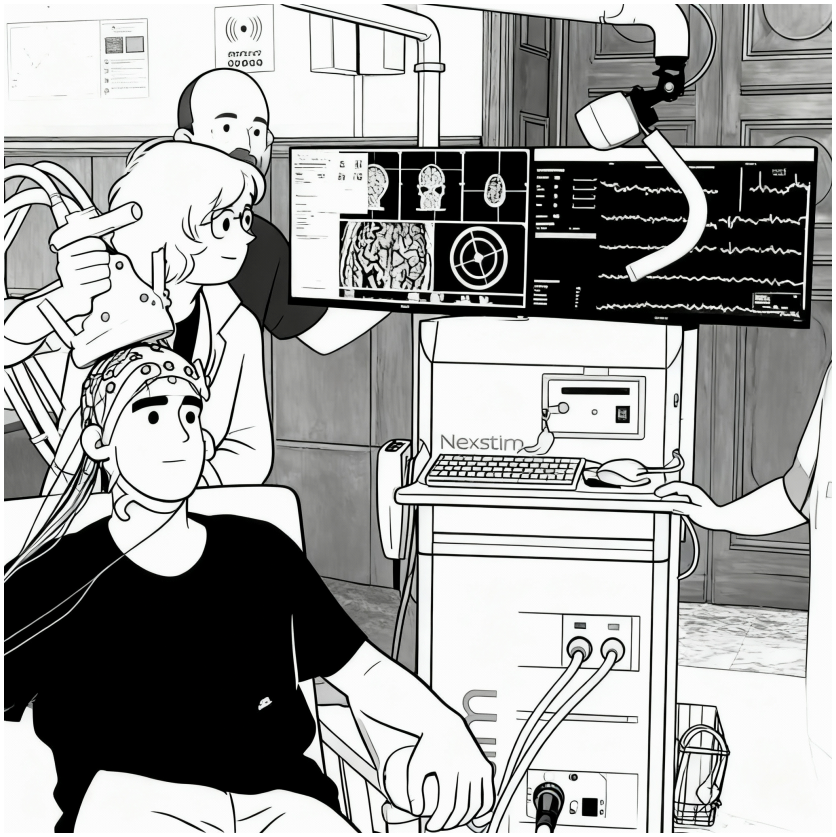

Figure 1.2 Schematic of a typical TMS-EEG recording session on a typical PhD student. This illustration shows the author as the experimental subject, wearing a high-density EEG cap while a neuronavigation-guided TMS coil targets a specific cortical region. The coil's brief magnetic pulse, visualized on the monitor co-registered to the author's MRI, induces an electric field that depolarizes superficial pyramidal neurons. Resulting action potentials propagate locally and to connected areas. Simultaneously, the EEG records summed postsynaptic potentials across the scalp.

1.2.2 Probing Circuit Differentiation with Site-Specific TMS

The early components of the TMS-evoked potential (TEP) provide a direct readout of local circuit properties and functional differentiation. These responses are highly focal, with maximal amplitudes observed at electrodes near the stimulation site, reflecting the intrinsic excitability and synaptic organization of the underlying cortical microcircuit (Fig. 1.3A-C) (Ilmoniemi et al., 1997; Komssi and Kähkönen, 2006). The characteristic waveform, defined by a sequence of peaks (e.g., P30, N45, P60), serves as an electrophysiological "fingerprint" of the stimulated neuronal circuit. The latencies and amplitudes of these peaks are sensitive to

GABAergic neurotransmission (e.g., N45 to GABAA, N100 to GABAB; Premoli et al., 2014), as well as to brain state (Massimini et al., 2005) and pathology (Ferrarelli et al., 2008).

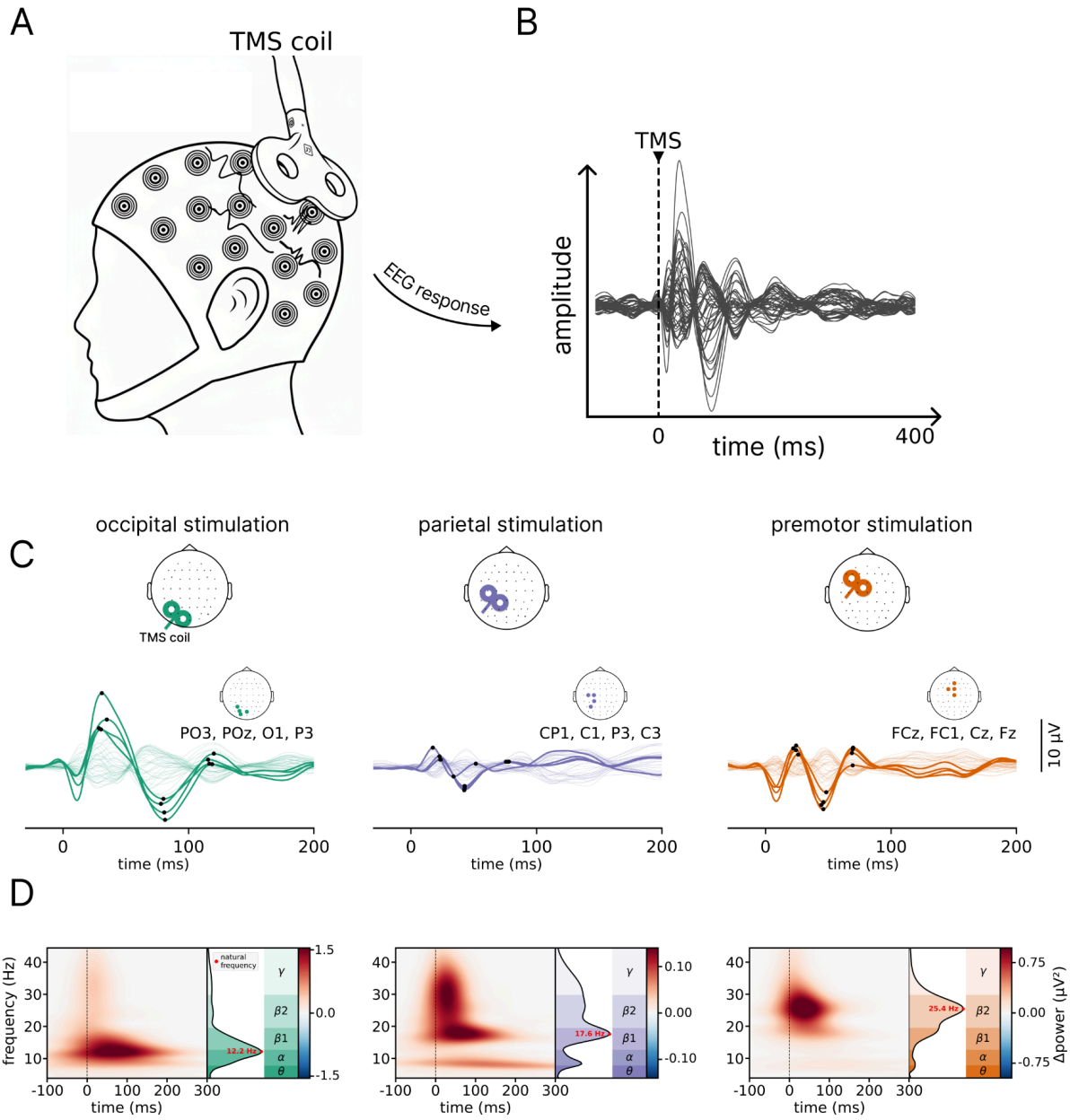

Figure 1.3 TMS-Evoked Potentials Reveal Circuit-Specific Properties and Natural Frequencies. **(A)** Schematic of the TMS-EEG experimental setup, where a magnetic coil delivers brief pulses to targeted cortical areas while high-density EEG simultaneously records neural responses across the scalp. **(B)** Representative butterfly plot displaying TMS-evoked potentials (TEPs) from all EEG channels after averaging across repeated stimulations, revealing the characteristic sequence of voltage deflections that constitute the cortical response signature. **(C)** Exemplary TEP waveforms from three distinct cortical regions—occipital (green), parietal (purple), and premotor (orange)

areas—demonstrating region-specific peak patterns and amplitudes. **(D)** Time-frequency analysis of the same three regions, showing how TMS induces frequency-specific oscillatory responses that manifest as "natural frequencies" characteristic of each cortical area. The power spectra reveal a posterior-to-anterior gradient in dominant frequencies, with occipital areas exhibiting lower natural frequencies than frontal regions, reflecting the intrinsic resonance properties of distinct cortico-thalamic circuits. Adapted from Article 1.

In the frequency domain, TMS evokes a resonant response at the stimulated area, which can be characterized by its natural frequency (Rosanova et al., 2009). Systematic mapping has shown that the natural frequency increased along the posterior-to-anterior axis (Fig. 1.3D). These frequency-specific responses reflect the intrinsic resonance of distinct cortico-thalamic circuits and provide a robust marker of local functional differentiation. Interestingly, shifts in natural frequency have been observed in the occipital cortex of blind individuals (Hassan et al., 2025) and in perilesional stimulations in stroke patients (Sarasso et al., 2020), suggesting its sensitivity to functional reorganization or disruption.

These circuit-level signatures form the foundation for *TEPpy* (Article 1; section 2.1), a standardized computational framework developed during the PhD. *TEPpy* is a python package enabling the reproducible extraction of peak amplitudes, latencies, and frequency-specific responses, providing a systematic method for characterizing circuit-level differentiation across the cortex.

1.2.3 Probing Large-Scale Integration through Propagation Dynamics

The later components of the TMS-evoked potential (TEP) provide a direct measure of the brain's capacity for large-scale integration, complementing early components that primarily reflect local circuit differentiation (see sec. 1.2.2). Unlike early, focal responses, late TEPs exhibit widespread spatial distributions dependent on the efficiency of long-range white matter connections and recurrent network feedback. Source-localized TMS-EEG combined with connectome-based computational modeling (Momi et al., 2023) demonstrates that early TEP components are primarily generated by local reverberatory activity, whereas late components (>100 ms) emerge from activity that propagates through distributed cortical and subcortical networks and re-converges on the stimulation site, reflecting recurrent, re-entrant processing essential for integrating information across specialized regions (Llinás et al., 1998; Lau and Bi, 2005; Edelman and Gally, 2013; López-González et al., 2021). Recent optogenetic and electrophysiological evidence further shows that these late TEPs are causally driven by thalamo-cortical rebound dynamics—stimulation-evoked thalamic hyperpolarization de-inactivates low-threshold Ca^{2+} currents and h-currents, triggering thalamic rebound bursts that precede and drive the widespread late cortical responses (Russo et al., 2025).
The spatiotemporal evolution of late TEPs indexes effective connectivity: activity spreads through anatomically constrained pathways, producing characteristic sequences of regional activation consistent with the structural connectome (Atalay et al., 2025). The extent, complexity, and persistence of these responses indicate the system's ability to sustain

coordinated, causally driven interactions, a hallmark of conscious brain function (Casali et al., 2013; Sarasso et al., 2015). This integrative capacity exhibits a hierarchical cortical gradient, with high-order transmodal regions (e.g., default mode and frontoparietal networks) producing more complex and sustained responses than unimodal sensory regions (Momi et al., 2025). Virtual lesion experiments confirm that silencing long-range feedback connections selectively reduces late responses in high-order areas, demonstrating their reliance on distributed network interactions (Momi et al., 2025).

Crucially, integration capacity is strongly state-dependent. In wakefulness, TMS evokes complex, widespread responses with sustained propagation and rich oscillatory structure. By contrast, during non-REM sleep, anesthesia, or pathological states such as coma, responses become simplified, with reduced spatial spread and temporal evolution (Massimini et al., 2005; Ferrarelli et al., 2010; Sarasso et al., 2015). This causal probing of large-scale effective connectivity thus provides a sensitive means of distinguishing between physiological and pathological states of consciousness, even when spontaneous EEG activity appears similar (Rosanova et al., 2012; Casarotto et al., 2024).

1.2.4 PCI as a Benchmark for Perturbational Complexity

Building on these empirical insights, the Perturbational Complexity Index (PCI) has emerged as a benchmark measure for quantifying the integration–differentiation balance using TMS-EEG (Casali et al., 2013). PCI captures the spatiotemporal richness of TMS-evoked responses by assessing their algorithmic compressibility, thereby providing a principled readout of the brain's capacity for complex dynamics. High PCI values reflect responses that are both spatially extensive (integration) and temporally diverse (differentiation), whereas low values reflect either fragmented local responses or globally stereotyped activity.

PCI has been validated across a range of contexts, including sleep (Casali et al., 2013), anesthesia (Sarasso et al., 2015), and disorders of consciousness (Casarotto et al., 2016). Its strength lies in three key features: first, by relying on controlled perturbations, PCI bypasses confounds inherent to resting-state analyses, such as spurious correlations driven by common inputs. Second, PCI forces the cortex to engage its endogenous causal interactions, providing a direct readout of the network's capacity for generating complex dynamics rather than inferring it from observations of ongoing fluctuations (Cattani et al., 2023). Third, the TMS-EEG methodology underpinning PCI directly stimulates and records cortical activity, entirely bypassing sensory transduction pathways, subcortical structures, and the motor system. This unique feature ensures that the measure is independent of the functional integrity of sensory and motor pathways, allowing for its reliable application in severely compromised patient populations (e.g., paralyzed, deafferented, or unconscious individuals) and enabling the assessment of any cortical region, from primary to associative areas (Rosanova et al., 2009).

The computational studies in chapter 2 substantiate PCI's theoretical foundations. Article 2 shows that whole-brain models exhibiting criticality also generate high PCI values in responses to perturbation, confirming the linkage between criticality and perturbational complexity (see section 1.1.2). Article 3 demonstrates that PCI is most sensitive to lesions of posterior structural hubs, highlighting its dependence on integration. Finally, Article 5 systematically compares PCI against observational measures across networks rewired from segregated to integrated architectures, demonstrating that PCI identifies the optimal integration–differentiation balance and remains robust under common driver confounds.

1.3 Mechanisms Underlying Brain Complexity and Its Loss

Brain complexity emerges from the interaction of architectural and dynamical mechanisms that balance integration and differentiation. Disruptions at multiple scales, structural or functional, can compromise this balance, leading to reduced complexity and impaired brain function. This section examines the fundamental mechanisms that govern brain complexity and their disruption across physiological conditions (sleep and anesthesia) and pathological states (brain injury), with particular emphasis on how these mechanisms contribute to alterations in consciousness and cognitive function.

1.3.1 Mechanisms for Complex Dynamics

1.3.1.1 Architecture Level

At the macroscale, the brain's structural topology provides the substrate for generating complex dynamics. The emergence of such dynamics is thought to directly reflect the anatomical arrangement of neuronal circuitry (Sporns et al., 2000, 2005; Honey et al., 2009; Betzel and Bassett, 2017; Fukushima and Sporns, 2020). Long-range connections link distributed regions to support global integration, while dense local clustering enables specialized processing and functional differentiation (Bullmore and Sporns, 2009; Bullmore and Sporns, 2012; Sporns, 2013; Cohen and D'Esposito, 2016). This balance is implemented through several canonical organizing principles. *Small-world organization* combines high clustering, which supports local specialization, with short path lengths that enable efficient global communication (Fig. 1.4A) (Watts and Strogatz, 1998; Bassett and Bullmore, 2017). *Modularity* provides functional segregation across subnetworks, allowing distributed specialization (Bertolero et al., 2015; Sporns and Betzel, 2016). *Hierarchical organization* allows interactions across multiple levels of processing, from local to global scales (Meunier et al., 2010; Hilgetag and Goulas, 2020; Pathak et al., 2024).

Crucially, this architecture is supported by highly connected hub regions that form a *rich-club organization*, acting as convergence points for distributed information and supporting global integration (Heuvel and Sporns, 2011, 2013; Senden et al., 2014; Gollo et al., 2015; Zamora-López et al., 2016; Griffa and Van den Heuvel, 2018). Conversely, spatial constraints

imposed by wiring cost favor local connectivity and metabolic efficiency, reinforcing functional segregation (Boucsein et al., 2011; Ercsey-Ravasz et al., 2013; Horvát et al., 2016). Within these densely connected clusters, recurrent connections and feedback loops form *triangular motifs* that sustain reverberatory activity (Kaiser et al., 2007; Hilgetag and Hütt, 2014), supporting both criticality and increased responsiveness to external perturbation (Fig. 1.4B) (Spiegler et al., 2016). The ubiquity of such recurrence across scales provides the structural basis for *re-entrant signaling* (Tononi et al., 1992; Edelman and Gally, 2013), whereby bidirectional, recursive exchanges between distributed regions enable spatiotemporal synchronization.

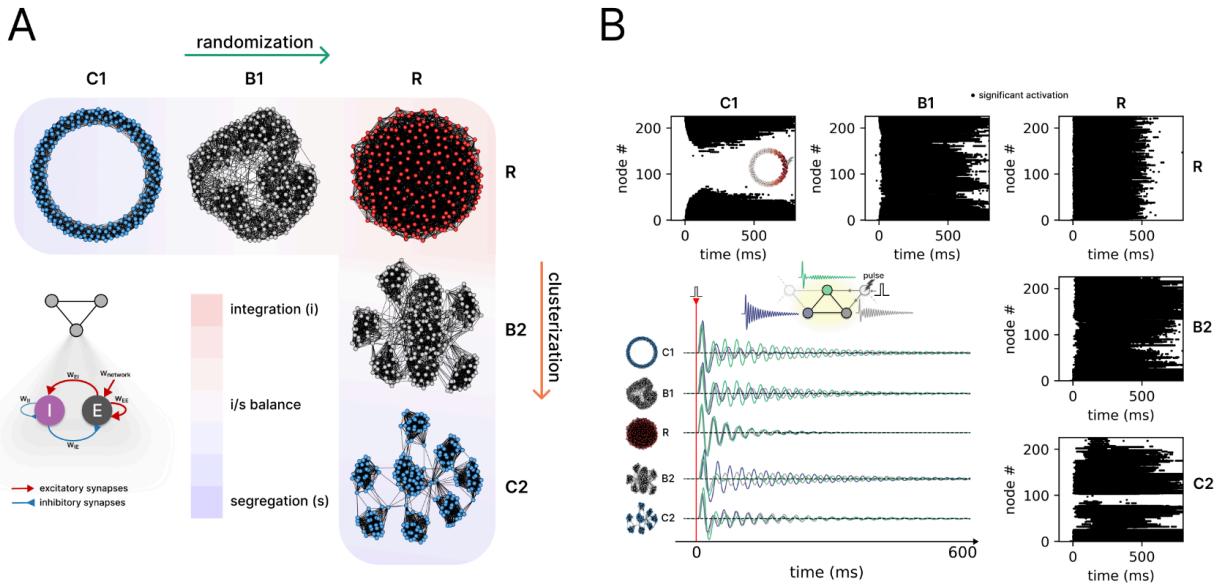

Fig. 1.4 Integration–Segregation Continuum: Network Construction and Signal Propagation. (A) Construction of network families spanning integration to segregation. Starting from a regular ring lattice (C1, top left), edges are gradually rewired to produce small-world architectures (B1) and ultimately a fully random network (R, top right). From R, a degree-preserving reclustering algorithm incrementally enhances community structure, yielding a modular intermediate (B2) and a highly segregated network (C2, bottom right). The resulting continuum captures regimes dominated by global integration (warm colors), local segregation (cool colors), or a balance of both (neutral shading). Each node is instantiated as a Wilson–Cowan unit (inset), comprising excitatory (E) and inhibitory (I) populations. **(B)** Spatiotemporal activation profiles following a single excitatory pulse to one node (schematized inset). Raster-style matrices show the times at which each node exhibits significant excitatory responses across network types along the randomization (C1→B1→R) and reclustering (R→B2→C2) axes. Below, averaged E activity across stimulation trials for three exemplar nodes—selected by highest area-under-curve in the first 20 ms—illustrate how network topology shapes the extent of signal propagation. C1 networks rapidly fail to recruit distant nodes, whereas R and C2 topologies support broader and more sustained activations. Adapted from Article 5.

At the microscale, the cerebral cortex is organized into minicolumns and local circuits that often display grid-like arrangements, particularly in posterior regions (Salin and Bullier, 1995;

Mountcastle, 1997; Buzsáki and Draguhn, 2004; Haun and Tononi, 2019). Such architectures are thought to provide an optimal balance between integration and differentiation, unlike strictly modular systems such as the cerebellum, whose feedforward, largely independent microzones appear ill-suited for sustaining high levels of complexity (Tononi, 2004). In posterior cortical areas, neurons are not only locally clustered but also interconnected in a convergent–divergent manner across areas, generating systematic overlap that supports strong integration and reentrant activity. These grid-like circuits, characterized by dense short-range connectivity, patchy long-range projections, and high overlap among connections, have been proposed as structural substrates of both brain complexity and conscious experience (Haun and Tononi, 2019). Empirical evidence supports this view: macroscopic measures such as EEG and fMRI indicate that loss and recovery of consciousness in sleep, anesthesia, or brain injury are closely tied to changes in posterior cortical complexity (King et al., 2013; Sitt et al., 2014; Luppi et al., 2019). Moreover, the topographic organization of grid-like areas ensures that variations in sensory space map systematically onto neural activity, such that lesions, disconnections, or stimulations of these circuits directly alter the structure of subjective experience, for example, producing hemianopia, neglect, or spatially localized phosphenes (Haun and Tononi, 2019). Thus, grid-like local architectures not only provide a mechanistic foundation for neural integration but may also underlie the phenomenology of extended space in conscious perception.

In Article 5 (section 2.5), I quantitatively linked these architectural principles to complexity by systematically rewiring networks from segregated to integrated regimes and benchmarking multiple complexity metrics; I showed that perturbational complexity peaks in small-world regimes where clustering and efficiency are jointly optimized, whereas observational metrics are biased toward either segregation or integration and are more vulnerable to common-driver confounds. I further demonstrated that recurrent motifs bolster late reverberation without sacrificing early propagation only when embedded in architectures that preserve short paths, thereby providing a structural explanation for the coexistence of integration and differentiation captured by PCI in balanced networks.

1.3.1.2 Dynamics: Criticality and the Order–Disorder Balance

Beyond architecture, complex dynamics require the brain to operate in an appropriate dynamical regime. As detailed in Section 1.1.2, the brain functions near critical points between order and disorder, a state that maximizes information processing capacities while avoiding pathological synchronization or uncorrelated noise (Beggs and Plenz, 2003; Chialvo, 2010). This criticality is not a uniform property across the brain. This architecture-dependent criticality suggests that heterogeneity across brain networks may support functional specialization. Different regions need not operate at the same point along the criticality continuum: variations in connectivity, for example, between sensory and association cortices, may place regions in distinct dynamical regimes. Recent electrophysiological analyses confirm this view: higher-order regions of the mouse visual cortex were found to be positioned closer

to criticality than primary sensory regions, consistent with their longer integration timescales and increased computational demands (Harris et al., 2024). Complementary large-scale neuronal recordings further reveal that signatures of near-critical scaling are widespread across the brain, with each area operating to a greater or lesser degree near the edge of instability (Morales et al., 2023).

In Article 2, I tuned whole-brain models to regimes exhibiting hallmarks of criticality—scale-free temporal fluctuations, long-range temporal correlations, infra-slow rhythms, and critical slowing down—and showed that only near these regimes do perturbations elicit widespread yet non-stereotyped responses with high PCI, mirroring conscious-state dynamics in empirical data. In Article 5, I provided complementary evidence by demonstrating that the architectural transition toward an optimal integration–segregation balance coincides with critical slowing down in evoked responses and yields an inverted-U relationship between PCI and network topology, thereby linking structural small-worldness, critical dynamics, and perturbational complexity within a unified framework.

1.3.2 Mechanisms Underlying Loss of Complexity in Physiological and Pathological Conditions

1.3.2.1 Graph-Level Disruption

Targeted alterations to brain network topology, including lesions or hub disruption, compromise global integration and the brain's capacity for long-range information propagation. Network theory demonstrates that removal of high-degree or high-betweenness nodes in scale-free networks produces rapid fragmentation and marked reductions in global efficiency, whereas random failures have limited impact (Albert et al., 2000). Extending these principles to human connectomes, Alstott et al., (2009) showed that lesions to high-centrality nodes induce nonlinear collapses in communication efficiency, yielding network "blackouts" far exceeding random node removal. Graph-theoretical metrics formalize this vulnerability: removal of critical nodes increases characteristic path length and reduces clustering, impairing both integration and segregation (Crucitti et al., 2004). Functional MRI studies corroborate these predictions, showing that hub lesions reduce small-worldness and modularity, diminishing the network's dynamic repertoire (Achard and Bullmore, 2007). Targeted disruption of rich-club hubs further compromises long-range communication, shifting processing toward local, less efficient pathways and triggering cascading connectivity failures (Rubinov and Sporns, 2010). Collectively, these findings establish that the loss of central nodes transforms networks from globally integrated, small-world architectures into fragmented, locally clustered states, mechanistically explaining reductions in brain complexity and the brain's capacity for coordinated, causally driven activity.

In Article 3, I addressed this principle of targeted hub disruption directly by implementing a large-scale computational model to systematically silence local nodes and quantify the

ensuing impact on brain complexity (Gaglioti et al., 2024). My findings confirmed that silencing highly central posterior hubs induced the most severe reductions in PCI, demonstrating a direct link between the disconnection of critical network nodes and the collapse of integrated, complex brain dynamics.

1.3.2.2 Electrophysiological Mechanisms: Cortical Bistability

A central mechanism underlying the loss of complexity is cortical bistability—the alternation between depolarized Up-states (ON-periods) with sustained firing and hyperpolarized Down-states (OFF-periods) of silence (Fig. 1.5) (Steriade et al., 1993). This bistability is the fundamental cellular mechanism underlying the large-scale, high-amplitude slow-wave activity observed in the EEG during deep NREM sleep and in pathological conditions such as coma and severe brain injury. It has been described as the "default activity pattern of cortical networks" (Sanchez-Vives et al., 2017) and arises from local circuit dynamics: recurrent excitatory reverberation sustains firing during the Up-state, but activity-dependent adaptation, such as the buildup of hyperpolarizing K+ currents, progressively destabilizes it, leading the network into a silent Down-state. Recovery is enabled by the relaxation of adaptation and stochastic fluctuations that can trigger reactivation.

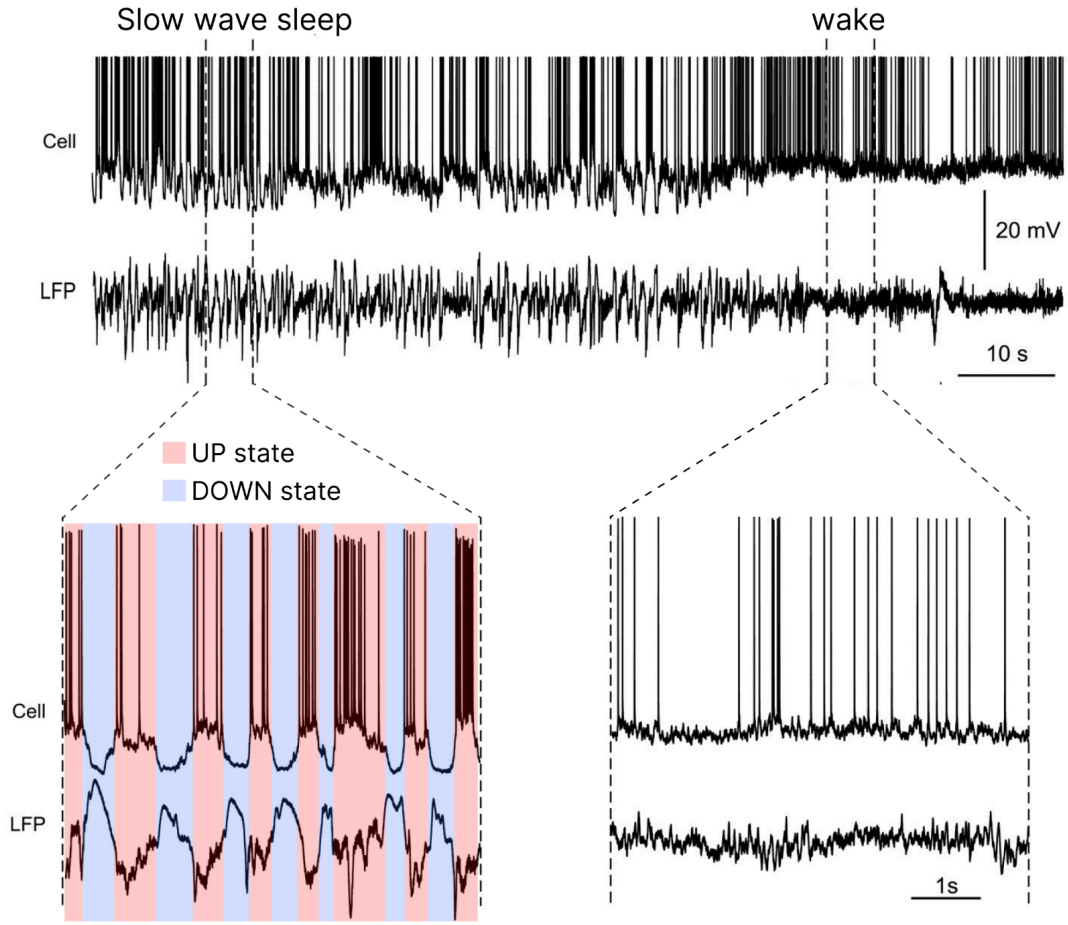

Fig. 1.5 Cortical Bistability During Slow-Wave Sleep. This figure illustrates the hallmark alternation between active (Up) and silent (Down) states in cortical neurons underlying slow-wave sleep. The top panels show a long-duration intracellular recording (Cell) alongside the corresponding local field potential (LFP) trace during deep NREM sleep (left) and wakefulness (right). Dashed boxes highlight segments expanded below. In the sleep inset, the cell trace alternates between depolarized Up-states—with sustained, high-frequency spiking—and hyperpolarized Down-states—marked by near-silence—reflected in the LFP as large-amplitude slow waves. Up-states (shaded pink) arise from recurrent excitatory feedback, while Down-states (shaded blue) result from activity-dependent adaptation (e.g., K^+ current buildup). The wake inset shows continuous depolarization and desynchronized LFP activity, indicating the absence of bistable switching. Adapted from Mukovski et al., (2007)

During NREM sleep and anesthesia, neuromodulatory changes (e.g., reduced acetylcholine) enhance adaptation, making cortical networks more prone to bistability (Fig. 1.6A). Functionally, this disrupts large-scale interactions: when a cortical module falls into a Down-state after activation, it becomes transiently unresponsive, breaking chains of causal propagation (Cattani et al., 2023). TMS-EEG studies capture this contrast directly: while a TMS pulse during wakefulness evokes complex, distributed activity, the same perturbation in sleep

or anesthesia produces a local, stereotypical slow wave—an evoked OFF-period—that halts propagation and reduces measures of complexity such as PCI (Casali et al., 2013).

Importantly, sleep-like bistability can also intrude during pathological wakefulness, though its spatial distribution and underlying causes differ between diffuse and focal injuries. In severe, multifocal brain damage leading to Unresponsive Wakefulness Syndrome (UWS), bistability manifests as a global phenomenon: TMS-EEG reveals stereotypical OFF-period-like responses across widespread cortical regions, including structurally intact areas. This suggests a systemic failure of neuromodulatory regulation or a critical degree of network disconnection that reveals the default bistable mode of the cortex, severely impairing large-scale integration and correlating with the absence of behavioral responsiveness (Rosanova et al., 2012; Casarotto et al., 2016). By contrast, after focal ischemic stroke, bistability emerges locally within perilesional zones, extending beyond the structural lesion core, where altered connectivity, neuromodulation, or inflammatory processes bias cortical circuits toward bistability (Massimini et al., 2024). Intracranial recordings demonstrate that this local bistability is not confined to the perilesional region but propagates along long-range axonal pathways, generating sleep-like slow waves in distant, connected cortical sites and producing a functional alteration that exceeds the structural damage (Russo et al., 2021). In both diffuse and focal cases, cortical bistability diminishes in parallel with clinical recovery, underscoring its role as a dynamic and reversible mechanism at the core of the breakdown, and restoration, of brain complexity.

In Article 4, I addressed the mechanisms of slow wave generation and propagation by developing a multiscale computational model of cortical circuits following a focal lesion. My work demonstrated that structural disconnection alone is a sufficient driver of local cortical bistability through a mechanism of disfacilitation. Furthermore, I identified that the propagation of these slow waves to distant areas is governed by both the hierarchical network structure and, crucially, the temporal coherence of slow oscillations from multiple afferent nodes, providing a mechanistic explanation for the percolation of sleep-like activity in the awake injured brain.

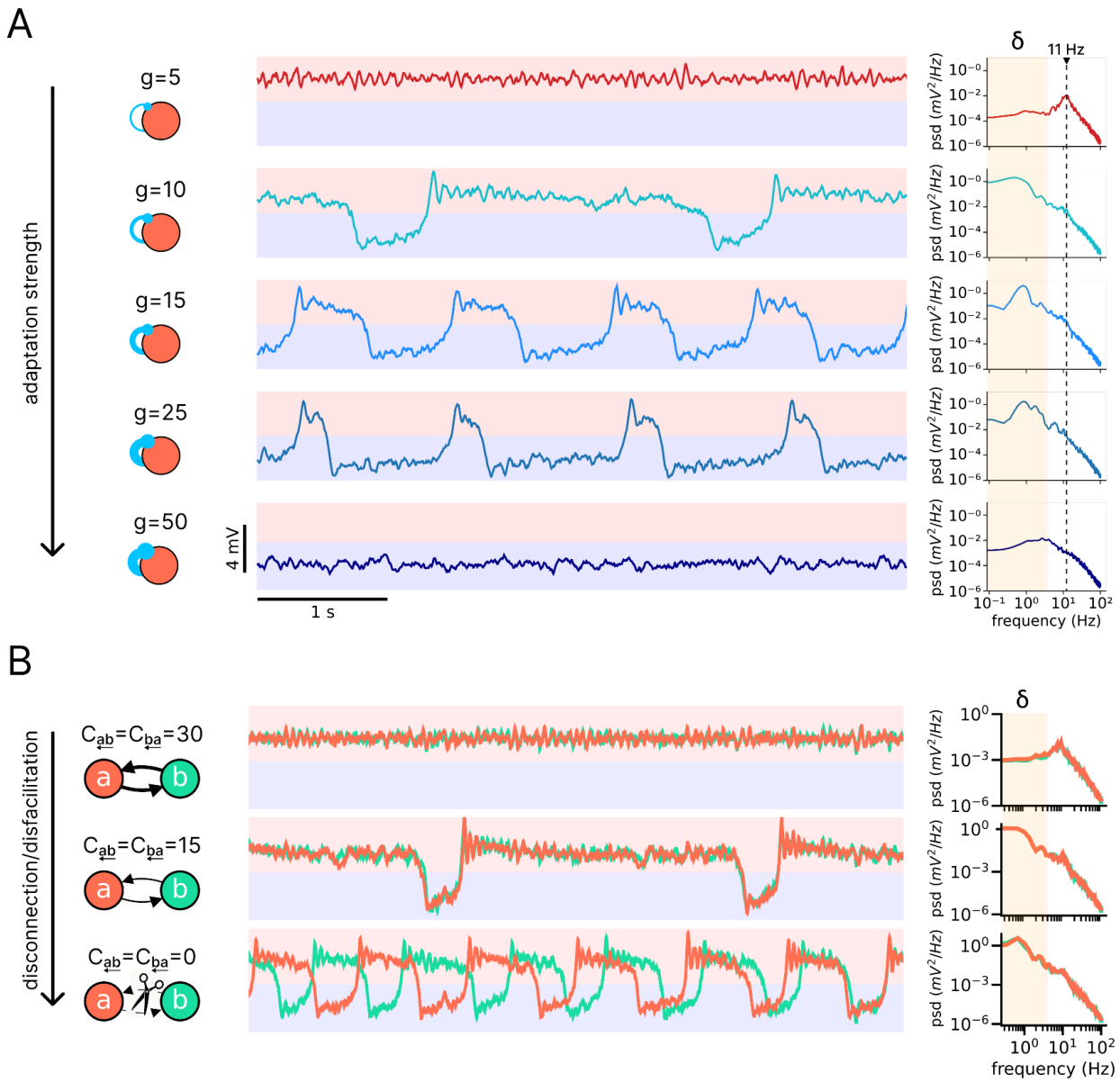

Fig. 1.6 Cortical bistability in a neural mass model. (A) Single-population dynamics as adaptation strength (g) increases. At low g (e.g., g = 5), the population exhibits a persistent Up-state with ~10 Hz oscillations and ~7 mV amplitude, mimicking wake-like cortical activity. Intermediate g yields slow oscillations with alternating Up (≈7 mV) and Down (≈4 mV) states and increased δ-band power, characteristic of slow-wave sleep. At high g (e.g., g = 50), Down-states dominate. The panels on the right show corresponding power spectral densities highlighting the shift from alpha to delta peaks. (B) Two symmetrically coupled neural masses (a and b) with fixed adaptation and varying excitatory coupling strength (C). Strong coupling (C = 30) produces alpha-band Up-states. Reducing C drives a transition to slow waves with enhanced δ power and intermittent Down-states, reflecting increased "disfacilitation" (i.e., reduced excitatory input). When decoupled (C = 0), each mass enters frequent, regular slow oscillations but loses synchrony due to the absence of coupling. Model details and further analyses are presented in Article 4. Adapter from article 4.

1.3.2.3 Complementary Neural Mechanisms

The balance between excitatory and inhibitory neural activity (E/I balance) represents another crucial mechanism affecting brain complexity. This balance is fundamental to cortical function, determining network dynamics, computational capacity, and information processing capabilities (van Vreeswijk and Sompolinsky, 1996; Brunel, 2000). Disruption of E/I balance in either direction can lead to convergence toward bistability as a default cortical state, since bistability represents the natural attractor for cortical networks when normal activation patterns are perturbed (Sanchez-Vives et al., 2017). An optimal E/I balance is thought to be necessary for maintaining networks near a critical point, maximizing dynamic range and information processing (Shew et al., 2009; Shew and Plenz, 2013). Alterations to this balance can push networks toward pathological states. For instance, a strong shift toward inhibition (e.g., via enhanced GABAAergic tone by propofol) can promote bistability and unconsciousness (Colombo et al., 2019). A similar inhibitory shift may also arise from structural lesions, where the disruption of excitatory fibers alters the E/I balance (Massimini et al., 2024), resulting in cortical bistability (Fig. 1.6B). Conversely, a shift toward excitation can lead to hyper-synchronized, epileptiform activity, also incompatible with complex dynamics.

Another candidate mechanism for the breakdown of complexity involves the decoupling of apical and basal dendritic compartments in layer 5 pyramidal neurons (Takahashi et al., 2016; Aru et al., 2020; Suzuki and Larkum, 2020). These neurons integrate bottom-up and top-down signals through backpropagation-activated calcium firing, whereby coincident somatic and dendritic inputs elicit dendritic calcium spikes that convert single spikes into bursts (Larkum et al., 2004; Larkum, 2013). Anatomically, basal dendrites predominantly receive feedforward inputs from lower hierarchical areas, while apical dendrites, extending into layer 1, receive feedback from corticocortical and thalamocortical loops, making apical–basal coupling a critical substrate for large-scale integration (Larkum, 2013). During anesthesia and other states of reduced consciousness, this coupling is disrupted: apical and basal compartments operate independently, selectively impairing feedback while preserving feedforward processing (Suzuki and Larkum, 2020). Experimental work shows that diverse anesthetics (isoflurane, ketamine, propofol) converge on this mechanism, blocking apical integration and thereby preventing the reverberant interactions required for complex dynamics (Suzuki and Larkum, 2020). In vivo imaging further demonstrates compartment-specific effects: under anesthesia, both apical and basal dendrites show internal synchrony, but only basal dendrites remain coupled to somatic activity, indicating selective apical decoupling (Bharioke et al., 2022). This disruption effectively blocks cortico-thalamic feedback loops while sparing feedforward transmission, breaking the balance of integration and segregation that sustains complexity. Importantly, higher-order thalamic nuclei may regulate this gating of apical inputs, positioning the thalamus as a key modulator of dendritic computation and cortical integration. Thus, dendritic decoupling provides a unifying cellular-level mechanism through which

distinct anesthetics, and potentially sleep or brain injury, converge to impair large-scale effective connectivity and reduce the complexity of cortical dynamics.

1.4 Computational Modeling of Large-scale Complex Brain Dynamics

Computational modeling provides a complementary framework to empirical measures for investigating the mechanisms underlying brain complexity. While techniques like TMS–EEG and PCI offer direct causal probes of the brain's capacity for integrated and differentiated dynamics, models enable controlled causal inference through systematic parameter manipulation, network reconfiguration, and simulation of perturbations that are ethically or technically infeasible in vivo. This approach bridges scales from subcellular processes to whole-brain networks, revealing how local biophysics, connectivity topology, and emergent dynamics contribute to the emergent complexity. By reproducing empirical observables, such as spectral signatures, functional connectivity patterns, and perturbational responses, models furnish testable predictions about the structural and dynamical substrates of consciousness, cognition, and pathology (Deco et al., 2008; Breakspear, 2017). This section will briefly introduce the main modeling approaches and the types of questions they allow us to address, while more detailed methodological descriptions are deferred to the methods sections of the articles presented in Chapter 2.

1.4.1 Modeling Approaches: From Single Neurons to Neural Masses to Whole-Brain Networks

The computational modeling of brain dynamics operates across multiple spatial and temporal scales, each associated with distinct mathematical frameworks, assumptions, and applications. These levels of abstraction are not isolated but complementary, allowing researchers to bridge detailed biophysical mechanisms with large-scale emergent phenomena such as rhythms, synchronization, and complexity.

Microscale models. At the cellular level, the gold standard is the Hodgkin–Huxley type model (Hodgkin and Huxley, 1952), which provides a biophysically detailed description of how ionic currents give rise to action potentials. The dynamics of the membrane potential $V(t)$ of a single neuron are governed by the balance between capacitive and ionic currents:

$$C_m \frac{dV}{dt} = -\sum_i I_i(V,t) + I_{\text{ext}}(t),$$

where C_m is the membrane capacitance, I_i are ionic currents (e.g., sodium, potassium, leak), and I_{ext} is an externally applied current. Each ionic current is typically controlled by gating variables that follow voltage-dependent kinetics of the form:

$$\frac{dx}{dt} = \alpha_x(V)(1-x) - \beta_x(V)x,$$

where x represents the open probability of a channel gate. Such models reproduce the full richness of neuronal excitability, including spike initiation, refractoriness, bursting, and adaptation, but their complexity makes them computationally expensive when simulating large networks of interacting neurons (Herz et al., 2006).

To address this limitation, simplified spiking models have been developed. The leaky integrate-and-fire (LIF) model, for example, abstracts the neuron as a linear RC circuit with a threshold mechanism:

$$\tau_m \frac{dV}{dt} = -(V - V_{\text{rest}}) + RI_{\text{syn}}(t),$$

where τ_m is the membrane time constant, V_{rest} is the resting potential, and I_{syn} is the total synaptic input. When the potential reaches a threshold V_{th}, the neuron emits a spike and is reset. While highly reductive, LIF models permit the simulation of large neuronal networks and still capture important collective phenomena such as oscillations and synchronization. More refined spiking models, such as the adaptive exponential integrate-and-fire (AdEx) model (Brette and Gerstner, 2005), introduce nonlinear spike initiation dynamics and adaptation currents, striking a balance between realism and efficiency. Importantly, it has been shown that networks of AdEx neurons can reproduce fundamental aspects of cortical dynamics, including the transition from wake-like asynchronous irregular firing to sleep-like synchronous slow oscillations (Destexhe, 2009; Zerlaut et al., 2018). In these models, activity-dependent adaptation currents promote alternating phases of high (Up-state) and low (Down-state) activity, thereby generating the bistability that characterizes cortical slow waves, as described in Section 1.3.2.2. This line of work shows how relatively simple neuron models, when embedded in recurrent networks, can account for macroscopic state changes such as the onset of sleep, bridging single-cell properties with emergent large-scale bistable dynamics.

Mesoscale models. At the level of local populations or cortical columns, neural mass models provide a natural abstraction by describing average activity (e.g., mean firing rate or mean membrane potential) rather than tracking individual spikes. This approach relies on assumptions of homogeneity and large numbers, effectively smoothing out microscopic fluctuations.

One of the canonical frameworks is the Wilson–Cowan model (Wilson and Cowan, 1972, 1973), which captures the interaction between excitatory (E) and inhibitory (I) subpopulations:

$$\tau_E \frac{dE}{dt} = -E + S_E\big(w_{EE}E - w_{EI}I + P_E + \eta_E(t)\big),$$

$$\tau_I \frac{dI}{dt} = -I + S_I\big(w_{IE}E - w_{II}I + P_I + \eta_I(t)\big),$$

where w_{ab} denote coupling weights between populations, P_E and P_I are external inputs, S are nonlinear sigmoidal transfer functions, and η represents fluctuations. Despite its simplicity, this model reproduces essential dynamical features such as oscillations, bistability, and traveling waves (Harris and Ermentrout, 2018), and it provides an interpretable link between physiology and network-level phenomena. An implementation of the Wilson–Cowan model was employed in Article 5 (Section 2.5) to assess the structural determinants of complexity metrics.

Another widely used mesoscale model is the Jansen–Rit neural mass model (Jansen and Rit, 1995), originally designed to model the generation of EEG rhythms in a cortical column. It comprises three interacting populations (i.e., pyramidal cells, inhibitory interneurons, and excitatory interneurons) connected in a loop through synaptic kernels and nonlinear firing rate functions. This model naturally generates oscillatory rhythms in the alpha band and has been applied extensively in the study of evoked responses (David et al., 2005; Momi et al., 2023, 2025). In Article 4 (Section 2.4), I extended the Jansen–Rit model with a spike-frequency adaptation mechanism to investigate how local and external circuit properties shape slow-wave dynamics.

Macroscale models. At the whole-brain level, population models are embedded in anatomically informed networks derived from structural connectivity (e.g., diffusion MRI tractography). These large-scale network models integrate local population dynamics with long-range axonal connections and conduction delays, thereby simulating brain-wide activity. A general formulation takes the form:

$$\frac{d\mathbf{x}_i}{dt} = F(\mathbf{x}_i) + \sum_{j=1}^{N} C_{ij} G(\mathbf{x}_i, \mathbf{x}_j(t - \tau_{ij})) + \xi_i(t),$$

where $\mathbf{x}_i$ is the state vector of region i, F describes the intrinsic local dynamics (often given by a neural mass model), C_{ij} is the structural connectivity weight from region j to region i, G is a coupling function, τ_{ij} is the axonal conduction delay, and $\xi_i(t)$ accounts for stochastic fluctuations.

Such models enable the study of resting-state dynamics, large-scale oscillations, responses to perturbations (e.g., TMS or sensory stimulation), and pathological states such as seizures or brain injury. They form the basis of simulation platforms such as The Virtual Brain (Sanz Leon

et al., 2013) and neurolib (Cakan et al., 2021), which integrate empirical connectomic data with neural mass modeling. In Articles 2–5 (Chapter 2), I employed this framework to investigate the mechanisms of brain complexity and its breakdown, systematically testing how different local models (e.g., Wilson–Cowan, Larter-Breakspear, Jansen–Rit) interact with the structural connectome to give rise to large-scale network dynamics.

1.4.2 The Role of Modeling in Studying Brain Complexity

Computational modeling plays a pivotal role in studying brain complexity by providing a controlled environment to test mechanistic hypotheses about how brain architecture and dynamics give rise to the balance between integration and differentiation. Unlike empirical methods, which are constrained by ethical and technical limitations, models allow systematic manipulation of parameters, network topology, and perturbation protocols, thereby isolating causal factors underlying complex dynamics (Deco et al., 2015; Breakspear, 2017). Modeling bridges theoretical frameworks—such as those linking brain complexity and criticality—with empirical data, revealing how local circuit properties scale up to global network behaviors and how local or global disruptions lead to the loss of complexity.

A key contribution of modeling is the simulation of perturbational dynamics that mimic TMS–EEG experiments, enabling the quantification of how evoked responses depend on structural and dynamical regimes. By injecting brief pulses into selected nodes, models generate synthetic time series from which PCI can be computed, testing how factors such as global coupling strength, conduction delays, and local excitability modulate the spatiotemporal richness of responses (Gaglioti et al., 2024, 2025). Near criticality, networks exhibit prolonged, non-stereotyped cascades with high perturbational complexity, whereas subcritical regimes yield fragmented responses and supercritical regimes produce synchronized but undifferentiated activity.

Modeling also elucidates the structural dependencies of complexity through network rewiring experiments. By varying topologies from segregated lattices to integrated random graphs, simulations show that complexity peaks in small-world architectures, where local clustering supports differentiation and short paths enable integration (Rubinov and Sporns, 2010). As shown in Article 5 (Section 2.5), PCI exhibits an inverted-U sensitivity to this balance, while spontaneous measures show systematic biases—some increasing with integration, others with segregation—underscoring modeling's ability to dissect metric-specific behaviors. Local manipulations, such as virtual lesions, further reveal how focal disruptions cascade to reduce global complexity, often preserving spontaneous diversity while collapsing evoked spatiotemporal propagation (Gaglioti et al., 2024).

Moreover, models incorporating biophysical mechanisms such as activity-dependent adaptation clarify how pathological states emerge from structural and dynamical alterations. In Article 4 (Section 2.4), I implemented a neural mass model with spike-frequency

adaptation, showing how local disconnection induces cortical bistability that propagates along structural pathways, consistent with experimental evidence. Recent work by Sacha et al. (2025) further extends this framework by integrating $GABA_A$ and NMDA receptor modulation into a biophysically grounded mean-field model of anesthesia, demonstrating that anesthetic-induced shifts in excitatory/inhibitory dynamics give rise to emergent cortical Up–Down bistability which markedly reduces perturbational complexity.

Articles 2–5 in Chapter 2 collectively illustrate modeling's role in complexity research. Article 2 tunes whole-brain models to reproduce critical-like regimes with high PCI. Article 3 quantifies how local manipulations differentially affect spontaneous and evoked complexity indices. Article 4 models slow-wave generation and propagation after brain lesions, exploring mechanisms of complexity loss. Article 5 evaluates the sensitivity of different metrics to integration–segregation balance, validating PCI as a robust index of the theoretical notion of brain complexity.

1.4.3 Standardization, Parameter Tuning, and Calibration

The reproducible investigation of complex brain dynamics via computational modeling requires standardized frameworks integrating simulation platforms, analysis pipelines, and validation protocols. Without such standardization, the diversity of ad-hoc modeling approaches produces inconsistent parameter choices, limited transferability, and reduced comparability across studies (Gutzen et al., 2018; Trensch et al., 2018). This challenge is particularly acute in whole-brain modeling, where the high-dimensional parameter space of neural mass models—spanning local excitatory and inhibitory couplings, conduction delays, and intrinsic timescales—combined with complex empirical validation targets renders models prone to overfitting and poor generalization.

Whole-brain models based on neural mass approximations can reproduce large-scale neural dynamics, but their biological realism critically depends on careful parameter calibration (Breakspear, 2017; Griffiths et al., 2022). The fundamental goal is to simultaneously capture features of spontaneous and evoked activity within a unified framework. Spontaneous dynamics must display rhythmic oscillations, infra-slow fluctuations (<0.1 Hz), scale-free spectral properties, and spatiotemporal heterogeneity characteristic of resting-state complexity (Palva and Palva, 2012; Deco et al., 2017), while evoked dynamics must yield spatially distributed, non-stereotyped responses to perturbations, quantified for instance by the Perturbational Complexity Index (PCI) (Casali et al., 2013). The relationship between intrinsic variability and evoked complexity reflects a general principle: networks with richer spontaneous fluctuations and critical-like dynamics are more capable of sustaining complex, non-stereotyped responses (Beggs and Plenz, 2003; Shew and Plenz, 2013). Accordingly, parameter tuning targets regimes exhibiting criticality signatures, such as 1/f spectral scaling, long-range temporal correlations, and heightened sensitivity to perturbations, collectively maximizing the system's dynamic range and information-processing capacity.

To address these challenges, Article 2 (section 2.2) introduces an integrated workflow combining The Virtual Brain (TVB) simulation platform with the Collaborative Brain Wave Analysis Pipeline (Cobrawap). TVB supports whole-brain simulations with neural mass models such as Wilson-Cowan and Jansen-Rit, coupled via realistic connectomes including conduction delays and heterogeneous local parameters, while Cobrawap provides standardized, quantitative metrics for characterizing brain dynamics across heterogeneous datasets (Gutzen et al., 2024). This integration maps neural masses in the TVB simulation to analysis channels in Cobrawap, transforming parameter selection into a quantitative optimization guided by biologically relevant observables. The TVB–Cobrawap framework establishes fully reproducible workflows from whole-brain simulation and analysis to parameter tuning, enabling cross-laboratory replication and direct comparison between simulated and empirical data. Automated parameter exploration is supported through tools like the Learning-to-Learn framework (Yegenoglu et al., 2022), allowing data-driven refinement of global coupling, local time constants, conduction velocities, and other biophysical parameters. Delivered through EBRAINS, this framework ensures broad accessibility and fosters collaborative standardization in computational neuroscience.

1.5 Aims and Thesis Outline

The overarching goal of this thesis is to elucidate the mechanistic foundations of brain complexity, conceptualized as the optimal balance between integration and differentiation, by combining empirical TMS-EEG approaches, standardized computational modeling, and systematic evaluation of complexity metrics. The work is structured around five interrelated articles, presented in Chapter 2, each addressing a distinct but complementary aim:

Aim 1: Establish a reproducible framework for quantifying local circuit differentiation

- *Article 1 ("A Standardized Framework for Mapping the Temporal and Spectral Signatures of TMS–Evoked Potentials")* develops and validates an open-source toolbox that automates detection of early TMS-EEG components, computes interpeak latencies, and estimates natural frequencies. These measures provide quantitative proxies for local circuit resonance and excitability across cortical regions, operationalizing differentiation at the local circuit level (section 2.1).

Aim 2: Standardize whole-brain computational models to capture complex brain dynamics

- *Article 2 ("Emergent complexity and rhythms in evoked and spontaneous dynamics of human whole-brain models after tuning through analysis tools")* implements biologically realistic neural mass models within The Virtual Brain and Cobrawap pipelines. Parameter tuning reproduces empirical spectral and evoked response features, establishing a robust modeling foundation for subsequent perturbational

analyses and bridging empirical TMS-EEG findings with mechanistic simulations (Chapter 2.2).

Aim 3: Quantify the impact of local manipulation on global complex dynamics

- *Article 3 ("Investigating the Impact of Local Manipulations on Brain Complexity Indices")* examines how targeted virtual lesions implemented via local node manipulations influence large-scale network dynamics. Silencing high-control nodes produces the largest declines in perturbational complexity, and lesion-induced slow waves propagate coherently to disrupt integration, highlighting the sensitivity of global complexity to local perturbations (section 2.3).

Aim 4: Model pathological slow-wave generation and propagation after brain lesions

- *Article 4 ("Slow Wave Generation and Propagation in a Model of Brain Lesion")* extends the Jansen-Rit model by incorporating activity-dependent adaptation, replicating Up–Down oscillations. These simulations reveal how structural disconnection drives slow-wave generation and propagation after cortical disconnection, providing mechanistic insight into the emergence of pathological dynamics observed in brain injured patients (section 2.4).

Aim 5: Evaluate and validate complexity metrics across integration–segregation regimes

- *Article 5 ("Different Sensitivity of Complexity Measures to Network Integration and Segregation")* systematically compares observational (e.g., LZc, neural complexity, functional complexity) and perturbational (PCI) metrics in rewired network architectures. Results confirm PCI's unique inverted-U sensitivity to integration-differentiation balance and its robustness against spurious correlations, validating its use as a principled measure of brain complexity (Chapter 2.5).

While the integration-differentiation framework is well-established, key challenges remain: a lack of standardized tools for quantifying circuit-level differentiation; a need for whole-brain models that accurately capture both spontaneous and evoked complex dynamics; and an unclear understanding of how different complexity metrics relate to the underlying theoretical construct. Furthermore, the mechanistic link between focal lesions and global complexity loss and the specific dynamics of pathological slow waves are not fully understood. This thesis addresses these gaps through a combined computational-empirical approach.

Consequently, the five articles of Chapter 2 form a coherent trajectory: from empirical quantification of local circuit differentiation (Aim 1), through standardized multi-scale modeling (Aim 2), to targeted manipulation of network dynamics (Aims 3–4), culminating in comprehensive evaluations of complexity metrics (Aim 5). This multi-tiered approach

provides mechanistic insight into brain complexity and establishes a framework with significant translational relevance for both fundamental neuroscience and clinical applications.

2

Results

2.1 Article 1

Title: *A Standardized Framework for Mapping the Temporal and Spectral Signatures of TMS–Evoked Potentials*

Authors: ***Gabriel Hassan****, ***Gianluca Gaglioti****, *Giulia Furregoni, Marta Porro, Letizia Bernardelli, Elena Focacci, Simone Sarasso, Mario Rosanova, Marcello Massimini, Silvia Casarotto*

Abstract: *Transcranial magnetic stimulation with EEG (TMS–EEG) provides a unique window into cortical circuit dynamics, but feature extraction from TMS-evoked potentials (TEPs) remains poorly standardized. We present TEPpy, a Python pipeline for reproducible and scalable quantification of canonical time- and frequency-domain TEP features. Applying TEPpy to stimulation of occipital, parietal, and premotor cortices in healthy adults, we find that early responses are spatially focal but region-specific in their dynamics. Importantly, temporal and spectral signatures revealed a shared posterior–anterior gradient: peak latencies shortened and inter-peak intervals decreased in parallel with a shift of natural frequency from occipital alpha to parietal and premotor beta rhythms. A simple temporal measure—the reciprocal inter-peak interval—closely tracked natural frequency and generalized across analysis settings, enabling robust, real-time estimation of local oscillatory tuning. These findings establish TEPpy as a standardized framework for TMS–EEG feature extraction and uncover a direct temporal–spectral coupling in cortical reactivity, providing a foundation for normative mapping and sensitive detection of pathological deviations.*

DOI: *forthcoming*

**These authors contributed equally*

1. Introduction

Transcranial Magnetic Stimulation combined with Electroencephalography (TMS-EEG) has emerged as a powerful perturb-and-measure paradigm for non-invasively probing human cortical reactivity across local and distributed networks (Ilmoniemi and Kicić, 2010). A single TMS pulse triggers a deterministic cascade of oscillations spanning several hundred milliseconds that propagate through cortico-thalamo-cortical circuits (Atalay et al., 2025; Momi et al., 2023; Russo et al., 2025). When responses from multiple pulses are averaged, TMS-evoked potentials (TEPs) form a reproducible waveform characterized by successive elicited components (Casarotto et al., 2010; Couto et al., 2025; Lioumis et al., 2009)

At a qualitative level, TEPs can be evaluated at first glance just by the shape of the waveform, to appreciate the differences between conditions and stimulation parameters. For example, real-time graphical user interfaces enable live monitoring of signal quality during data acquisition, thus providing an immediate visual readout of the evoked response and allowing to fine-tune coil orientation, intensity and minimize artifacts (Casarotto et al., 2022).

This first "pictorial" intuition of the TEPs features can be further investigated in a time domain perspective. In fact, evoked waveforms are defined by a sequence of peaks, each occurring at a characteristic latency and carrying amplitude information that varies with the cortical state and the stimulated site (Tremblay et al., 2019). Much of the literature has focused on stimulation of primary motor cortex (M1), uncovering highly reproducible latency invariants comparable to sensory evoked potentials (Beck et al., 2024a; Nuyts et al., 2025; Komssi and Kähkönen, 2006; Ferreri and Rossini, 2013; Nikulin et al., 2003). Such electrophysiological "fingerprints" allow inference about local excitability and synaptic activity. In this context, early components like N45 have been associated with $GABA_A$-mediated inhibition, whereas later components such as N100 implicate $GABA_B$-dependent processes (Premoli et al., 2014). These latency and amplitude features have been shown to be sensitive also to brain state transitions such as sleep (Massimini et al., 2005), anesthesia (Ferrarelli et al., 2010), psychiatric disorders (Dworkin et al., 2025) or neuropathology (Casarotto et al., 2019; Meneghini et al., 2025; Rosanova et al., 2018) beyond the primary motor cortex.

In parallel with time-domain analysis, frequency features of the TEPs have been used to study the intrinsic resonance properties of the brain. For example, Rosanova et al., (2009) demonstrated that stimulating occipital, parietal, or premotor areas consistently evokes α (8-12Hz), β (13-30Hz), or γ (>30Hz) activity respectively, indicating site-specific peaks in post-stimulus spectral power, the so-called "natural frequencies", that remain stable across healthy subjects. Spectral changes in the TEPs has also been linked to motor evoked potentials amplitude (Fecchio et al., 2017), schizophrenia symptoms (Donati et al., 2025; Ferrarelli et al.,

2012), stroke sequelae (Sarasso et al., 2020a) and induced pain (De Martino et al., 2024), potentially linking the functional state of the cortex to its frequency content.

Given this abundance of evidence, it's clear that TEPs contain a vast amount of information concerning brain reactivity and thus its functioning. However, this richness entails the challenge of unraveling all the information that can be extracted from the signal and the relationship between results stemming from different domains like time and frequency.

Although several TMS-EEG preprocessing pipelines (Atluri et al., 2016; Hassan et al., 2022; Rogasch et al., 2017; Wu et al., 2018) exist, the field presently lacks standardized tools for extracting a canonical and consensus established set of TEP features, leading to a large amount of different analysis methods with a vast parameters space.

Here, we present TEPpy, a Python-based pipeline (Fig. 1) designed to semi-automatically extract a comprehensive set of quantitative features from preprocessed single-pulse TMS-EEG data: (i) peak-to-peak amplitude of the early response, (ii) latencies of the first evoked peaks complex, (iii) inter-peak time, defined as the time lag between successive peaks of the same polarity, offering an estimate of the oscillatory period of the evoked response, and (iv) the natural frequency via time–frequency decomposition. We tested this tool on a dataset comprising 75 TMS-EEG sessions, evenly distributed across stimulation of the left occipital, parietal, and premotor cortices. The extracted features, systematically distinguished between stimulated areas. Notably, time-domain inter-peak intervals covaried robustly with frequency-based natural frequency, corroborating the physiological validity of the measures (consistent with the spectral tuning discussed in Rosanova et al., 2009). This tool thus responds to the field's need for a reproducible, scalable solution enabling rigorous, data-driven analysis of TEP latency, amplitude, and frequency features in both basic and clinical TMS-EEG studies.

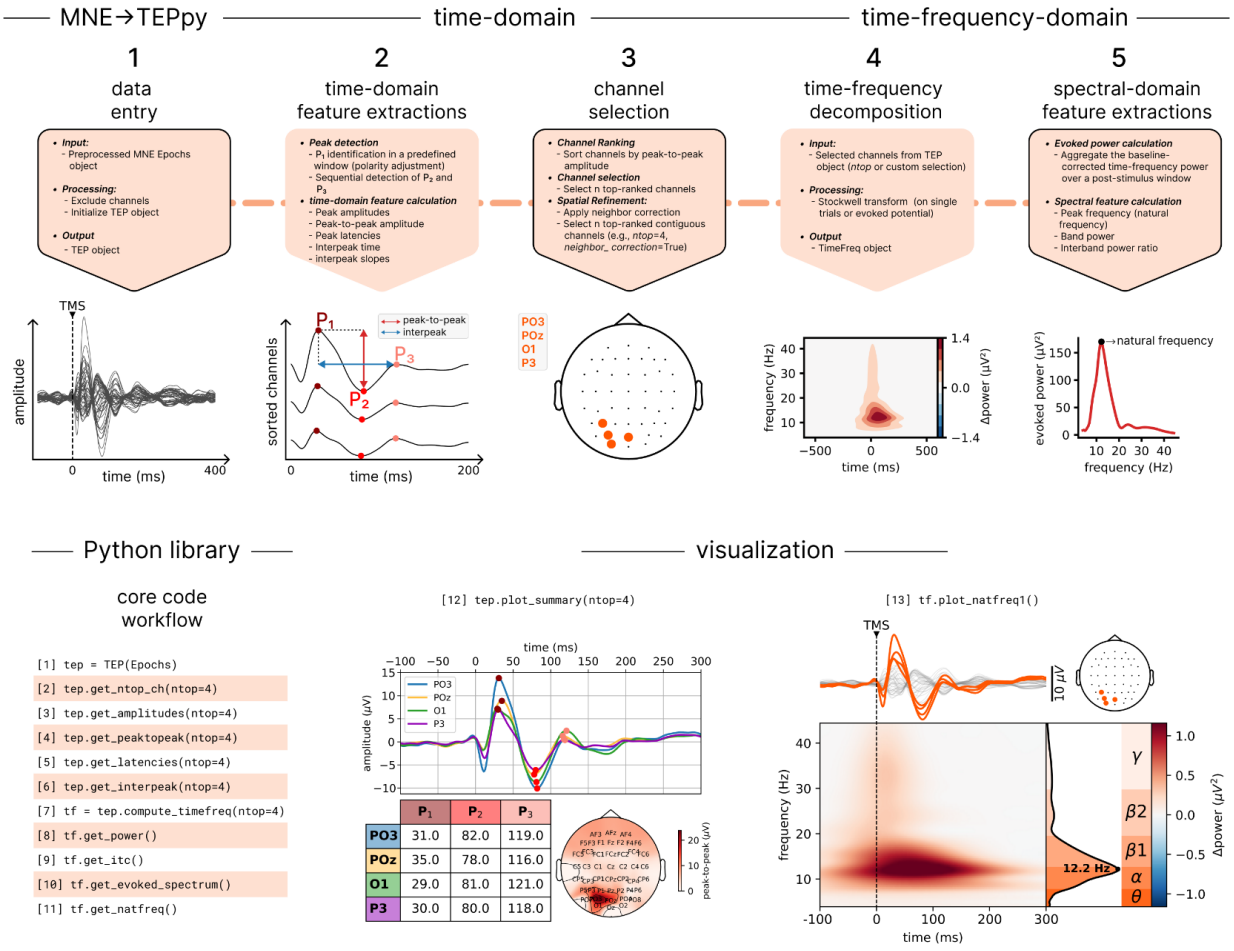

	P1	P2	P3
PO3	31.0	82.0	119.0
POz	35.0	78.0	116.0
O1	29.0	81.0	121.0
P3	30.0	80.0	118.0

Figure 1. Framework for extracting time- and frequency-domain features from TEPs. MNE-Python Epochs are converted into TEP objects (1), and peak components (P1, P2, P3) are detected semi-automatically with a predefined detection window for P_1. Temporal features—including amplitudes, latencies, peak-to-peak amplitudes, and interpeak times—are extracted (2). Channels are ranked by peak-to-peak amplitude, and the top n (set by the *ntop* parameter) are selected, with neighbor correction ensuring spatial contiguity (3). Signals from the selected channels (*ntop* or user-defined) are then decomposed with the Stockwell transform to generate time–frequency representations (4). From these, spectral-domain features are extracted, such as the evoked power spectrum—obtained by aggregating baseline-corrected power in a post-stimulus window—and the natural frequency (its peak frequency) (5). The example visualization (bottom panels) shows, on the left, the waveforms from the top four channels, detected peaks, a latency table, and a peak-to-peak amplitude topography, and on the right, a combined plot with TEP traces, sensor topography of the selected channels, time–frequency maps, and the evoked power spectrum.

2. Methods

Subjects

All procedures conformed to the Declaration of Helsinki and were approved by the local ethics committee (Comitato Etico Milano Area 1; TMS-EEG Prot. n. 609/07/27/05/AP). All participants provided written informed consent prior to enrollment.

The dataset comprised 75 single-pulse TMS-EEG sessions collected from 40 healthy adults (mean age = 32.7 ± 9.8; 20F). Participants reported no neurological or psychiatric disorders, no relevant medical conditions, and were not taking psychoactive or other medications.
Stimulation targeted the left occipital, parietal, and premotor cortices (25 sessions per site). Ten participants (mean age = 34.7 ± 10.6; 6F) completed three sessions each—one per target—yielding 30 paired sessions.

TMS-EEG Data Acquisition:

TMS was administered with a focal figure-of-eight coil connected to a Mobile Stimulator Unit (Nexstim Ltd.). Occipital, Parietal and Premotor stimulation targets were defined using a Navigated Brain Stimulation (NBS) system (Nexstim Ltd.) co-registered with individualized T1-weighted MRI scans. The left occipital (Brodmann areas 18/19) and the left premotor (Brodmann area 6) and the left parietal (Brodmann area 7) cortices were selected as stimulation targets. TMS-evoked EEG responses were recorded using TMS-compatible EEG amplifiers (64-channel Ag/AgCl electrode setup; Brain Products GmbH) at a 5000 Hz sampling rate with hardware filtering at 1000 Hz. The reference and ground electrodes were placed over the frontal sinus on the forehead, and input impedance was kept below 5 kΩ. Participants were seated comfortably and wore headphones playing customized noise to mask the TMS discharge sound (Russo et al., 2022). Stimulation parameters (intensity, coil orientation, and positioning) were individualized for each participant and cortical site to optimize cortical activation and to minimize scalp muscle artifacts, using the real-time TEP visualization tool described in Casarotto et al., 2022. Specifically, we targeted a minimum estimated electric field of 100 V/m and an early TEP peak-to-peak amplitude of at least 6 μV.

TMS-EEG Data Preprocessing:

First, the TMS pulse artifact was addressed by replacing the signal from −2 to 5 ms around each pulse with a mirrored segment taken from the pre-stimulus baseline, followed by a moving-average filter (4 ms window). Subsequently, EEG data were high-pass filtered at 1 Hz

using a zero-phase Butterworth filter (3rd order) and segmented into epochs spanning ±800 ms relative to the TMS pulse. Trials and channels containing artifacts were manually excluded via visual inspection. Retained epochs were re-referenced to the average reference and baseline-corrected using the pre-stimulus period. To mitigate ocular and muscular artifacts, Independent Component Analysis (ICA) was applied using the infomax algorithm (via EEGLAB's runica function); components reflecting muscular and ocular activity were identified and removed. Following ICA, data were low-pass filtered at 45 Hz (zero-phase Butterworth filter, 3rd order) and downsampled to 1000 Hz. Finally, bad channels were interpolated using spherical splines, and all epochs were trimmed to a final window of −600 to 600 ms around the TMS pulse

Time domain analysis

Peak detection. We developed a semi-automated algorithm to detect early TEP components (P_1, P_2, P_3) starting from MNE-Python Epochs objects (Fig. 1, step 1).
P_1 was searched for within a predefined window (10–40 ms post-TMS). Signal polarity (whether P_1 is a peak or trough) was determined using the TEPpy *convexity* method, which compares the TEP amplitude at the midpoint of the window to the mean amplitude at its edges:

$$\text{sign} = \text{sgn}\left(A_{\text{mid}} - \frac{A_{\text{start}} + A_{\text{end}}}{2}\right)$$

where A_{mid}, A_{start}, A_{end} are TEP amplitudes at the midpoint, start, and end of the P_1 window, respectively. A positive sign indicated that the algorithm searched for a peak (local maximum) within the window to define P1, whereas a negative sign indicated that it searched for a trough (local minimum). Sequential peak detection proceeded with temporal constraints: if P_1 was a peak, P_2 was the first subsequent trough; if P_1 was a trough, P_2 was the first subsequent peak. P_3 was then identified as the next peak (if P_2 was a trough) or the next trough (if P_2 was a peak). A minimum interval between consecutive peaks of $1/(2\times low\_limit)$ seconds was enforced, with *low_limit*=35 Hz corresponding to 14 ms. Peak/trough detection in TEPpy used SciPy's *find_peaks* function.

Temporal feature extraction. From the detected peaks, we extracted (Fig. 1, step 2) peak-to-peak amplitude (absolute difference in μV between P_1 and P_2), peak latencies (time occurrences in seconds of P_1, P_2, and P_3), interpeak time (temporal interval in seconds between P_1 and P_3), and 1/interpeak (reciprocal transformation to convert the unit from seconds to Hz). All features were computed for each individual channel and subsequently averaged across the selected channels for group-level analysis.

Channel selection. Channels were ranked by peak-to-peak amplitude (P_1-P_2 amplitude), and the top 4 channels were selected throughout the study (*ntop* parameter) unless otherwise specified (Fig. 1, step 3). Spatial contiguity was controlled using EEG sensor adjacency matrices: the algorithm (*neighbor_correction* method in TEPpy) retained channels within the connected component containing the channel with the highest-amplitude peak-to-peak, supplementing selections with the next highest-amplitude neighbors in the same component when fewer than *ntop* contiguous channels were initially identified. This ensured selected channels represented focal cortical responses rather than spatially disconnected sensors.

Time-frequency domain analysis

Spectral decomposition. Time-frequency analysis (Fig. 1, step 4) employed the Stockwell transform (ST), a decomposition method providing frequency-dependent resolution by combining Fourier and Gaussian windowing. The ST was computed via MNE-Python's implementation (*stock1* method in TEPpy) on the TEP time-series, with width=0.7, a parameter used to balance temporal precision and frequency resolution. Analyses focused on 4-45 Hz activity from the same 4 channels selected for temporal feature extraction (*ntop* = 4).

Natural frequency quantification. Time-frequency power was baseline-corrected by subtracting the mean pre-stimulus power (-500 to -100 ms) for each frequency bin. Evoked power was computed by summing baseline-corrected power within a post-TMS window:

$$P_{\text{evoked}}(f) = \sum_{t=t_{\text{start}}}^{t_{\text{end}}} P(f,t)$$

where $P(f,t)$ is the baseline-corrected power at frequency f and time t, with t_{start}=20 ms and t_{end}=120 ms. Finally, the natural frequency (Fig. 1, step 5) was defined as the frequency f at which the evoked power $P_{evoked}(f)$ reached its maximum value (peak frequency), as in (Mario Rosanova et al., 2009).

We assessed parameter sensitivity by varying Stockwell width (0.5–1.5 in 0.1 increments), temporal summation window (20–120 ms, 20–150 ms, 20–200 ms, 20–250 ms), and number of selected channels (*ntop* = 1, 2, 3, 4, 5, 6, 8, 10, 15, 20, 30, 46).

Statistical analysis

All statistical analyses were performed using Python (check version, REF) with SciPy (check version, REF) and scikit-posthocs (check version, REF) libraries. Non-parametric methods were employed throughout due to violations of normality (Shapiro-Wilk test) and/or heterogeneity of variance (Levene test). For between-group comparisons across stimulation sites (occipital, parietal, premotor), we applied Kruskal-Wallis tests to examine differences in peak latencies,

interpeak times, and natural frequencies. Significant main effects ($p < 0.05$) were followed by Dunn's post-hoc tests with Holm-Bonferroni correction. Within-subject analyses for participants receiving all three stimulations ($n = 10$) used Friedman tests with post-hoc Wilcoxon signed-rank tests and Holm-Bonferroni correction. Correlation analyses between features employed Pearson correlation (r), while the relationship between 1/interpeak times and natural frequencies was modeled using ordinary least squares regression (*linregress* function from SciPy). Throughout the text, data are presented as mean ± standard deviation (SD). In figures, box plots depict the 5th and 95th percentiles (vertical lines), interquartile range (boxes), and median (horizontal line).

3. Results

We investigated the oscillatory responses evoked by TMS delivered to three distinct left-hemispheric sites: occipital, parietal, and premotor cortices. Using a novel Python-based analytical framework, we demonstrate that the early local TEP reflects spatially, temporally and spectrally specific properties of the underlying cortical circuits, enabling robust discrimination between stimulated areas.

On average, 200.6 ± 45.7 trials were retained per session across all 75 recordings. When broken down by stimulation site, the mean number of accepted trials was 202.5 ± 42.0 for premotor stimulation, 192.4 ± 52.3 for parietal stimulation, and 202.0 ± 44.0 for occipital stimulation. The number of bad channels per session was minimal, averaging 0.28 ± 0.58 across all sessions, with site-specific averages of 0.16 ± 0.47 (premotor), 0.44 ± 0.78 (parietal), and 0.25 ± 0.44 (occipital). No significant differences across stimulation sites were observed for either trials or bad channels.

3.1 Focal specificity of early local TMS-evoked responses

We first characterized the spatial specificity of early TMS-evoked responses using an automated peak-detection algorithm (see Methods). The group-average peak-to-peak amplitude distributions reported in the EEG topographic map revealed spatially constrained early responses centered on each stimulation site (Fig. 2A). Notably, occipital stimulation elicited higher amplitudes (max peak-to-peak across channels: 20.56 ± 8.77; group mean ± SD) than parietal (10.8 ± 3.88; group mean ± SD) or premotor sites (11.93 ± 3.58; group mean ± SD)—a finding independent of stimulation intensity (Supplementary Fig. S1A-C), confirming that response magnitude reflects intrinsic circuit properties rather than technical confounds.

To quantify the spatial consistency of early TMS-evoked responses across subjects, we systematically evaluated our channel selection algorithm (see Methods) by varying the number of top-ranked selected channels (*ntop* parameter) and computing the maximum channel overlap percentage across subjects (Fig. 2B). Strikingly, occipital and premotor stimulation achieved

100% overlap (i.e., ≥1 common channel across all subjects) with just *ntop* = 4 channels, indicating highly focal and reproducible responses.

In contrast, parietal responses required selection of >20 channels to approach comparable overlap, suggesting greater inter-subject variability in this area. Visualizing channel-wise overlap for *ntop*=4 (Fig. 2C) exposed distinct topographical patterns. In the occipital stimulation, PO3 channel was universally present (100% overlap), flanked by P3 (64%) and O1 (60%). In premotor site, FC1 showed complete consistency (100%), followed by FCz (80%) and F1 (64%). In parietal stimulation, C1 showed 52% overlap across subjects, while P1 and CP1 appeared in 44% of subjects. Crucially, this apparent spatial diffuseness reflected underlying subject heterogeneity rather than true response dispersion. Specifically, C1 and P1 co-occurred in only 2 subjects, while 11 subjects featured exclusively C1 (without P1) in their four top-ranked channels and 9 featured exclusively P1 (without C1). This bimodal pattern became evident when the peak-to-peak amplitude topographies were displayed separately for the two subgroups (Supplementary Fig. S1D). Critically, this dichotomy remained unexplained by stimulation parameters.

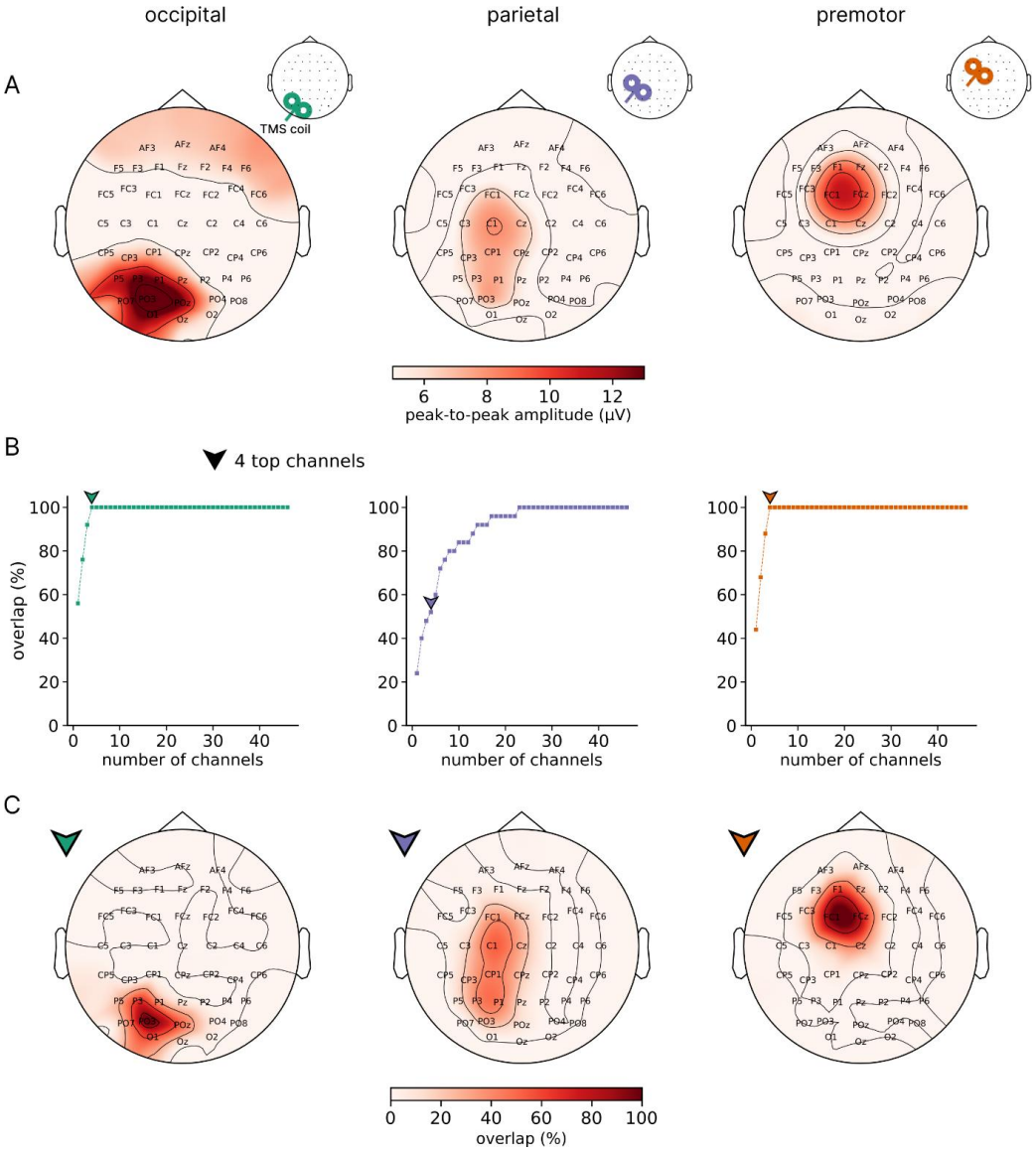

Figure 2. Spatial characteristics of early TMS-evoked responses across cortical sites. (A) Group-average topographic maps of peak-to-peak amplitude (in µV) across subjects for each stimulation site: occipital (left), parietal (center), and premotor (right). In all three conditions, the early TEP response is spatially confined around the stimulation site (green, violet, and orange coils indicate TMS locations), reflecting the local excitability of the targeted cortical circuit. **(B)** Inter-subject overlap (%) of the EEG channels automatically selected as most responsive (based on peak-to-peak amplitude), shown as a function of the number of selected top-ranked channels ("*ntop*"). **(C)** Topographic maps showing the percentage of overlap across subjects for the top four selected channels (corresponding to the triangles in panel B). Warmer colors indicate higher overlap. Occipital stimulation shows maximal overlap centered on PO3 (100%), followed by P3 (64%) and O1 (60%). Premotor stimulation yields consistent selection of FC1 (100%), FCz (80%), and F1 (64%). In contrast, parietal stimulation displays a more distributed response with no channel exceeding 52% overlap (C1).

3.2 Distinct temporal dynamics across cortical sites

Leveraging the spatial specificity established above, we next analyzed temporal dynamics of TEPs from the four top-ranked channels per subject and stimulation site. We extracted the latencies of the first three subsequent peaks (P_1, P_2, and P_3; see Methods) in the TEP waveform.

Figure 3A shows example TEPs with peak detections for a representative subject in each stimulation site. These waveforms revealed marked qualitative differences: occipital stimulation produced slower, high-amplitude deflections, while parietal and premotor responses were markedly faster and smaller. Quantitative analysis confirmed a systematic posterior-to-anterior reduction in peak latencies (Fig. 3B): slowest at occipital (P_1 = 26.55 ± 3.86 ms, P_2 = 66.45 ± 16.24 ms, P_3 = 113.6 ± 23.25 ms; group mean ± SD), intermediate at parietal (P_1 = 23.86 ± 3.91 ms, P_2 = 44.79 ± 5.55 ms, P_3 = 75.48 ± 12.73 ms; group mean ± SD), and fastest at premotor sites (P_1 = 22.03 ± 3.05 ms, P_2 = 41.99 ± 4.85 ms, P_3 = 65.43 ± 9.2 ms; group mean ± SD). Statistical analyses demonstrated significant inter-site differences (Kruskal-Wallis: P_1: $p = 7\times10^{-5}$; P_2: $p = 5\times10^{-9}$; P_3: $p = 4\times10^{-11}$), where P_3 latency robustly distinguished all site pairs in post-hoc comparisons (Fig. 3E; all $p < 0.05$ after Holm–Bonferroni correction).

We then computed the interpeak time (P_3-P_1 latency difference) to estimate the oscillatory period of the TEP, serving as a proxy for its spectral content. The interpeak time shortened progressively from the occipital (87.05 ± 21.14 ms; group mean ± SD) to parietal (51.62 ± 11.90 ms; group mean ± SD) to premotor sites (43.4 ± 6.73 ms; group mean ± SD), exhibiting significant pairwise differences (Fig. 3F; all $p < 0.05$ after Holm–Bonferroni correction).

Critically, within-subject analysis in participants receiving all three stimulations confirmed that both P_3 latency and interpeak time reliably discriminated stimulated areas (Supplementary Fig. S2A-D).

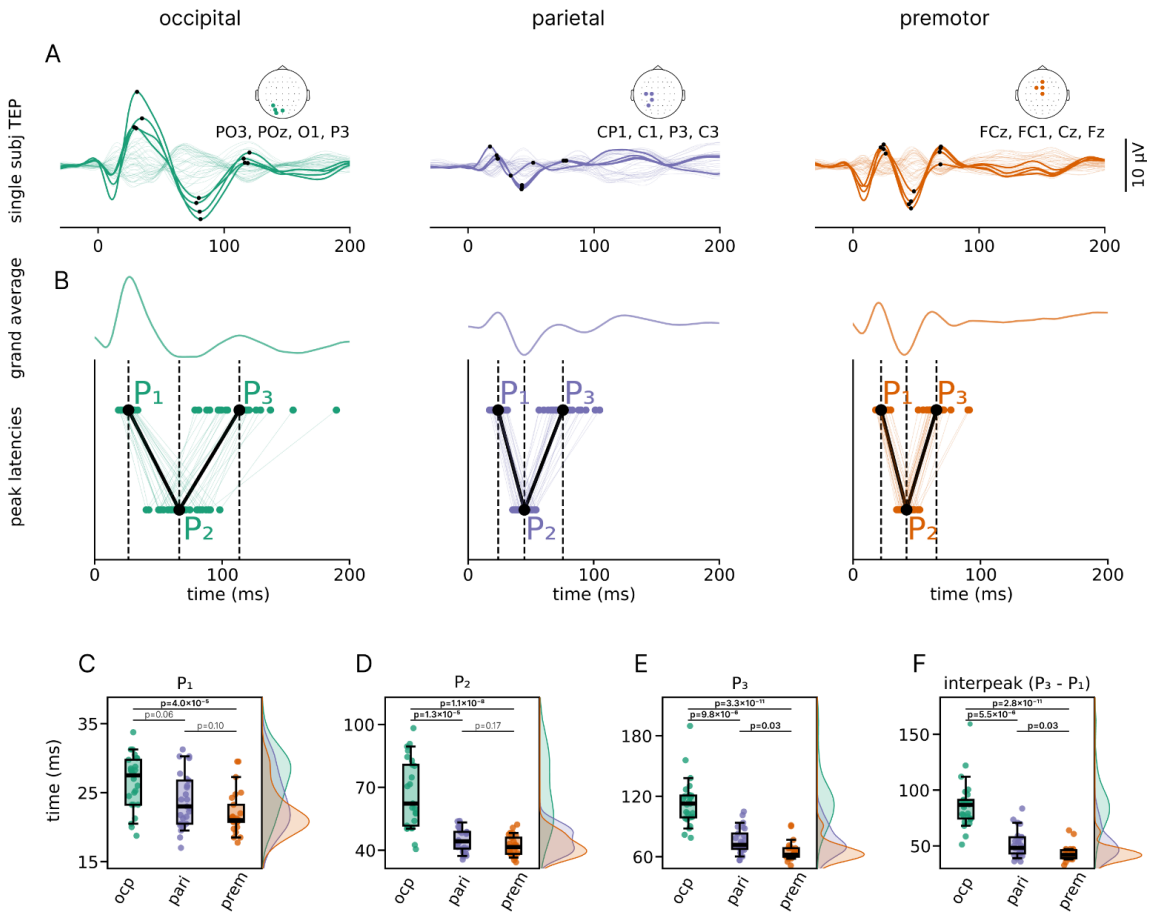

Figure 3. Temporal dynamics of early TEPs reflect stimulation areas. (A) TEP waveforms and detected peaks for a representative subject following occipital (left), parietal (middle), and premotor (right) stimulation. Responses from four selected channels (indicated by colored dots on the topographic map) are highlighted with thicker lines; responses from other channels are shown in the background. Black dots mark the detected peaks (P_1, P_2, and P_3). **(B)** Top: Grand average TEP across subjects and selected channels for each stimulation site. Bottom: Distribution of the average peak latencies (P_1, P_2, P_3) across the four selected channels for all subjects and stimulated areas. Black markers indicate the mean latency across subjects. **(C–F)** Box plots of P_1 (C), P_2 (D), P_3 (E) latencies and interpeak time (F) across subjects for each stimulation site (occipital: green, parietal: violet, premotor: orange). All features show significant differences across stimulated areas (Kruskal–Wallis test). P-values for post-hoc pairwise comparisons (Dunn test), corrected using the Holm–Bonferroni method, are reported in the figure (significant p-values in bold). Density plots to the right of each box plot summarize the full latency distribution across subjects.

3.3 Spectral signatures of cortical circuits revealed by time-frequency analysis

To directly examine the spectral content of TEPs, we conducted a time–frequency analysis using the Stockwell transform on the same four top-ranked channels selected in the previous section. Figure 4A displays the resulting time–frequency power plots for the same representative TEPs

shown in Fig. 3A. Time-frequency power was baseline-corrected (baseline subtraction) and aggregated in the 20–120 ms window to yield the evoked power, from which the peak frequency—termed the natural frequency—was extracted.

Group-level results revealed clear distinctions in dominant frequency content of the evoked power depending on the stimulation site (Fig. 4B). Consistent with prior work (Rosanova et al., 2009), the natural frequency increased along the posterior-to-anterior axis (Fig. 4C), with values in the *alpha* band for occipital stimulation (12.62 ± 2.09 Hz; group mean ± SD), between $beta_1$ and $beta_2$ for parietal (20.37 ± 4.09 Hz; group mean ± SD), and $beta_2$ for premotor (24.80 ± 2.61 Hz; group mean ± SD), exhibiting significant pairwise differences across all stimulation sites (all $p < 0.05$ after Holm–Bonferroni correction).

We next tested whether the interpeak time—a simpler, waveform-derived metric—could serve as a proxy for natural frequency. Linear regression confirmed a strong relationship (Fig. 4D; $r = 0.84$, $p = 4\times10^{-21}$) between natural frequency and 1/interpeak (see Methods), validating the interpeak as a time-domain approximation of TEP spectral content. This correlation held even when the interpeak was computed from a single top-ranked selected channel (i.e., *ntop* = 1; $r = 0.87$, $p = 2\times10^{-24}$), highlighting its practical utility for real-time frequency estimation during recording sessions (Casarotto et al., 2022).

Within-subject analyses confirmed consistent natural frequency differences across sites and a significant correlation with the interpeak time (Supplementary Fig. S2E-F).

To assess the stability of the natural frequency estimate, we systematically varied the width of the Stockwell transform (a parameter used to balance the time-frequency trade-off), the number of selected channels, and the time window used for computing evoked power (Supplementary Fig. S3). Findings were robust across a wide range of widths, number of channels, and analysis windows. These results highlight the method's reliability and provide flexibility for tailoring parameters to specific research questions (e.g., emphasizing early local TEP components via shorter windows and selected channels).

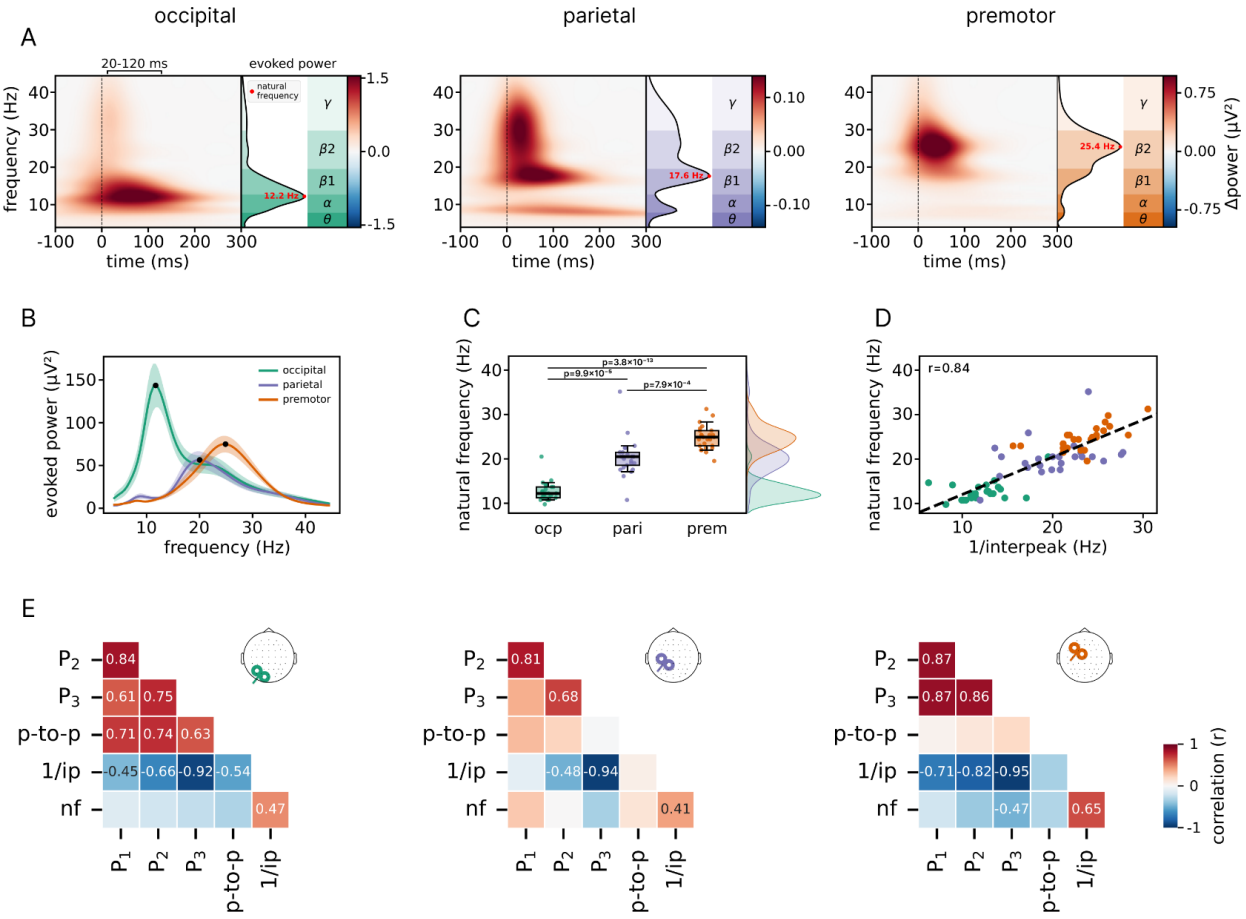

Figure 4. Time-frequency analysis of TEPs reveals stimulation-specific natural frequencies and relationships with temporal features. (A) Time–frequency power representations of the TEP for a representative subject following occipital (left), parietal (middle), and premotor (right) stimulation. Time–frequency decomposition was performed using the Stockwell transform on the four automatically selected channels. Power was first averaged across channels and baseline-corrected by subtracting the average pre-stimulus power within each frequency bin; evoked power was then computed by summing post-stimulus power over the 20–120 ms window (spectral plots shown to the right of each panel). The frequency corresponding to the peak of the evoked power was defined as the natural frequency (red dot; value labeled). **(B)** Grand average of the evoked power spectra across subjects for the three stimulation conditions. Shaded areas indicate the standard error of the mean (SEM). **(C)** Box plots of the natural frequency across subjects for each stimulation site (occipital: green, parietal: violet, premotor: orange), with overlaid subject-level distributions. P-values for post-hoc pairwise comparisons (Dunn test), corrected using the Holm–Bonferroni method, are reported in the figure. Density plots to the right of the box plot summarize the natural frequency distribution across subjects for each stimulation site. **(D)** Positive linear correlation ($r = 0.84$, $p = 4\times10^{-21}$) between natural frequency and 1/interpeak, across all conditions. The 1/interpeak converts the seconds-based interpeak times to Hz. Each point represents one subject and stimulation site (using the same color scheme as panels B and C). **(E)** Pairwise correlations among all extracted features for each stimulation site: P_1, P_2, P_3 latencies; peak-to-peak amplitude

(p-to-p); 1/interpeak (1/ip); and natural frequency (nf). Warm/cool colors denote positive/negative correlations, respectively. Only significant correlations ($p < 0.05$) are shown.

3.4 Feature relationships revealed circuit-specific fingerprints

To synthesize our findings, we examined interrelationships between the extracted features: peak latencies (P_1, P_2, P_3), peak-to-peak amplitude (p-to-p), interpeak time (1/ip), and natural frequency (nf) (Fig. 4E). While peak latencies correlated across sites, premotor responses showed the tightest coupling (e.g., P1→P3), suggesting deterministic sequential activation. Peak-to-peak amplitude positively correlated with peak latencies only for occipital stimulation, implying a distinct amplitude-dependent response. Crucially, 1/interpeak and natural frequency exhibited significant intra-site correlations, consolidating their relationship as frequency markers of TMS-evoked response.

Collectively, these feature interactions demonstrate how local circuit properties shape distinct response "fingerprints" identifiable through our automated framework.

4. Discussion

In this work, we introduce TEPpy, a standardized analytical framework for extracting features from TMS evoked potentials. This approach is agnostic to preprocessing pipelines, data acquisition hardware, and stimulation protocols, making it highly adaptable across studies. Alongside the development of this tool, we conducted a systematic analysis of reproducible TEP features across stimulation sites and participants, examining both time and frequency-domain metrics. Finally, we explored relationships among the extracted measures to uncover potential interdependencies.

Amplitude-Based Measures

The initial stage of our feature extraction recapture one of the primary checks performed during real-time monitoring: spatial specificity of TEPs, determined by sensors showing maximal responses (Casarotto et al., 2022). Our automated peak-to-peak detection confirmed that the amplitude distribution of TEPs across channels aligns with the stimulated cortical region (Fig. 2C). This is particularly evident during occipital and premotor stimulation. In contrast, parietal stimulation resulted in a more dispersed amplitude pattern, possibly due to stimulation parameters but also due to the inherently interconnected nature of the area (Thomas Yeo et al., 2011; van den Heuvel and Sporns, 2013). Interestingly, two distinct clusters emerged within the parietal group: one peaked in more anterior channels (e.g., C1) and another in canonical parietal sensors (e.g., P1) (see Supplementary Figure S1). Notably, only two subjects exhibited both clusters among their top four responsive channels.

Regarding absolute peak-to-peak amplitudes, occipital stimulation consistently produced the highest responses compared to other regions. Importantly, these amplitude differences persisted even after controlling for stimulation intensity and estimated electric field strength, suggesting a genuinely distinct reactivity profile of occipital cortex rather than methodological confounds. Overall, this first exploration highlights how these data-driven simple amplitude metrics can provide meaningful insights into the local properties of stimulated cortical circuits.
Furthermore, the features captured by our tool can serve as a foundation for deeper investigations, such as analyzing absolute amplitude variations across peaks or examining later TEP components that reflect circuit-specific activity, state-dependent modulation, or ongoing cognitive processes (Kallioniemi et al., 2022). Finally, in our integrated workflow, these amplitude measures are inherited by other analysis steps to guide the TEPs features extraction, helping to focus on the most responsive and specific to the stimulation target sensors.

Peaks latencies-based measures

Starting from the channels selected for amplitude-based measures, the next step of our tool focuses on extracting and characterizing the timing of prominent evoked peaks. We observed a clear progression in peak latencies across the three stimulated cortical regions. While the first peak (P_1) latency was significantly different only when comparing occipital with premotor stimulation (Fig. 3C), the second peak (P_2) was able to additionally differentiate parietal from occipital responses (Fig. 3D). Notably, the third peak (P_3) distinguished all three sites, following a posterior-to-anterior gradient, with the longest latency in the occipital region, followed by parietal, and then premotor (Fig. 3E).

This pattern aligns with existing literature indicating that early TEP components exhibit region-specific timing: M1 stimulation studies consistently show distinct early peaks such as N15, P30, N45, P60, N100, and P180, with reliable latencies serving as a hallmark of cortical reactivity (Beck et al., 2024b;).

Our findings extend this framework by demonstrating that, beyond the primary motor cortex, latency gradients in TEP peaks can serve as sensitive markers to dissociate stimulation sites across occipital, parietal, and premotor cortices. In particular, the P_3 component behaves like a “temporal fingerprint” for each region. In this context, whereas earlier TEP peaks predominantly reflect stimulation site-specific activity, later peaks likely index re-entrant, circuit-level dynamics, with their latency shaped by the architecture and conduction delays of connections linking the perturbed site to the rest of the brain (Rogasch et al., 2020; Momi et al., 2023). This seems especially salient considering state-dependent TMS-EEG evidence showing that, when large-scale integration is compromised during NREM sleep or anesthesia, the initial TEP is often

preserved but the subsequent long-latency reverberation collapses (Massimini et al., 2005, Ferrarelli et al., 2010).

Beyond considering each peak in isolation, we examined temporal dependencies among peaks and found that the latency of the first peak significantly predicted the latencies of the subsequent peaks for premotor TEPs, but less for occipital or parietal responses. This pattern suggests a more tightly phase-locked, chain-like temporal organization in premotor circuits.

Taken together, this vast amount of information yielded by our tool provides support for the use of latency measures as robust, sensitive indicators of regional cortical dynamics. Moreover, the combination of the automatically extracted latency metrics further characterizes stimulated areas and opens the way to derive composite indices of cortical reactivity within a standardized, data-driven framework.

Interpeak and spectral-based measures

The shift of the P_3 component across stimulation sites (Fig. 3E) provides evidence for differences in the velocity of cortical responses. This observation motivated the introduction of an additional time-domain feature—the interpeak time, defined as the latency between P_1 and P_3—which summarizes the duration of the first oscillatory cycle evoked by TMS. This measure reliably distinguished the three stimulated areas (Fig. 3F), being longest in occipital, intermediate in parietal, and shortest in premotor sites. These temporal differences mirror and extend previous spectral findings from both spontaneous (Frauscher et al., 2018; Capilla et al., 2022) and evoked activity (Rosanova et al., 2009), reinforcing the notion of an anteroposterior gradient toward slower frequencies. In this sense, interpeak time offers a complementary perspective on a well-established spatial organization of cortical dynamics.

To further explore this gradient in the frequency domain, we directly characterized the spectral profile of the TMS-evoked response using time–frequency decomposition via the Stockwell transform implemented in TEPpy (Fig. 4). By applying the analysis to the same four channels used in the time-domain analysis, we established a standardized approach to extract key spectral features, such as the natural frequency of the evoked response (Rosanova et al., 2009). This methodological consistency addresses a common limitation in the field, where heterogeneous protocols (Bai et al., 2023; D'Ambrosio et al., 2022; De Martino et al., 2024; Donati et al., 2025, 2023; Ferrarelli et al., 2012; Johnson et al., 2012; Vallesi et al., 2021) hampers direct comparability across studies. Our approach successfully captured a clear spectral gradient (Fig. 4C)—occipital responses peaking in the alpha range and progressively faster rhythms in parietal and premotor regions—aligning with prior work and supporting the value of methodological standardization in TMS–EEG research.

The robustness of this method was confirmed by testing its sensitivity to variations in the Stockwell transform parameters (e.g., width), post-stimulus analysis windows, and number of channels (Supplementary Fig. S3). The stability of the results across these variations suggests that the method is adaptable to different experimental applications and settings, which is particularly advantageous for clinical research. Notably, systematic slowing of TMS–EEG responses has been reported in stroke, when stimulating perilesional sites or structurally disconnected regions (D'Ambrosio et al., 2023; Sarasso et al., 2020b; Tscherpel et al., 2024, 2020), with renormalization tracking recovery (Sarasso et al., 2025). In this context, our standardized framework could first be applied to establish a large-scale normative map of natural frequencies across cortical areas, and then used to detect pathological deviations in patient populations.

Importantly, the observed correlation between interpeak time and natural frequency (Fig. 4D) underscores the utility of combining temporal and spectral perspectives. Even when derived from a single channel, interpeak time can serve as a reliable time-domain proxy for the spectral content of the TEP, enabling rapid assessments during experiments. This opens the door to integrating interpeak time detection into real-time TEP visualization tools (e.g., Casarotto et al., 2022) to verify whether the stimulated site expresses the expected dynamics. Such integration, particularly when combined with other time-domain features, could enhance the real-time monitoring of cortical responses in both research and clinical environments.

Finally, while the present work concentrated on the early TEP response and its dominant spectral content, the same framework can be extended to more detailed spectral metrics, such as band-specific power or interband power ratios. Applying these measures to later TEP components could capture their spectral evolution over time (e.g., calculating the evoked power in consecutive windows) and reveal the involvement of distinct circuits—for example, thalamo-cortical loops known to modulate late TEP components (Russo et al., 2025). Time-resolved spectral tracking may thus provide a richer account of how different brain networks contribute to cortical reactivity under various conditions (e.g., task vs. rest).

In summary, our results show that simple features extracted from early TEPs can robustly capture the spatial, temporal, and spectral properties of local cortical responses. The proposed framework offers a standardized, reliable, and interpretable method for characterizing TMS-evoked dynamics, with potential applications in defining normative cortical fingerprints and probing the integrity of cortical circuits in health and disease.

References

Atalay, A.S., Fecchio, M., Edlow, B.L., 2025. Visualizing Effective Connectivity in the Human Brain. bioRxiv 2025.03.06.641642. https://doi.org/10.1101/2025.03.06.641642

Atluri, S., Frehlich, M., Mei, Y., Garcia Dominguez, L., Rogasch, N.C., Wong, W., Daskalakis, Z.J., Farzan, F., 2016. TMSEEG: A MATLAB-Based Graphical User Interface for Processing Electrophysiological Signals during Transcranial Magnetic Stimulation. Front Neural Circuits 10, 78. https://doi.org/10.3389/fncir.2016.00078

Bai, Y., Xuan, J., Jia, S., Ziemann, U., 2023. TMS of parietal and occipital cortex locked to spontaneous transient large-scale brain states enhances natural oscillations in EEG. Brain Stimulation: Basic, Translational, and Clinical Research in Neuromodulation 16, 1588–1597. https://doi.org/10.1016/j.brs.2023.10.008

Beck, M.M., Christiansen, L., Madsen, M.A.J., Jadidi, A.F., Vinding, M.C., Thielscher, A., Bergmann, T.O., Siebner, H.R., Tomasevic, L., 2024a. Transcranial magnetic stimulation of primary motor cortex elicits an immediate transcranial evoked potential. Brain Stimulation 17, 802–812. https://doi.org/10.1016/j.brs.2024.06.008

Beck, M.M., Heyl, M., Mejer, L., Vinding, M.C., Christiansen, L., Tomasevic, L., Siebner, H.R., 2024b. Methodological Choices Matter: A Systematic Comparison of TMS-EEG Studies Targeting the Primary Motor Cortex. Human Brain Mapping 45, e70048. https://doi.org/10.1002/hbm.70048

Capilla, A., Arana, L., García-Huéscar, M., Melcón, M., Gross, J., Campo, P., 2022. The natural frequencies of the resting human brain: An MEG-based atlas. NeuroImage 258, 119373. https://doi.org/10.1016/j.neuroimage.2022.119373

Casarotto, S., Fecchio, M., Rosanova, M., Varone, G., D'Ambrosio, S., Sarasso, S., Pigorini, A., Russo, S., Comanducci, A., Ilmoniemi, R.J., Massimini, M., 2022. The rt-TEP tool: real-time visualization of TMS-Evoked Potentials to maximize cortical activation and minimize artifacts. Journal of Neuroscience Methods 370, 109486. https://doi.org/10.1016/j.jneumeth.2022.109486

Casarotto, S., Romero Lauro, L.J., Bellina, V., Casali, A.G., Rosanova, M., Pigorini, A., Defendi, S., Mariotti, M., Massimini, M., 2010. EEG responses to TMS are sensitive to changes in

the perturbation parameters and repeatable over time. PLoS One 5, e10281. https://doi.org/10.1371/journal.pone.0010281

Casarotto, S., Turco, F., Comanducci, A., Perretti, A., Marotta, G., Pezzoli, G., Rosanova, M., Isaias, I.U., 2019. Excitability of the supplementary motor area in Parkinson's disease depends on subcortical damage. Brain Stimul 12, 152–160. https://doi.org/10.1016/j.brs.2018.10.011

Couto, B.A., Fecchio, M., Russo, S., Martino, E.D., Parmigiani, S., Sarasso, S., Graven-Nielsen, T., Andrade, D.C. de, Massimini, M., Rosanova, M., Casali, A.G., 2025. Extracting Reproducible Components from Electroencephalographic Responses to Transcranial Magnetic Stimulation with Group Task-Related Component Analysis. https://doi.org/10.1101/2025.06.02.657489

D'Ambrosio, S., Certo, F., Bernardelli, L., Pini, L., Corbetta, M., Pantoni, L., Massimini, M., Sarasso, S., 2023. Detecting cortical reactivity alterations induced by structural disconnection in subcortical stroke. Clinical Neurophysiology 156, 1–3. https://doi.org/10.1016/j.clinph.2023.09.007

D'Ambrosio, S., Jiménez-Jiménez, D., Silvennoinen, K., Zagaglia, S., Perulli, M., Poole, J., Comolatti, R., Fecchio, M., Sisodiya, S.M., Balestrini, S., 2022. Physiological symmetry of transcranial magnetic stimulation-evoked EEG spectral features. Hum Brain Mapp 43, 5465–5477. https://doi.org/10.1002/hbm.26022

De Martino, E., Casali, A., Casarotto, S., Hassan, G., Couto, B.A., Rosanova, M., Graven-Nielsen, T., De Andrade, D.C., 2024. Evoked oscillatory cortical activity during acute pain: Probing brain in pain by transcranial magnetic stimulation combined with electroencephalogram. Human Brain Mapping 45, e26679. https://doi.org/10.1002/hbm.26679

Donati, F.L., Mayeli, A., Nascimento Couto, B.A., Sharma, K., Janssen, S., Krafty, R.J., Casali, A.G., Ferrarelli, F., 2025. Prefrontal Oscillatory Slowing in Early-Course Schizophrenia Is Associated With Worse Cognitive Performance and Negative Symptoms: A Transcranial Magnetic Stimulation-Electroencephalography Study. Biol Psychiatry Cogn Neurosci Neuroimaging 10, 158–166. https://doi.org/10.1016/j.bpsc.2024.07.013

Donati, F.L., Mayeli, A., Sharma, K., Janssen, S.A., Lagoy, A.D., Casali, A.G., Ferrarelli, F., 2023. Natural Oscillatory Frequency Slowing in the Premotor Cortex of Early-Course Schizophrenia Patients: A TMS-EEG Study. Brain Sciences 13, 534. https://doi.org/10.3390/brainsci13040534

Dworkin, A., Jiménez-Jiménez, D., Ravenscroft, C., Turco, F., Johnson, C., Chowdhury, F.A., Pizarro, J., D'Ambrosio, S., Sisodiya, S.M., Vivekananda, U., Balestrini, S., 2025. TMS-EEG in postictal psychosis of epilepsy. Schizophr Res 282, 176–183. https://doi.org/10.1016/j.schres.2025.06.015

Fecchio, M., Pigorini, A., Comanducci, A., Sarasso, S., Casarotto, S., Premoli, I., Derchi, C.-C., Mazza, A., Russo, S., Resta, F., Ferrarelli, F., Mariotti, M., Ziemann, U., Massimini, M., Rosanova, M., 2017. The spectral features of EEG responses to transcranial magnetic stimulation of the primary motor cortex depend on the amplitude of the motor evoked potentials. PLOS ONE 12, e0184910. https://doi.org/10.1371/journal.pone.0184910

Ferrarelli, F., Massimini, M., Sarasso, S., Casali, A., Riedner, B.A., Angelini, G., Tononi, G., Pearce, R.A., 2010. Breakdown in cortical effective connectivity during midazolam-induced loss of consciousness. Proc Natl Acad Sci U S A 107, 2681–2686. https://doi.org/10.1073/pnas.0913008107

Ferrarelli, F., Sarasso, S., Guller, Y., Riedner, B.A., Peterson, M.J., Bellesi, M., Massimini, M., Postle, B.R., Tononi, G., 2012. Reduced Natural Oscillatory Frequency of Frontal Thalamocortical Circuits in Schizophrenia. Arch Gen Psychiatry 69. https://doi.org/10.1001/archgenpsychiatry.2012.147

Ferreri, F., Rossini, P.M., 2013. TMS and TMS-EEG techniques in the study of the excitability, connectivity, and plasticity of the human motor cortex. Reviews in the Neurosciences 24. https://doi.org/10.1515/revneuro-2013-0019

Frauscher, B., von Ellenrieder, N., Zelmann, R., Doležalová, I., Minotti, L., Olivier, A., Hall, J., Hoffmann, D., Nguyen, D.K., Kahane, P., Dubeau, F., Gotman, J., 2018. Atlas of the normal intracranial electroencephalogram: neurophysiological awake activity in different cortical areas. Brain 141, 1130–1144. https://doi.org/10.1093/brain/awy035

Hassan, U., Pillen, S., Zrenner, C., Bergmann, T.O., 2022. The Brain Electrophysiological recording & STimulation (BEST) toolbox. Brain Stimulation 15, 109–115. https://doi.org/10.1016/j.brs.2021.11.017

Ilmoniemi, R.J., Kicić, D., 2010. Methodology for combined TMS and EEG. Brain Topogr 22, 233–248. https://doi.org/10.1007/s10548-009-0123-4

Johnson, J.S., Kundu, B., Casali, A.G., Postle, B.R., 2012. Task-dependent changes in cortical excitability and effective connectivity: a combined TMS-EEG study. J Neurophysiol 107, 2383–2392. https://doi.org/10.1152/jn.00707.2011

Komssi, S., Kähkönen, S., 2006. The novelty value of the combined use of electroencephalography and transcranial magnetic stimulation for neuroscience research. Brain Research Reviews 52, 183–192. https://doi.org/10.1016/j.brainresrev.2006.01.008

Lioumis, P., Kicić, D., Savolainen, P., Mäkelä, J.P., Kähkönen, S., 2009. Reproducibility of TMS-Evoked EEG responses. Hum Brain Mapp 30, 1387–1396. https://doi.org/10.1002/hbm.20608

Massimini, M., Ferrarelli, F., Huber, R., Esser, S.K., Singh, H., Tononi, G., 2005. Breakdown of cortical effective connectivity during sleep. Science 309, 2228–2232. https://doi.org/10.1126/science.1117256

Meneghini, G., Engelhardt, M., Burzlaff, M., Zaykova, A., Vajkoczy, P., Lioumis, P., Rosanova, M., Picht, T., 2025. Probing cortical reactivity before and after brain tumor resection: A TMS-EEG case. Brain Stimulation: Basic, Translational, and Clinical Research in Neuromodulation 18, 19–21. https://doi.org/10.1016/j.brs.2024.12.004

Momi, D., Wang, Z., Griffiths, J.D., 2023. TMS-evoked responses are driven by recurrent large-scale network dynamics. eLife 12, e83232. https://doi.org/10.7554/eLife.83232

Nikulin, V.V., Kičić, D., Kähkönen, S., Ilmoniemi, R.J., 2003. Modulation of electroencephalographic responses to transcranial magnetic stimulation: evidence for changes in cortical excitability related to movement. Eur J of Neuroscience 18, 1206–1212. https://doi.org/10.1046/j.1460-9568.2003.02858.x

Nuyts, M., Beck, M.M., Banach, A., Thielscher, A., Meesen, R., Tomasevic, L., Siebner, H.R., Christiansen, L., 2025. Rostro-caudal TMS mapping of immediate transcranial evoked potentials reveals a pericentral crescendo-decrescendo pattern. https://doi.org/10.1101/2025.02.14.638272

Premoli, I., Castellanos, N., Rivolta, D., Belardinelli, P., Bajo, R., Zipser, C., Espenhahn, S., Heidegger, T., Müller-Dahlhaus, F., Ziemann, U., 2014. TMS-EEG signatures of GABAergic neurotransmission in the human cortex. J Neurosci 34, 5603–5612. https://doi.org/10.1523/JNEUROSCI.5089-13.2014

Rogasch, N.C., n.d. The effects of NMDA receptor blockade on TMS-evoked EEG potentials from prefrontal and parietal cortex.

Rogasch, N.C., Sullivan, C., Thomson, R.H., Rose, N.S., Bailey, N.W., Fitzgerald, P.B., Farzan, F., Hernandez-Pavon, J.C., 2017. Analysing concurrent transcranial magnetic stimulation and electroencephalographic data: A review and introduction to the open-source TESA software. Neuroimage 147, 934–951. https://doi.org/10.1016/j.neuroimage.2016.10.031

Rosanova, M., Casali, A., Bellina, V., Resta, F., Mariotti, M., Massimini, M., 2009. Natural Frequencies of Human Corticothalamic Circuits. Journal of Neuroscience 29, 7679–7685. https://doi.org/10.1523/JNEUROSCI.0445-09.2009

Rosanova, Mario, Casali, A., Bellina, V., Resta, F., Mariotti, M., Massimini, M., 2009. Natural Frequencies of Human Corticothalamic Circuits. J. Neurosci. 29, 7679–7685. https://doi.org/10.1523/JNEUROSCI.0445-09.2009

Rosanova, M., Fecchio, M., Casarotto, S., Sarasso, S., Casali, A.G., Pigorini, A., Comanducci, A., Seregni, F., Devalle, G., Citerio, G., Bodart, O., Boly, M., Gosseries, O., Laureys, S., Massimini, M., 2018. Sleep-like cortical OFF-periods disrupt causality and complexity in the brain of unresponsive wakefulness syndrome patients. Nat Commun 9, 4427. https://doi.org/10.1038/s41467-018-06871-1

Russo, S., Claar, L.D., Furregoni, G., Marks, L.C., Krishnan, G., Zauli, F.M., Hassan, G., Solbiati, M., d'Orio, P., Mikulan, E., Sarasso, S., Rosanova, M., Sartori, I., Bazhenov, M., Pigorini, A., Massimini, M., Koch, C., Rembado, I., 2025. Thalamic feedback shapes brain responses evoked by cortical stimulation in mice and humans. Nat Commun 16, 3627. https://doi.org/10.1038/s41467-025-58717-2

Russo, S., Sarasso, S., Puglisi, G.E., Dal Palù, D., Pigorini, A., Casarotto, S., D'Ambrosio, S., Astolfi, A., Massimini, M., Rosanova, M., Fecchio, M., 2022. TAAC - TMS Adaptable Auditory Control: A universal tool to mask TMS clicks. Journal of Neuroscience Methods 370, 109491. https://doi.org/10.1016/j.jneumeth.2022.109491

Sarasso, S., D'Ambrosio, S., Fecchio, M., Casarotto, S., Viganò, A., Landi, C., Mattavelli, G., Gosseries, O., Quarenghi, M., Laureys, S., Devalle, G., Rosanova, M., Massimini, M.,

2020a. Local sleep-like cortical reactivity in the awake brain after focal injury. Brain 143, 3672–3684. https://doi.org/10.1093/brain/awaa338

Sarasso, S., D'Ambrosio, S., Fecchio, M., Casarotto, S., Viganò, A., Landi, C., Mattavelli, G., Gosseries, O., Quarenghi, M., Laureys, S., Devalle, G., Rosanova, M., Massimini, M., 2020b. Local sleep-like cortical reactivity in the awake brain after focal injury. Brain 143, 3672–3684. https://doi.org/10.1093/brain/awaa338

Sarasso, S., D'Ambrosio, S., Russo, S., Bernardelli, L., Hassan, G., Comanducci, A., De Giampaulis, P., Dalla Vecchia, L.A., Lanzone, J., Massimini, M., 2025. Reduction of sleep-like perilesional slow waves and clinical evolution after stroke: A TMS-EEG study. Clinical Neurophysiology 175, 2110746. https://doi.org/10.1016/j.clinph.2025.2110746

Thomas Yeo, B.T., Krienen, F.M., Sepulcre, J., Sabuncu, M.R., Lashkari, D., Hollinshead, M., Roffman, J.L., Smoller, J.W., Zöllei, L., Polimeni, J.R., Fischl, B., Liu, H., Buckner, R.L., 2011. The organization of the human cerebral cortex estimated by intrinsic functional connectivity. J Neurophysiol 106, 1125–1165. https://doi.org/10.1152/jn.00338.2011

Tremblay, S., Rogasch, N.C., Premoli, I., Blumberger, D.M., Casarotto, S., Chen, R., Di Lazzaro, V., Farzan, F., Ferrarelli, F., Fitzgerald, P.B., Hui, J., Ilmoniemi, R.J., Kimiskidis, V.K., Kugiumtzis, D., Lioumis, P., Pascual-Leone, A., Pellicciari, M.C., Rajji, T., Thut, G., Zomorrodi, R., Ziemann, U., Daskalakis, Z.J., 2019. Clinical utility and prospective of TMS–EEG. Clinical Neurophysiology 130, 802–844. https://doi.org/10.1016/j.clinph.2019.01.001

Tscherpel, C., Dern, S., Hensel, L., Ziemann, U., Fink, G.R., Grefkes, C., 2020. Brain responsivity provides an individual readout for motor recovery after stroke. Brain 143, 1873–1888. https://doi.org/10.1093/brain/awaa127

Tscherpel, C., Mustin, M., Massimini, M., Paul, T., Ziemann, U., Fink, G.R., Grefkes, C., 2024. Local neuronal sleep after stroke: The role of cortical bistability in brain reorganization. Brain Stimulation: Basic, Translational, and Clinical Research in Neuromodulation 17, 836–846. https://doi.org/10.1016/j.brs.2024.07.008

Vallesi, A., Del Felice, A., Capizzi, M., Tafuro, A., Formaggio, E., Bisiacchi, P., Masiero, S., Ambrosini, E., 2021. Natural oscillation frequencies in the two lateral prefrontal cortices induced by Transcranial Magnetic Stimulation. NeuroImage 227, 117655. https://doi.org/10.1016/j.neuroimage.2020.117655

van den Heuvel, M.P., Sporns, O., 2013. Network hubs in the human brain. Trends Cogn Sci 17, 683–696. https://doi.org/10.1016/j.tics.2013.09.012

Wu, W., Keller, C.J., Rogasch, N.C., Longwell, P., Shpigel, E., Rolle, C.E., Etkin, A., 2018. ARTIST: A fully automated artifact rejection algorithm for single-pulse TMS-EEG data. Human Brain Mapping 39, 1607–1625. https://doi.org/10.1002/hbm.23938

Supplementary Material

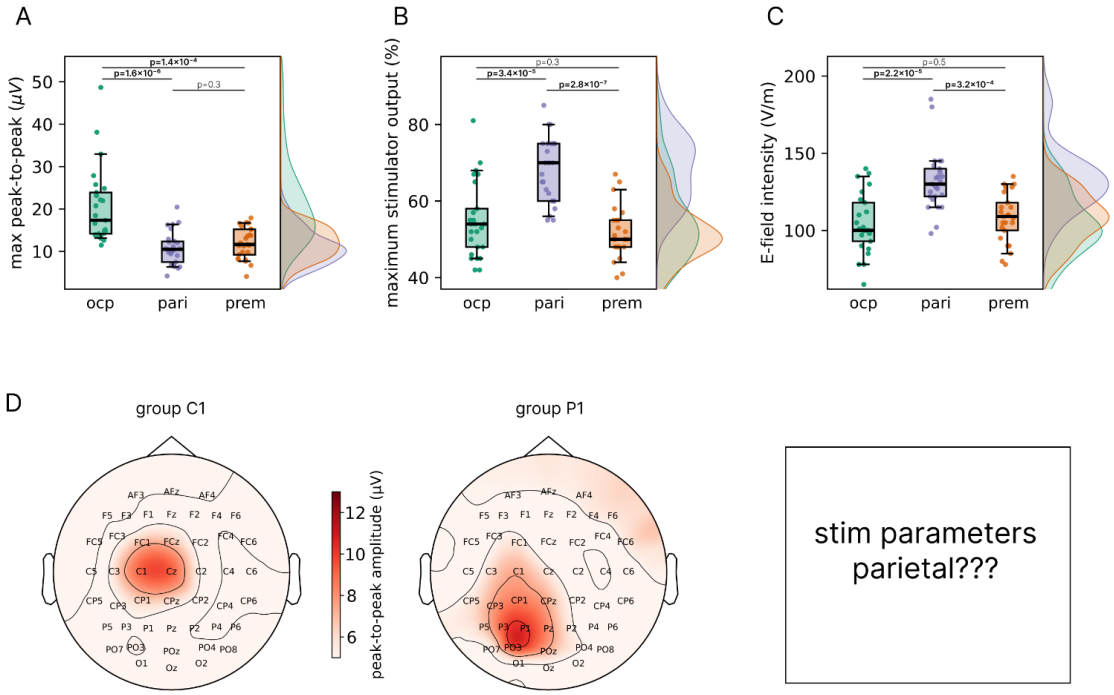

Figure S1. Stimulation parameters and subgroup-specific amplitude topographies. (A) Maximum peak-to-peak amplitude across channels of TEPs across occipital (ocp), parietal (pari), and premotor (prem) stimulation sites. **(B)** Maximum stimulator output used for each site. **(C)** Estimated electric field (E-field) intensity at the cortical target (V/m) for each site. In the box plots, each point represents a subject, and p-values for post-hoc pairwise comparisons (Holm–Bonferroni corrected) are reported within the figures (significant p-values in bold). Density plots to the right of each box plot show the full distribution across subjects. **(D)** Peak-to-peak amplitude topographies for the two parietal stimulation subgroups identified in Fig. 2C: subjects with C1 among the top ntop channels (group C1, left) and subjects with P1 among the top channels (group P1, right). Color maps represent group-average peak-to-peak amplitude (μV). **(E) …**

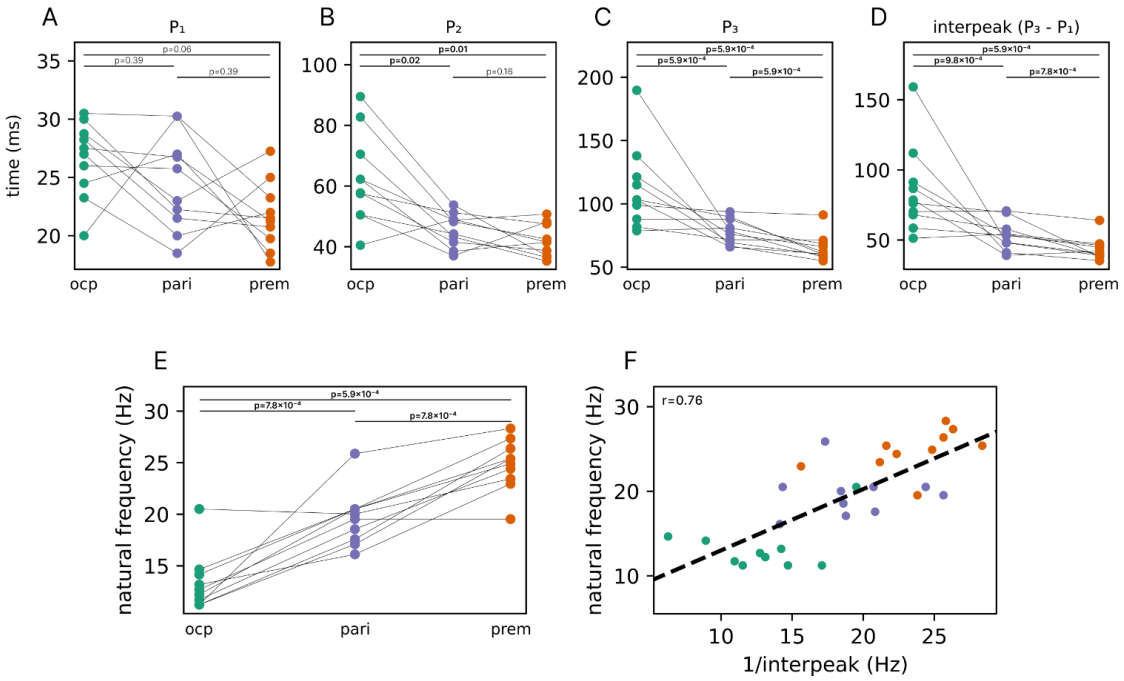

Figure S2. Within-subject comparisons of temporal and spectral TEP features across stimulation sites. (A–C) Latencies of the first three TEP peaks (P1, P2, P3) and **(D)** interpeak time, measured in occipital (ocp), parietal (pari), and premotor (prem) stimulation, shown for each participant (colored points) who received all three stimulations. **(E)** Natural frequency estimated from time–frequency analysis for each site, shown for each participant (colored points) who received all three stimulations. In the panels, each line connects measurements from the same subject. Within-subject analyses for participants receiving all three stimulations (n = 10) were performed using Friedman tests with post-hoc Wilcoxon signed-rank tests and Holm–Bonferroni correction; p-values are shown in the figure, with significant values in bold. **(F)** Correlation between natural frequency and the reciprocal of the interpeak time (1/interpeak) in the paired subgroup, confirming a strong relationship ($r = 0.76$, $p = 9.7\times10^{-7}$) between these temporal and spectral measures.

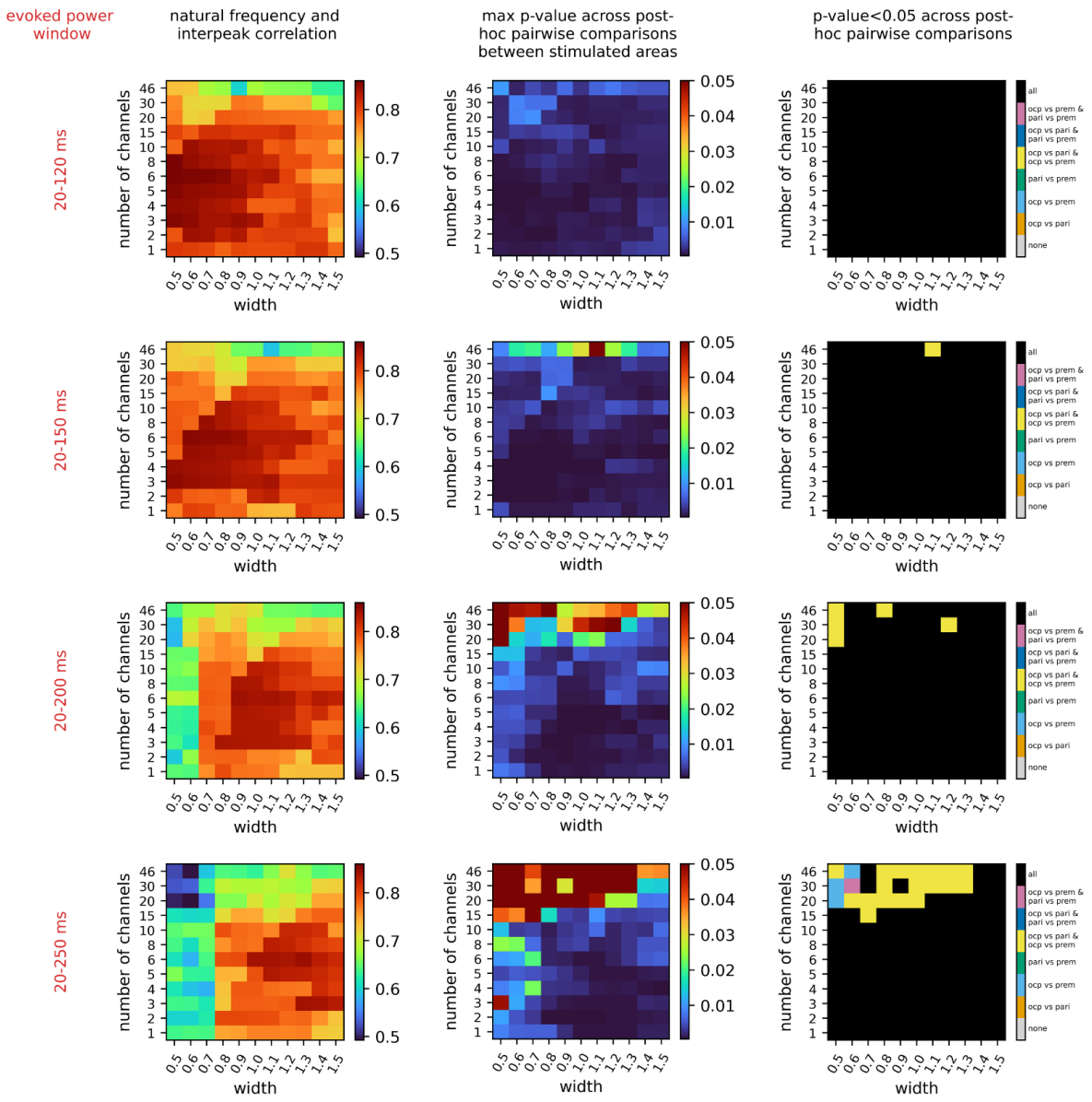

Figure S3. Robustness of natural frequency estimation across parameter variations. Parameter exploration analysis demonstrating stability of natural frequency metrics. Each row represents a different evoked power summation window: 20–120 ms (top), 20–150 ms, 20–200 ms, and 20–250 ms (bottom). Columns 1-3 display heatmaps evaluating the effects of Stockwell transform width (x-axis) and number of selected channels (y-axis; via *ntop* parameter) on key statistical metrics. Column 1: Correlation coefficients (r) between natural frequency and 1/interpeak time. Red hues indicate strong correlations ($r > 0.8$), confirming the robustness of this relationship across parameter combinations. Column 2: Maximum p-values across all post-hoc pairwise comparisons (occipital vs. parietal, occipital vs. premotor, parietal vs. premotor). Dark red indicates parameter combinations where at least one comparison was non-significant ($p > 0.05$). Column 3: Significance patterns of post-hoc comparisons. Colors denote specific combinations of significant pairwise differences (see colorbar), with black indicating all three comparisons remained significant ($p < 0.05$). P-values are corrected with the Holm-Bonferroni method.

2.2 Article 2

Title: *Emergent complexity and rhythms in evoked and spontaneous dynamics of human whole-brain models after tuning through analysis tools*

Authors: ***Gianluca Gaglioti****, ***Alessandra Cardinale****, *Cosimo Lupo, Thierry Nieus, Federico Marmoreo, Robin Gutzen, Michael Denker, Andrea Pigorini, Marcello Massimini, Simone Sarasso, Pier Stanislao Paolucci, Giulia De Bonis*

Abstract: *The simulation of whole-brain dynamics should reproduce realistic spontaneous and evoked neural activity across different scales, including emergent rhythms, spatio-temporal activation patterns, and macroscale complexity. Once a mathematical model is selected, its configuration must be determined by properly setting its parameters. A critical preliminary step in this process is defining an appropriate set of observables to guide the selection of model configurations (parameter tuning), laying the groundwork for quantitative calibration of accurate whole-brain models. Here, we address this challenge by presenting a framework that integrates two complementary tools: The Virtual Brain (TVB) platform for simulating whole-brain dynamics, and the Collaborative Brain Wave Analysis Pipeline (Cobrawap) for analyzing simulation outputs using a set of standardized metrics. We apply this framework to a 998-node human connectome, using two configurations of the Larter-Breakspear neural mass model: one with the TVB default parameters, the other tuned using Cobrawap. The results reveal that the tuned configuration exhibits several biologically relevant features, absent in the default model for both spontaneous and evoked dynamics. In response to external perturbations, the tuned model generates non-stereotyped, complex spatio-temporal activity, as measured by the perturbational complexity index. In spontaneous activity, it exhibits robust alpha-band oscillations, infra-slow rhythms, scale-free characteristics, greater spatio-temporal heterogeneity, and asymmetric functional connectivity. This work demonstrates how combining TVB and Cobrawap can guide parameter tuning and lays the groundwork for data-driven calibration and validation of accurate whole-brain models.*

DOI: *https://doi.org/10.1016/j.neucom.2026.132735*

**These authors contributed equally*

Neurocomputing 678 (2026) 132735

Contents lists available at ScienceDirect

Neurocomputing

journal homepage: www.elsevier.com/locate/neucom

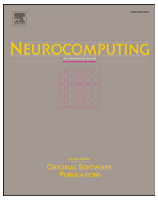

Emergent complexity and rhythms in evoked and spontaneous dynamics of human whole-brain models after tuning through analysis tools

Gianluca Gaglioti [a,b,1,*], Alessandra Cardinale [c,d,1], Cosimo Lupo [d,1,**], Thierry Nieus [e], Federico Marmoreo [d], Elena Focacci [a,b], Robin Gutzen [f], Michael Denker [g], Andrea Pigorini [h,i], Marcello Massimini [a,j,k,2], Simone Sarasso [a,2], Pier Stanislao Paolucci [d,2], Giulia De Bonis [d,2]

[a] Dep. of Biomedical and Clinical Sciences, Univ. of Milan, Milan, Italy
[b] Dep. of Philosophy "Piero Martinetti", Univ. of Milan, Milan, Italy
[c] Università Campus Bio-medico di Roma, Rome, Italy
[d] Istituto Nazionale di Fisica Nucleare (INFN), Sezione di Roma, Rome, Italy
[e] Dep. of Environmental Science and Policy, Univ. of Milan, Milan, Italy
[f] Center for Data Science, New York University, New York, NY 10012, USA
[g] Institute for Advanced Simulation (IAS-6), Jülich Research Centre, Jülich, Germany
[h] Dep. of Biomedical, Surgical and Dental Sciences, Univ. of Milan, Milan, Italy
[i] UOC Maxillo-facial Surgery and dentistry, Fondazione IRCCS Cà Granda, Ospedale Maggiore Policlinico, Milan, Italy
[j] IRCCS Fondazione Don Carlo Gnocchi ONLUS, Milan, Italy
[k] Azrieli Program in Brain, Mind and Consciousness, Canadian Institute for Advanced Research, Toronto, Canada

ARTICLE INFO

Communicated by K. Liu

Keywords:
Whole-brain simulations
Emergent complexity
Brain rhythms
Model tuning
Human connectome
Larter-breakspear model

ABSTRACT

The simulation of whole-brain dynamics should reproduce realistic spontaneous and evoked neural activity across different scales, including emergent rhythms, spatio-temporal activation patterns, and macroscale complexity. Once a mathematical model is selected, its configuration must be determined by properly setting its parameters. A critical preliminary step in this process is defining an appropriate set of observables to guide the selection of model configurations (parameter tuning), laying the groundwork for quantitative calibration of accurate whole-brain models. Here, we address this challenge by presenting a framework that integrates two complementary tools: The Virtual Brain (TVB) platform for simulating whole-brain dynamics, and the Collaborative Brain Wave Analysis Pipeline (Cobrawap) for analyzing simulation outputs using a set of standardized metrics. We apply this framework to a 998-node human connectome, using two configurations of the Larter-Breakspear neural mass model: one with the TVB default parameters, the other tuned using Cobrawap. The results reveal that the tuned configuration exhibits several biologically relevant features, absent in the default model for both spontaneous and evoked dynamics. In response to external perturbations, the tuned model generates non-stereotyped, complex spatio-temporal activity, as measured by the perturbational complexity index. In spontaneous activity, it exhibits robust alpha-band oscillations, infra-slow rhythms, scale-free characteristics, greater spatio-temporal heterogeneity, and asymmetric functional connectivity. This work demonstrates how combining TVB and Cobrawap can guide parameter tuning and lays the groundwork for data-driven calibration and validation of accurate whole-brain models.

1. Introduction

Whole-brain computational models based on the neural mass approximation provide a framework for investigating the fundamental mechanisms underlying large-scale neural dynamics [5,47]. However, a crucial challenge remains: how to configure and adjust such a model so that it simultaneously captures key features of spontaneous and evoked

* Corresponding author at: Dep. of Biomedical and Clinical Sciences, Univ. of Milan, Milan, Italy.
** Corresponding author.
Email addresses: gaglioti.gianluca@gmail.com (G. Gaglioti), cosimo.lupo89@gmail.com (C. Lupo).
[1] These authors contributed equally.
[2] These authors jointly supervised this work.

https://doi.org/10.1016/j.neucom.2026.132735
Received 10 October 2025; Received in revised form 15 December 2025; Accepted 14 January 2026
Available online 21 January 2026

brain activity, and ultimately matches empirical data. Among the essential features that a biologically realistic whole-brain model should reproduce, the alpha rhythm (8–12Hz) stands out as a fundamental oscillation in large-scale brain dynamics. First described by Berger [4], it is closely associated with states of relaxed wakefulness and is thought to play a role in cognitive processes [60,63]. While alpha oscillations are a hallmark of resting-state dynamics, their fluctuating and multistable nature reflects the inherent variability and the transient state shifts of the brain [38,39]. In addition, they do not act in isolation but rather coexist with fluctuations occurring across multiple timescales [36,81]. At rest, brain activity fluctuates over time, exhibiting complex patterns of spontaneous variation in neuronal signals shaping the functional organization of the brain [26]. Fluctuations also exhibit significant regional heterogeneity, with varying degrees of signal variability influenced by anatomical connectivity and functional roles [24]. High-fluctuation regions act as integrative hubs, crucial for coordinating information flow across the network [56,83]. These regions may contribute to infra-slow fluctuations (< 0.1Hz), which shape large-scale brain dynamics [48,81,83,99] and drive dynamic functional connectivity and brain state reconfiguration [48,95]. Beyond this spontaneous dynamics, the awake brain also exhibits sustained and spatially complex responses evoked by external focal perturbations, a phenomenon that has been extensively studied in experimental settings, such as in transcranial magnetic stimulation combined with simultaneous electroencephalography (TMS-EEG) experiments, where the spatio-temporal complexity of the evoked cortical response has been shown to correlate with the level of consciousness [12,13,86]. In this context, various forms of external brain stimulation, including non-invasive neuromodulatory techniques, are capable of directly modulating these spontaneous and evoked features, producing measurable changes in both the periodic and aperiodic components of neural activity, as well as in functional connectivity patterns [42,62,70,75,78,102–104].

These features – multistability, scale-free and infra-slow fluctuations, dynamic reconfiguration, and complex evoked responses – have been increasingly linked to critical dynamics in the brain [23,80]. The hypothesis of brain criticality posits that neural systems operate near a critical point between order and disorder, a regime that supports maximal variability, long-range correlations, and optimal responsiveness to external inputs [3,15,16,74,82,91].

As anticipated, a key question emerging from these considerations is whether a single, unified model can simultaneously reproduce both features of spontaneous and evoked brain activity. Indeed, traditionally, these two have been treated as separate problems in computational modeling. However, a relationship is expected between the richness of spontaneous activity patterns and the ability of the brain to sustain complex responses to external perturbations through its network dynamics. Therefore, capturing the interplay of spontaneous and evoked dynamics, while assessing their consistency with empirical data, should be considered as a non-trivial requirement for the simulated network.

This assessment process is grounded on an initial parameter *tuning*, aimed at addressing the correct sub-region in the parameter space, and exploring how changes in model settings influence target observables. The set of quantitative observables – defined in the tuning to assess the quality of the model – will be referred to from now on as *metrics*. Tuning is followed by a *calibration*, which adjusts the model parameters – ideally using an automated optimization process – by leveraging the metrics defined during the tuning to match a specific/personalized dataset. When discrepancies occur, these metrics offer feedback for refining the model and identifying its region of applicability, ensuring that the model reproduces not only isolated features, but also the brain broader dynamical landscape. It is worth noting that the identification of the starting parameter domain performed during the tuning is an essential ingredient for any automated calibration process that explores a high dimensional parameter space. Finally, a more thorough *validation* should be performed against a range of statistical features to establish their agreement with respect to independent experimental data [e.g.,52,96], leveraging the wealth of heterogeneous data available and facilitating cross-study comparisons. This tuning/calibration/validation procedure should rely on a processing of simulation outputs that is methodologically consistent with the analysis of experimental outcomes, especially when aiming to embrace a wider range of case studies for a more precise alignment between theoretical predictions and experimental observations. In addition, to enhance the reproducibility and the scope of application of the simulations, the model setup and the metrics used for data analysis should be accessible to the broader neuroscientific community, standardized across the calibration/validation loops and carried out by a robust simulation/analysis workflow.

A number of frameworks address these needs for standardization, both for simulation and data analytics. Platforms like The Virtual Brain (TVB) [87,88], the Brain Dynamics Toolbox [55], and Neurolib [9] facilitate and standardize whole-brain simulations using neural mass models, which describe large-scale neural interactions via phenomenological or mean-field approaches [5]. Among the advantages of these solutions, the prebuilt, validated models offered by these platforms streamline calibration against empirical data, allowing researchers to focus on scientific questions rather than custom coding. Active user communities further enhance reproducibility and collaboration. Tools like MNE [46] for EEG/MEG, FreeSurfer [34] for Magnetic Resonance Imaging (MRI), fMRIPrep [32] and CPAC [72] for functional MRI (fMRI), and Elephant [28] for electrophysiological data already provide reproducible analyses. To varying extents, such methodologies integrate heterogeneous data, minimize inconsistencies, and enhance comparability, which are crucial for addressing the challenges of multimodal neuroscience. However, tools like the above are usually designed to address specific experimental cases, resulting in highly tailored solutions but also potentially reduced generalizability, which may require separate approaches when performing data versus model comparisons. Extending this principle to complete analytics workflows, the Collaborative Brain Wave Analysis Pipeline (Cobrawap) [49,50] has been developed as an open-source tool providing standardized and quantitative descriptions of brain wave phenomena in both experimental recordings and in silico data [11], addressing the growing need for shared and agreed metrics and methodologies in the field. Complementing this ecosystem of tools, broad initiatives like the Human Connectome Project [98], the Allen Brain Atlas [94], and EBRAINS [30] provide publicly available curated data and frameworks.

In this study, we take the first steps toward the calibration of a whole-brain model able to simultaneously reproduce key features of both spontaneous and evoked brain dynamics. To this end, we employ a recently developed whole-brain model implemented in TVB [41] and identify the most relevant parameters to be tuned. Because the visualization and analysis tools included with TVB neither support systematic evaluation of metrics in response to changes in model parameters, nor allow quantitative comparison with experimental data, we set up an iterative approach (Fig. 1(A)) that leverages analysis methods already implemented in Cobrawap (adding new ones suitably developed, when necessary). Specifically, we identify the features that are relevant for describing both spontaneous and evoked activity of the whole-brain model: alpha-band oscillations, infra-slow fluctuations, and the spatio-temporal complexity of evoked responses. By recognizing and varying the related parameters, we can drive the model simulations into activity regimes that show more similarities to the heterogeneous, multiscale features of large-scale brain activity. The approach we propose aims at offering a first tackle to the above depicted process of tuning/calibration/validation of TVB-based brain models, a process that is not trivial, as discussed in [90,97], especially when aiming at personalized models. Our results show that an accurately tuned model can account for both the variability of resting-state activity and the complexity of stimulus-evoked

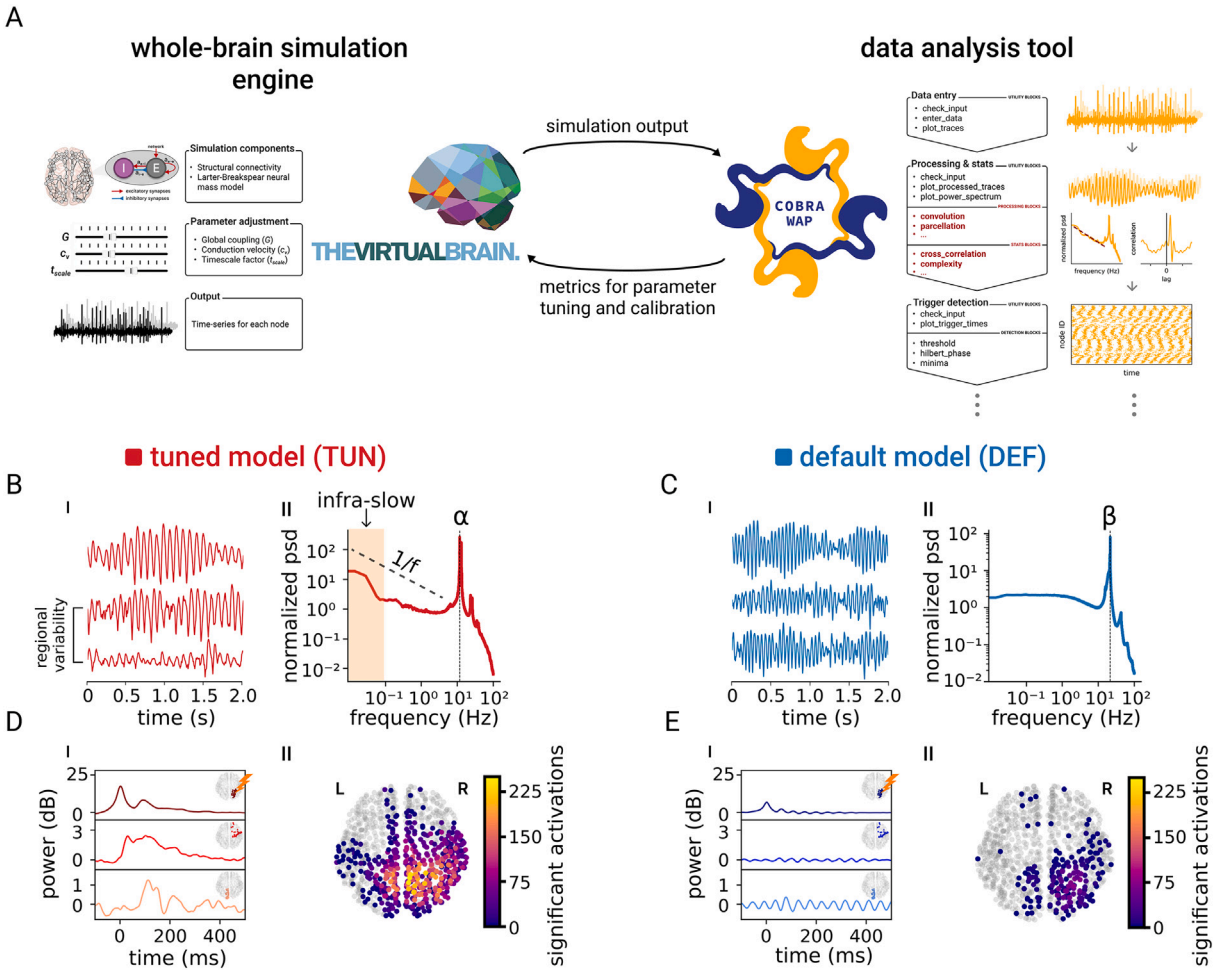

Fig. 1. TVB simulations and analysis with Cobrawap. **A)** The TVB-Cobrawap workflow (center) facilitates tuning, calibration and validation of TVB model parameters; left and right diagrams sketch the sequence of actions requested, respectively, for launching TVB simulations and for processing TVB output with Cobrawap. The latter is adapted from [49] and illustrates the sequence of stages and blocks arranged along the pipeline for the study of brain dynamics; text in red highlights methods and metrics specifically implemented for addressing the TVB-tuning use-case, like cross correlations, parcellation reduction, complexity, in addition to what already provided by the Cobrawap pipeline – such as trace statistics, spectral analysis, event detection. Plots are included in the diagrams as exemplary for illustration purposes; detailed discussion is given later in the manuscript. **B)** Illustrative examples of three spontaneous activity traces from three cortical regions of the tuned (TUN) configuration (B_I). These represent proxies of synaptic activity, obtained by convolving the voltage traces with a bi-exponential kernel (see Section 2.5.2) at the single-node level, and subsequently averaging the resulting signals across nodes belonging to each region. From top to bottom, the traces correspond to the average synaptic activity across left-hemisphere nodes belonging to the IP, IT, and PARC regions, respectively (see Suppl. Table A.1). The average Power Spectral Density (PSD) across all regions displays a clear peak in the alpha band, at approximately 12Hz, together with an enriched infra-slow spectral component (B_{II}). **C)** Same as B), referred to the default (DEF) configuration. In this case, the dominant peak in the PSD is observed within the beta frequency band, centered around 21.6Hz, with no relevant infra-slow activity. **D-E)** A brief stimulus (2ms) was applied to the same nodes of the TUN and DEF configurations, to assess the spatio-temporal propagation of evoked activity. The post-stimulus power (see Section 2.5.3) of three subsets of nodes (specifically, the subset of stimulated nodes, a subset of far nodes connected to the stimulated nodes but in the same hemisphere where stimulation occurred, and the farthest set of nodes – in terms of connectome tracts – connected to the stimulated nodes), averaged across the same subset, displayed a consistent increase in all subsets in the TUN configuration with respect to DEF, together with a higher heterogeneity in the temporal evolution (compare D_I with E_I). The extent of significant post-stimulus activity (see Section 2.5.5), computed by summing the significant activations of each node between 10 and 500ms, was mapped onto the brain map for TUN (D_{II}) and DEF (E_{II}). The panels indicate a more widespread propagation in TUN compared to DEF.

responses, thus bridging a gap between traditionally separate modeling efforts for the two conditions. Moreover, we lay the groundwork for generalizable calibration/validation metrics that provide a robust foundation for future empirical testing and integration into automated workflows.

2. Materials and methods

In the following, we first detail the TVB implementation of the whole-brain model to be later tuned, followed by a description of the analysis steps used for measuring model features and performance.

2.1. Model equations

We use the Larter-Breakspear (LB) model [6–8,66], a voltage-based phenomenological neural mass model commonly used to simulate whole-brain activity [2,31,41,44,45,57–59,84], implemented within the TVB simulator.

Connectivity is implemented by means of a 998-node bi-hemispherical connectome [53], where each node represents a source of signals reproducing the spontaneous dynamics of a neural mass model in the resting state. The connectome specifies the strength of connections between nodes and the corresponding time delays, globally modulated

by the coupling parameter G. Time delays between nodes can be globally rescaled by adjusting the global conduction velocity parameter c_v.

The dynamics of a given node in the brain network are described by the following set of ordinary differential equations:

$$\frac{1}{t_{\text{scale}}}\frac{dV}{dt} = -\left[g_{\text{Ca}} + (1-C) r_{\text{NMDA}}\, a_{e\to e}\, Q_{\text{V}} + C\, r_{\text{NMDA}}\, a_{e\to e}\, Q_{\text{V,network}}\right] m_{\text{Ca}}(V - V_{\text{Ca}}) - \left[g_{\text{Na}}\, m_{\text{Na}} + (1-C)\, a_{e\to e}\, Q_{\text{V}} + C\, a_{e\to e}\, Q_{\text{V,network}}\right](V - V_{\text{Na}}) - g_{\text{K}}\, W (V - V_{\text{K}}) - g_{\text{L}}(V - V_{\text{L}}) - a_{i\to e}\, Z\, Q_{\text{Z}} + a_{n\to e}\, I + \xi_{\text{V}}, \tag{1a}$$

$$\frac{1}{t_{\text{scale}}}\frac{dZ}{dt} = b\,\left(a_{n\to i}\, I + a_{i\to e}\, Q_{\text{V}}\, V\right) + \xi_{\text{Z}}, \tag{1b}$$

$$\frac{1}{t_{\text{scale}}}\frac{dW}{dt} = \frac{\phi\,(m_{\text{K}} - W)}{\tau_{\text{K}}} + \xi_{\text{W}}, \tag{1c}$$

where V and Z are the mean membrane potentials of the excitatory pyramidal neurons and inhibitory interneurons for that node, respectively, while W corresponds to the average number of open potassium (K) channels. The term t_{scale} is a dimensionless time-scaling factor that rescales the temporal dynamics of all state variables. The ratio of NMDA receptors to AMPA receptors is captured by r_{NMDA}, and $a_{x\to y}$ defines the synaptic strength between the source population x (where x is one of e: excitatory, i: inhibitory, or n: nonspecific input) and the target population y (where y is e or i). I represents an external input current, modeling nonspecific excitatory drive, such as subcortical or thalamic inputs, that influence the activity of excitatory (V) and inhibitory (Z) populations. The dynamics of Z and W are governed by the constant rate terms b, τ_{K} and ϕ, which respectively represent a time constant for inhibitory activity (Z), a time constant for W relaxation, and a temperature scaling factor for the evolution of W.

For each ion species, g_{ion} (where ion is one of Ca: calcium, Na: sodium, or K: potassium) represents the maximum ion conductance and V_{ion} represents its reversal potential. Similarly, g_{L} and V_{L} represent the maximum leakage conductance and reversal potential, respectively. The voltage-dependent fraction of open channels is governed by m_{ion}, following a sigmoidal shape function for each node:

$$m_{\text{ion}}(t) = \frac{1}{2}\left[1 + \tanh\left(\frac{V(t) - T_{\text{ion}}}{\delta_{\text{ion}}}\right)\right], \tag{2}$$

where T_{ion} term represents the mean threshold membrane potential for a given ion channel population, while δ_{ion} denotes its standard deviation. The mean firing rates of the excitatory and inhibitory node populations are governed by the voltage-dependent activation functions Q_{V} and Q_{Z}, respectively, which are modeled as sigmoidal as well:

$$Q_{\text{V}}(t) = \frac{1}{2}\, Q_{\text{V}_{\max}}\left[1 + \tanh\left(\frac{V(t) - V_{\text{T}}}{\delta_{\text{V}}}\right)\right], \tag{3a}$$

$$Q_{\text{Z}}(t) = \frac{1}{2}\, Q_{\text{Z}_{\max}}\left[1 + \tanh\left(\frac{Z(t) - Z_{\text{T}}}{\delta_{\text{Z}}}\right)\right], \tag{3b}$$

where the terms $Q_{\text{V}_{\max}}$ and $Q_{\text{Z}_{\max}}$ are the maximum firing rates of the excitatory and inhibitory populations, respectively. The thresholds for action potential generation for these populations are given by V_{T} and Z_{T}, with corresponding standard deviations δ_{V} and δ_{Z}, respectively. Finally, the input to a node k coming from the rest of the network, $Q^{(k)}_{\text{V,network}}$, is defined as:

$$Q^{(k)}_{\text{V,network}}(t) = G \sum_{\{j\}} u_{j\to k}\, Q^{(j)}_{\text{V}}(t - \tau_{j\to k}), \tag{4}$$

with the sum running over all the nodes $\{j\}$ connected to k with connection weight $u_{j\to k}$, and $\tau_{j\to k}$ denoting the related input delay time. G is the aforementioned global coupling that scales all the connection weights. The parameter C in Eq. (1) varies between 0 and 1 and controls the balance between the strength of self-connections and the connections with the rest of the network. Finally, an additive Gaussian noise ξ enters into Eq. (1) through the stochastic Heun integration method of TVB.

2.2. Model configurations and parameters

We implement two parameter configurations for the LB model, with their values fully listed in Suppl. Table A.2. The first configuration, referred to as the tuned configuration (TUN) from here on, is based on the work by Gaglioti et al. [41], with some further refinements here. The second configuration, derived from the default parameters in TVB, follows the work of [2] and will be referred to as the default configuration (DEF). The TUN configuration is capable of generating complex evoked patterns following external stimulation [41], resembling empirical results from the healthy awake brain. In this study, we focus on resting-state activity and, to better align with empirical data, we adjust the timescale t_{scale} of the TUN configuration from 1.0 to 0.6 to reproduce the alpha-band location of the experimentally observed peak in the power spectrum of the global resting state activity [4,60,63]. Notice that a time rescaling in Eq. (1) implies a coherent rescaling of the connectome conduction velocity c_v and of the additive Gaussian noise ξ in the TVB integrator (see Suppl. Table A.2). Consistently, the TUN configuration exhibits a peak at 11.7Hz in the resting condition Fig. 1(B) and displays complex dynamics following perturbation (Fig. 1(D); see the following section for further details on the simulation of resting-state and evoked activity). The corresponding measures for the DEF configuration are depicted in Fig. 1(C) and (E), respectively.

2.3. Model activity simulation in TVB

Each simulation is run in TVB (RRID: SCR_002249) with an integration time step of $\delta_t = 0.1ms$ using the stochastic Heun integration method. A Gaussian white noise is added to the state variables to emulate an additional background input to the node (standard deviation $\sigma_\xi = 10^{-7}$ for the DEF configuration, then rescaled by t_{scale} for TUN). The signal is then resampled to a temporal resolution of 1ms (i.e., averaging over 1ms time windows with the *temporal average monitor* of TVB).

For resting state, five minutes of continuous brain activity are simulated. Initial conditions are randomly assigned, with the values of the state variables (V, Z, W) drawn from a uniform distribution between −0.1 and 0.1. A conservative choice is made based on the observation that the initial transient phenomenon concludes after roughly 5s, hence an initial period of 10s is excluded.

For evoked activity, 200 trials are simulated. A stimulus of 1 arbitrary unit (a.u.) in amplitude and 2ms in duration is applied to the 27 nodes belonging to the right superior parietal (rSP) cortex region. Each trial begins with random initial conditions. The onset timing of the stimulus is randomized within a window between 10s and 12s, thus allowing for a long enough thermalization period after the random initialization. Finally, we retain 400ms of pre-stimulus activity (baseline) and 700ms of post-stimulus activity.

2.4. Tuning TVB model parameters with cobrawap

We use the Cobrawap framework (RRID: SCR_022966; [50,51]) to implement the tuning process of TVB-simulated models. Cobrawap is an open-source Python-based modular analysis workflow that generates standardized quantitative descriptions of brain wave phenomena, so far used for heterogeneous murine datasets of both experimental [49] and simulated [11] origins. Cobrawap extensibility to a wider variety of use-cases – among which, notably, the analysis of human data – stems from its modular design: it consists of a series of workflow components

implemented as scripts, each representing an elementary analysis or visualization operation; these *blocks* are then organized into a series of sequential *stages*, the selection and execution order of blocks in each stage being suitably configurable to fit the requirements of the input data and the analysis goal.

In this work we lay the foundations for the interoperability of TVB and Cobrawap – acting on single blocks and on the Cobrawap structure itself – as an integrated use-case for the complete calibration and the validation of TVB-simulated models. Intrinsically, Cobrawap operates on matrices, reflecting the regular organization of sensors: each matrix element represents a *channel* associated with the spatial position corresponding to an elementary source of experimental or simulated activity – e.g., a camera pixel or an electrode – sampled at discrete points in time. To map TVB output to the Cobrawap framework, the individual neural mass of a particular node in the model is hence associated with a channel. In more detail, the 3D spatial arrangement of the N connectome nodes is reorganized as a 1D vector containing the same number of channels, arranged following the connectome ordering [53]. This simplified computational solution is sufficient for our analysis, since the focus is on node cross-correlations, for which only the distance among nodes in the connectome is relevant, together with TVB-encoded temporal delays.

New processing and visualization blocks are designed for this specific TVB-tuning use-case (see following section), improving and expanding what is already available within the latest Cobrawap release [51]; these new features are currently implemented in a dedicated development software branch, and will be fully integrated into the official Cobrawap software release 0.3.0.

2.5. Metrics employed for data analysis

The following metrics are employed to comprehensively analyze the dynamics of simulated brain activity across both spontaneous and evoked conditions in the TUN and DEF configurations, unless otherwise specified.

2.5.1. Events

To characterize the node dynamics at the channel level, we identify the timestamps of transitions from low to high levels of activity in the signal evolution. Hereafter, we refer to such transitions as *events*. Events are detected for each node by applying a threshold to the phase signal derived as the angle of the complex-valued analytic signal of the node (obtained via a Hilbert transform operation). In this study, a threshold of $-\pi/2$ is chosen, corresponding to the start of the upstroke. To ensure robustness, the algorithm selects only the time points where the threshold is crossed in an upward direction (from smaller to larger values), reaching a clearly identifiable peak (phase = 0) before the next threshold downward crossing. We obtain the *average event rate* by counting the total number of events during the simulation divided by the time length of the simulation itself. Additionally, we define the time interval between events as *inter-event-time* (IET), and calculate the related coefficient of variation $\mathrm{CV}_{\mathrm{IET}}$ (see details in the following).

2.5.2. Power spectral density analysis

According to the cortical organization principles summarized in Larkum [65], superficial layers of the cortex are reached mainly by non-specific thalamic nuclei projections and inter-areal cortical association fibers, and the apical tuft of pyramidal neurons is functionally enriched for NMDA-dependent regenerative integration of these long-range paths. However, $Q_{\mathrm{V,network}}$ and Q_{V} excitatory contributions in Eq. (1a) are not endowed with the slow injection times that are associated with NMDA receptors. To create a better proxy for the EEG signal and investigate it in the frequency domain, we convolve V with a bi-exponential kernel aimed at mimicking synaptic currents. Also, this approach enables direct compatibility with the output of TVB simulations representing the average membrane potential of the pyramidal population and not the impinging currents on that population. We select NMDA-like parameters to emulate the synaptic activity profile in the high-activation regime rise time constant $\tau_{\mathrm{rise}} = 5ms$ and decay time constant $\tau_{\mathrm{decay}} = 20ms$, following [43]. Then, to obtain the synaptic activity profile of each cortical region, we average the convolved signal across all nodes corresponding to a given region (see Suppl. Table A.1), thus producing 66 regional synaptic activity profiles. The power spectral density (PSD) of this synaptic activity proxy is then computed using the Welch method with time segments of 70s and a 50% overlap.

As an additional measure, the PSD is computed on the hemispheric event data, obtained by cumulating the number of events that occur at any node of each hemisphere using temporal bins of 5ms; this results in two aggregated signals (one per hemisphere) with a sampling resolution of 200Hz. To detect infra-slow frequencies, the Welch method is applied with time segments of 140s and a 50% overlap. On the resulting PSDs, the $1/f$ background scaling is estimated by fitting a linear function in log-log space to obtain the PSD slope, following [19].

2.5.3. Time-frequency analysis

Time-frequency decomposition is performed using a continuous wavelet transform with complex Morlet wavelets, implemented via the `PyWavelets` package [67]. In the resting state, scales (i.e., the temporal span of wavelets) are computed for frequencies around the main peak in the frequency spectrum (8–12Hz for TUN and 18–22Hz for DEF configurations) in 1Hz steps; for the evoked activity, scales range instead within 8–100Hz, still in 1Hz steps, to account for a potentially wider evoked spectrum. Each wavelet is parameterized with a normalized bandwidth of 1 and a normalized center frequency of 1; normalization depends on the sampling frequency (1kHz). The transformation is applied using a Fast Fourier Transform (FFT)-based method, yielding complex wavelet coefficients.

The time-frequency power representation is then obtained as the squared magnitude of the complex coefficients for each frequency, then averaged over the frequency range. Only for the analysis of the evoked activity, power is also averaged across all trials, to obtain the temporal evolution of broadband post-stimulus power. To account for baseline variability, the trial-averaged power time-course $\mathcal{P}$ is normalized using a decibel (dB) transformation with respect to the pre-stimulus mean:

$$\widetilde{\mathcal{P}} \equiv 10 \log_{10} \left(\mathcal{P}_{\mathrm{post}} / \langle \mathcal{P}_{\mathrm{pre}} \rangle \right), \tag{5}$$

where $\mathcal{P}_{\mathrm{post}}$ represents the post-stimulus power at each time point, while $\langle \mathcal{P}_{\mathrm{pre}} \rangle$ is the time average from −350ms to −50ms with respect to the stimulus onset.

To assess long-range temporal correlations in resting-state neural dynamics, we apply the Detrended Fluctuation Analysis (DFA) to the amplitude envelope from the wavelet transform (i.e., the frequency average of the magnitude of complex coefficients). DFA quantifies long-range temporal correlations – a hallmark of critical dynamics [69] – by measuring how fluctuations persist over increasing time window sizes. We use the implementation provided in the `neurodsp` package [18], which first detrends the signal by removing its mean and computes the cumulative sum. The resulting signal is then divided into equal-sized windows, and within each, a linear trend is fitted. The fluctuation is computed as the mean squared deviation from this trend, and the procedure is repeated over multiple window sizes to estimate the scaling exponent. In our analysis, we use 50 window sizes, logarithmically spaced between 0.5 and 50 s.

2.5.4. Correlation functions

The auto-correlation function quantifies the temporal correlation of a signal with itself across varying time lags. In this study, we apply it to channel signals from both TUN and DEF configurations, considering lags up to ± 120ms, in steps of 1ms. The analysis focuses on identifying the largest auto-correlation peak at $\mathrm{lags} \neq 0$, and the corresponding *optimal* value of the lag is recorded for further analysis. Analogously, the cross-correlation function is employed to quantify the similarity between signals originating from different brain nodes across varying time

lags, also in this case up to ± 120ms in steps of 1ms. This analysis allows us to extract two key measures for each ordered pair of nodes: functional connectivity $\mathbb{FC}$, defined as the peak value of the cross-correlation function, and functional lag $\mathbb{FL}$, corresponding to the lag (in ms) at which the peak occurred, where the sign of the lag reflects the direction of the interaction (e.g., a negative lag between nodes i and j would indicate a directional relation from i to j). In general, this approach results in non-symmetric $\mathbb{FC}$ and $\mathbb{FL}$ matrices, thereby capturing the directionality of interactions between brain nodes. Hence, we quantify such asymmetry as $\mathbb{FC}_{\text{asym}} \equiv \mathbb{FC} - \mathbb{FC}^{\intercal}$ and $\mathbb{FL}_{\text{asym}} \equiv \mathbb{FL} - \mathbb{FL}^{\intercal}$, where $(\cdot)^{\intercal}$ denotes the matrix transpose. In particular, the matrix $\mathbb{FC}_{\text{asym}}$ captures directional differences in communication, with positive values $\mathbb{FC}_{\text{asym},ij} > 0$ indicating that node i exerts a stronger influence on node j than vice versa, and negative values $\mathbb{FC}_{\text{asym},ij} < 0$ indicating the opposite. To derive a nodal asymmetry score, we finally compute the sum of asymmetry values across each row of $\mathbb{FC}_{\text{asym}}$, thus projecting the 2D representation of the matrix into 1D vectors, and yielding a single asymmetry score per node:

$$\mathbb{A}_{\text{i}} = \sum_{j} \mathbb{FC}_{\text{asym},ij}\,, \tag{6}$$

where $\mathbb{A}_i$ represents the net asymmetry of node i, with positive values indicating a global leading role (*parent*) in the network, and negative values indicating nodes behaving as "followers" (*children*).

2.5.5. Complexity metrics: PCI and functional complexity

The *Perturbational Complexity Index* (PCI), originally introduced by Casali et al. [12], provides a quantitative measure of the inherent complexity of spatio-temporal EEG activity patterns evoked by Transcranial Magnetic Stimulation (TMS). In this study, we adopt a similar framework, leveraging evoked whole-brain activity simulated using TVB as a proxy for the signal reconstructed at the "sources". To identify the significant spatio-temporal patterns of stimulus-evoked responses, we apply the non-parametric bootstrap-based statistical analysis of Casali et al. [12] on the voltage signal of each node. The procedure, also known as the *maximal statistic* [79], is organized as follows. First, the evoked activity is rescaled with respect to the pre-stimulus baseline by subtracting the mean and dividing by the standard deviation of the pre-stimulus period. Second, for each node, pre-stimulus activities are randomly sampled with replacement (*bootstrapped*) from the original distribution across trials and pre-stimulus time samples. Third, for each node and time point, the mean across trials of the bootstrapped values is computed (*Jboot*). Fourth, for each pre-stimulus time point, the maximum absolute value of Jboot across nodes is obtained. This process (steps 2, 3 and 4) is repeated 500 times to build a null distribution from which the $(1 - \alpha)$ percentile is used to define a significance threshold (we use $\alpha = 0.05$). Finally, a binary spatio-temporal mask is obtained by marking samples exceeding this threshold as significant, as in [12]. Eventually, PCI is computed by quantifying the Lempel-Ziv complexity [68] of the binarized matrix representing significant activations, then normalized by the source entropy.

In addition, in order to assess the richness of interactions within the functional connectivity matrix $\mathbb{FC}$, *functional complexity* can be computed, which quantifies the balance between functional integration and functional segregation [105]. A low functional complexity is characterized by narrow distributions of values in the matrix, indicating either near-total statistical independence ($\langle \mathbb{FC} \rangle \approx 0$, i.e., total functional segregation) or global synchrony ($\langle \mathbb{FC} \rangle \approx 1$, i.e., total functional integration). In contrast, complex interactions arise when the collective activity is characterized by intermediate states yielding a broad distribution of the $\mathbb{FC}$ values. Following this methodology, functional complexity is computed as the sum of the absolute differences over the m bins between the distribution of $\mathbb{FC}$ values and the uniform distribution over the same range, as described in [105].

2.5.6. Statistical metrics

Standard statistical metrics are employed in this study, including the standard deviation (SD), representing the dispersion around the mean, and the inter-quartile range (IQR), describing the spread of the middle 50% of the data. The coefficient of variation (CV) is used to assess relative variability (defined as the ratio of the standard deviation to the mean), while the median is used as a robust measure of central tendency.

3. Results

We simulate a whole-brain model via TVB, relying on a Larter-Breakspear neural mass model with a 998-node human connectome (see Sections 2.1–2.3), considering both the spontaneous activity in the resting state and the *evoked* activity (i.e., in response to an external perturbation). To assess the robustness of the approach, we also run a subset of the analyses on a smaller scale 74-node human connectome, as detailed in Supplementary Methods. We leverage Cobrawap (see Section 2.4) to analyze the simulation output and tune the model parameters to match a set of quantitative metrics based on relevant biological features (see Section 2.5) not expressed by the initial default (DEF) model configuration. Specifically: in response to external perturbations, the tuned (TUN) model generates non-stereotyped, complex spatio-temporal activity, as quantified by the perturbational complexity index; in spontaneous activity, it displays robust alpha-band oscillations, infra-slow rhythms, scale-free characteristics, greater spatio-temporal heterogeneity, and asymmetric functional connectivity.

We focus the tuning procedure essentially on the connectome global coupling G, the connectome conduction velocity c_v, the overall timescale factor t_{scale}, and a subset of parameters in the equations governing the single-node dynamics. Refer to Section 2 for details about their definition, and to Suppl. Table A.2 for their values in both DEF and TUN configurations.

The relevance of properly tuning the global coupling G (here increased from 1 to 3) to induce complex, non-stereotyped dynamics in this model – resembling the experimentally observed dynamics – has been preliminarily demonstrated in [41], where the target is to match functional and structural connectivity, along the lines proposed by Deco et al. [27]. In the same study [41], the tuning of node parameters is instrumental in obtaining evoked responses comparable to TMS-EEG experiments, as also discussed hereafter. In addition, here we focus on reproducing the previously listed biological features relevant to the spontaneous resting-state activity, again acting on single-node equation parameters. Among them, concerning the expression of proper rhythms, we identify as essential parameters to be tuned the overall timescale factor t_{scale} (moved from 1.0 to 0.6) and the conduction velocity c_v (rescaled for coherence by the same amount as t_{scale}; see Suppl. Table A.2).

In what follows, we quantitatively detail the different behavior of the two model configurations, highlighting the importance of accurately tuning the model parameters to move from a stereotyped simulation toward a more biologically plausible one.

3.1. Characterizing spontaneous dynamics: divergent temporal and spectral patterns in tuned vs. default configurations

We start by examining the membrane potential traces recorded in the resting-state condition, shown for three representative nodes (picked from FUS, PREC, and RMF regions of the right hemisphere, respectively; see Suppl. Table A.1) in TUN (Fig. 2(A)) and DEF (Fig. 2(C)) configurations; the corresponding amplitude distributions are shown in Fig. 2(B) and (D), respectively. Qualitatively, the TUN configuration exhibits more diverse activity patterns, with some nodes also displaying bursting dynamics (e.g., middle trace in Fig. 2(A)).

To identify the events of our interest, i.e., changes in the neural activity, we analyze the Hilbert phase of the membrane potential and apply a threshold of $-\pi/2$, following the methodology outlined by Gutzen et al. [49] (see Section 2.5.1). Fig. 2(E) and (G) show the raster plots of upgoing events for the two configurations, whereas Fig. 2(F) and (H)

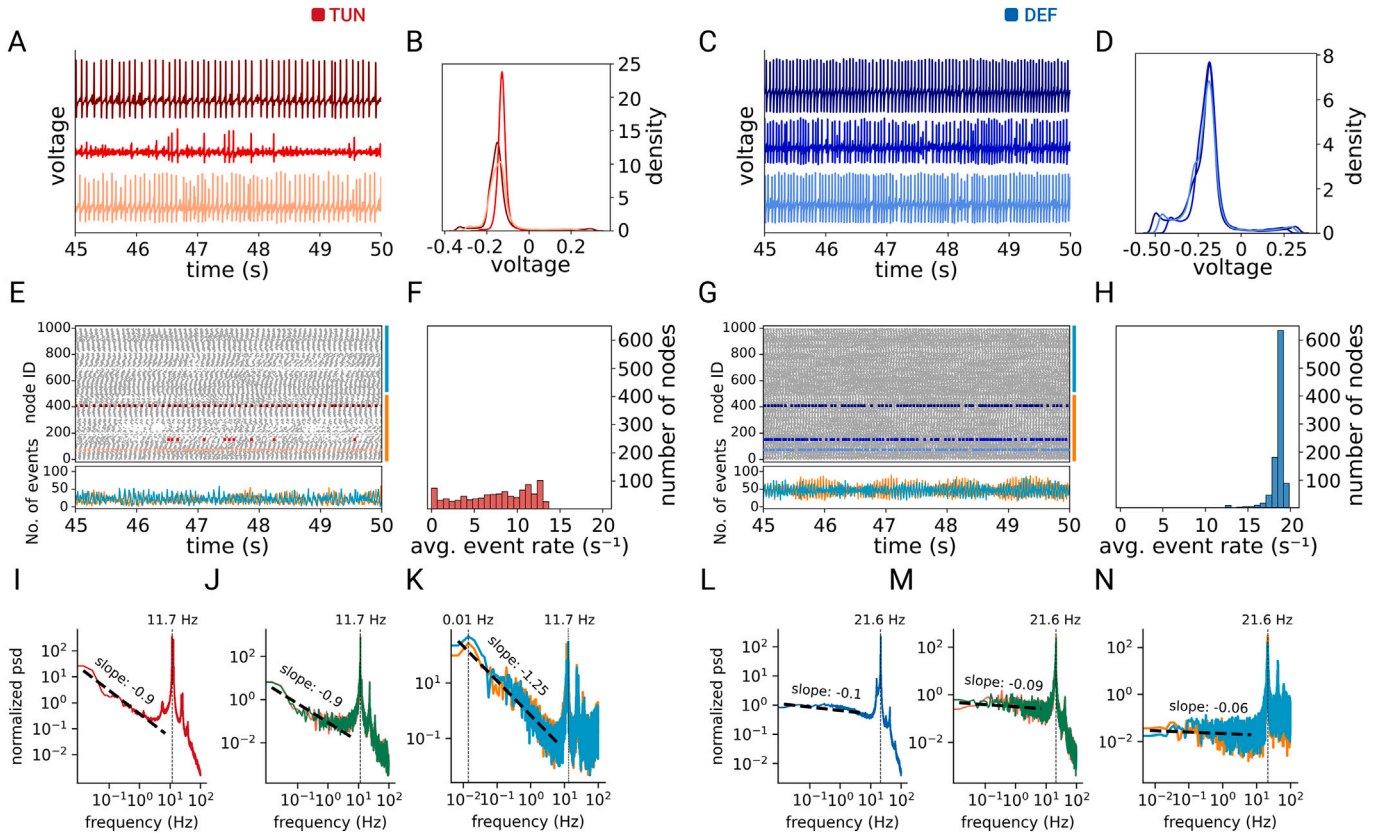

Fig. 2. Comparison of spontaneous dynamics in TUN and DEF configurations: time-domain and frequency-domain analyses. A) Voltage traces from three representative nodes from right-hemisphere FUS, PREC, and RMF regions (brown, red, and salmon lines, respectively) in the TUN configuration. **B)** The probability density functions of voltage distributions from nodes in A). **C-D)** Same as A) and B), respectively, for the DEF configuration. **E)** Rasterplots of upgoing transition events for each node (gray, top panel), alongside the cumulated number of detected events on the right and left hemisphere (orange and cyan, respectively, bottom panel), in the TUN configuration. Colored events in the upper panel are relative to the same sample traces shown in A). **F)** Histograms of the average event rate (red filled bars) across all nodes in TUN. **G-H)** Same as E) and F), respectively, for the DEF configuration. **I)** Average PSD of synaptic activity proxy across all regions in TUN, highlighting a peak frequency at 11.7Hz (black vertical dashed line). **J)** PSD of synaptic activity proxy of left LOCC (green line) and right LOCC (red line) in TUN, with a peak frequency at 11.7Hz. The synaptic activity was averaged over the nodes of right and left LOCC before computing the PSD. **K)** PSD of the cumulated event signals from both hemispheres (right hemisphere: orange line; left hemisphere: cyan line), showing a low-frequency content ($\sim$ 0.01Hz) in TUN. The black dashed oblique line represents the spectral slope, obtained by fitting a line to the average PSD in log-log space, in the frequency range 0.01–7Hz. **L-N)** Same as I), J) and K), respectively, for the DEF configuration; notice the peak frequency at 21.6Hz, and the absence of both the low-frequency content and the $1/f$ trend in the PSD of the default configuration.

illustrate the histograms of the average event rate across nodes (see Section 2.5.1); cyan and orange bars on the left side of the two rastergrams identify nodes belonging to the two hemispheres (left and right, respectively). The same color coding is used in the bottom part of Fig. 2(E) and (G), where cyan and orange traces represent the cumulative event signal of each hemisphere (see Section 2.5.2). A clear distinction emerges in the distribution of the average event rate across nodes: TUN shows a more heterogeneous pattern, compared to DEF (mean and standard deviation across channels: 9.60 $\pm$ 7.41Hz for TUN, 18.56 $\pm$ 0.91Hz for DEF).

The synaptic activity proxy (see Section 2.5.2) is derived from the voltage traces to approximate post-synaptic currents and obtain synaptic activity profiles for each cortical region (exemplary traces shown in Fig. 1(B)-(C)). We compute both the average PSD across all cortical regions (Fig. 2(I) for TUN, and Fig. 2(L) for DEF) and the PSD for specific regions of interest (Fig. 2(J) for TUN, and Fig. 2(M) for DEF) – here, the left and right lateral occipital cortex (LOCC; see Suppl. Table A.1). Additionally, to study the collective dynamics of the network, we compute the PSD from the cumulative event signal of the two hemispheres (Fig. 2(K) for TUN, and Fig. 2(N) for DEF; see Section 2.5.2), derived from the raster plots of events. By construction of the configurations, DEF displays a dominant frequency peak at 21.6Hz, whereas TUN shows a peak in the alpha band at 11.7Hz. This shift is primarily driven by the change in the timescale parameter t_{scale} with respect to the default setting (from 1.0 to 0.6; see Suppl. Table A.2 and Section 2). Furthermore, TUN reveals a distinct peak at 0.01Hz in the PSD of the cumulative event signal – absent in DEF – highlighting infra-slow network fluctuations; in contrast to the dominant frequency, this effect cannot be readily attributed to the tuning of a single parameter. Notably, a $1/f$ trend is also observed in TUN, but is absent in DEF, suggesting scale-free dynamics in the former configuration only.

The spectral features of the TUN configuration, namely alpha-band power and $1/f$ scaling, also show a closer correspondence to empirical EEG recordings obtained during resting state with eyes closed (Suppl. Fig. A.1), further supporting its biological plausibility.

Overall, these findings indicate that the TUN configuration supports a richer repertoire of dynamical activity across nodes, characterized by more heterogeneous average event rates, prominent infra-slow network fluctuations, and a scale-free $1/f$ spectral profile – hallmarks of dynamics closer to a critical regime [15,82].

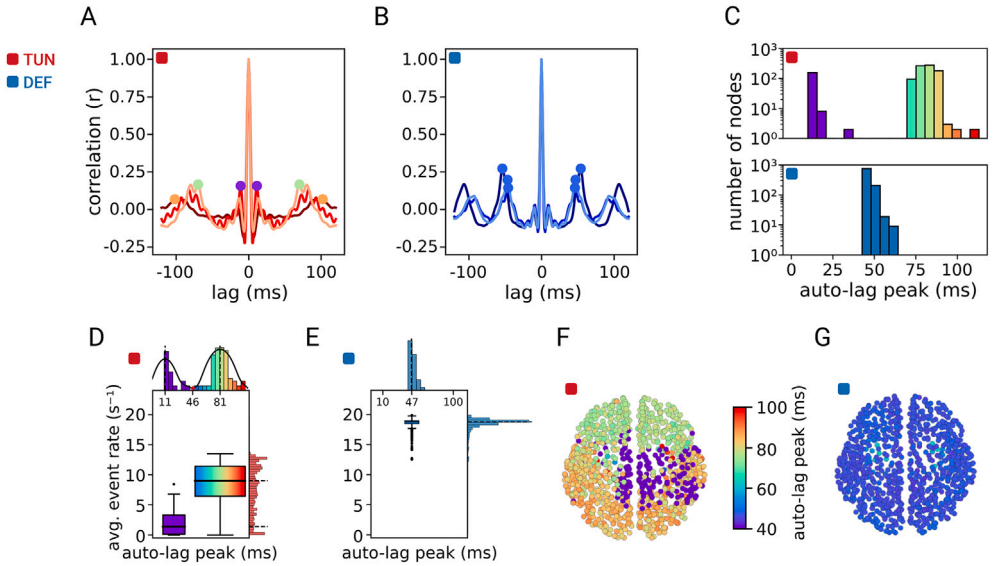

Fig. 3. Auto-correlation analysis and spatial distribution of periodicity in TUN and DEF. A-B) Auto-correlation functions of the spontaneous voltage signal from three representative nodes (same as in Fig. 2) for TUN (red palette) and DEF (blue palette). The largest peak at lag $\neq 0$ is marked by coloured dots. **C)** Distribution of the latencies of the dominant auto-correlation peaks (lag > 0) across brain nodes, revealing a bimodal distribution in TUN (top), while DEF (bottom) exhibits a narrow distribution centered around 50ms. **D)** Relationship between signal periodicity and average event rate in TUN. Boxplots depict the average event rate for nodes grouped by short (<46ms) and long (> 46ms) auto-correlation peaks. The nodes exhibiting periodicity in the first mode (i.e., < 46ms) are 17% of the total. The vertical and horizontal black dashed lines on the histogram mark the median of the distributions. **E)** Same as D), but for DEF. Here nodes are considered all together, not split into subgroups according to their auto-lag peaks. **F-G)** Spatial distribution of peak latencies mapped onto brain nodes for TUN and DEF configurations. TUN displays structured clustering, with faster periodicities in medial-central regions and a gradient between frontal and posterior regions. DEF exhibits a more homogeneous distribution of periodicities across the brain.

3.2. Signal periodicity analysis reveals spatially organized spectral features in the tuned configuration

To better understand the apparent mismatch in TUN between the heterogeneous event rates across nodes (Fig. 2(F)) and the spectral peak at ~12Hz that dominates at the global scale (Fig. 2(I)-(K)), we turn to auto-correlation analysis of the spontaneous voltage activity to capture the degree of temporal regularity of oscillations at each node. We therefore compute the auto-correlation function for each node in both TUN and DEF configurations.

These functions are illustrated in Fig. 3(A) and (B) for three different nodes (the same as in Fig. 2, from right FUS, PREC, and RMF regions). By examining the largest auto-correlation peak at lag $\neq 0$, we observe a median periodicity of 80ms (12.5Hz) in TUN and 47ms (21.3Hz) in DEF. This periodicity aligns with the PSD results in Fig. 2(I) and (L), where a peak around 12Hz is observed for TUN, and around 22Hz for DEF.

We therefore hypothesize that the median periodicity of 80ms and 47ms observed in TUN and DEF, respectively, is driven by the temporal arrangement of events in the two configurations. Supporting this hypothesis, the node-averaged PSD of the events (see Suppl. Fig. A.2) reveals peaks at approximately 12Hz in TUN and 22Hz in DEF. We interpret this as a signature of the network periodicity (as also suggested by the PSD of the hemispheric signal in Fig. 2(K) and (N), which we suggest is predictably influenced by global model parameters, such as conduction velocity c_v and global coupling G, as detailed in Suppl. Fig. A.3.

In addition to differences in the median peak, TUN also exhibits shorter peak latencies of approximately 11ms, as shown for a node of the right PREC region in Fig. 3(A) (red line and purple circles).

The distribution across nodes of the latencies of the dominant auto-correlogram peaks (Fig. 3(C), with lag > 0) highlights a clear difference between the TUN (Fig. 3(C), top panel) and the DEF (Fig. 3(C), bottom panel) configurations. In DEF the distribution is centered around 50ms (median = 47ms) with low variability (SD = 2.15ms), while in TUN a bimodal distribution emerges, with a larger standard deviation (SD = 26.48ms) driven by the presence of two distinct modes centered around 11ms and 81ms. The underlying cause of this bimodality is the relative difference in the strength of the ~80ms and ~11ms auto-correlogram peaks, varying node by node.

Since the auto-lag at ~80ms is mainly driven by the model events, we hypothesize that nodes expressing a higher strength of ~11ms peaks are those with a low average event rate (i.e., lower number of events), reflecting sub-threshold activity typical of nodes with irregular and bursty dynamics. An example is shown in the middle trace of Fig. 2(A), corresponding to the node in the right PREC region with a peak at 11ms in Fig. 3(A).

To test this, the two modes in the TUN auto-lag peak distribution are split considering the minimum of its Kernel Density Estimate function (found at 46ms); this allows separation of the nodes into two groups, depending on the dominant peak in the auto-correlogram. Relating the nodes of either group to their average event rate (Fig. 3(D)), we observe that the average event rate in TUN is lower for nodes in the group with short lags (median = 1.38Hz; mean = 1.92Hz; SD = 1.93Hz) than for nodes in the group with long lags (median = 9.00Hz; mean = 8.66Hz; SD = 3.35Hz). We repeat the same analysis for DEF in Fig. 3(E): the unimodality of DEF in the distribution of the latency is reflected by an analogous unimodality in the distribution of the average event rate (median = 18.78Hz; mean = 18.56Hz; SD = 0.91Hz). In summary, we interpret these findings such that the broad distribution of events and auto-lag peaks in the TUN configuration (vertical and horizontal histograms in Fig. 3(D), respectively) is due to a superposition of regular alpha-band activity and a component at 11ms, driven by the irregular, bursting activity of nodes exhibiting more sub-threshold dynamics (i.e., a lower number of events). In comparison, the DEF configuration shows a stereotyped beta oscillation that dominates the lags (Fig. 3(E)).

To visualize the spatial organization of these differences, we map the peak latencies onto a brain map (Fig. 3(F) and (G)), finding that TUN exhibits a more spatially organized clustering structure compared

to DEF. Indeed, in TUN (Fig. 3(F)) nodes with peak latencies around 11ms are clustered within central-parietal areas. Additionally, considering the second mode after 46ms, shorter peak latencies (corresponding to faster oscillations in the auto-correlation trace) are observed in frontal compared to posterior regions (Fig. 3(F)), an emergent feature of the model configuration that trends toward experimental findings [10,37,85]. Conversely, DEF displays a homogeneous spatial distribution, corresponding to more stereotypical simulated dynamics (Fig. 3(G)).

Together, these results demonstrate that the tuned configuration generates richer spatio-temporal dynamics characterized by *i)* a non-trivial spatial organization of the rhythms (with both frontal-posterior latency gradients and distinct central-parietal clusters showing shorter latencies and reduced average event rates), and *ii)* an enhanced overall heterogeneity – all contrasting sharply with the homogeneous, stereotyped activity patterns in the default configuration of the model.

3.3. Spatio-temporal irregularity and scale-free dynamics in the tuned configuration

The results presented in Fig. 3 demonstrate that the TUN configuration exhibits spectral heterogeneity which is reflected in a distinctive spatial topography of auto-correlation peak latencies. To explore how this heterogeneity manifests in the temporal domain, we next compute the coefficient of variation of the inter-event-time (CV_{IET}; see Section 2.5.1) across nodes. Fig. 4(A) and (B) show the distribution of CV_{IET} for TUN and DEF, respectively, while Fig. 4(C) and (D) map these values onto the brain. Once again, we observe a more pronounced heterogeneity in TUN, which is also reflected in a non-trivial spatial organization, in contrast to DEF. Specifically, TUN exhibits more irregular (i.e., higher CV_{IET} overall, particularly in central-parietal areas) and spatially heterogeneous events, while DEF shows more regular (i.e., lower CV_{IET}) and spatially homogeneous event patterns.

Building on this observation of irregularity and heterogeneity in event timing, a complementary and related aspect to consider is the temporal fluctuation of the neural signals themselves. To examine these dynamics more closely, we perform a time-frequency decomposition using Morlet wavelet convolution to extract the power time-course within the frequency band associated with events, specifically, the 8–12Hz range for TUN and the 18–22Hz range for DEF, corresponding to the respective dominant frequencies in their PSDs. The power time-courses (see Section 2.5.3) of a representative node in TUN and DEF are reported in Suppl. Fig. A.4(A). To quantify power fluctuations over time, we compute their coefficient of variation (CV_{power}) across nodes (Fig. 4(E) and (F)) and map it onto brain maps (Fig. 4(G) and (H)). Also in this case, power exhibits a high temporal and spatial regularity for the DEF configuration, resulting in a more homogeneous brain map with low and quite concentrated CV_{power} values. Conversely, we observe a heterogeneous distribution for TUN, with central areas displaying high CV_{power} values, indicative of pronounced power fluctuations. Interestingly, the average PSD across nodes of the power time-courses for TUN reveals significant $1/f$ scaling and infra-slow fluctuations (Suppl. Fig. A.4(B)) – mirroring the 0.01Hz components observed in the network-level PSD (Fig. 2(K)). This pattern of fluctuations in the TUN configuration also aligns with empirical EEG recordings: the PSD of the alpha power time-course in real EEG data shows a comparable $1/f$ scaling (Suppl. Fig. A.4(B)), and the distribution of CV_{power} across channels is more consistent with the TUN configuration than with DEF (Suppl. Fig. A.4(C)).

The dual manifestation of infra-slow rhythms across both nodal power time-courses and network-level activity suggests a scale-free spatio-temporal organization, where infra-slow fluctuations coherently modulate the dominant alpha-band dynamics in TUN. In stark contrast, DEF exhibits a flat PSD profile for power time-courses, consistent with uncorrelated (white-noise-like) dynamics. Together with the $1/f$ scaling (Fig. 2(K)), these findings suggest that TUN may operate near a critical regime. To test this hypothesis, we perform Detrended Fluctuation Analysis (DFA) (see Section 2.5.3 for details) on the 8–12Hz (18–22Hz for DEF) amplitude envelope. DFA exponents in TUN (Fig. 4(I)) span a broad range (exponent $\approx$ 0.5–1.2; IQR = 0.6–0.93), encompassing uncorrelated signals ($\approx$0.5), weak to strong long-range temporal correlations ($\approx$ 0.6–1.0), and persistent trends ($>$ 1.0). This heterogeneity suggests distinct dynamical sub-populations with a specific spatial distribution (Fig. 4(K)): approximately 30% of nodes fall within the range 0.8–1.0, often associated with near-critical or critical dynamics and also in line with empirical values observed in EEG data (Suppl. Fig. A.4(D)), while others exhibit either noise-like ($\approx$0.5; $\sim$16% of nodes) or more persistent ($>$ 1.0; $\sim$17% of nodes) behavior. In contrast, DEF consistently shows noise-dominated dynamics (exponent $\sim$ 0.5–0.6) across all nodes (Fig. 4(J) and (L)).

3.4. Emergent complex and asymmetric interactions in the tuned configuration

Up to this point, we have analyzed the dynamics of individual nodes, without examining their mutual interactions. To this specific aim, by leveraging cross-correlation functions one can derive two key metrics: the functional connectivity ($\mathbb{FC}$) and the functional lag ($\mathbb{FL}$) between each pair of nodes (see Section 2.5.4 for details). This procedure is illustrated in Fig. 5(A), where, for a given pair of nodes i and j, the cross-correlation between their time series is computed at different time lags.

The distributions of $\mathbb{FC}$ and $\mathbb{FL}$ values across all node pairs are reported in Fig. 5(B) and (C). Coherently with what has been seen so far, TUN exhibits higher and more dispersed $\mathbb{FC}$ values than DEF, reflecting stronger and richer interactions.

It has been suggested [105] that the richness of $\mathbb{FC}$ values can serve as an index of functional complexity (see Section 2.5.5), where the coexistence of high and low $\mathbb{FC}$ values supports a balance between functional integration (high $\mathbb{FC}$ values) and functional segregation (low $\mathbb{FC}$ values). We quantify this complexity during spontaneous activity, confirming that TUN exhibits higher functional complexity compared to DEF (inset of Fig. 5(C)).

The Functional Lag ($\mathbb{FL}$) (absolute values) and the Functional Connectivity($\mathbb{FC}$) matrices are displayed in Fig. 5(D)–(E) and (G)–(H), respectively, alongside the corresponding asymmetry values in Fig. 5(F) and (I), derived from $\mathbb{FC}_{asym}$ (see Suppl. Fig. A.5) and $\mathbb{FL}_{asym}$ (see Section 2.5.4 for further details). Notably, $\mathbb{FC}$ shows a greater asymmetry in TUN, compared to the DEF configuration (IQR = 0.01 for TUN; IQR = 0.006 for DEF), highlighting a prominent emergence of directional interactions in the tuned configuration. This reflects an emergent network phenomenon, because TUN differs from DEF in single-node equation parameters, global coupling and global conduction velocity, without modifying the relative connection strengths and the time delays of the underlying connectome.

In Fig. 5(J) and (K), we then quantify the asymmetry score $\mathbb{A}$ for each brain node in TUN and DEF, respectively: starting from $\mathbb{FC}_{asym}$, we marginalize its values along each row to obtain a single asymmetry score per node (see Section 2.5.4 for details). Positive values indicate nodes that predominantly exert influence on others (“leading” or “parent” nodes), while negative values denote nodes that are primarily influenced by others (“following” or “child” nodes). First, we observe differences between the left and the right hemisphere, with the right hemisphere expressing more “leading” nodes. Then, mapping the asymmetry scores of the nodes to brain regions and sorting them (see Suppl. Fig. A.6), we find that the posterior cingulate cortex (PC) has the highest positive asymmetry value in both the left and right hemispheres for the TUN configuration. This result aligns with experimental literature showing that the PC region is a primary driver of the spontaneous brain activity [17]. Suppl. Fig. A.6 further highlights the differences between the left and the right hemisphere, already illustrated in Fig. 5(J). Once again, DEF shows a more homogeneous behavior, with very little asymmetry values across the whole brain.

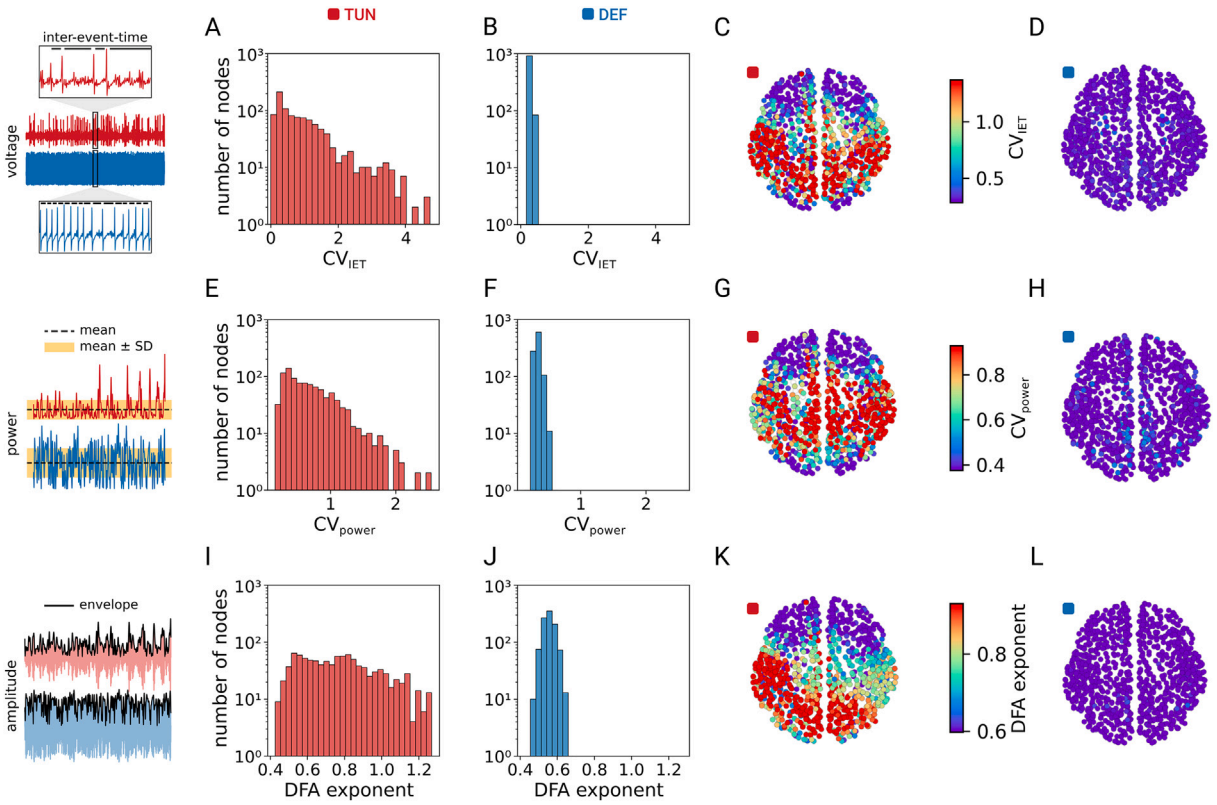

Fig. 4. Temporal and spatial variability of signal fluctuations in TUN and DEF. Signal processing steps are illustrated in the leftmost panels of each row: Top: Example traces show voltage fluctuations and inter-event-time (IET) used to calculate the CV_{IET}. Middle: Example power time courses used to compute the CV_{power}, with shaded regions indicating mean ± standard deviation. Bottom: Example amplitude envelope traces used to estimate the DFA exponent across nodes. **A-B)** Histograms showing the coefficient of variation of inter-event-time (CV_{IET}) across nodes for TUN and DEF configurations. **C-D)** Spatial distribution of the CV_{IET} mapped onto brain nodes for TUN and DEF configurations. **E-F)** Histograms showing the coefficient of variation of the power time-courses (CV_{power}) across nodes, computed via Morlet wavelet convolution for TUN and DEF configurations. Power was obtained by summing within the 8–12Hz range for TUN and the 18–22Hz range for DEF. **G-H)** Brain maps displaying the spatial distribution of CV_{power} in TUN and DEF configurations. **I-J)** Histograms showing the DFA exponent computed for each node on the amplitude envelope in the 8–12Hz range for TUN and the 18–22Hz range for DEF. **K-L)** Brain maps displaying the spatial distribution of DFA exponents for TUN and DEF configurations.

In Fig. 5(L), eventually, we examine the relationship between the asymmetry score and power fluctuations, measured by CV_{power}. Notably, we find a significant positive correlation ($r = 0.51$, $p = 10^{-66}$), indicating that nodes with greater power variability tend to have stronger leading roles for the TUN configuration. In contrast, the same analysis for DEF reveals a non-significant relationship ($r = 0.009$, $p = 0.77$) (see Suppl. Fig. A.7).

3.5. Evoked responses reveal higher spatiotemporal complexity in the tuned configuration

To assess the model capacity to sustain complex stimulus-evoked dynamics, we apply 200 independent brief (2ms) perturbations to the right superior parietal (rSP) nodes in both TUN and DEF configurations. The resulting evoked activity reveals striking differences between the two: in the TUN configuration, the average post-stimulus voltage exhibits richer and less stereotyped dynamics (Fig. 6(A)), compared to the more uniform and rapidly decaying responses observed in the DEF configuration (Fig. 6(B)).

To characterize the spatio-temporal profile of the evoked activity, we derive a binary spatio-temporal matrix of significant activations (see Section 2.5.5 for details). In TUN, the evoked activity is sustained over a broader temporal and spatial window (Fig. 6(C)), whereas in DEF it remains spatio-temporally confined to the immediate post-stimulus period and to the surroundings of the perturbed region (Fig. 6(D)). The prolonged perturbation effects in the TUN configuration cannot be explained solely by the reduction of the timescale parameter: while t_{scale} decreases by less than half (from 1.0 to 0.6) compared to DEF, perturbations in TUN persist nearly 2.5 times longer. The broader spatial extent of the TUN response becomes especially evident when the number of significant activations is reported onto the brain maps, suggesting that in TUN the stimulus propagates far from the stimulation site, recruiting distant regions of the network (Fig. 6(E)). In contrast, the DEF response remains tightly localized around the stimulation site (Fig. 6(F)).

To further explore the spread and heterogeneity of the evoked activity, we compute the post-stimulus broadband power (see Section 2.5.3) in three equal-sized node subsets: the directly stimulated nodes; a set of spatially nearby but non-stimulated nodes within the same hemisphere; and the most distant nodes connected to the stimulation site, as determined by structural connectivity (i.e., tract lengths). In all three subsets, the TUN configuration exhibits higher power overall, as well as greater variability in its temporal dynamics compared to the DEF configuration (Fig. 6(G) vs (H)).

Finally, we quantify the overall complexity of the evoked spatiotemporal patterns using the perturbational complexity index (PCI; see Section 2.5.5). TUN reaches PCI = 0.54, a substantially higher value with respect to PCI = 0.39 observed for DEF, confirming its ability to sustain richer, more spatially distributed and temporally diverse patterns of activity in response to brief perturbations. Notwithstanding an absolute comparison with PCI values from the literature is not reliable, due to strong dependencies on the experimental protocols for the EEG

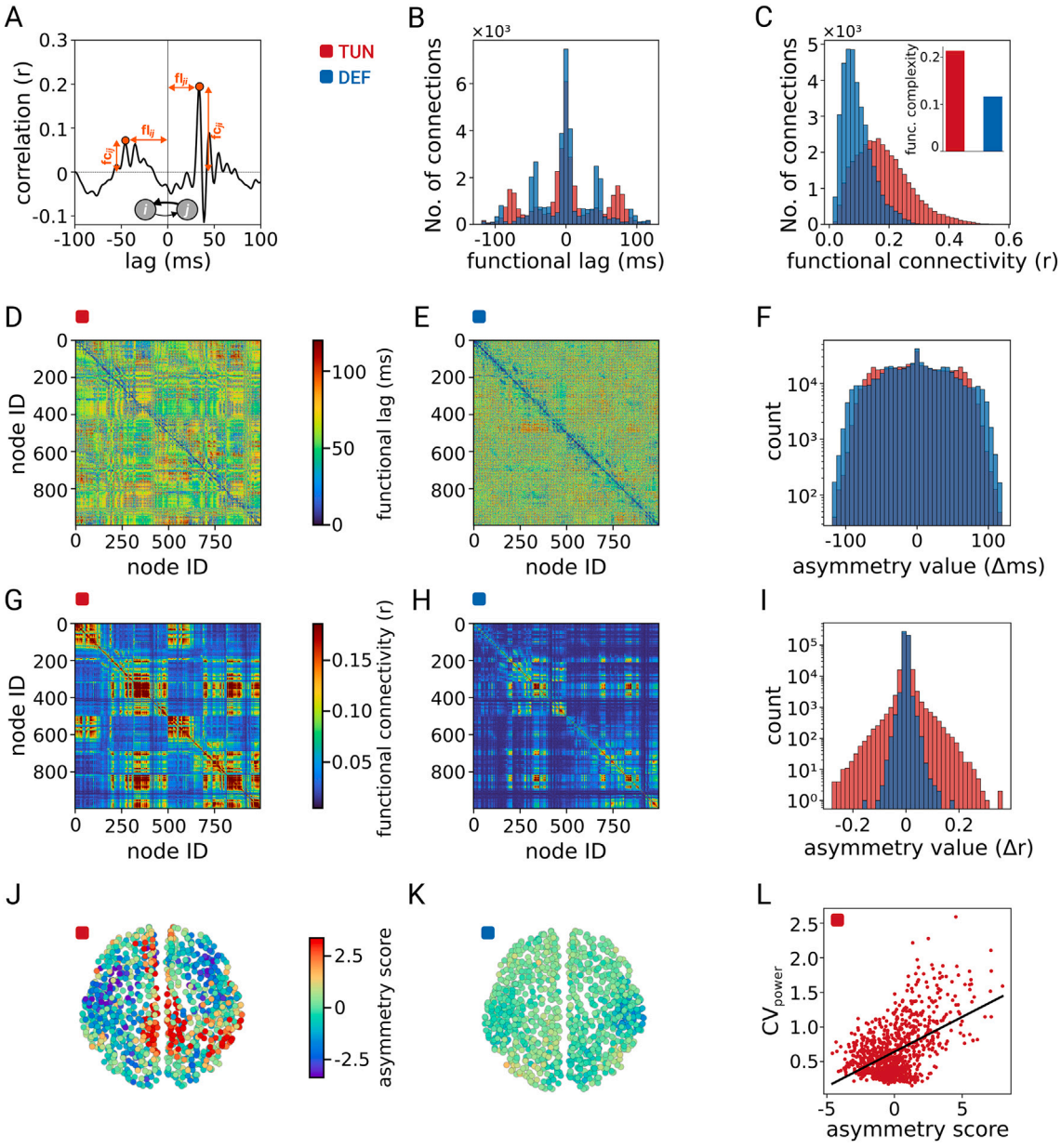

Fig. 5. Functional connectivity, functional lags, and asymmetry in TUN and DEF configurations. A) Illustration of the cross-correlation function applied to investigate pairwise interactions between nodes. The correlation between the time series of nodes i and j is computed at various time lags. Negative lags indicate a directional relation from i to j, while positive lags indicate the other way round. The functional connectivity ($\mathbb{FC}$) is defined as the height of the maximum correlation peak, with the corresponding lag being the functional lag ($\mathbb{FL}$). **B)** Distributions of functional lag values across all (ordered) node pairs for the two configurations. **C)** Distributions of functional connectivity values across all (ordered) node pairs. TUN exhibits a broader $\mathbb{FC}$ distribution compared to DEF, indicating stronger and richer interactions. The inset shows the value of functional complexity. **D-E)** $\mathbb{FL}$ matrices (absolute values for the entries) for TUN and DEF configurations. **F)** Distributions of asymmetry values in $\mathbb{FL}$ matrices, derived from $\mathbb{FL}_{asym}$. **G-H)** $\mathbb{FC}$ matrices for TUN and DEF configurations. **I)** Distributions of asymmetry values in $\mathbb{FC}$ matrices, derived from $\mathbb{FC}_{asym}$. **J-K)** Nodal asymmetry scores $\mathbb{A}$ derived from $\mathbb{FC}$ for TUN and DEF configurations. **L)** Linear regression ($r = 0.51$, $p = 10^{-66}$) between nodal asymmetry scores $\mathbb{A}$ and CV_{power} in TUN. Each point represents a brain node.

recording and on the inverse model employed, the relative difference between the two PCI values found here is consistent with experimentally observed ones in healthy control individuals and subjects with reduced levels of consciousness (either responsive or not) (see, e.g.,[13]).

4. Discussion

This study is grounded on two fundamental questions: *i)* How can a brain network model be tuned to simultaneously reproduce key characteristics of both spontaneous and externally evoked neural activity? *ii)* How can we systematically evaluate the model consistency with expectations from biology and ultimately with empirical data? This work contributes to answering these questions by defining physiologically relevant metrics that are useful in guiding the exploration and the initial tuning of model parameters, thus setting up a convenient starting point for the calibration process. The approach is iterative, where discrepancies between features exhibited by the model and biological datasets provide valuable feedback that helps refine the model parameters and improve its accuracy in reproducing the neural dynamics. These metrics could be applied equally to synthetic and experimentally obtained data to yield directly comparable results, thereby strengthening

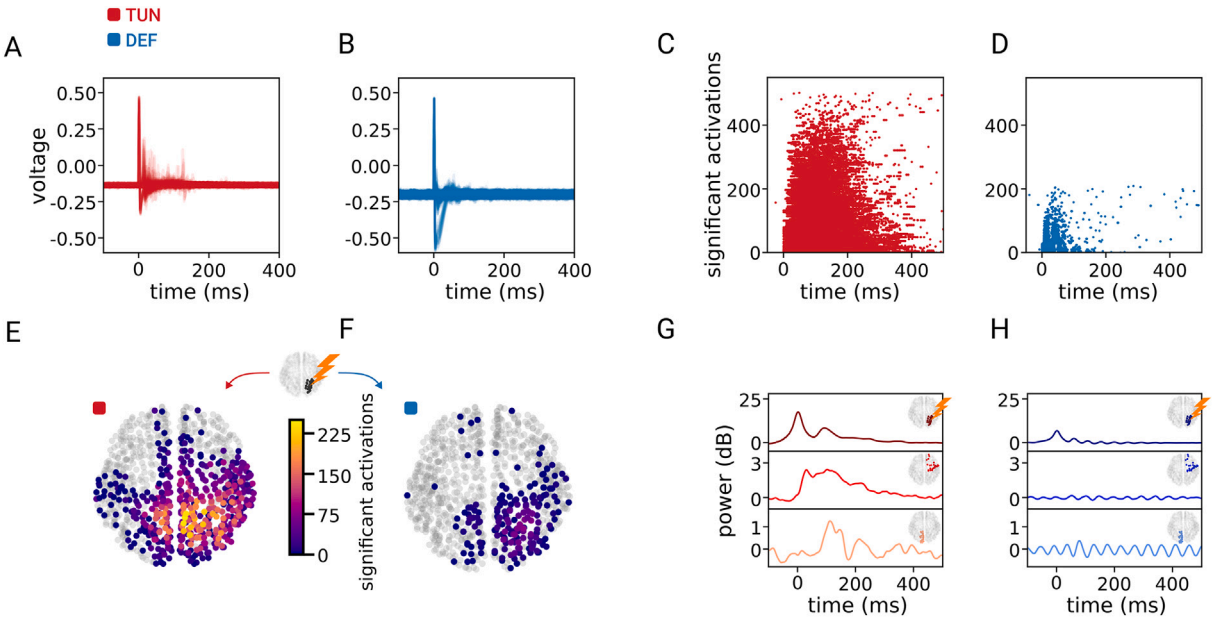

Fig. 6. Stimulus-evoked activity in TUN and DEF configurations. A-B) 200 independent 2ms perturbations (i.e., 200 trials) were applied to the right superior parietal nodes (rSP) of the brain model, for both TUN and DEF configurations, to assess the spatio-temporal complexity of the evoked activity. Voltage traces averaged across trials in TUN (A, red) and DEF (B, blue) are here reported for each of the 998 nodes. **C-D)** Binary spatio-temporal matrices of significant activations across nodes (y-axis) and time (x-axis), showing more sustained and spatially distributed activity in TUN (C) relative to DEF (D), where activations are sparse and temporally constrained. **E-F)** Brain maps showing the spatial distribution of significant activations (sum over 10–500ms post-stimulus) across nodes. The smaller brain on top of the colorbar illustrates the stimulated nodes located on the rSP cortex. In TUN (E), the stimulus spreads across distant cortical areas, while in DEF (F), the activity remains localized around the stimulation site. **G-H)** Post-stimulus broadband power (dB) averaged across three equal-sized node subsets (27 nodes): directly stimulated nodes (top), nearby connected but non-stimulated nodes (middle), and distant connected nodes (bottom). Insets indicate node locations. TUN (G) displays higher power and greater temporal variability than DEF (H), where responses are weaker and more stereotyped.

the robustness of the model and exploring the boundaries of its applicability. Additionally, to enhance the reproducibility and facilitate cross-study comparisons, these metrics should be accessible to the broader neuroscience community and generalizable to accommodate diverse experimental contexts.

To achieve this, we leverage TVB, a versatile software framework that enables the simulation of large-scale brain network models. In this study, we use TVB to simulate whole-brain dynamics in both spontaneous and evoked conditions, exploring how different parameter configurations of the same model shape the emergent neural activity. However, extracting meaningful insights from these simulations and quantitatively comparing them to empirical findings requires dedicated tools for their processing and analysis, and then back to the model for its calibration. Here, we use Cobrawap to process the TVB simulation output for tuning model parameters, aiming at matching expectations from empirical neurophysiological patterns. This approach enables meaningful comparisons between the default TVB configuration of the model and its tuned counterpart. Cobrawap capabilities for monitoring, analyzing, and visualizing dynamic variables are instrumental in ensuring that the eventually selected network model configuration captures both spontaneous and evoked brain activity. Finally, this approach proves to be essential not only for guiding the tuning process, but also for revealing significant differences in the inner dynamics of the two model configurations, thus allowing for a deeper understanding of the model itself. Notably, both TVB and Cobrawap are delivered to the EBRAINS community as *tools* of the EBRAINS Software Distribution (ESD) [29]. Therefore, representing a showcase of their integration, this work is also a proof of concept toward the construction of integrated workflows in EBRAINS.

In the following, we summarize the main outcomes obtained in this work, and we arrive at conclusions complementing their interpretation with findings and results from the literature. First, tuning is performed such that an alpha-band peak can be observed, consistent with empirical evidence highlighting the prominence of alpha rhythms during resting-state brain activity [63]. This effect results from tuning the global timescale of the model dynamics, while at variance alpha oscillations are absent in the default model.

Second, the tuning also significantly influences both the spectral and spatial organization of brain activity. The analysis of the temporal fluctuation of transition events from the baseline to a higher activity regime and power spectral content reveals a clear spatial organization in the tuned configuration, characterized by marked heterogeneity – a feature consistent with more realistic brain dynamics [106]. In contrast, the default configuration exhibits more homogeneous and stereotyped dynamics, with reduced spatio-temporal variability in both events and power. Notably, these differences stem from the tuning of the model equation parameters, the global coupling strength, and the conduction velocity (as both configurations are based on the same underlying connectome, i.e., structural connectivity: relative weights of synaptic connections are not changed).

Mapping the auto-correlation peak latencies onto the brain regions further highlights the non-trivial spatial organization of the tuned model, where faster periodicities are observed in frontal regions, whereas slower oscillations are present in posterior regions. This spatio-temporal gradient is consistent with experimental observations [10,37,85]. Interestingly, centro-parietal regions exhibit auto-correlation peak latencies shorter than the median periodicity of other cortical regions, thus forming a distinct cluster of cortical nodes. These populations also display lower average event rates, indicating fewer periods of neural mass synchronization. This pattern corresponds to more differentiated and fluctuating dynamics, as reflected by the increased variability in their power time-course.

Furthermore, our study examines the communication between nodes using cross-correlation functions. We extract two relevant metrics to analyze nodal interactions: functional connectivity ($\mathbb{FC}$) and functional lag ($\mathbb{FL}$). Our analysis reveals that the tuned configuration of the model exhibits a wider distribution of functional connectivity ($\mathbb{FC}$) values compared to the default one, suggesting a greater diversity of interactions in the former. This reflects a characteristic of complex brain dynamics, that maintains a balance between integration and segregation across the network [105,107].

The emergence of a greater $\mathbb{FC}$ asymmetry in the tuned configuration is another key finding. We find more directional interactions in the tuned model with respect to the default behavior, underscoring the effect of parameter tuning in promoting asymmetric network dynamics. In turn, this could indicate the presence of emergent network motifs that are crucial for sustaining complex neuronal patterns [17,77]. Notably, centro-parietal regions with higher asymmetry scores also exhibit greater power fluctuations, as reflected by a significant correlation between asymmetry scores and the CV_{power}. This finding suggests that nodes with stronger leading roles in the network exhibit more variable neural activity, potentially enhancing their ability to coordinate information propagation, thus acting as *hubs*. Such variability may drive neuronal cascades – transient bursts of activity that could shape communication across large-scale brain networks [35,83]. Notably, this asymmetry is particularly pronounced in the posterior cingulate cortex, consistent with previous experimental evidence [17].

Also, we observe the emergence of infra-slow rhythms (~0.01Hz) in the tuned configuration, well-documented in experiments [48,81]. A particularly interesting question arising from these findings is whether the observed spatial heterogeneity in terms of temporal variability influences these infra-slow fluctuations. Specifically, it remains unclear whether centro-parietal regions, already identified as potential hubs because of their high temporal variability and stronger leading role, act as "orchestrators" of these network infra-slow rhythms, or whether they act as "gates" that facilitate the propagation of fronto-posterior (or posterofrontal) waves across the network. This question, which we intend to explore in future research, offers a promising direction for investigating how specific regions interact with infra-slow dynamics and contribute to the reconfiguration of brain states within large-scale networks [83].

Crucially, the results on spontaneous activity are also accompanied by evidence that properly tuning the model parameters can generate complex, stimulus-evoked dynamics. In line with empirical studies of brain activity [12,89], we find that the model is able to sustain complex spatio-temporal patterns of activation in response to external perturbations, quantified with the PCI. Notably, in this work we reduce the stimulus duration from 5ms to 2ms – compared to the protocol used in [41] – to better match experimental conditions, including both intra- and extra-cranial stimulations [20]. Despite the shorter stimulus, the model still exhibits a realistic complex response, further corroborating its ability to capture essential features of neural dynamics beyond spontaneous fluctuations.

A theoretical framework able to integrate our results on spontaneous and evoked dynamics is provided by criticality – a dynamical regime emerging near phase transitions, where systems exhibit a unique balance between ordered and disordered activity [3,15,80]. In this regime, scale-free properties naturally arise, collectively maximizing information capacity [91]: $1/f$ spectral scaling [54], long-range temporal correlations [21,69], infra-slow fluctuations [81,82], and heightened sensitivity to external perturbations [80]. In the tuned configuration, such signatures emerge naturally in both spontaneous and evoked activity. In particular, the heightened sensitivity of TUN to brief external stimuli – manifested as prolonged and complex responses, with longer relaxation timescales – resembles the amplified perturbation effects typical of the *critical slowing down* phenomenon [76]. In addition, the richness of spatio-temporal patterns measured with PCI suggests a more efficient signal propagation through the network. Together with empirical links between PCI and criticality [74], these results seem to indicate that parameter tuning shifts the model toward a critical-like regime, closer to the dynamical richness of biological systems.

4.1. Limitations and perspective

Our study showcases how to tune models to capture macroscopic features of brain dynamics, however it is important to acknowledge some limitations. First, we focus on reproducing large-scale characteristics of neural activity as resulting from the corpus of experimental evidence. As a proof of concept of the comparability with experimental data, we propose a close comparison between simulated and empirical features in Suppl. Fig. A.8, which also demonstrates the generalizability of our approach to other connectomes (specifically, a 74-node connectome). Further steps toward an accurate calibration between TVB outputs and extra-cortical recordings (like hd-EEG) would require refined forward models [46]. Nevertheless, our approach lays the foundation for such quantitative calibration by adopting metrics that have proved effective in assessing experimental features in the Cobrawap framework [11,14,22,49].

Secondly, the Larter-Breakspear model has been designed for reproducing the dynamics of cortical columns and does not include detailed contributions from subcortical inputs, which conversely are known to play a fundamental role in orchestrating brain rhythms and propagating neural activity. Some recent works [e.g.,71] tackle this task with TVB-based simulations, offering indications for incorporating some advances in the Larter-Breakspear framework. Nevertheless, even if the TVB simulation engine leverages simplified representations of cortical dynamics as neural mass models that describe synchronization processes at a population level, this abstraction still enables the study of several physiological and pathological conditions. Indeed, neural mechanisms relevant to brain diseases can be modeled even just by acting on easily interpretable global parameters, such as the conduction speed or the global coupling [1,25,33,64,93], once more evidencing the importance of an accurate tuning.

Additionally, TVB simulations can serve as the basis for surgical and clinical treatments, such as epilepsy: see the experience of EPINOV, the world's first clinical trial on predictive brain modeling in epilepsy surgery [61]. Again, careful parameter tuning – including personalization, toward a digital twin approach [73,100] – is crucial for achieving reliable and effective results.

The Larter-Breakspear model employed here has been extensively used for simulating fMRI BOLD signals [2,31,57,59,84]. Neural mass activity can be converted into BOLD signals using the nonlinear Balloon-Windkessel hemodynamic model, which translates neuronal dynamics into blood-oxygen-level-dependent responses [40]. This model is readily available as a built-in monitor in the TVB platform [88], and its integration into our modeling framework is straightforward, as demonstrated by Gaglioti et al. [41]. Therefore, extending our current framework to simulate fMRI data is an easily implementable step in future work, enabling direct validation against empirical resting-state fMRI recordings and opening new avenues for clinical applications and brain-computer interface development [92].

Finally, our analysis primarily focuses on a stationary characterization of the model dynamics, identifying fixed patterns of spontaneous activity. However, the brain does not operate in a steady state – it exhibits transient dynamics, shifting between different functional configurations over time. Future studies will aim to extend this work by exploring the temporal evolution of network states, classifying these transient states, and ultimately comparing them with empirical data. This will further improve model calibration and help refine our understanding of how large-scale neural networks reconfigure over time.

4.2. Conclusion

In summary, this study demonstrates the importance of parameter tuning in capturing the full complexity of spontaneous and evoked brain dynamics. The use of Cobrawap is instrumental in refining the model

and ensuring its consistency with empirical expectations, allowing us to reproduce key brain activity features such as alpha-band oscillations, infra-slow rhythms, spatio-temporal heterogeneity in network activity and complex evoked responses. The independently developed metrics, applicable to any simulation engine, enable a more systematic approach that creates opportunities for iterative automatic data-driven refinement of model parameters through tools like the Learning-to-Learn (L2L) framework [101]. Our findings establish a proof of concept for a structured methodology that bridges computational simulations and experimental data in humans. This paves the way for quantitative calibration and validation of accurate, interpretable, reliable and personalized models of whole-brain dynamics, in both healthy and diseased conditions.

Appendix A. Supplementary material

Supplementary data for this article can be found online at doi:10.1016/j.neucom.2026.132735.

CRediT authorship contribution statement

Gianluca Gaglioti: Writing – review & editing, Writing – original draft, Visualization, Software, Methodology, Investigation, Formal analysis, Conceptualization. **Alessandra Cardinale:** Writing – review & editing, Writing – original draft, Visualization, Software, Methodology, Formal analysis. **Cosimo Lupo:** Writing – review & editing, Writing – original draft, Supervision, Software, Methodology, Investigation, Formal analysis, Conceptualization. **Thierry Nieus:** Writing – review & editing, Writing – original draft, Supervision, Methodology, Investigation, Formal analysis, Conceptualization. **Federico Marmoreo:** Writing – review & editing, Software, Methodology. **Elena Focacci:** Data curation, Methodology, Writing – review & editing. **Robin Gutzen:** Writing – review & editing, Software, Methodology. **Michael Denker:** Writing – review & editing, Software, Methodology. **Andrea Pigorini:** Writing – review & editing, Project administration, Funding acquisition, Conceptualization. **Marcello Massimini:** Writing – review & editing, Supervision, Project administration, Funding acquisition, Conceptualization. **Simone Sarasso:** Writing – review & editing, Supervision, Funding acquisition, Conceptualization. **Pier Stanislao Paolucci:** Writing – review & editing, Writing – original draft, Supervision, Project administration, Methodology, Investigation, Funding acquisition, Formal analysis, Conceptualization. **Giulia De Bonis:** Writing – review & editing, Writing – original draft, Supervision, Software, Methodology, Investigation, Formal analysis, Conceptualization.

Data and code availability

Whole-brain simulations rely on software release 2.7.2 of TheVirtualBrain (TVB) (https://www.thevirtualbrain.org/tvb/zwei/brainsimulator-software), with parameters as in Suppl. Table A.2. Simulation outputs are then analyzed with dedicated tools; their integration into the next official Cobrawap software release 0.3.0 is currently underway (the latest stable release is always accessible at https://doi.org/10.5281/zenodo.10198748), though new software features developed for this paper are already available as a development branch at https://github.com/APE-group/cobrawap/tree/devs/TVB. The data from simulations and the code for reproducing the figures presented in this paper are available upon request.

Fundings

This work has been co-funded by: the European Next Generation EU through Italian MUR grants CUP B51E22000150006 (EBRAINS-Italy IR00011 PNRR Project) (CL, FM, PSP, GDB, AP, MM); the European Union's Horizon Europe Programme under the Specific Grant Agreement No. 101147319 (EBRAINS 2.0 Project) (MD, AP); the European Research Council (ERC-2022-SYG-101071900-NEMESIS) (MM); the Tiny Blue Dot Foundation (MM); the Ministero dell'Università e della Ricerca PRIN 2022 20228ARNXS "DARKSCANNER" (SS); the Italian Ministry of Foreign Affairs and International Cooperation, MultiScale Brain Function (MSBFIINE) India-Italy Network of Excellence (DST-MAE) IN22NOE02 (TN); Progetto Di Ricerca Di Rilevante Interesse Nazionale (PRIN) P2022FMK77 (AP). AC is a PhD student enrolled in the National PhD in Artificial Intelligence, XXXVIII cycle BIS, course on Health and life sciences, organized by Università Campus Bio-Medico di Roma.

Declaration of competing interest

The authors declare the following financial interests/personal relationships that may be considered as potential competing interests: Marcello Massimini is a co-founder and shareholder of Intrinsic Powers, a spin-off of the University of Milan. Simone Sarasso is advisor of Intrinsic Powers. These affiliations in no way affect the content of this article. The other authors declare that they have no known competing financial interests or personal relationships that could have appeared to influence the work reported in this paper.

References

[1] H. Aerts, M. Schirner, T. Dhollander, B. Jeurissen, E. Achten, D. Van Roost, P. Ritter, D. Marinazzo, Modeling brain dynamics after tumor resection using the virtual brain, NeuroImage 213 (2020) 116738, https://doi.org/10.1016/j.neuroimage.2020.116738
[2] J. Alstott, M. Breakspear, P. Hagmann, L. Cammoun, O. Sporns, Modeling the impact of lesions in the human brain, PLOS Comput. Biol. 5 (2009) e1000408, https://doi.org/10.1371/journal.pcbi.1000408
[3] J.M. Beggs, D. Plenz, Neuronal avalanches in neocortical circuits, J. Neurosci. 23 (2003) 11167–11177, https://doi.org/10.1523/jneurosci.23-35-11167.2003
[4] H. Berger, Über das elektrenkephalogramm des menschen, Arch. Psychiatr. Nervenkr. 87 (1929) 527–570, https://doi.org/10.1007/BF01797193
[5] M. Breakspear, Dynamic models of large-scale brain activity, Nat. Neurosci. 20 (2017) 340–352, https://doi.org/10.1038/nn.4497
[6] M. Breakspear, C.J. Stam, Dynamics of a neural system with a multiscale architecture, Philos. Trans. R. Soc. B Biol. Sci. 360 (2005) 1051–1074, https://doi.org/10.1098/rstb.2005.1643
[7] M. Breakspear, J.R. Terry, Nonlinear interdependence in neural systems: motivation, theory, and relevance, Int. J. Neurosci. 112 (2002) 1263–1284, https://doi.org/10.1080/00207450290026193
[8] M. Breakspear, J.R. Terry, K.J. Friston, Modulation of excitatory synaptic coupling facilitates synchronization and complex dynamics in a biophysical model of neuronal dynamics, Netw.: Comput. Neural Syst. 14 (2003) 703–732, https://doi.org/10.1088/0954-898X_14_4_305
[9] C. Cakan, N. Jajcay, K. Obermayer, Neurolib: a simulation framework for Whole-Brain neural mass modeling, Cogn. Comput. 15 (2023) 1132–1152, https://doi.org/10.1007/s12559-021-09931-9
[10] A. Capilla, L. Arana, M. García-Huéscar, M. Melcón, J. Gross, P. Campo, The natural frequencies of the resting human brain: an MEG-based atlas, NeuroImage 258 (2022) 119373, https://doi.org/10.1016/j.neuroimage.2022.119373
[11] C. Capone, C. De Luca, G. De Bonis, R. Gutzen, I. Bernava, E. Pastorelli, F. Simula, C. Lupo, L. Tonielli, F. Resta, A.L. Allegra Mascaro, F. Pavone, M. Denker, P.S. Paolucci, Simulations approaching data: cortical slow waves in inferred models of the whole hemisphere of mouse, Commun. Biol. 6 (2023) 266, https://doi.org/10.1038/s42003-023-04580-0
[12] A.G. Casali, O. Gosseries, M. Rosanova, M. Boly, S. Sarasso, K.R. Casali, S. Casarotto, M.-A. Bruno, S. Laureys, G. Tononi, M. Massimini, A theoretically based index of consciousness independent of sensory processing and behavior, Sci. Transl. Med. 5 (2013) 198ra105, https://doi.org/10.1126/scitranslmed.3006294
[13] S. Casarotto, A. Comanducci, M. Rosanova, S. Sarasso, M. Fecchio, M. Napolitani, A. Pigorini, A.G. Casali, P.D. Trimarchi, M. Boly, O. Gosseries, O. Bodart, F. Curto, C. Landi, M. Mariotti, G. Devalle, S. Laureys, G. Tononi, M. Massimini, Stratification of unresponsive patients by an independently validated index of brain complexity, Ann. Neurol. 80 (2016) 718–729, https://doi.org/10.1002/ana.24779
[14] M. Celotto, C. De Luca, P. Muratore, F. Resta, A.L. Allegra Mascaro, F.S. Pavone, G. De Bonis, P.S. Paolucci, Analysis and model of cortical slow waves acquired with optical techniques, Methods Protoc. 3 (2020) 14, https://doi.org/10.3390/mps3010014
[15] D.R. Chialvo, Emergent complex neural dynamics, Nat. Phys. 6 (2010) 744–750, https://doi.org/10.1038/nphys1803
[16] L. Cocchi, L.L. Gollo, A. Zalesky, M. Breakspear, Criticality in the brain: a synthesis of neurobiology, models and cognition, Prog. Neurobiol. 158 (2017) 132–152, https://doi.org/10.1016/j.pneurobio.2017.07.002
[17] A. Coito, C.M. Michel, S. Vulliemoz, G. Plomp, Directed functional connections underlying spontaneous brain activity, Hum. Brain Mapp. 40 (2019) 879–888, https://doi.org/10.1002/hbm.24418
[18] S. Cole, T. Donoghue, R. Gao, B. Voytek, Neurodsp: a package for neural digital signal processing, J. Open Source Softw. 4 (2019) 1272, https://doi.org/10.21105/joss.01272

[19] M.A. Colombo, M. Napolitani, M. Boly, O. Gosseries, S. Casarotto, M. Rosanova, J.-F. Brichant, P. Boveroux, S. Rex, S. Laureys, M. Massimini, A. Chieregato, S. Sarasso, The spectral exponent of the resting EEG indexes the presence of consciousness during unresponsiveness induced by propofol, xenon, and ketamine, NeuroImage 189 (2019) 631–644, https://doi.org/10.1016/j.neuroimage.2019.01.024

[20] R. Comolatti, G. Hassan, E. Mikulan, S. Russo, M.A. Colombo, E. Litterio, G. Furregoni, S. D'Ambrosio, M. Fecchio, S. Parmigiani, I. Sartori, S. Casarotto, A. Pigorini, M. Massimini, Transcranial magnetic VS intracranial electric stimulation: a direct comparison of their effects via scalp EEG recordings, Brain Stimul. 18 (2025) 1444–1454, https://doi.org/10.1016/j.brs.2025.07.016

[21] L. Dalla Porta, M. Copelli, Modeling neuronal avalanches and long-range temporal correlations at the emergence of collective oscillations: continuously varying exponents mimic m/EEG results, PLoS Comput. Biol. 15 (2019) e1006924, https://doi.org/10.1371/journal.pcbi.1006924

[22] G. De Bonis, M. Dasilva, A. Pazienti, M.V. Sanchez-Vives, M. Mattia, P.P. Stanislao, Analysis pipeline for extracting features of cortical slow oscillations, Front. Syst. Neurosci. 13 (2019) 70, https://doi.org/10.3389/fnsys.2019.00070

[23] G. Deco, V.K. Jirsa, Ongoing cortical activity at rest: criticality, multistability, and ghost attractors, J. Neurosci. 32 (2012) 3366–3375, https://doi.org/10.1523/jneurosci.2523-11.2012

[24] G. Deco, V.K. Jirsa, A.R. McIntosh, Emerging concepts for the dynamical organization of resting-state activity in the brain, Nat. Rev. Neurosci. 12 (2011) 43–56, https://doi.org/10.1038/nrn2961

[25] G. Deco, V.K. Jirsa, A.R. McIntosh, Resting brains never rest: computational insights into potential cognitive architectures, Trends Neurosci. 36 (2013) 268–274, https://doi.org/10.1016/j.tins.2013.03.001

[26] G. Deco, M.L. Kringelbach, V.K. Jirsa, P. Ritter, The dynamics of resting fluctuations in the brain: metastability and its dynamical cortical core, Sci. Rep. 7 (2017) 3095, https://doi.org/10.1038/s41598-017-03073-5

[27] G. Deco, A.R. McIntosh, K. Shen, R.M. Hutchison, R.S. Menon, S. Everling, P. Hagmann, V.K. Jirsa, Identification of optimal structural connectivity using functional connectivity and neural modeling, J. Neurosci. 34 (2014) 7910–7916, https://doi.org/10.1523/JNEUROSCI.4423-13.2014

[28] M. Denker, A. Yegenoglu, S. Grün, Collaborative HPC-enabled workflows on the HBP collaboratory using the elephant framework, in: Neuroinformatics 2018, 2018, pp. P19, https://doi.org/10.12751/incf.ni2018.0019

[29] EBRAINS ESD, 2025, https://gitlab.ebrains.eu/ri/tech-hub/platform/esd

[30] EBRAINS: Europe Research Infrastructure for Brain Research, 2023, https://ebrains.eu

[31] H. Endo, N. Hiroe, O. Yamashita, Evaluation of resting Spatio-Temporal dynamics of a neural mass model using resting fMRI connectivity and EEG microstates, Front. Comput. Neurosci. 13 (2019) 91, https://doi.org/10.3389/fncom.2019.00091

[32] O. Esteban, C.J. Markiewicz, R.W. Blair, C.A. Moodie, A.I. Isik, A. Erramuzpe, J.D. Kent, M. Goncalves, E. DuPre, M. Snyder, H. Oya, S.S. Ghosh, J. Wright, J. Durnez, R.A. Poldrack, K.J. Gorgolewski, fMRIPrep: a robust preprocessing pipeline for functional MRI, Nat. Methods 16 (2019) 111–116, https://doi.org/10.1038/s41592-018-0235-4

[33] M.I. Falcon, J.D. Riley, V. Jirsa, A.R. McIntosh, E. Elinor Chen, A. Solodkin, Functional mechanisms of recovery after chronic stroke: modeling with the virtual brain, eNeuro 3 (2016) e0158–15.2016, https://doi.org/10.1523/eneuro.0158-15.2016

[34] B. Fischl, FreeSurfer, NeuroImage 62 (2012) 774–781, https://doi.org/10.1016/j.neuroimage.2012.01.021

[35] J. Fousek, G. Rabuffo, K. Gudibanda, H. Sheheitli, S. Petkoski, V. Jirsa, Symmetry breaking organizes the brain's resting state manifold, Sci. Rep. 14 (2024) 31970, https://doi.org/10.1038/s41598-024-83542-w

[36] M.D. Fox, M.E. Raichle, Spontaneous fluctuations in brain activity observed with functional magnetic resonance imaging, Nat. Rev. Neurosci. 8 (2007) 700–711, https://doi.org/10.1038/nrn2201

[37] B. Frauscher, N. von Ellenrieder, R. Zelmann, I. Doležalová, L. Minotti, A. Olivier, J. Hall, D. Hoffmann, D. K. Nguyen, P. Kahane, F. Dubeau, J. Gotman, Atlas of the normal intracranial electroencephalogram: neurophysiological awake activity in different cortical areas, Brain 141 (2018) 1130–1144, https://doi.org/10.1093/brain/awy035

[38] F. Freyer, K. Aquino, P.A. Robinson, P. Ritter, M. Breakspear, Bistability and Non-Gaussian fluctuations in spontaneous cortical activity, J. Neurosci. 29 (2009) 8512–8524, https://doi.org/10.1523/JNEUROSCI.0754-09.2009

[39] F. Freyer, J.A. Roberts, R. Becker, P.A. Robinson, P. Ritter, M. Breakspear, Biophysical mechanisms of multistability in Resting-State cortical rhythms, J. Neurosci. 31 (2011) 6353–6361, https://doi.org/10.1523/JNEUROSCI.6693-10.2011

[40] K.J. Friston, A. Mechelli, R. Turner, C.J. Price, Nonlinear responses in FMRI: the balloon model, volterra kernels, and other hemodynamics, NeuroImage 12 (2000) 466–477, https://doi.org/10.1006/nimg.2000.0630

[41] G. Gaglioti, T.R. Nieus, M. Massimini, S. Sarasso, Investigating the impact of local manipulations on spontaneous and evoked brain complexity indices: a Large-Scale computational model, Appl. Sci. 14 (2024) 890, https://doi.org/10.3390/app14020890

[42] Y. Gao, A.H. Koyun, V. Roessner, A.-K. Stock, M. Mückschel, L. Colzato, B. Hommel, C. Beste, Transcranial direct current stimulation and methylphenidate interact to increase cognitive persistence as a core component of metacontrol: evidence from aperiodic activity analyses, Brain Stimul. 18 (2025) 720–729, https://doi.org/10.1016/j.brs.2025.03.024

[43] W. Gerstner, W.M. Kistler, R. Naud, L. Paninski, Neuronal Dynamics: from Single Neurons to Networks and Models of Cognition, Cambridge University Press, 2014, https://doi.org/10.1017/CBO9781107447615

[44] L.L. Gollo, M. Breakspear, The frustrated brain: from dynamics on motifs to communities and networks, Philos. Trans. R. Soc. B Biol. Sci. 369 (2014) 20130532, https://doi.org/10.1098/rstb.2013.0532

[45] L.L. Gollo, A. Zalesky, R.M. Hutchison, M. van den Heuvel, M. Breakspear, Dwelling quietly in the rich club: brain network determinants of slow cortical fluctuations, Philos. Trans. R. Soc. B Biol. Sci. 370 (2015) 20140165, https://doi.org/10.1098/rstb.2014.0165

[46] A. Gramfort, M. Luessi, E. Larson, D.A. Engemann, D. Strohmeier, C. Brodbeck, R. Goj, M. Jas, T. Brooks, L. Parkkonen, M. Hämäläinen, MEG and EEG data analysis with MNE-python, Front. Neurosci. 7 (2013) 267, https://doi.org/10.3389/fnins.2013.00267

[47] J.D. Griffiths, S.P. Bastiaens, N. Kaboodvand, Whole-Brain modelling: past, present, and future, Adv. Exp. Med. Biol. 1359 (2022) 313–355, https://doi.org/10.1007/978-3-030-89439-9_13

[48] D. Gutierrez-Barragan, M.A. Basson, S. Panzeri, A. Gozzi, Infraslow state fluctuations govern spontaneous fMRI network dynamics, Curr. Biol. 29 (2019) 2295–2306.e5, https://doi.org/10.1016/j.cub.2019.06.017

[49] R. Gutzen, G. De Bonis, C. De Luca, E. Pastorelli, C. Capone, A.L. Allegra Mascaro, F. Resta, A. Manasanch, F.S. Pavone, M.V. Sanchez-Vives, M. Mattia, S. Grün, P.S. Paolucci, M. Denker, A modular and adaptable analysis pipeline to compare slow cerebral rhythms across heterogeneous datasets, Cell Rep. Methods 4 (2024) 100681, https://doi.org/10.1016/j.crmeth.2023.100681

[50] R. Gutzen, C. Lupo, F. Marmoreo, G. De Bonis, C. De Luca, E. Pastorelli, C. Capone, A.L. Allegra Mascaro, F. Resta, A. Manasanch, F.S. Pavone, M.V. Sanchez-Vives, M. Mattia, S. Grün, P.S. Paolucci, M. Denker, Cobrawap documentation (2025) https://cobrawap.readthedocs.io

[51] R. Gutzen, C. Lupo, F. Marmoreo, G. De Bonis, C. De Luca, E. Pastorelli, C. Capone, A.L. Allegra Mascaro, F. Resta, A. Manasanch, F.S. Pavone, M.V. Sanchez-Vives, M. Mattia, S. Grün, P.S. Paolucci, M. Denker, Cobrawap official releases on zenodo (2025), https://doi.org/10.5281/zenodo.10198748

[52] R. Gutzen, M. von Papen, G. Trensch, P. Quaglio, S. Grün, M. Denker, Reproducible neural network simulations: statistical methods for model validation on the level of network activity data, Front. Neuroinform. 12 (2018) 90, https://doi.org/10.3389/fninf.2018.00090

[53] P. Hagmann, L. Cammoun, X. Gigandet, R. Meuli, C.J. Honey, V.J. Wedeen, O. Sporns, Mapping the structural core of human cerebral cortex, PLoS Biol. 6 (2008) e159, https://doi.org/10.1371/journal.pbio.0060159

[54] B.J. He, J.M. Zempel, A.Z. Snyder, M.E. Raichle, The temporal structures and functional significance of scale-free brain activity, Neuron 66 (2010) 353–369, https://doi.org/10.1016/j.neuron.2010.04.020

[55] S. Heitmann, M.J. Aburn, M. Breakspear, The brain dynamics toolbox for matlab, Neurocomputing 315 (2018) 82–88, https://doi.org/10.1016/j.neucom.2018.06.026

[56] M.P. van den Heuvel, O. Sporns, Network hubs in the human brain, Trends Cogn. Sci. 17 (2013) 683–696, https://doi.org/10.1016/j.tics.2013.09.012

[57] C.J. Honey, R. Kötter, M. Breakspear, O. Sporns, Network structure of cerebral cortex shapes functional connectivity on multiple time scales, Proc. Natl. Acad. Sci. U.S.A. 104 (2007) 10240–10245, https://doi.org/10.1073/pnas.0701519104

[58] C.J. Honey, O. Sporns, Dynamical consequences of lesions in cortical networks, Hum. Brain Mapp. 29 (2008) 802–809, https://doi.org/10.1002/hbm.20579

[59] C.J. Honey, O. Sporns, L. Cammoun, X. Gigandet, J.P. Thiran, R. Meuli, P. Hagmann, Predicting human resting-state functional connectivity from structural connectivity, Proc. Natl. Acad. Sci. 106 (2009) 2035–2040, https://doi.org/10.1073/pnas.0811168106

[60] O. Jensen, A. Mazaheri, Shaping functional architecture by oscillatory alpha activity: gating by inhibition, Front. Hum. Neurosci. 4 (2010) 186, https://doi.org/10.3389/fnhum.2010.00186

[61] V. Jirsa, H. Wang, P. Triebkorn, M. Hashemi, J. Jha, J. Gonzalez-Martinez, M. Guye, J. Makhalova, F. Bartolomei, Personalised virtual brain models in epilepsy, Lancet Neurol. 22 (2023) 443–454, https://doi.org/10.1016/S1474-4422(23)00008-X

[62] K. Kar, T. Ito, M.W. Cole, B. Krekelberg, Transcranial alternating current stimulation attenuates BOLD adaptation and increases functional connectivity, J. Neurophysiol. 123 (2020) 428–438, https://doi.org/10.1152/jn.00376.2019

[63] W. Klimesch, EEG alpha and theta oscillations reflect cognitive and memory performance: a review and analysis, Brain Res. Rev. 29 (1999) 169–195, https://doi.org/10.1016/s0165-0173(98)00056-3

[64] M.L. Kringelbach, A.R. McIntosh, P. Ritter, V.K. Jirsa, G. Deco, The rediscovery of slowness: exploring the timing of cognition, Trends Cogn. Sci. 19 (2015) 616–628, https://doi.org/10.1016/j.tics.2015.07.011

[65] M.E. Larkum, A cellular mechanism for cortical associations: an organizing principle for the cerebral cortex, Trends Neurosci. 36 (2013) 141–151, https://doi.org/10.1016/j.tins.2012.11.006

[66] R. Larter, B. Speelman, R.M. Worth, A coupled ordinary differential equation lattice model for the simulation of epileptic seizures, Chaos 9 (1999) 795–804, https://doi.org/10.1063/1.166453

[67] G. Lee, R. Gommers, F. Waselewski, K. Wohlfahrt, A. O'Leary, PyWavelets: a Python package for wavelet analysis, J. Open Source Softw. 4 (2019) 1237, https://doi.org/10.21105/joss.01237

[68] A. Lempel, J. Ziv, On the complexity of finite sequences, IEEE Trans. Inf. Theory 22 (1976) 75–81, https://doi.org/10.1109/TIT.1976.1055501

[69] K. Linkenkaer-Hansen, V.V. Nikouline, J.M. Palva, R.J. Ilmoniemi, Long-range temporal correlations and scaling behavior in human brain oscillations, J. Neurosci. 21 (2001) 1370–1377, https://doi.org/10.1523/jneurosci.21-04-01370.2001
[70] Y. Liu, N. Sun, J. Xiong, Y. Zhou, X. Ye, H. Jiang, H. Guo, N. Zhi, J. Lu, P. He, H. Yang, Q. Li, R. Sun, J. He, Modulation of cerebral cortex activity by acupuncture in patients with prolonged disorder of consciousness: an fNIRS study, Front. Neurosci. 16 (2022) 1043133, https://doi.org/10.3389/fnins.2022.1043133
[71] R.M. Lorenzi, F. Palesi, C. Casellato, C.A.M. Gandini Wheeler-Kingshott, E. D'Angelo, Region-specific mean field models enhance simulations of local and global brain dynamics, npj Syst. Biol. Appl. 11 (2025) 66, https://doi.org/10.1038/s41540-025-00543-9
[72] F. Mainas, B. Golosio, A. Retico, P. Oliva, Exploring autism spectrum disorder: a comparative study of traditional classifiers and deep learning classifiers to analyze functional connectivity measures from a multicenter dataset, Appl. Sci. 14 (2024) 7632, https://doi.org/10.3390/app14177632
[73] I. Martín, G. Zamora-López, J. Fousek, M. Schirner, P. Ritter, V. Jirsa, G. Deco, G. Patow, TVB C++: a fast and flexible Back-End for the virtual brain, Adv. Sci. 13 (2026) e06440, https://doi.org/10.1002/advs.202406440
[74] C. Maschke, J. O'Byrne, M.A. Colombo, M. Boly, O. Gosseries, S. Laureys, M. Rosanova, K. Jerbi, S. Blain-Moraes, Critical dynamics in spontaneous EEG predict anesthetic-induced loss of consciousness and perturbational complexity, Commun. Biol. 7 (2024) 946, https://doi.org/10.1038/s42003-024-06613-8
[75] F. Masina, E. Napoli, P. Santacesaria, A. Giustiniani, S. Zago, M. Marino, R. Pezzetta, S. Montemurro, N. Manzo, G. Cona, D. Mapelli, G. Arcara, Transcranial alternating current stimulation selectively modulates aperiodic EEG component: unveiling alternative mechanisms of modulation, Clin. Neurophysiol. 177 (2025) 2110929, https://doi.org/10.1016/j.clinph.2025.2110929
[76] C. Meisel, A. Klaus, C. Kuehn, D. Plenz, Critical slowing down governs the transition to neuron spiking, PLoS Comput. Biol. 11 (2015) e1004097, https://doi.org/10.1371/journal.pcbi.1004097
[77] N. Monma, H. Yamamoto, N. Fujiwara, H. Murota, S. Moriya, A. Hirano-Iwata, S. Sato, Directional intermodular coupling enriches functional complexity in biological neuronal networks, Neural Networks 184 (2025) 106967, https://doi.org/10.1016/j.neunet.2024.106967
[78] D. Müller, U. Habel, E.S. Brodkin, B. Clemens, C. Weidler, HD-tDCS induced changes in resting-state functional connectivity: insights from EF modeling, Brain Stimul. 16 (2023) 1722–1732, https://doi.org/10.1016/j.brs.2023.11.012
[79] T.E. Nichols, A.P. Holmes, Nonparametric permutation tests for functional neuroimaging: a primer with examples, Hum. Brain Mapp. 15 (2001) 1–25, https://doi.org/10.1002/hbm.1058
[80] J. O'Byrne, K. Jerbi, How critical is brain criticality? Trends Neurosci. 45 (2022) 820–837, https://doi.org/10.1016/j.tins.2022.08.007
[81] J.M. Palva, S. Palva, Infra-slow fluctuations in electrophysiological recordings, blood-oxygenation-level-dependent signals, and psychophysical time series, NeuroImage 62 (2012) 2201–2211, https://doi.org/10.1016/j.neuroimage.2012.02.060
[82] S. Palva, J.M. Palva, Roles of brain criticality and multiscale oscillations in temporal predictions for sensorimotor processing, Trends Neurosci. 41 (2018) 729–743, https://doi.org/10.1016/j.tins.2018.08.008
[83] G. Rabuffo, J. Fousek, C. Bernard, V. Jirsa, Neuronal cascades shape whole-brain functional dynamics at rest, eNeuro 8 (2021) ENEURO.0283-21.2021, https://doi.org/10.1523/eneuro.0283-21.2021.
[84] J.A. Roberts, L.L. Gollo, R.G. Abeysuriya, G. Roberts, P.B. Mitchell, M.W. Woolrich, M. Breakspear, Metastable brain waves, Nat. Commun. 10 (2019) 1056, https://doi.org/10.1038/s41467-019-08999-0
[85] M. Rosanova, A.G. Casali, V. Bellina, F. Resta, M. Mariotti, M. Massimini, Natural frequencies of human corticothalamic circuits, J. Neurosci. 29 (2009) 7679–7685, https://doi.org/10.1523/JNEUROSCI.0445-09.2009
[86] M. Rosanova, O. Gosseries, S. Casarotto, M. Boly, A.G. Casali, M.-A. Bruno, M. Mariotti, P. Boveroux, G. Tononi, S. Laureys, M. Massimini, Recovery of cortical effective connectivity and recovery of consciousness in vegetative patients, Brain 135 (2012) 1308–1320, https://doi.org/10.1093/brain/awr340
[87] P. Sanz-Leon, S.A. Knock, A. Spiegler, V.K. Jirsa, Mathematical framework for large-scale brain network modeling in the virtual brain, NeuroImage 111 (2015) 385–430, https://doi.org/10.1016/j.neuroimage.2015.01.002
[88] P. Sanz-Leon, S.A. Knock, M.M. Woodman, L. Domide, J. Mersmann, A.R. McIntosh, V. Jirsa, The virtual brain: a simulator of primate brain network dynamics, Front. Neuroinform. 7 (2013) 10, https://doi.org/10.3389/fninf.2013.00010
[89] S. Sarasso, M. Rosanova, A.G. Casali, S. Casarotto, M. Fecchio, M. Boly, O. Gosseries, G. Tononi, S. Laureys, M. Massimini, Quantifying cortical EEG responses to TMS in (un)consciousness, Clin. EEG Neurosci. 45 (2014) 40–49, https://doi.org/10.1177/1550059413513723
[90] M. Schirner, L. Domide, D. Perdikis, P. Triebkorn, L. Stefanovski, R. Pai, P. Prodan, B. Valean, J. Palmer, C. Langford, A. Blickensdörfer, M. van der Vlag, S. Diaz-Pier, A. Peyser, W. Klijn, D. Pleiter, A. Nahm, O. Schmid, M. Woodman, L. Zehl, J. Fousek, S. Petkoski, L. Kusch, M. Hashemi, D. Marinazzo, J.-F. Mangin, A. Flöel, S. Akintoye, B.C. Stahl, M. Cepic, E. Johnson, G. Deco, A.R. McIntosh, C.C. Hilgetag, M. Morgan, B. Schuller, A. Upton, C. McMurtrie, T. Dickscheid, J.G. Bjaalie, K. Amunts, J. Mersmann, V. Jirsa, P. Ritter, Brain simulation as a cloud service: the virtual brain on EBRAINS, NeuroImage 251 (2022) 118973, https://doi.org/10.1016/j.neuroimage.2022.118973
[91] W.L. Shew, D. Plenz, The functional benefits of criticality in the cortex, The Neuroscientist 19 (2012) 88–100, https://doi.org/10.1177/1073858412445487
[92] R. Sitaram, A. Caria, R. Veit, T. Gaber, G. Rota, A. Kuebler, N. Birbaumer, fMRI Brain-Computer interface: a tool for neuroscientific research and treatment, Comput. Intell. Neurosci. 2007 (2007) 25487, https://doi.org/10.1155/2007/25487
[93] L. Stefanovski, P. Triebkorn, A. Spiegler, M.-A. Diaz-Cortes, A. Solodkin, V. Jirsa, A.R. McIntosh, P. Ritter, Linking molecular pathways and large-scale computational modeling to assess candidate disease mechanisms and pharmacodynamics in alzheimer's disease, Front. Comput. Neurosci. 13 (2019) 54, https://doi.org/10.3389/fncom.2019.00054
[94] S.M. Sunkin, L. Ng, C. Lau, T. Dolbeare, T.L. Gilbert, C.L. Thompson, M. Hawrylycz, C. Dang, Allen brain atlas: an integrated spatio-temporal portal for exploring the central nervous system, Nucleic Acids Res. 41 (2013) D996–D1008, https://doi.org/10.1093/nar/gks1042
[95] E. Tagliazucchi, F. von Wegner, A. Morzelewski, V. Brodbeck, H. Laufs, Dynamic BOLD functional connectivity in humans and its electrophysiological correlates, Front. Hum. Neurosci. 6 (2012) 339, https://doi.org/10.3389/fnhum.2012.00339
[96] G. Trensch, R. Gutzen, I. Blundell, M. Denker, A. Morrison, Rigorous neural network simulations: a model substantiation methodology for increasing the correctness of simulation results in the absence of experimental validation data, Front. Neuroinform. 12 (2018) 81, https://doi.org/10.3389/fninf.2018.00081
[97] P. Triebkorn, J. Meier, J. Zimmermann, L. Stefanovski, D. Roy, A. Solodkin, V. Jirsa, G. Deco, M. Breakspear, M. Schirner, A.R. McIntosh, P. Ritter, Fifty shades of the virtual brain: converging optimal working points yield biologically plausible electrophysiological and imaging features, biorXiv (2024), https://doi.org/10.1101/2020.03.26.009795
[98] D.C. Van Essen, K. Ugurbil, E. Auerbach, D. Barch, T.E.J. Behrens, R. Bucholz, A. Chang, L. Chen, M. Corbetta, S.W. Curtiss, S. Della Penna, D. Feinberg, M.F. Glasser, N. Harel, A.C. Heath, L. Larson-Prior, D. Marcus, G. Michalareas, S. Moeller, R. Oostenveld, S.E. Petersen, F. Prior, B.L. Schlaggar, S.M. Smith, A.Z. Snyder, J. Xu, E. Yacoub, WU-Minn HCP Consortium, The human connectome project: a data acquisition perspective, NeuroImage 62 (2012) 2222–2231, https://doi.org/10.1016/j.neuroimage.2012.02.018
[99] T. Väyrynen, H. Helakari, V. Korhonen, J. Tuunanen, N. Huotari, J. Piispala, M. Kallio, L. Raitamaa, J. Kananen, M. Järvelä, J. Matias Palva, V. Kiviniemi, Infra-slow fluctuations in cortical potentials and respiration drive fast cortical EEG rhythms in sleeping and waking states, Clin. Neurophysiol. 156 (2023) 207–219, https://doi.org/10.1016/j.clinph.2023.10.013
[100] H.E. Wang, B. Dollomaja, P. Triebkorn, G.M. Duma, A. Williamson, J. Makhalova, J.-D. Lemarechal, F. Bartolomei, V. Jirsa, Virtual brain twins for stimulation in epilepsy, Nat. Comput. Sci. 5 (2025) 754–768, https://doi.org/10.1038/s43588-025-00841-6
[101] A. Yegenoglu, A. Subramoney, T. Hater, C. Jimenez-Romero, W. Klijn, A. Pérez Martín, M. van der Vlag, M. Herty, A. Morrison, S. Diaz-Pier, Exploring parameter and Hyper-Parameter spaces of Neuroscience models on high performance computers with learning to learn, Front. Comput. Neurosci. 16 (2022) 885207, https://doi.org/10.3389/fncom.2022.885207
[102] H. Yu, F. Li, J. Liu, D. Liu, H. Guo, J. Wang, G. Li, Evaluation of acupuncture efficacy in modulating brain activity with periodic-aperiodic EEG measurements, IEEE Trans. Neural Syst. Rehabil. Eng. 32 (2024) 2450–2459, https://doi.org/10.1109/tnsre.2024.3421648
[103] H. Yu, X. Li, X. Lei, J. Wang, Modulation effect of acupuncture on functional brain networks and classification of its manipulation with EEG signals, IEEE Trans. Neural Syst. Rehabil. Eng. 27 (2019) 1973–1984, https://doi.org/10.1109/tnsre.2019.2939655
[104] H. Yu, X. Wu, L. Cai, B. Deng, J. Wang, Modulation of spectral power and functional connectivity in human brain by acupuncture stimulation, IEEE Trans. Neural Syst. Rehabil. Eng. 26 (2018) 977–986, https://doi.org/10.1109/tnsre.2018.2828143
[105] G. Zamora-López, Y. Chen, G. Deco, M.L. Kringelbach, C. Zhou, Functional complexity emerging from anatomical constraints in the brain: the significance of network modularity and rich-clubs, Sci. Rep. 6 (2016) 38424, https://doi.org/10.1038/srep38424
[106] J. Zhang, K. Wu, J. Dong, J. Feng, L. Yu, Modeling the interplay between regional heterogeneity and critical dynamics underlying brain functional networks, Neural Networks 184 (2025) 107100, https://doi.org/10.1016/j.neunet.2024.107100
[107] M. Zhao, C. Zhou, Y. Chen, B. Hu, B.-H. Wang, Complexity versus modularity and heterogeneity in oscillatory networks: combining segregation and integration in neural systems, Phys. Rev. E 82 (2010) 046225, https://doi.org/10.1103/physreve.82.046225

Author biography

Gianluca Gaglioti holds a Master's degree in Cognitive Science and is currently a PhD student in the HUME doctoral program at the University of Milan, Italy, where he works in the Human Physiology Lab led by Dr. Marcello Massimini. His research focuses on how the brain transitions between different states—such as wakefulness, sleep, anesthesia, and states following brain injury—by combining computational modeling of neural circuits at mesoscopic and macroscopic scales with TMS-EEG data analysis to study spontaneous and evoked cortical dynamics.

Alessandra Cardinale holds a Master's degree in Statistical Sciences and is currently working at ISS, Italy. She is a INFN-supervised PhD student in the National Doctoral Program in Health and Life Sciences. Her research focuses on the development and application of Cobrawap, a collaborative brain wave analysis pipeline that integrates multi-scale neuronal data and advanced statistical and computational methods to characterize dynamic cortical wave activity and support rigorous cross-dataset comparisons and model validation in neuroscience. She combines cutting-edge data analysis frameworks with high-performance computing to address complex challenges in brain signal interpretation and computational neuroscience.

Cosimo Lupo received his PhD in Physics from Sapienza University of Rome, working in the complex and disordered systems group led by Giorgio Parisi. After covering a PostDoc position at École Normale Supérieure in Paris, focusing on quantitative computational approaches to the generation and maturation statistics of human antibodies, he moved to the National Institute of Nuclear Physics (INFN), Rome, to work as a Technological Researcher on neuroscience-related topics within Human Brain Project, EBRAINS and EBRAINS-Italy initiatives: neural networks; bio-inspired AI architectures; proof-of-concept models of cognition, learning, and sleep; whole-brain simulation models; data analysis on experimental recordings. He is leading current developments of the Cobrawap data analysis pipeline, with a particular attention to its deployment and execution on HPC facilities.

Thierry Nieus received his PhD in Applied Mathematics at the Department of Mathematics F. Enriques in Milan (Italy). His research focuses on the computations performed by neuronal networks. His work involves the analysis and modeling of multiscale data, ranging from single synapses to population recordings. In September 2016 he joined Marcello Massimini's laboratory (University of Milan, Italy), working on computational models of the thalamocortical circuit and on complexity measures of TMS/EEG data. From November 2021 to November 2023 he served as a scientific consultant and data scientist at the HPC Indaco (University of Milan). From January 2024 he got a position as data scientist at the Department of Environmental Science and Policy (University of Milan) where he is serving as HPC scientific consultant and investigates the impact of climate change on crop and oil production with data analysis and computational modeling approaches.

Federico Marmoreo holds a Master's degree in Mathematics from the University of Rome Tor Vergata and a PhD in Computer Vision and Machine Learning obtained through a joint program between the University of Genoa and the Italian Institute of Technology (IIT). He worked as a Research Technologist at INFN APE Computing lab, in collaboration with Pier Stanislao Paolucci and Giulia De Bonis, within the EBRAINS-Italy framework. With a background in data analysis, numerical analysis, and computer science, his contributions focused on code and pipeline parallelization and vectorization strategies to significantly reduce the execution time of large-scale computational workflows.

Elena Focacci holds a Master's degree in Psychobiology and Cognitive Neuroscience from the University of Parma and is a PhD student in the HUME doctoral program at the University of Milan, Italy. She carries out her research at the Human Physiology Lab directed by Dr. Marcello Massimini. Her research activity focuses on the design and execution of TMS-EEG and EEG experiments in both healthy participants and neurological patients, including individuals with traumatic brain injury, spatial neglect, and visual impairment. She is involved in the analysis of electrophysiological data to investigate cortical dynamics across different sensory and cognitive conditions.

Robin Gutzen is a Postdoc at the NYU Center for Data Science and the Department of Psychology, working with Assistant Professor Grace Lindsay. He holds a Master's degree in Physics from RWTH Aachen University and completed his PhD at the Research Center Jülich, where he specialized in statistical methods and research software for neural data analysis. Robin has been actively involved in the Human Brain Project and has contributed to various community initiatives promoting research reproducibility. His current research focuses on modeling the rhythmic dynamics of perception in machine learning models of the primate visual system.

Michael Denker received his diploma in physics from the University of Göttingen, Germany, in 2002, and defended his PhD in 2009 at the Free University, Berlin, in the Neuroinformatics and Theoretical Neuroscience lab of Sonja Grün. In 2011 he joined the Institute of Neuroscience and Medicine (INM-6 and INM-10) at the Research Centre Jülich, where he now heads the team "Data Science for Electro- and Optophysiology Behavioural Neuroscience" at the Institute for Advanced Simulation (IAS-6). His team works on improving the reproducibility of data analysis workflows in electrophysiology by designing dedicated software, such as Elephant. His main scientific interest is in understanding the relationship between the correlation structure and spatio-temporal organization of neural activity.

Andrea Pigorini was trained as a Biomedical Engineer, received a PhD in Physiology and is currently Research Fellow of Human Physiology at the University of Milan, Italy. His research focuses on the analysis of electroencephalographic activity recorded simultaneously at the scalp level and within the brain in treatment-resistant epileptic patients implanted with intracerebral electrodes for presurgical evaluation. During his doctorate he investigated the role of bistable dynamics in the reduction of the level of consciousness occurring during NREM sleep with respect to wakefulness.

Marcello Massimini was trained as a Medical Doctor, received a PhD in Neurophysiology and is currently Full Professor of Human Physiology at the University of Milan, Italy. Spanning from intracranial recordings to neuroimaging, his research activity is devoted to understanding the neuronal and network mechanisms underlying physiological and pathological transitions across different brain states, such as wakefulness, sleep, anesthesia, and coma. Over the last twenty years, he has refined a strategy, based on cortical stimulations and recordings with TMS-EEG, to detect and monitor recovery of consciousness after coma and to study the electrophysiological consequences of focal and multifocal brain injury.

Simone Sarasso is Associate Professor of Human Physiology at the Department of Biomedical and Clinical Sciences, University of Milan, a position held since 2022. Previously he was Researcher and Postdoctoral Fellow at the same department. He earned a PhD in Psychological Sciences- Psychobiology from the University of Padua in 2008. Trained at the University of Wisconsin-Madison as Honorary Fellow and Research Associate (2006-2011), he studied neural correlates of consciousness, sleep, and plasticity using TMS-EEG and high-density EEG. His current work applies these methods to investigate functional recovery after brain injury.

Pier Stanislao Paolucci is a Physicist, and currently coordinates INFN research activities in the bioinspired Future Artificial Intelligence Research (FAIR) and EBRAINS-Italy projects funded by the Next Generation EU program. Previously, he served as technological research leader of the "Networks underlying cognition and consciousness" activities in the Human Brain Project. He served as CTO of the Diopsis multi-processor Systems-on-Chip design center of a major semiconductor manufacturer. Since 1984, he has been part of the APE Parallel/Distributed Computing Laboratory of INFN, focusing on the co-design of algorithms, system software and hardware for the acceleration of complex systems simulations. He authored several international patents and invented widely used numerical algorithms for parallel/distributed computing platforms.

Giulia De Bonis is a researcher at INFN, Italy. She received her PhD in Physics in 2005 from Sapienza University of Rome. Her current research activity builds on her background in experimental particle physics and focuses on exploring how technologies, methods, and approaches (particularly the codesign of algorithms, procedures and software) can be developed in multidisciplinary fields (such as neuroscience) and transferred to fundamental physics, and vice versa. She has been involved in the European initiatives Human Brain Project and EBRAINS, as well as in the Italian project EBRAINS-Italy; she is part of the INFN APE Computing Laboratory. She is one of the originators of the Cobrawap solution and serves as its scientific coordinator, specifically interested in measuring the performance of bio-inspired AI architectures using metrics derived from observation of biological systems.

Emergent complexity and rhythms in evoked and spontaneous dynamics of human whole-brain models after tuning through analysis tools – Supplementary Material

Gianluca Gaglioti[a,b,1,*], Alessandra Cardinale[c,d,1], Cosimo Lupo[d,1], Thierry Nieus[e], Federico Marmoreo[d], Elena Focacci[a,b], Robin Gutzen[f], Michael Denker[g], Andrea Pigorini[h,i], Marcello Massimini[a,j,k,2], Simone Sarasso[a,2], Pier Stanislao Paolucci[d,2], Giulia De Bonis[d,2]

[a] *Dep. of Biomedical and Clinical Sciences, Univ. of Milan, Milan, Italy*
[b] *Dep. of Philosophy "Piero Martinetti", Univ. of Milan, Milan, Italy*
[c] *Università Campus Bio-Medico di Roma, Rome, Italy*
[d] *Istituto Nazionale di Fisica Nucleare (INFN), Sezione di Roma, Rome, Italy*
[e] *Dep. Environmental Science and Policy, Univ. of Milan, Milan, Italy*
[f] *Center for Data Science, New York University, New York, U.S.A.*
[g] *Institute for Advanced Simulation (IAS-6), Jülich Research Centre, Jülich, Germany*
[h] *Dep. of Biomedical, Surgical and Dental Sciences, Univ. of Milan, Milan, Italy*
[i] *UOC Maxillo-facial Surgery and dentistry, Fondazione IRCCS Cà Granda, Ospedale Maggiore Policlinico, Milan, Italy*
[j] *IRCCS Fondazione Don Carlo Gnocchi ONLUS, Milan, Italy*
[k] *Azrieli Program in Brain, Mind and Consciousness, Canadian Institute for Advanced Research, Toronto, Canada*

Supplementary Methods

EEG preprocessing, 4 subjects, 62 channels

We recorded resting-state electroencephalography (EEG) from 4 healthy subjects with eyes closed. Each recording session lasted between 5 and 10 minutes. EEG measurements were acquired using a 64-channel EEG amplifier (Brain Products GmbH) sampled at 5000 Hz with hardware filtering at 1000 Hz, and electrode impedance was maintained below 10 kΩ. Reference and ground electrodes were placed on the forehead above the frontal sinus.

Resting-state EEG data were preprocessed using the MNE-Python software package (Gramfort et al., 2013). EEG recordings were first detrended to remove low-frequency drifts. A band-pass filter was applied with a high-pass cutoff at 0.5 Hz and a low-pass cutoff at 60 Hz. Additionally, a 50 Hz notch filter was applied to suppress line noise. Prior to independent component analysis (ICA), time segments containing prominent artifacts, such as those associated with muscle activity or other non-neural sources, were manually

*Corresponding author: gaglioti.gianluca@gmail.com
[1] These authors contributed equally.
[2] These authors jointly supervised this work.

Supplementary Material for Neurocomputing (2026), 132735, doi.10.1016/j.neucom.2026.132735

removed to improve ICA performance. The ICA decomposition was then applied to identify and remove remaining stereotypical artifacts, such as eye blinks and other physiological sources.

Frequency and time-frequency analysis of EEG signals

Frequency and time-frequency analyses of the EEG were performed using the MNE-Python package. The power spectral density (PSD) was computed using Welch's method with a Hamming window, 4 s segments and 75 % (i.e., 3 s) overlap. The PSD was averaged across channels, and both the peak frequency and spectral slope were computed to characterize the aperiodic $1/f$ trend of the signal. The spectral slope was calculated in the 0.7–7 Hz range using the method described by Colombo et al. (2019), adapted for Python implementation.

Time-frequency analysis was performed by extracting the envelope and instantaneous power time course in the alpha band (8–12 Hz) using Morlet wavelet transforms implemented in MNE-Python. To quantify the temporal dynamics of these signals, we computed the coefficient of variation (CV_{power}) of the power time course across time for each channel and applied detrended fluctuation analysis (DFA) to the envelope signal, as detailed in Sec. 2.5.3.

Simulation and analysis using a smaller 74 parcellation connectome

As a proof-of-principle demonstration of the generalizability of our framework and its direct applicability to experimental data, we performed additional simulations using a reduced-scale connectome. This supplementary analysis serves two purposes: first, to validate that the parameter tuning approach remains effective when applied to a different parcellation scheme; second, to establish a more quantitative benchmark by directly comparing simulated and empirical neurophysiological features.

We employed a publicly available human connectome provided within the TVB platform. This connectivity matrix has been utilized in prior computational studies (Kunze et al., 2016; Gaglioti et al., 2024) and comprises 74 cortical regions, with 37 areas per hemisphere. The anatomical parcellation represents a hybrid construction that integrates diffusion spectrum imaging tractography and data derived from the CoCoMac neuroinformatics database (Kötter, 2004).

We simulated neural mass dynamics using the Larter-Breakspear model under three distinct parameter configurations. First, we executed the default TVB parameter set to establish a baseline (referred to herein as DEF). Second, we implemented the parameters previously tuned in Gaglioti et al. (2024) (referred to herein as TUN1). Third, to further refine the model match to experimental electrophysiology, we conducted a systematic parameter space exploration centered on three key parameters used in the main analysis: global coupling strength (G), conduction velocity (c_v), and the timescale of the neural mass dynamics (t_{scale}).

The optimal parameter combination was identified by maximizing a composite score that quantifies the correspondence between simulated and empirical spectral characteristics. For each configuration, we computed the average PSD across all regions and extracted its $1/f$

spectral slope using the same estimation procedure described in the previous section on EEG analysis. The score was defined as:

$$\text{score} \equiv r_{\text{Pearson}}(\text{PSD}_{\text{model}}, \text{PSD}_{\text{EEG}}) - \left(\frac{\text{slope}_{\text{model}} - \text{slope}_{\text{EEG}}}{\text{slope}_{\text{EEG}}} \right)^2 \tag{A.1}$$

where r_{Pearson} denotes the Pearson correlation coefficient between model and EEG PSD, and "slope" represents the $1/f$ spectral slope. This metric rewards both spectral shape and spectral slope similarity. The parameter combination yielding the highest score was $G = 3.6$, $c_v = 4$, and $t_{\text{scale}} = 1$ (referred to herein as TUN2).

Following parameter selection, we computed two metrics of temporal variability for each model configuration: the coefficient of variation of the power time-course at the dominant frequency (CV_{power}), and detrended fluctuation analysis (DFA) of the envelope. Both metrics were calculated using the identical procedures described for the main analysis. The resulting values were compared directly with the corresponding experimental measurements to evaluate the extent to which TUN2 captures the temporal dynamics observed in real brain activity.

References

Alstott, J., Breakspear, M., Hagmann, P., Cammoun, L., Sporns, O., 2009. Modeling the Impact of Lesions in the Human Brain. PLOS Computational Biology 5, e1000408. doi:10.1371/journal.pcbi.1000408.

Colombo, M.A., Napolitani, M., Boly, M., Gosseries, O., Casarotto, S., Rosanova, M., Brichant, J.F., Boveroux, P., Rex, S., Laureys, S., Massimini, M., Chieregato, A., Sarasso, S., 2019. The spectral exponent of the resting eeg indexes the presence of consciousness during unresponsiveness induced by propofol, xenon, and ketamine. NeuroImage 189, 631–644. doi:10.1016/j.neuroimage.2019.01.024.

Gaglioti, G., Nieus, T.R., Massimini, M., Sarasso, S., 2024. Investigating the Impact of Local Manipulations on Spontaneous and Evoked Brain Complexity Indices: A Large-Scale Computational Model. Applied Sciences 14, 890. doi:10.3390/app14020890.

Gramfort, A., Luessi, M., Larson, E., Engemann, D.A., Strohmeier, D., Brodbeck, C., Goj, R., Jas, M., Brooks, T., Parkkonen, L., Hämäläinen, M., 2013. MEG and EEG data analysis with MNE-Python. Frontiers in Neuroscience 7, 267. doi:10.3389/fnins.2013.00267.

Kötter, R., 2004. Online Retrieval, Processing, and Visualization of Primate Connectivity Data From the CoCoMac Database. Neuroinformatics 2, 127–144. doi:10.1385/ni:2:2:127.

Kunze, T., Hunold, A., Haueisen, J., Jirsa, V., Spiegler, A., 2016. Transcranial direct current stimulation changes resting state functional connectivity: A large-scale brain network modeling study. NeuroImage 140, 174–187. doi:10.1016/j.neuroimage.2016.02.015.

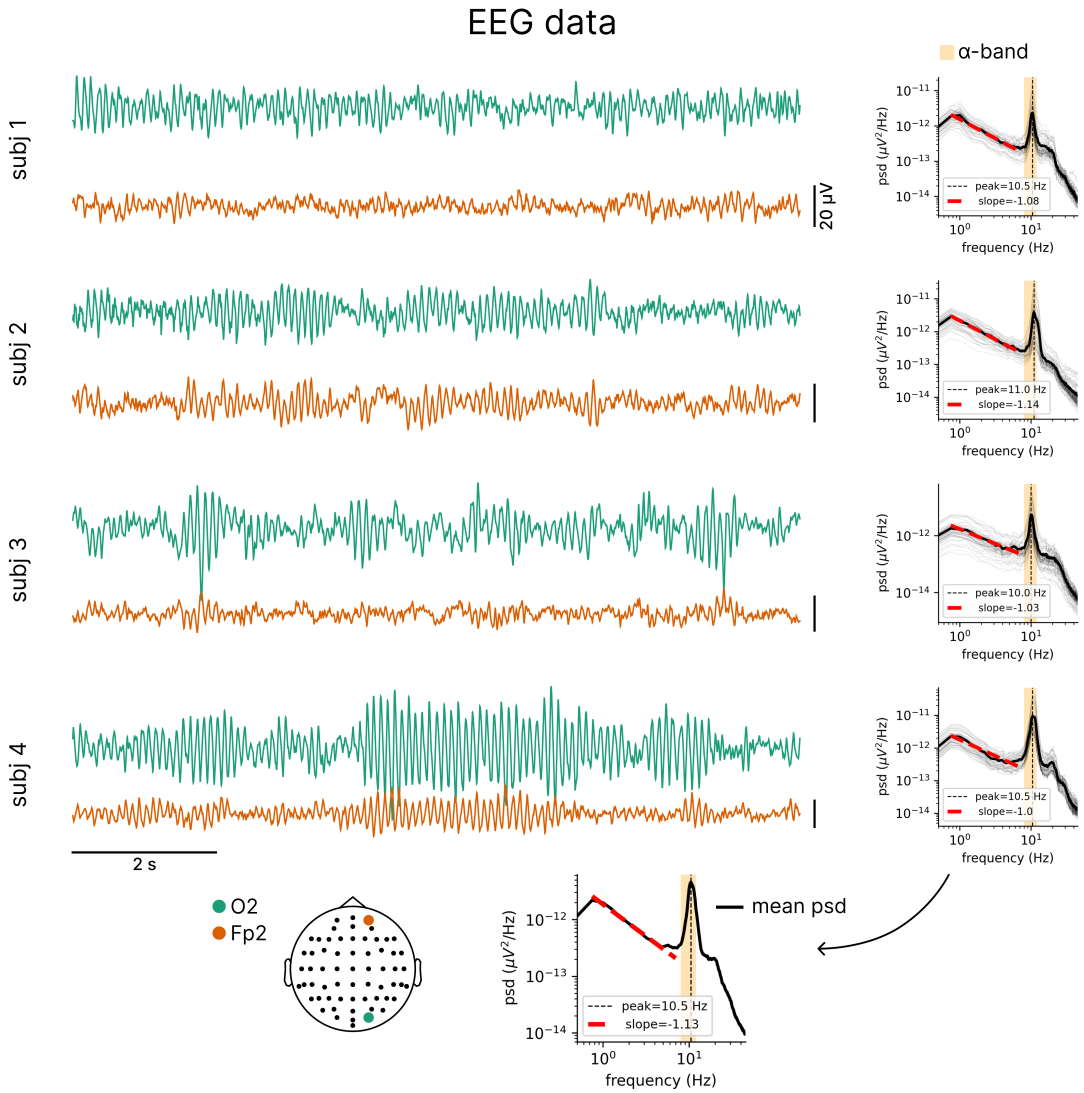

Figure A.1: **Representative empirical EEG signals and power spectra during eyes-closed rest**. Ten-second segments from an occipital (O2, green) and a frontal (Fp2, orange) electrode are shown for each of the four subjects. For each subject, the right panels display the power spectral density (PSD) of all 62 channels (thin gray lines) and their average (thick black line). The yellow shading marks the alpha band (8–12 Hz), which exhibits a prominent peak in all subjects. The red dashed line shows the spectral slope of the average PSD fitted (as in Colombo et al. (2019)) between 0.7 and 7 Hz, prior to the alpha peak, to capture the $1/f$ background scaling while avoiding the artificial 0.5 Hz peak introduced by the high-pass filter at 0.5 Hz. The bottom right panel shows the PSD averaged across subjects.

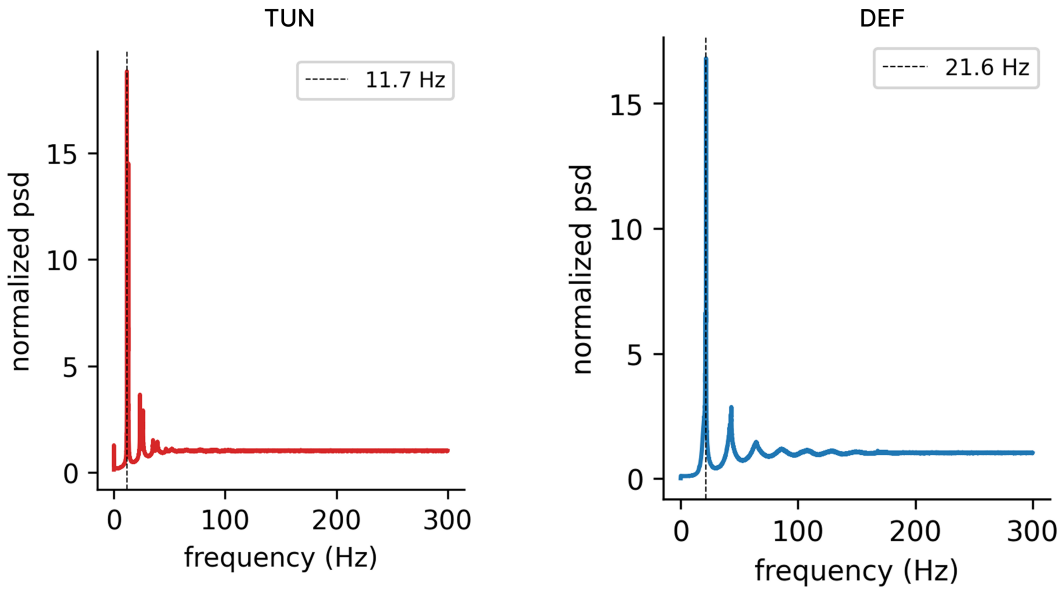

Figure A.2: **Power Spectral Density (PSD) of the events in TUN and DEF**.
PSDs are computed on the event time series for each node using the Welch method (with the same parameters as in Fig. 2), and then averaged across nodes for TUN and DEF.

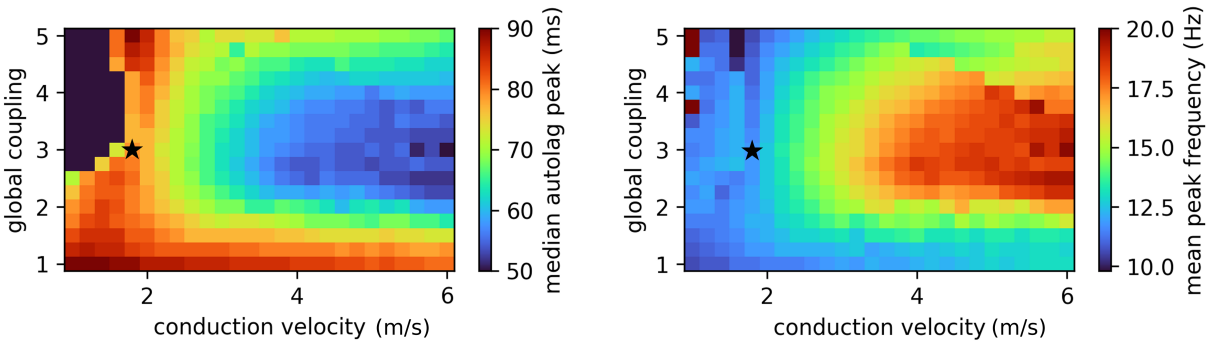

Figure A.3: **Global TVB simulation parameters influence the global periodicity of the model**. We vary the conduction velocity c_v (from 1 to 6 m/s) and the global coupling G (from 1 to 5), quantifying the resulting changes in the median auto-correlation peak (second mode), for simulations obtained with TUN configuration for the model. These manipulations induce variations in periodicity: higher conduction velocities are associated with faster periodicities (i.e., shorter median lags) across different global coupling values. The star identifies the actual values eventually used for simulations in this work.

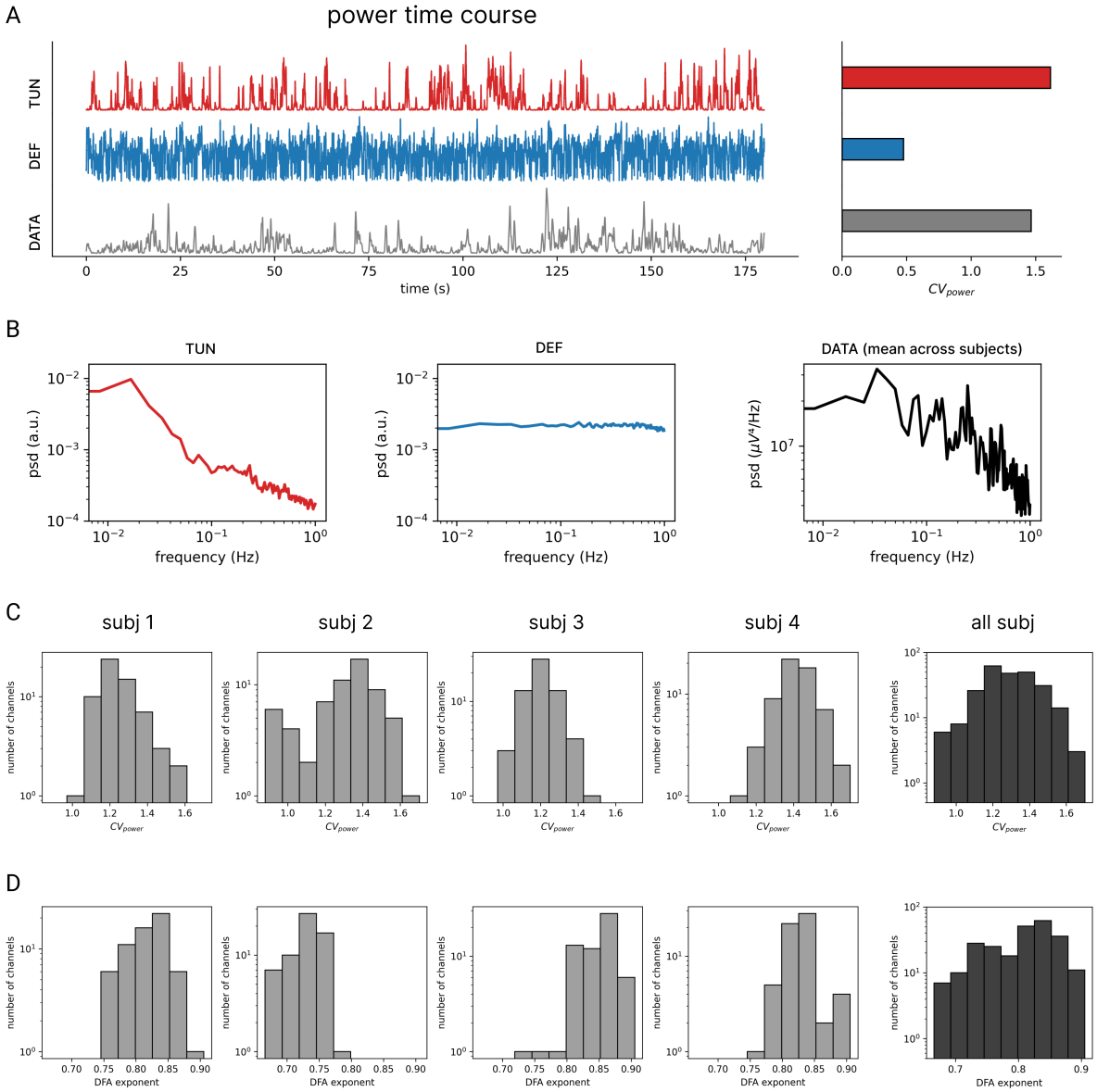

Figure A.4: **Signal fluctuations and long-range temporal correlation in EEG data (4 subjects, 62 channels) and model**.
A) The left panel shows the time course of band-limited power, summed over the dominant frequency, in a node of the superior parietal cortex from the TUN configuration (8–12 Hz, red), the DEF configuration (18–22 Hz, blue), and the occipital electrode O2 from EEG of one subject (8–12 Hz, gray). On the right, the coefficient of variation of power CV_{power} over time is displayed for each trace, indexing the degree of temporal fluctuation in each condition. **B)** Average power spectral density (PSD) of the power time courses for TUN (red), DEF (blue), and EEG data (black). PSD estimates are computed using 120-s segments with 70-s overlap. For model data, the PSD is averaged across nodes; for EEG, across channels and subjects. **C)** Distribution of CV_{power} across channels is shown for each EEG subject (gray), with the aggregated distribution across all channels and subjects shown on the right (black). **D)** Same as C), but for the detrended fluctuation analysis (DFA) exponent, calculated on the alpha envelope as described in Figs. 4E-F.

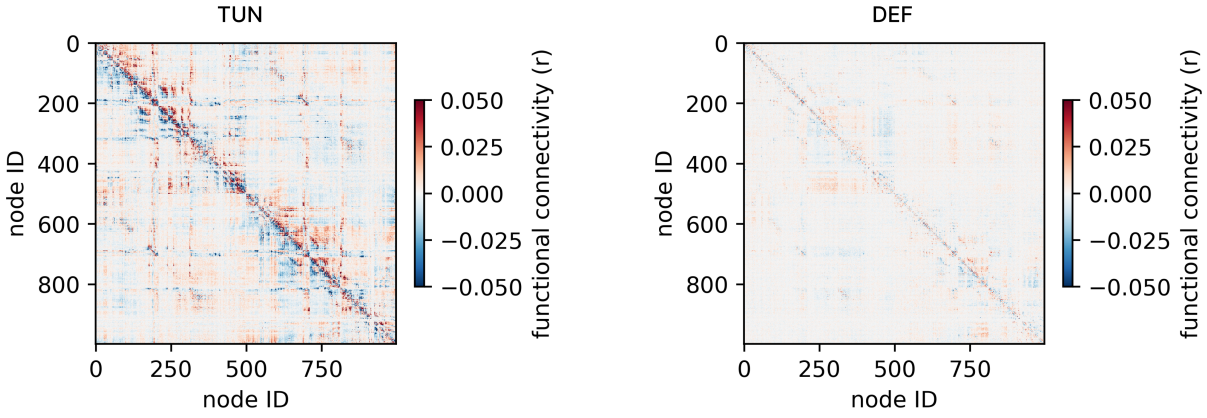

Figure A.5: **Functional connectivity asymmetry matrix in TUN and DEF configurations**. The $\mathbb{FC}_{\text{asym}}$ matrix is quantified as $\mathbb{FC}_{\text{asym}} = \mathbb{FC} - \mathbb{FC}^{\intercal}$, where $(\cdot)^{\intercal}$ denotes the matrix transpose. Positive values in $\mathbb{FC}_{\text{asym},ij}$ indicate that node i has a stronger influence on node j than vice versa; negative values indicate the opposite.

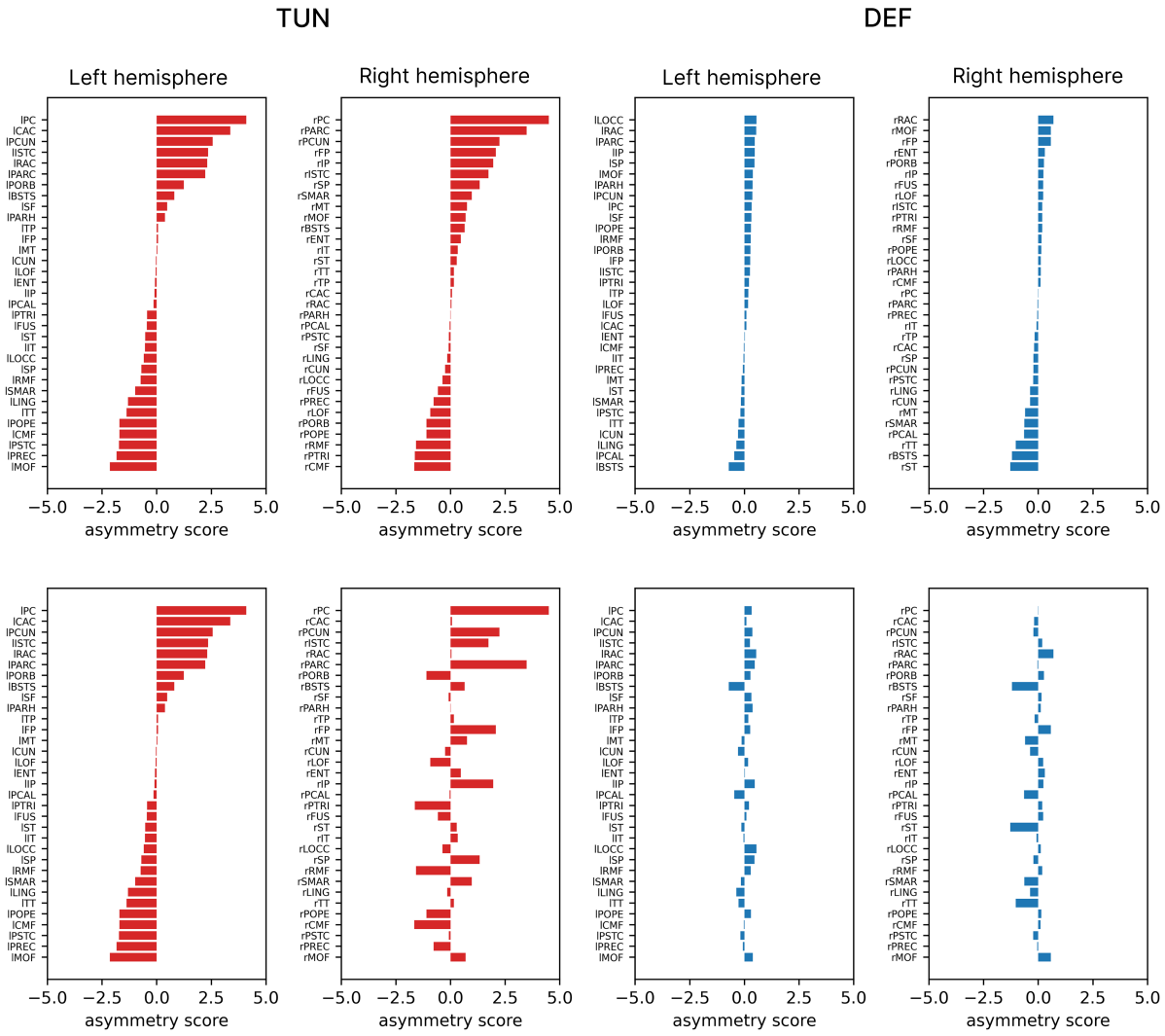

Figure A.6: **Average asymmetry score of each cortical region in TUN and DEF**.
Values for listed regions are obtained averaging the asymmetry score across the nodes located in the given region. In top panels, regions are sorted in their respective descending order. In bottom panels, regions are sorted in descending order according to the values of the first panel (left hemisphere of the TUN configuration).

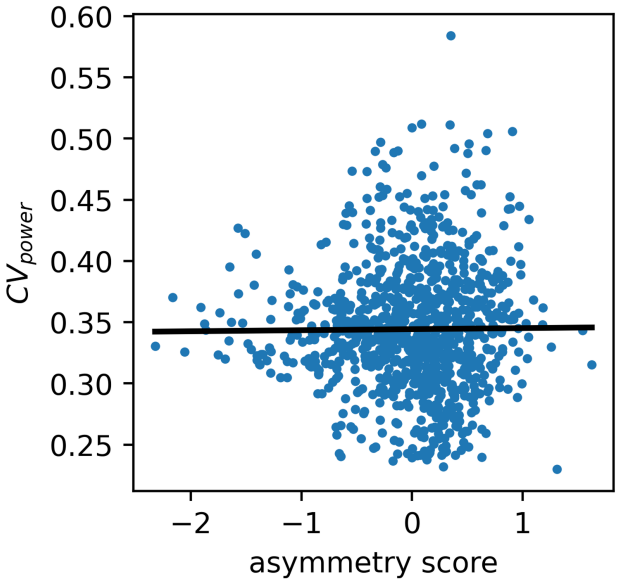

Figure A.7: **Relationship between asymmetry score and power fluctuations ($\mathrm{CV}_{\mathrm{power}}$) in DEF.** Linear regression (solid black line) shows a non-significant correlation ($r = 0.009$, $p = 0.77$).

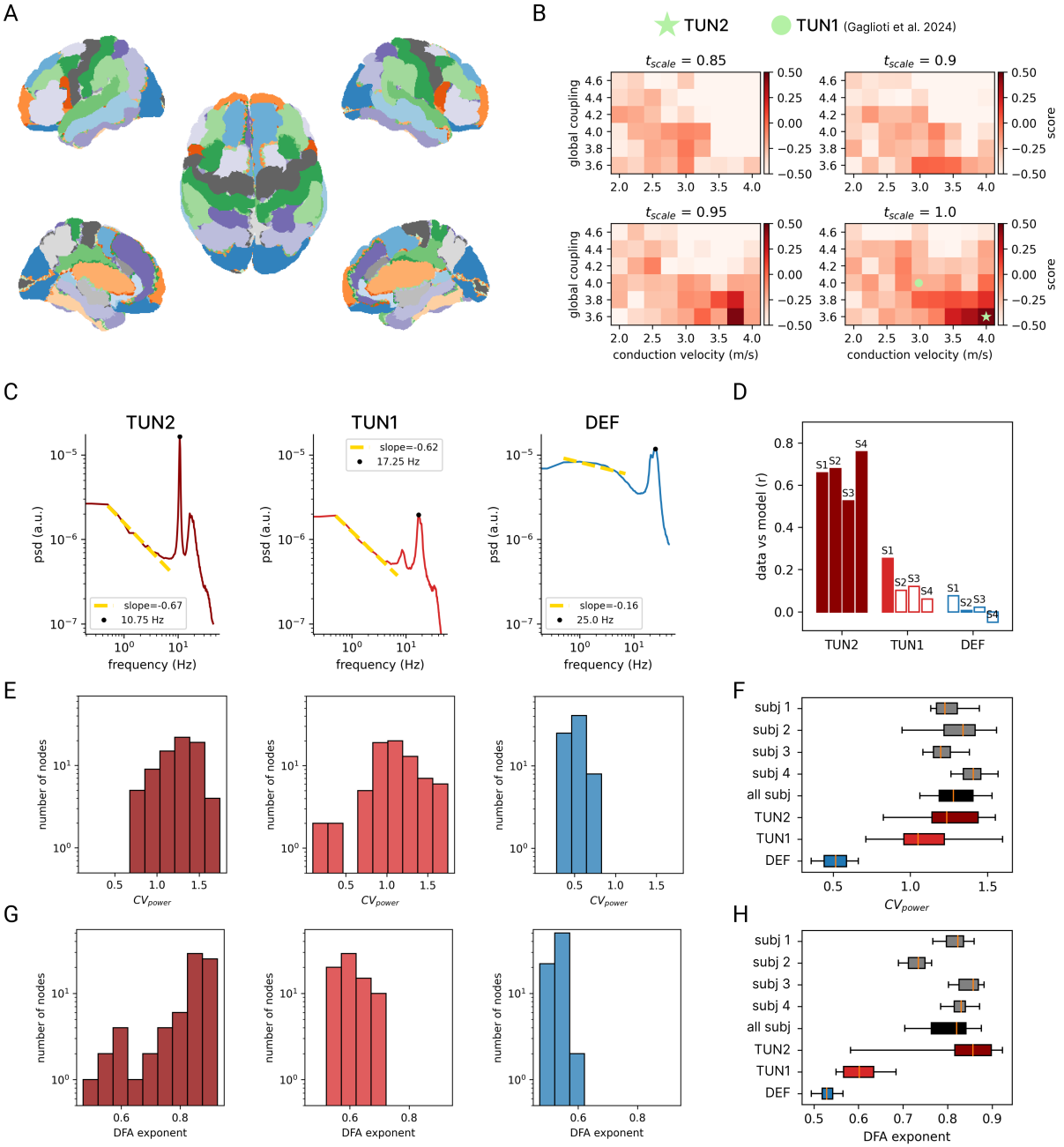

Figure A.8: **Tuning a 74-node connectome against empirical EEG data.**
A) Spatial layout of the 74-node parcellation used in the supplementary analysis. **B)** Heatmaps of the parameter space exploration showing the composite score assessing spectral similarity between simulated and empirical PSD. Global coupling strength (G, 3.6 to 4.6, step 0.2), conduction velocity (c_v, 2 to 4, step 0.25), and timescale (t_{scale}, 0.85 to 1.0, step 0.05) were varied. TUN1 (green dot) refers to the configuration of parameters used in Gaglioti et al. (2024), while TUN2 (green star) indicates the configuration with the maximum score. **C)** Average PSD across regions for the three model configurations: TUN2 (dark red), TUN1 (red), and the default TVB configuration (DEF, blue). The yellow line shows the fitted $1/f$ spectral slope, and black dots mark the spectral peak frequency. **D)** Pearson correlation coefficient (r) between model-simulated and empirically measured PSD for individual subjects (S1–S4) across all three model

configurations. White-filled bars indicate non-significant correlations ($p > 0.05$). **E)** Distributions of the CV_{power} at the dominant oscillation frequency for each configuration. Frequencies are 8–12 Hz for TUN1, 15–19 Hz for TUN2, and 23–27 Hz for DEF, as defined by the spectral peak in panel C. **F)** Boxplots comparing the CV_{power} distributions across subjects and models. Gray boxes show individual subject values (S1–S4); black boxes show aggregated data across all subjects. For EEG data, all channels are included; for model data, all regions are included. **G)** Distributions of detrended fluctuation analysis (DFA) exponents computed on the amplitude envelope of the dominant oscillation in each configuration, analogous to panel E. **H)** Boxplots comparing DFA exponents across subjects and models, with the same layout as panel F.

Table A.1: **List of cortical regions and number of associated nodes.**
Node counts are reported separately for the left and right hemispheres. The stimulated region (SP, superior parietal cortex, right hemisphere) is highlighted in bold, with the 27 nodes within this region stimulated simultaneously.

Label	**Description**	**Number of nodes**	
		Left	**Right**
BSTS	Bank of the superior temporal sulcus	5	7
CAC	Caudal anterior cingulate cortex	4	4
CMF	Caudal middle frontal cortex	13	13
CUN	Cuneus	8	10
ENT	Entorhinal cortex	3	2
FP	Frontal pole	2	2
FUS	Fusiform gyrus	22	22
IP	Inferior parietal cortex	25	28
IT	Inferior temporal cortex	17	19
ISTC	Isthmus of the cingulate cortex	8	8
LOCC	Lateral occipital cortex	22	19
LOF	Lateral orbitofrontal cortex	20	19
LING	Lingual gyrus	16	17
MOF	Medial orbitofrontal cortex	12	12
MT	Middle temporal cortex	19	20
PARC	Paracentral lobule	11	12
PARH	Parahippocampal cortex	6	6
PCAL	Pericalcarine cortex	9	10
POPE	Pars opercularis	11	10
PORB	Pars orbitalis	6	6
PTRI	Pars triangularis	7	8
PSTC	Postcentral gyrus	30	31
PC	Posterior cingulate cortex	7	7
PREC	Precentral gyrus	36	36
PCUN	Precuneus	23	23
RAC	Rostral anterior cingulate cortex	4	4
RMF	Rostral middle frontal cortex	19	22
SF	Superior frontal cortex	50	46
SP	**Superior parietal cortex**	**27**	**27**
ST	Superior temporal cortex	29	28
SMAR	Supramarginal gyrus	19	16
TP	Temporal pole	4	3
TT	Transverse temporal cortex	4	3

Table A.2: **TVB and Larter & Breakspear parameters**.
TUN column reports the parameters of the LB model tuned as described in the paper, starting from the default (DEF) configuration in Alstott et al. (2009). Parameter values that differ between the two configurations are indicated in bold, and reported before the unchanged ones. The first block of rows refers to the global parameters of the TVB simulator (notice the rescaling of some of them, as a straight consequence of the time rescaling in single-node equations), followed by parameters specific to the LB model.

Parameter	Description	Values	
		TUN	**DEF**
$\boldsymbol{G}$	**Global coupling strength**	**3**	**1**
$\boldsymbol{c_v}$	**Conduction velocity**	$\mathbf{3 \cdot t_{scale}}$	$\mathbf{3 \cdot t_{scale}}$
$\boldsymbol{\sigma_\xi}$	**Heun integrator noise**	$\mathbf{10^{-7} \cdot t_{scale}}$	$\mathbf{10^{-7} \cdot t_{scale}}$
$\boldsymbol{t_{scale}}$	**Timescale factor**	**0.6**	**1**
$\boldsymbol{V_{Ca}}$	**Ca Nernst potential**	**1.1**	**1.0**
$\boldsymbol{a_{e\to e}}$	**Excitatory-to-excitatory synaptic strength**	**0.5**	**0.4**
$\boldsymbol{g_K}$	**Conductance of K channels population**	**2.5**	**2.0**
$\boldsymbol{g_L}$	**Conductance of leak channels population**	**1.1**	**0.5**
$\boldsymbol{a_{n\to i}}$	**Non-specific-to-inhibitory synaptic strength**	**L: 0.4023; R: 0.4**	**0.4**
$\boldsymbol{T_{Na}}$	**Threshold potential for Na channels**	**0.26**	**0.30**
$\boldsymbol{\delta_K}$	**Variance of K channels threshold**	**0.4**	**0.3**
$\boldsymbol{V_T}$	**Threshold potential for excitatory neurons**	**-0.1**	**0.0**
$\boldsymbol{\delta_Z}$	**Variance of inhibitory threshold**	**0.60**	**0.65**
g_{Ca}	Conductance of population of Ca channels	1.1	1.1
r_{NMDA}	Ratio of NMDA to AMPA receptors	0.25	0.25
g_{Na}	Conductance of population of Na channels	6.7	6.7
V_{Na}	Na Nernst potential	0.53	0.53
V_{K}	K Nernst potential	-0.7	-0.7
V_{L}	Nernst potential of leak channels	-0.5	-0.5
$a_{i\to e}$	Inhibitory-to-excitatory synaptic strength	2.0	2.0
$a_{n\to e}$	Non-specific-to-excitatory synaptic strength	1.0	1.0
I	Subcortical input strength	0.3	0.3
b	Time constant scaling factor	0.1	0.1
$a_{e\to i}$	Excitatory-to-inhibitory synaptic strength	1.0	1.0
T_{Ca}	Threshold potential for Ca channels	-0.01	-0.01
T_{K}	Threshold potential for K channels	0	0
δ_{Ca}	Variance of Ca channels threshold	0.15	0.15
δ_{Na}	Variance of Na channels threshold	0.15	0.15
ϕ	Temperature scaling factor	0.7	0.7
τ_{K}	Time constant for K relaxation time	1	1
$Q_{\mathrm{V}_{\mathrm{max}}}$	Max firing rate for excitatory populations	1	1
δ_{V}	Variance of excitatory threshold	0.65	0.65
$Q_{\mathrm{Z}_{\mathrm{max}}}$	Max firing rate inhibitory populations	1	1
Z_{T}	Threshold potential for inhibitory neurons	0	0
C	Strength of excitatory coupling and balance between internal and global dynamics	0.1	0.1

2.3 Article 3

Title: *Investigating the Impact of Local Manipulations on Brain Complexity Indices: A Large-Scale Computational Model*

Authors: ***Gianluca Gaglioti***, **Thierry Ralph Nieus***, Marcello Massimini, Simone Sarasso*

Abstract: *Brain complexity relies on the integrity of structural and functional brain networks, where specialized areas synergistically cooperate on a large scale. Local alterations within these areas can lead to widespread consequences, leading to a reduction in overall network complexity. Investigating the mechanisms governing this occurrence and exploring potential compensatory interventions is a pressing research focus. In this study, we employed a whole-brain in silico model to simulate the large-scale impact of local node alterations. These were assessed by network complexity metrics derived from both the model's spontaneous activity (i.e., Lempel–Ziv complexity (LZc)) and its responses to simulated local perturbations (i.e., the Perturbational Complexity Index (PCI)). Compared to LZc, local node silencing of distinct brain regions induced large-scale alterations that were paralleled by a systematic drop of PCI. Specifically, while the intact model engaged in complex interactions closely resembling those obtained in empirical studies, it displayed reduced PCI values across all local manipulations. This approach also revealed the heterogeneous impact of different local manipulations on network alterations, emphasizing the importance of posterior hubs in sustaining brain complexity. This work marks an initial stride toward a comprehensive exploration of the mechanisms underlying the loss and recovery of brain complexity across different conditions.*

DOI: *https://doi.org/10.3390/app14020890*

**These authors contributed equally*

applied sciences

MDPI

Article

Investigating the Impact of Local Manipulations on Spontaneous and Evoked Brain Complexity Indices: A Large-Scale Computational Model

Gianluca Gaglioti [1,2,*,†], Thierry Ralph Nieus [3,*,†], Marcello Massimini [1,4,5] and Simone Sarasso [1]

[1] Department of Biomedical and Clinical Sciences, University of Milan, 20157 Milan, Italy; marcello.massimini@unimi.it (M.M.); simone.sarasso@unimi.it (S.S.)
[2] Department of Philosophy 'Piero Martinetti', University of Milan, 20122 Milan, Italy
[3] Core Facility Indaco, University of Milan, 20122 Milan, Italy
[4] IRCCS Fondazione Don Carlo Gnocchi ONLUS, 20162 Milan, Italy
[5] Azrieli Program in Brain, Mind and Consciousness, Canadian Institute for Advanced Research, Toronto, ON M5G 1M1, Canada
* Correspondence: gianluca.gaglioti@unimi.it (G.G.); thierry.nieus@unimi.it (T.R.N.)
† These authors contributed equally to this work.

Abstract: Brain complexity relies on the integrity of structural and functional brain networks, where specialized areas synergistically cooperate on a large scale. Local alterations within these areas can lead to widespread consequences, leading to a reduction in overall network complexity. Investigating the mechanisms governing this occurrence and exploring potential compensatory interventions is a pressing research focus. In this study, we employed a whole-brain in silico model to simulate the large-scale impact of local node alterations. These were assessed by network complexity metrics derived from both the model's spontaneous activity (i.e., Lempel–Ziv complexity (LZc)) and its responses to simulated local perturbations (i.e., the Perturbational Complexity Index (PCI)). Compared to LZc, local node silencing of distinct brain regions induced large-scale alterations that were paralleled by a systematic drop of PCI. Specifically, while the intact model engaged in complex interactions closely resembling those obtained in empirical studies, it displayed reduced PCI values across all local manipulations. This approach also revealed the heterogeneous impact of different local manipulations on network alterations, emphasizing the importance of posterior hubs in sustaining brain complexity. This work marks an initial stride toward a comprehensive exploration of the mechanisms underlying the loss and recovery of brain complexity across different conditions.

Keywords: brain complexity; whole-brain modeling; node silencing; perturbations; Lempel–Ziv complexity; Perturbational Complexity Index

Citation: Gaglioti, G.; Nieus, T.R.; Massimini, M.; Sarasso, S. Investigating the Impact of Local Manipulations on Spontaneous and Evoked Brain Complexity Indices: A Large-Scale Computational Model. *Appl. Sci.* **2024**, *14*, 890. https://doi.org/10.3390/app14020890

Academic Editor: Giulia De Bonis

Received: 21 December 2023
Revised: 10 January 2024
Accepted: 16 January 2024
Published: 20 January 2024

1. Introduction

Over the years, the concept of brain complexity has gained traction within neuroscientific research. In this general framework, brain networks strike an optimal balance between the requirement for functional specialization (differentiation) and that for tight interactions (integration) across modules [1–3]. Within a continuum ranging from segregated subsystems to an entirely homogeneous macrosystem, the brain would fall in between, in a complex regime where functionally differentiated groups of neurons are able to engage in tight reciprocal interactions so that the whole is more than the sum of its parts [4,5].

Recently, this theoretical notion has drawn extensive empirical attention with several human and animal studies proposing empirical estimates of brain complexity [6]. Specifically, a growing body of experimental literature has demonstrated a reliable correlation between complexity measures and the presence or absence of consciousness across different conditions, confirming early theoretical principles [7].

Recently, structural human brain networks, also known as 'connectomes' [8,9], became available thanks to different initiatives like the Human Connectome Project and the UK Biobank Imaging project [10–12]. When such networks are endowed with mathematical models of local excitability in each node, they allow the development of computational models to simulate whole-brain dynamics [13–15]. These models provide a controlled and mechanistic framework to explore a broad spectrum of parameters that are potentially relevant for better understanding global brain properties such as those implicated in brain complexity [2,16].

Most empirical and computational investigations have explored network complexity based on spontaneous neural activity [6]. Such an observational approach can be usefully complemented by a causal approach, whereby stimulations are used to assess the complexity of neuronal interactions from a causal, rather than correlational, perspective. Along these lines, the Perturbational Complexity Index (PCI) [17] empirically estimates the joint presence of differentiation and integration by quantifying the richness of the spatiotemporal patterns of cortical activity extracted from the electroencephalographic (EEG) response to a brief local perturbation with transcranial magnetic stimulation (TMS). PCI has provided a reliable index to assess the loss and recovery of consciousness in both physiological and pathological conditions [18]. Supported by a series of multiscale experiments in cell cultures [19,20], cortical slices [21], animal models [22–24], and intracranial and extracranial human studies [17,18,25–29], this perturb-and-measure approach has also recently been applied in silico. This computational neuroscience implementation can further elucidate the mechanistic link between brain complexity and anatomic-physiological brain properties. Specifically, the relationship between brain complexity and structural connectivity [30,31] as well as functional network properties [32] have been investigated. In addition, the modulations of brain complexity dependent on global neuromodulation [33] as well as local node properties [34] have been recently addressed.

Crucially, it is also possible to link single node properties to large-scale network dynamics [35,36] and explore the global effects of local manipulations, such as virtual lesions [37] and silencing [38].

Previous computational investigations have shown that large-scale spontaneous network dynamics change considerably upon local connectivity alterations (i.e., local node deletion within spatially defined regions) [39]. Along these lines, a strong reduction of brain-wide activity was observed particularly when simulating the regional inactivation of posterior areas [40]. These results are particularly relevant in view of a postulated critical role of posterior regions of the cortex [41,42] in supporting complexity and consciousness. So far, however, computational studies relating local properties to global brain states have focused mostly on spontaneous activity [37] and have not explored the complexity of neuronal interaction from a causal perspective (i.e., using controlled model perturbations).

Here, we exploited direct perturbations and investigated the large-scale impact of controlled local manipulations (i.e., local node silencing) on network activity and brain complexity in a whole-brain computational model. Specifically, using "The Virtual Brain" platform [13,43], we extensively and systematically varied the topology of the stimulated and the silenced nodes and performed a direct comparison between metrics derived from observational (Lempel–Ziv complexity) [44] and perturbational approaches (PCI). In addition, we explored critical properties governing the network information flow [45] and linked specific features of network organization (i.e., integration and segregation) to the above-mentioned network complexity metrics.

Our intact model exhibited complex spontaneous patterns emerging from the structural links of the connectome and engaged in complex and enduring cortical interactions following focal exogenous perturbations closely resembling the empirical TMS-EEG responses. Importantly, node manipulations revealed an overall reduction of network complexity measures, underlining interesting dissociations between observational and perturbational metrics. Interestingly, the impact of local manipulations was highly heterogeneous, and the comprehensive spatial sampling of the implemented node silencing

allowed assessing relevant regional aspects with respect to the role of posterior cortical regions for brain complexity.

Overall, our results aim at better characterizing the effects of local manipulations on large-scale network dynamics and may serve as a useful tool to systematically assess the mechanisms underlying the loss and recovery of brain complexity in pathological conditions.

2. Materials and Methods

2.1. Model Simulations

2.1.1. Structural Connectivity

For the main results of this study, we employed a connectome composed of 76 areas available in the TVB simulator (2.7.2) (named "Default" connectome, Dconn). Dconn is based on an anatomical tracing reconstruction (CoCoMac) [46] with directional connections and is therefore well suited to investigate propagating activities in brain networks [47]. Additionally, we implemented a subset of analyses on a connectome with finer parcellation consisting of 998 areas (named "Hagmann" connectome, Hconn [48]), as described in Section 2.1.5.

2.1.2. Neural Mass Model

To model the mesoscopic dynamics of cortical regions, we used the Larter and Breakspear model [49], a conductance-based neural mass model widely employed for simulating whole-brain dynamics in intact networks [50–58] and lesioned networks [39,59]. According to the model, the dynamics of a node k are governed by the following ordinary differential equations (ODEs):

$$\begin{aligned}\frac{dV^k}{dt} = &-\left(g_{Ca} + (1-C)\, r_{NMDA}\, a_{ee}\, Q_V + C\, r_{NMDA}\, a_{ee}\, Q_V^{network}\right) m_{Ca}(V - V_{Ca}) \\ &-\left(g_{Na}\, m_{Na} + (1-C)\, a_{ee}\, Q_V + C\, a_{ee}\, Q_V^{network}\right)(V - V_{Na}) \\ &- g_K W(V - V_K) - g_L(V - V_L) - a_{ie}\, Z\, Q_Z + a_{ne} I\end{aligned} \quad (1)$$

$$\frac{dZ^k}{dt} = b(a_{ni} I + a_{ie}\, V\, Q_V) \quad (2)$$

$$\frac{dW^k}{dt} = \frac{\Phi(m_K - W)}{\tau_K} \quad (3)$$

where V is the mean membrane potential of the excitatory pyramidal neurons, Z is the mean membrane potential of the inhibitory interneurons, and W is the average number of open potassium ion channels. The term r_{NMDA} is the ratio of NMDA receptors to AMPA receptors, and a_{xy} is the synaptic strength originating from population x (e.g., e, i, n, where e refers to the excitatory population, i to the inhibitory one, and n denotes a nonspecific input) to population y (e.g., e, i). The rate terms b and ϕ govern the time scales of Z and W, respectively. The term g_{ion} is the maximum conductance (i.e., when all channels are open) of the corresponding ion species. The voltage-dependent fractions of open channels for a given ion is determined by m_{ion} and is modeled by a sigmoidal shape function:

$$m_{ion} = 0.5\left(1 + \tanh\left(\frac{V - T_{ion}}{\delta_{ion}}\right)\right) \quad (4)$$

where T_{ion} is the mean threshold membrane potential of a given ion channel population, and δ_{ion} is its standard deviation. The mean firing rates of the excitatory and inhibitory populations are determined by the voltage-dependent activation functions Q_V and Q_Z, respectively, modeled as:

$$Q_V = 0.5\, Q_{Vmax}\left(1 + \tan h\left(\frac{V - V_T}{\delta_V}\right)\right) \quad (5)$$

$$Q_Z = 0.5\, Q_{Zmax}\, (1 + \tan h\left(\frac{V - Z_T}{\delta_{Zq}}\right)) \quad (6)$$

where QV_{max} and QZ_{max} are the maximum firing rates of the excitatory and inhibitory populations, respectively. Their corresponding thresholds for action potential generation are given by the terms V_T and Z_T, with standard deviations δ_V and δ_Z, respectively. The network input to node k is given by:

$$Q_V^{network} = \sum_j G\, u_{kj} Q_V\left(V_j\left(t - \tau_{kj}\right)\right) \quad (7)$$

where u_{kj} is the connection weight from node j to node k, τ is the input delay time, and G is the global coupling that scales the connection weights. The parameter C in Equation (1) ranges within [0, 1] and balances the strength of the self-connections against those of the rest of the network.

The ODEs were solved starting from random initial conditions with the stochastic Heun integration method available in TVB (with additive Gaussian noise, standard deviation SD = 10^{-7}) and an integration time step of 0.1 ms. A pre-processing step was performed to reduce the amount of data by temporally resampling the data to a resolution time of 1 ms (i.e., averaging over each 1 ms time step). In addition, the first 3 s of simulations were discarded (first 14 s in Hconn) to remove the initial transient activities in the model.

In order to improve the responsiveness of the nodes (e.g., propagating activities) to stimulation, we varied a set of parameters (indicated in bold in Table S2) with respect to other studies that investigated only the model's spontaneous activity (e.g., [39]). In addition, we set the global coupling G (Equation (7)) in such a way as to maximize the overlap between the functional and the structural connectivity (Figure 1c, see also [60]).

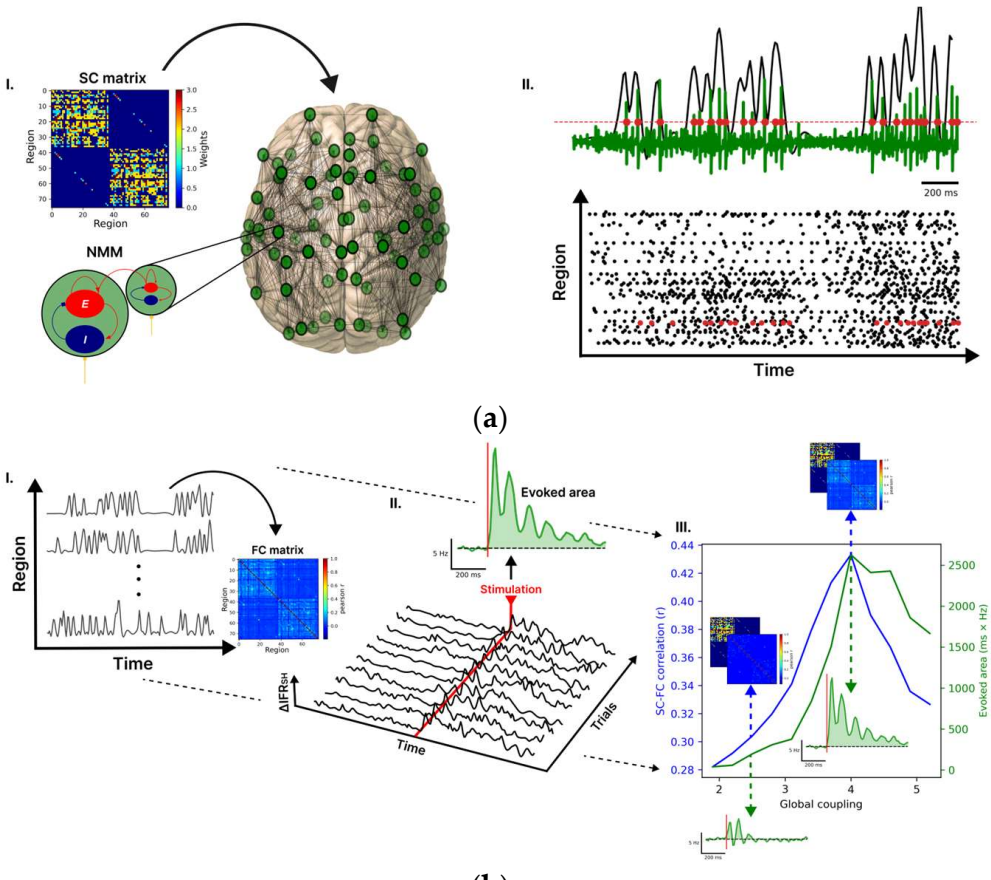

Figure 1. *Cont.*

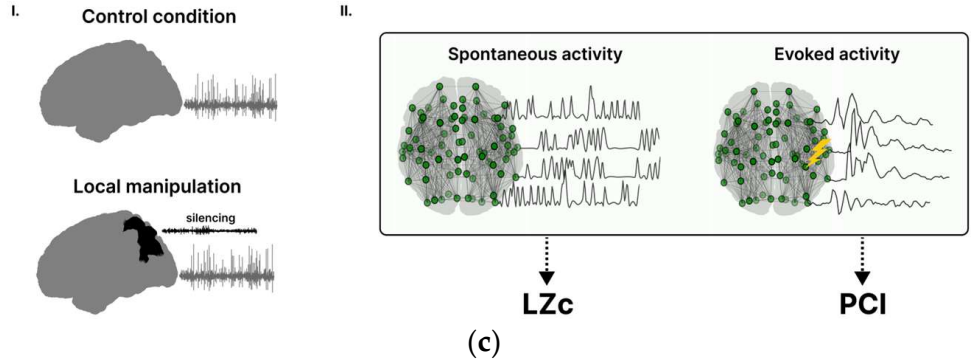

Figure 1. Whole-brain model for investigating brain complexity in silico. (**aI**) Each node of the whole-brain network is modelled by the Larter and Breakspear (LB) neural mass model (NMM), describing the interaction between excitatory (E) and inhibitory (I) neurons. The weights connecting the nodes are reported in the structural connectivity (SC) matrix. (**aII**) The output of the model of a given node is the mean membrane potential of the excitatory population (green trace), and the timing of the spikes (red dots), detected with a hard threshold on the voltage, are then converted to an instantaneous firing rate (IFR) (black overlay trace). (**b**) The working point of the model (i.e., set of model parameters) was obtained based on the spontaneous and evoked activity following three steps. First (**bI**), the correlations between the spontaneous IFR traces were computed to estimate a functional connectivity (FC) matrix. Then, the similarity between the FC and SC matrices was assessed through the Pearson correlation coefficient. Second (**bII**), by stimulating a node of the connectome (here rPCi), the propagation of activity in the network was quantified in terms of ΔIFR_{SH} (ΔIFR averaged over the nodes of the stimulated hemisphere), and some representative trials of ΔIFR_{SH} are reported. The evoked area is obtained as the integral after stimulation (red line, between 0 and 500 ms) of ΔIFR_{SH} averaged across trials. Third (**bIII**), the SC-FC correlation and the evoked area are reported for different global couplings (i.e., a scaling factor of the SC), and both metrics reached a peak at G = 4 (working point). The dashed blue lines and arrows illustrate the matches between the FC and the SC maps for different G values. The dashed green lines and arrows illustrate the evoked area by the stimulus. (**cI**) We simulated control and local manipulation conditions. Local manipulations were implemented by silencing selected nodes. (**cII**) To assess the impact of local node silencing on spontaneous complexity, we calculated Lempel–Ziv complexity (LZc) on ongoing network activity. Furthermore, we separately stimulated different connectome nodes under different local manipulations and calculated the Perturbational Complexity Index (PCI) to gauge the impact of local silencing on the evoked activity.

2.1.3. Spontaneous Activity and Stimulation Protocol

For the analysis of spontaneous activity, each condition was run for 4000 s, and the time-series were split into 10 segments of 400 s.

On the other hand, to examine the model's evoked response, a square wave pulse of 5 ms and amplitude 1 was applied to a single connectome node, specifically targeting the excitatory pyramidal cells (as an additive term to Equation (1)). In our study, we individually stimulated a total of 12 nodes located in the right hemisphere (see Section 2.1.4 below for details), homogeneously sampling all cortical lobes (Table 1).

In all conditions (control and lesions) a stimulus was delivered to the same node (i.e., same stimulus) 500 times (500 trials) by reinitializing each simulation. We also jittered the onset of the stimulus within a range of 2 s. Note that in the Larter–Breakspear model, all quantities are dimensionless except for time [56], which allows a straight comparison with the experimental time courses.

Table 1. Labels of the cortical nodes and their description in Dconn. The stimulated nodes are reported in bold.

Label	Description
A1	Primary auditory cortex
A2	Secondary auditory cortex
Amyg	Amygdala
CCa	Anterior cingulate cortex
CCp	Posterior cingulate cortex
CCr	Retrosplenial cingulate cortex
CCs	Subgenual cingulate cortex
FEF	Frontal eye field
G	Gustatory area
HC	Hippocampal cortex
IA	Anterior insula
IP	**Posterior insula**
M1	Primary motor area
PCi	**Inferior parietal cortex**
PCip	**Cortex of intraparietal sulcus**
PCm	Medial parietal cortex (i.e. precuneus)
PCs	**Dorsal parietal cortex (superior parietal lobule)**
PFCcl	**Centrolateral prefrontal cortex**
PFCdl	**Dorsolateral prefrontal cortex**
PFCdm	Dorsomedial prefrontal cortex
PFCm	Medial prefrontal cortex
PFCorb	**Orbitofrontal cortex**
PFCpol	**Pole of prefrontal cortex**
PFCvl	Ventrolateral prefrontal cortex
PHC	Parahippocampal cortex
PMCdl	Dorsolateral premotor cortex
PMCm	**Medial premotor cortex (i.e. supplementary motor area)**
PMCvl	Ventrolateral premotor cortex
S1	Primary somatosensory cortex
S2	**Secondary somatosensory cortex**
TCc	**Central temporal cortex**
TCi	Inferior temporal cortex
TCpol	Pole of temporal cortex
TCs	Superior temporal cortex
TCv	Ventral temporal cortex
V1	Primary visual cortex
V2	**Secondary visual cortex**

2.1.4. Local Manipulation Modeling

Building upon prior modeling studies [38,40,61], we simulated local network alterations by reducing the excitability of selected nodes. This silencing was achieved by hyperpolarizing the manipulated nodes (Figure 1c) to an extent which completely suppresses their firing activity (mean firing rate = 0). To achieve this, we abolished the excitatory nonspecific input (ane = 0) and increased the nonspecific inhibitory input (ani = 0.6). We implemented the different manipulations in one hemisphere (the right hemisphere) to simulate an affected hemisphere and an intact one (left hemisphere). Consistent with empirical studies [27], we stimulated the affected hemisphere to assess cortical reactivity following perturbation near the silenced node.

In line with previous work where 5% of the nodes were lesioned [39], in our study each manipulation involved approximately 4% of the connectome nodes (three nodes). As in [39], each local manipulation was defined by first choosing a central node (center of the manipulation) to be silenced and then selecting the remaining nodes to silence based on a geometrical distance criterion (Euclidean distance) from the central node. Manipulation details are reported in Table 2. Whenever the stimulated and manipulated nodes overlap, the latter were replaced with the closest non-manipulated nodes to the center of the manipulation. For instance, when stimulating rPCip, which was also part of local manipulation 1 (L1), we spared rPCip and silenced the next closest node (rV2). For a fair comparison across conditions between spontaneous and evoked metrics, non-identical manipulations were excluded whenever a correlation was performed (e.g., in Table S4 in Supplementary Material).

Table 2. Local manipulation labels in the Dconn connectome. The labels of the local manipulations and the corresponding nodes silenced in the Dconn connectome. The ranking is based on the MFR difference (from lowest to highest). Note that when a stimulus overlaps with a silenced node (in bold), the latter is replaced by a nearby node.

Local Manipulation Label	Nodes	Ranking (MFR_{Δ})
L1	**PCip, PCs**, PCm	10
L2	**PFCcl, PFCdl**, PMCvl	7
L3	**TCc**, TCs, TCi	4
L4	**V2**, V1, CCr	18
L5	CCs, **PFCorb**, Amyg	19
L6	CCa, CCp, CCr	13
L7	M1, S1, PMCdl	5
L8	PCm, **PCip**, CCp	15
L9	PFCdm, CCa, PFCm	11
L10	A1, A2, **S2**	16
L11	Amyg, PHC, CCs	17
L12	HC, PHC, TCv	2
L13	**PFCpol**, PFCm, PFCdm	9
L14	PFCvl, G, PMCvl	8
L15	TCpol, Amyg, **PFCorb**	20
L16	CCa, PFCdm, **PFCdl**	12
L17	IP, TCs, **S2**	14
L18	S1, M1, **PCs**	3
L19	**PFCdl**, CCa, **PFCcl**	6
L20	TCv, PHC, TCi	1

This procedure resulted in a total of 12 control conditions (stimulations without any node manipulation) and 240 manipulation conditions (silencing of 20 different nodes for each stimulation, 12 × 20).

2.1.5. Validation on a Larger Connectome (Hconn)

As a proof of concept aimed at confirming the validity of the observed findings, we repeated the analysis pertaining to PCI using a connectome endowed with finer parcellation (Hconn) consisting of 998 areas [48]. Hconn corresponds to a human connectome, with symmetric bidirectional connections, and has been used in several studies [39,51,56,62]. We tested a control condition and 20 local node manipulations, which are detailed in Table S3 (Supplementary Material). Each of them involved approximately 4% of the nodes (40 nodes), and the implementation procedure was the same as in Section 2.1.4 (with the only exception being that in Dconn, ani = 0.6, while in Hconn, ani = 0.65, as more inhibition was required to suppress firing activity). In Hconn, we limited the number of stimulations to one performed over a portion of the superior parietal cortex (SP, Table S1 in Supplementary Material) of the manipulated hemisphere. In particular, to maintain a comparable fraction of stimulated nodes with the Dconn connectome (1/76 = 0.013), a total of 14 nodes of SP were simultaneously stimulated (14/998 = 0.014) that were chosen based on their adjacency to a central node, following the same geometrical approach used in Section 2.1.4. As in Dconn, the stimulus was delivered 500 times (500 trials) in each condition (see Section 2.1.3).

2.2. Analysis of Network Simulations

2.2.1. Firing Activity Analysis

The first step of all analysis consisted in the detection of spiking activity of all nodes of the network. Spike timing was established as the passage of membrane potential of the nodes above a fixed threshold (−0.05, Figure 1a).

We defined the mean firing rate for each region/node of interest (MFR_{ROI}) as the amount of spikes divided by the time window of observation.

To characterize the global/population activity of the model (MFR), we averaged the MFR_{ROI} values across nodes (either all nodes or, when specified, the ones of the intact or the manipulated hemisphere):

$$MFR = \langle MFR_{ROI} \rangle_{nodes} \tag{8}$$

Then, to quantify the impact of the local manipulation on activity, we defined the MFR difference (MFR_{Δ}) as:

$$MFR_{\Delta} = MFR(\text{local manipulation}) - MFR(\text{control}) \tag{9}$$

where MFR(condition) refers to the MFR in a condition of interest. Note that the MFR_{Δ} involved only the nodes not affected by the local manipulation (i.e., excluding the silenced nodes also in the control condition).

Then, for each node we defined the time-dependent Instantaneous Firing Rate (IFR(t), in Hz) as the frequency of spikes in a time window of 25 ms, and the temporal dependence was obtained by sliding the time window by 10 ms on the simulated data. We varied the size of the time window (e.g., 50 ms) and found qualitatively similar results.

In order to quantify the impact of the stimulation on the node's activity, we defined the quantities:

$$\Delta IFR(t) = IFR(t, \text{ trial}) - \langle IFR(t, \text{ trial}) \rangle_{(t<0)} \tag{10}$$

$$\langle \Delta IFR(t) \rangle = \langle \Delta IFR(t, \text{trial}) \rangle_{\text{trials}} \tag{11}$$

where $<IFR(t, \text{ trial})>_{(t<0)}$ is the average IFR over the time prior to stimulation, and $<\Delta IFR(t)>_{\text{trials}}$ is the average ΔIFR across trials.

The level of network synchrony was quantified through the averaged pairwise cross-correlation between the spontaneous IFR signals:

$$CC_{IFR} = \left\langle \frac{Cov(IFR_i, IFR_j)}{\sigma(IFR_i)\ \sigma(IFR_j)} \right\rangle \quad (12)$$

where <. . .> denotes the average over all possible pairs of nodes (excluding silenced nodes), $Cov(IFR_i, IFR_j)$ is the covariance between two spontaneous IFR signals (IFR_i, IFR_j), and $\sigma(IFR_i)$, $\sigma(IFR_j)$ are the corresponding standard deviations of the IFR signals

2.2.2. Network Analysis

We employed graph metrics based on the weighted degree to assess the centrality of a node in the network [63]. In the Dconn connectome, we computed the weighted out-degree (WD) of each node (sum of weighted outgoing connections of a node) in order to analyze the relationship between network centrality and complexity index topographies (see below, Sections 2.2.3 and 2.2.4). Notice that in symmetrical graphs, such as Hconn and non-directional functional connectivity (see below), the out-degree of a node is equal to its in-degree.

We computed the same quantities on the spontaneous functional connectivity (FC) in the control condition. The strengths of the functional connections between node pairs were obtained as the pairwise Pearson's correlation coefficient between their spontaneous instantaneous firing rates (IFRs). In addition, to corroborate our findings, we computed the FC_{BOLD} on the BOLD signal, a widely used approach in the literature with this model [39,50,51,56–58]. The BOLD signal was estimated from the model's output following [39]. We used the nonlinear Balloon–Windkessel hemodynamic model [64], and the input to the model was the absolute value of the time derivative of the excitatory membrane potential within each node. All the hemodynamic parameters were taken from [64]. Lastly, the estimated BOLD signal was sampled every 2 s. The FC_{BOLD} is defined as the Pearson correlation coefficient between each pair of BOLD signals. Then, similar to the SC analysis, we used the WD from the FC_{IFR} and the FC_{BOLD} to investigate the relationship between node centrality and complexity topographies. We also conducted the analysis by performing global signal regression (GSR) on the BOLD signal [51].

2.2.3. Complexity Indices

- Lempel–Ziv Complexity

The spatiotemporal differentiation of the spontaneous instantaneous firing rate was calculated by the Lempel–Ziv complexity (LZc) [44]. The optimal time window to compute LZc was examined by selecting temporal segments of variable lengths (from 1 s to 800 s). LZc decreased when increasing the temporal segments and reached a plateau around 200 s, and starting from 400 s, the variability, quantified by the coefficient of variation (CV), was less than 0.0004. For each condition, we calculated LZc over 10 segments of spontaneous activity (400 s each) and reported its mean ± SD.

- Perturbational Complexity Index

The Perturbational Complexity Index (PCI) quantifies the spatiotemporal complexity of brain activity evoked by an external perturbation [17]. To compute PCI, we followed the procedure outlined in [17], with the notable difference that we applied it to the IFR time series of the brain nodes.

In short, the significant evoked activities of each node, with respect to baseline, were determined by applying a non-parametric permutation test to the IFR. The baseline activity (pre-stimulus, time window = [−1000, 0 ms]) was used to determine, for each node, thresholds of significance (significance level set to 0.01, 500 bootstraps) and accounting for multiple comparison testing using the maximum test statistic. In this way, we derived a spatiotemporal matrix of significant activity [SS(x,t)], where SS(x,t) = 1 for significant

activity in node x at time t, and SS(x,t) = 0 otherwise. The SS matrix was then sorted according to the amount of significant activity during the post-stimulus interval of each node (e.g., most/less active at the bottom/top rows). Then, the Lempel–Ziv complexity (CL) was calculated on the binary matrix [SS(x,t)] of the significant IFR (first 500 ms after the pulse).

Finally, PCI^{LZ} is defined as the normalized CL of the evoked spatiotemporal patterns SS(x,t):

$$PCI = CL \cdot \frac{\log_2(L)}{(L \cdot Hsrc(L))} \quad (13)$$

where L is the size of the matrix [SS(x,t)] (L = number of nodes × number of time samples), and Hsrc is the source entropy given by:

$$Hsrc(L) = -p_1 \cdot \log_2(p_1) - (1 - p_1) \cdot \log_2(1 - p_1) \quad (14)$$

where p_1 and $(1 - p_1)$ are the fraction of "1" (significant activity) and "0" (non-significant activity) in the binary matrix.

Spatial temporal maps were represented based on SS and the <ΔIFR(t)> (Equation (10)). In particular, for each time point t, the ΔIFR(t) of the nodes with significant activity (i.e., SS(., t) = 1) were reported.

In all conditions (control and manipulations), each stimulus was repeated 500 times. Then, 10 resamples of 300 trials (without repetitions) were formed, and the PCI was computed on each subgroup. We assessed the stability of PCI versus the number of trials (ranging from 10 to 500 trials) and observed that the PCI values reached a plateau around 200 trials, and starting from 300 trials, the variability (CV) was less than 0.01.

2.2.4. Complexity Topographies

The contribution of each node to the complexity indices used was investigated by performing linear regressions between the complexity values (LZc and PCI) and the spontaneous activity of each node (MFR_{ROI}) for different conditions (local manipulations and control). The coefficient of determination (R^2) for each node was then computed and mapped onto the brain topographies. Thus, LZc-R^2 and PCI-R^2 topographies were derived. Given the 12 stimulation sites for PCI, 12 topographies were generated, which were then averaged into a single PCI-<R^2> topography.

2.2.5. Statistical Analysis

Statistical analyses were performed using Python 3.7, employing the SciPy (1.9.3), statsmodels (0.13.5), and scikit-posthocs (0.8.1) packages. The data are expressed as mean ± standard deviation (SD) unless otherwise indicated. The boxplots report the first and third quartiles (lower/upper line of the box), the mean of the distribution (horizontal line in the box), and the whiskers (5th and 95th percentiles). The data were checked for normal distribution and homogeneity of variance using Shapiro–Wilk test and Levene test, respectively. According to the results, either parametric (e.g., one-way ANOVA and *t*-test) or non-parametric (e.g., Kruskal–Wallis H-test and Dunn's test) tests were performed. *p* values were adjusted for multiple comparisons using the Benjamini–Hochberg method to control the false discovery rate. Multiple one-sample *t*-tests were conducted with Bonferroni–Holm *p*-values correction to test the impact of each local manipulation compared with the control. Linear correlation between the metrics was computed with the Pearson correlation coefficient and its associated two-sided *p*-value. We conducted simple and multivariate linear regressions, calculating the coefficient of determination (R^2, and $R^2_{adjusted}$ to account for multiple regressors) and the *p*-value of the F-statistic. Additionally, we computed the slope coefficients of the regressors and their corresponding two-sided 95% confidence intervals (95% CI). For all statistical analyses, alpha = 0.05.

3. Results

3.1. Spontaneous Activity

Impact of Local Node Silencing on Spontaneous Complexity Measures

We first investigated the impact of local silencing on the model's spontaneous activity by quantifying the mean firing rate difference (MFR_Δ) on the nodes within the manipulated hemisphere, the intact one, as well as in the entire model compared with the same nodes in the control condition (Figure 2a). This analysis revealed that the MFR decreased the most in the affected hemisphere ($MFR_\Delta = -3.621 \pm 1.629$ Hz, mean across all manipulations ± SD) and to a lesser extent in the intact hemisphere (-1.431 ± 0.992 Hz).

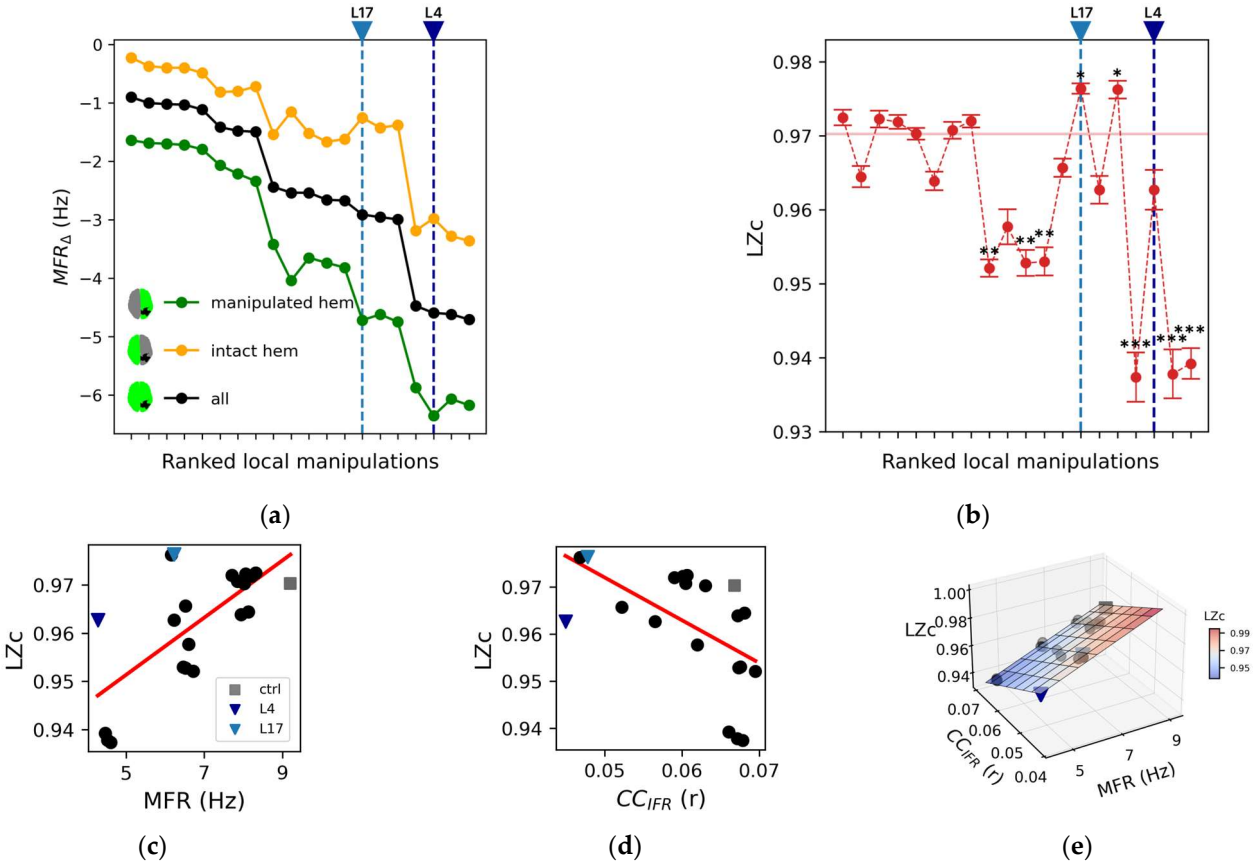

Figure 2. Impact of local manipulations on whole-brain spontaneous activity. (**a**) Mean firing rate difference (MFR_Δ, see Methods) for each silencing condition of the manipulated hemisphere (green), the intact one (yellow), and overall nodes (black). Note that the ranking (i.e., ranked local manipulations, see Table 2) is based on the black curve. (**b**) The Lempel–Ziv complexity (LZc) metric is reported versus the same ranked local manipulations. The red horizontal lines mark the average value of LZc in the control condition. Error bars represent one standard deviation and asterisks indicate a statistically significant difference from the control condition (* $p < 0.05$, ** $p < 0.01$, *** $p < 0.001$; Kruskal–Wallis and Dunn post hoc test with Benjamini–Hochberg correction). (**c**) Linear regressions relating the mean firing rate of all nodes (MFR) to LZc (r = 0.69; $p = 0.0005$). (**d**) Linear regression relating the averaged pairwise cross-correlation (CC_{IFR}) to LZc (r = −0.55, $p = 0.009$). (**e**) Multivariate regression of LZc with respect to the independent variables MFR and CC_{IFR} ($R^2 = 0.98$, $R^2_{adjusted} = 0.98$, $p = 2 \times 10^{-16}$).

We then quantified the impact of local node silencing on the complexity of spontaneous brain dynamics by computing Lempel–Ziv complexity (LZc) on the instantaneous firing rate (IFR) derived from the model time-series (Figure 2b). Notably, in 12 out of 20 local manipulations, LZc was not statistically different from control (Kruskal–Wallis and Dunn post hoc test with Benjamini–Hochberg correction). As a consequence, even though LZc

positively correlated with MFR (LZc: r = 0.69; $p = 0.0005$, Figure 2c), it did not reflect the changes of network complexity with respect to control condition.

Further exploring the network properties relevant for complexity, we computed the averaged pairwise cross-correlation (CC_{IFR}, see methods) between nodes as a measure of the synchrony of network interactions. CC_{IFR} was lower across local manipulations when compared to control (control: 0.067, average across manipulations: 0.061 ± 0.007; Figure 2d), which corresponds to a larger segregation of the network patterns. We found a negative correlation between LZc and CC_{IFR} (r = −0.55, $p = 0.009$; Figure 2d).

Considering the combined role of brain activity levels (MFR) and network interactions (CC_{IFR}) in shaping brain complexity, we performed a multivariate regression between MFR and CC_{IFR} in explaining LZc across all conditions (Figure 2e). This model effectively captured the variance of LZc ($R^2 = 0.98$, $R^2_{adjusted} = 0.98$, $p = 2 \times 10^{-16}$). Confirming the results obtained with the univariate analyses, a positive relationship was found for LZc with respect to MFR (slope coefficient, $\beta_{MFR} = 0.0072$, 95% CI [0.0066, 0.0078]), while CC_{IFR} was found to be negatively correlated with LZc ($\beta_{CC} = -1.2$, 95% CI [−1.3, −1.1]).

3.2. Evoked Activity

3.2.1. Local Node Silencing and PCI

We performed an extensive investigation of the responses to different stimuli for different node silencing within the connectome (12 stimuli × 20 manipulations). The impact of local node silencing on stimulus-evoked spatiotemporal activity was quantified by the Perturbational Complexity Index (PCI).

All manipulations caused a decrease of PCI with respect to the control condition (PCI_Δ) across stimuli (for each local manipulation $p < 0.01$, one sample t-test with Bonferroni–Holm correction; Figure 3a), albeit with a great variability depending on the specific stimulus-silencing pair (individual PCI values and statistical comparisons with respect to the control condition are reported in Figure S2).

In this respect, the responses of the model to stimulation of the right inferior parietal cortex (rPCi) for the control and two highly segregated local manipulations (L4 and L17, see Table 2 for a description of the manipulated nodes) serve as an illustrative example of such variability.

Specifically, the spatiotemporal distribution of the significant activities (see Methods) elicited by the stimulation pulse in the control and in the two representative manipulations displayed marked differences (Figure 3b). In particular, compared to the control condition, in the case of L4 silencing, the response was sustained in time but spatially redundant (i.e., the significant activities often involved the same areas), and it did not involve the non-stimulated hemisphere as confirmed by the <ΔIFR> temporal profile (Figure 3c top panel). On the other hand, in the case L17 silencing, significant evoked activity extended to the non-stimulated hemisphere (Figure 3c top panel) but was short-lived. The richness of the significant spatial-temporal patterns evoked by a stimulus can also be described by the SS matrices (see Methods, Figure 3c bottom panels). Compared to the control condition, the SS matrix of both L4 and L17 were either restricted in space (i.e., evoked activity remained more local, as in L4) or in time (i.e., the significant evoked activity decayed rapidly, as in L17). Interestingly, in L4, the significant activity described by the source entropy (Hsrc) was comparable to the control (0.79 ± 0.03 and 0.79 ± 0.02, respectively), but the evoked activity was more redundant in time (compare Figure 3a), confirming the dissociations between PCI and Hsrc (Supplementary Results, Section S2, Figure S3) also found in empirical studies [17]. Consistent with these observations, we found a significant reduction of PCI ($p < 0.00001$, ANOVA and post hoc pairwise T t-test with Benjamini–Hochberg correction) for both L4 and L17 (Figure S2, grey arrows. Control: 0.49 ± 0.03; L4: 0.25 ± 0.01; L17: 0.37 ± 0.04).

Furthermore, to corroborate our results, we performed a similar analysis with the more detailed connectome, Hconn (Figure S4A,B). Again, we found a significant reduction of PCI (Figure S4C) in all manipulation conditions (for each $p < 0.000001$, ANOVA and post hoc pairwise T t-test with Benjamini–Hochberg correction). The higher reduction of PCI

with Hconn compared to Dconn is likely due to a larger impact of node silencing on the local connectivity (i.e., areas surrounding the manipulation) as well as on the long-range connections reducing the communication between areas that are far apart.

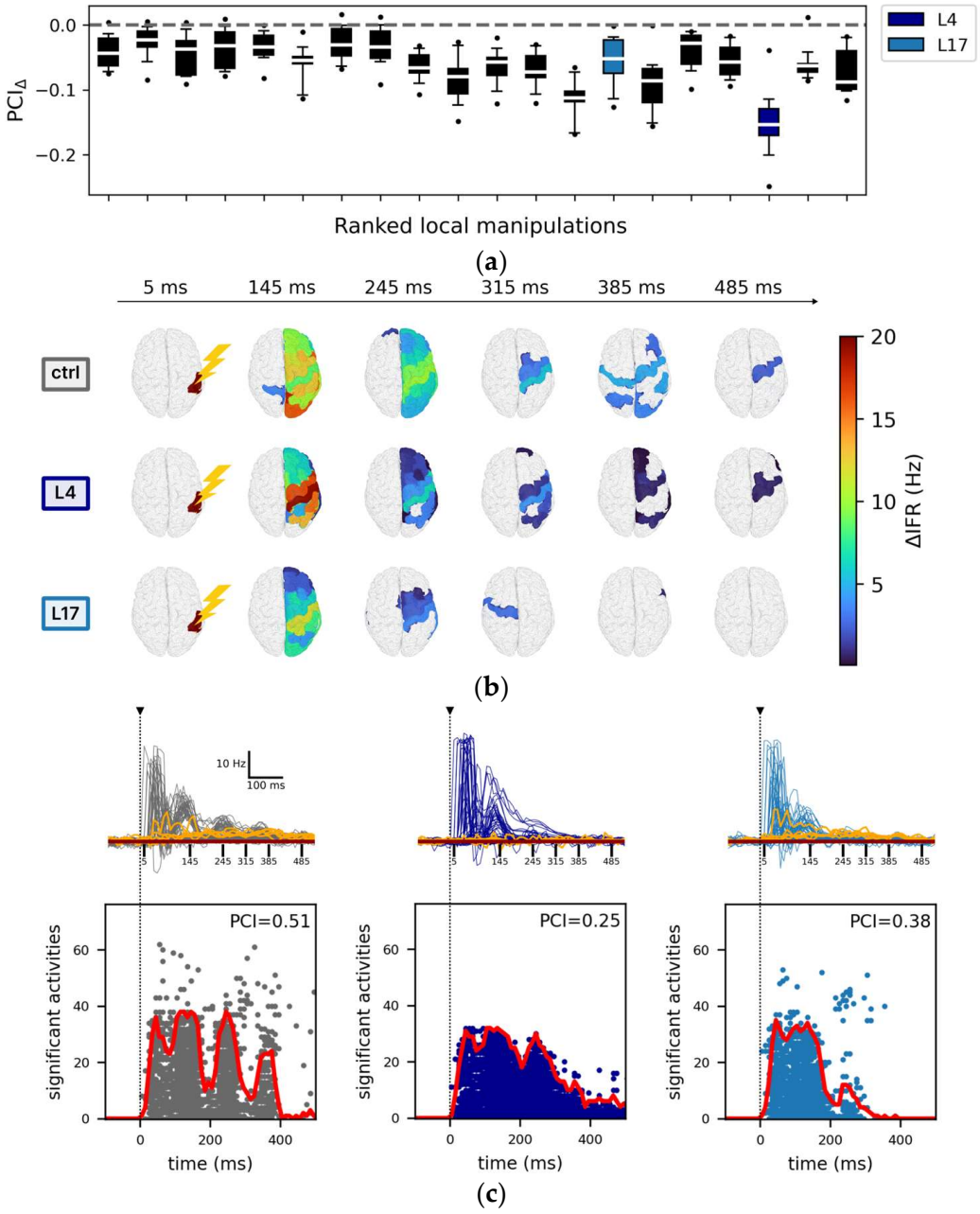

Figure 3. Impact of local manipulations on evoked activity. (**a**) Each box, corresponding to a local manipulation (ordered according to the ranking in Figure 2), displays the difference in PCI compared to the control (PCI$_\Delta$) for a given stimulation site (12 values per box, e.g., stimulation of rPCi: PCI$_\Delta$ (local manipulation) = <PCI$_{\text{local manipulation}}$> − <PCI$_{\text{ctrl}}$>, where <. . .> indicates mean across resamples). For each local manipulation, $p < 0.01$ (one sample *t*-test against mean zero with Bonferroni–Holm correction). (**b**) Spatiotemporal distribution of the areas with significant changes of their firing rate with respect to baseline activity following stimulation. Representative snapshots are reported at time t = 5 ms, t = 145 ms, t = 245 ms, t = 285 ms, t = 375 ms, and t = 485 ms in the control condition (top row), for the local manipulations L4 (middle row), and L17 (bottom row). (**c**) Top: the temporal courses of the instantaneous firing rate (<ΔIFR>) are reported for all nodes and separately for the representative conditions: ctrl (grey), L4 (dark blue), and L17 (light blue). For each condition,

the highest five <ΔIFR> (quantified as the total activity in the interval [0, 500] ms) of the non-stimulated hemisphere (orange traces) are also reported. The horizontal brown line indicates the mean baseline (defined as <ΔIFR(t)> averaged over the interval [−1000, 0] ms and over the latter highest five <ΔIFR(t)>). The vertical dotted black line marks the time of the stimulus, and the vertical continuous black lines are relative to the snapshots reported in panel b. Bottom: the corresponding sorted binary spatiotemporal matrices of significant activities highlight the impact of the local manipulations with respect to the control condition (the red line is the sum of significant activity over time). The Perturbational Complexity Index (PCI) decreases significantly ($p < 0.00001$, ANOVA and post hoc pairwise T test with Benjamini–Hochberg correction) in L4 and L17 compared with control (see Figure S2).

3.2.2. The Impact of Regional Silencing on PCI

By taking advantage of the systematic and extensive investigation of stimulation/silencing pairs, we further explored the variability of the impact of local silencing on both spontaneous and evoked metrics and investigated the contribution of individual region activity (i.e., MFR) to PCI across all conditions. Thus, for each stimulation, we performed a linear regression of the PCI values (i.e., mean across resamples) versus the spontaneous mean firing rate of a node/region of interest (MFR_{ROI}) across all conditions (including the control condition and all local manipulations). Figure 4a shows the linear regressions for two representative ROIs (right posterior cingulate cortex; rCCp and right parahippocampal cortex; rPHC), corresponding to the ROIs showing the third highest and third lowest average correlations across stimuli, respectively. For each of the two ROIs, we show two representative stimulations delivered to the inferior parietal cortex (PCi; $R^2 = 0.59$, $p = 5 \times 10^{-5}$ and $R^2 = 0.02$, $p = 0.58$) and the dorsolateral prefrontal cortex (PFCdl; $R^2 = 0.23$, $p = 0.03$ and $R^2 = 0.01$, $p = 0.60$). We found that PCI correlated well with MFR_{ROI} (CCp) for most stimulations (F-statistic of R^2, 11 with $p < 0.05$, one with $p = 0.051$), ranging from 0.19 to 0.59 (0.41 ± 0.14) (Figure 4b). On the other hand, MFR_{ROI} (PHC) was always non-significantly correlated with PCI across the 12 stimulations ($p > 0.05$).

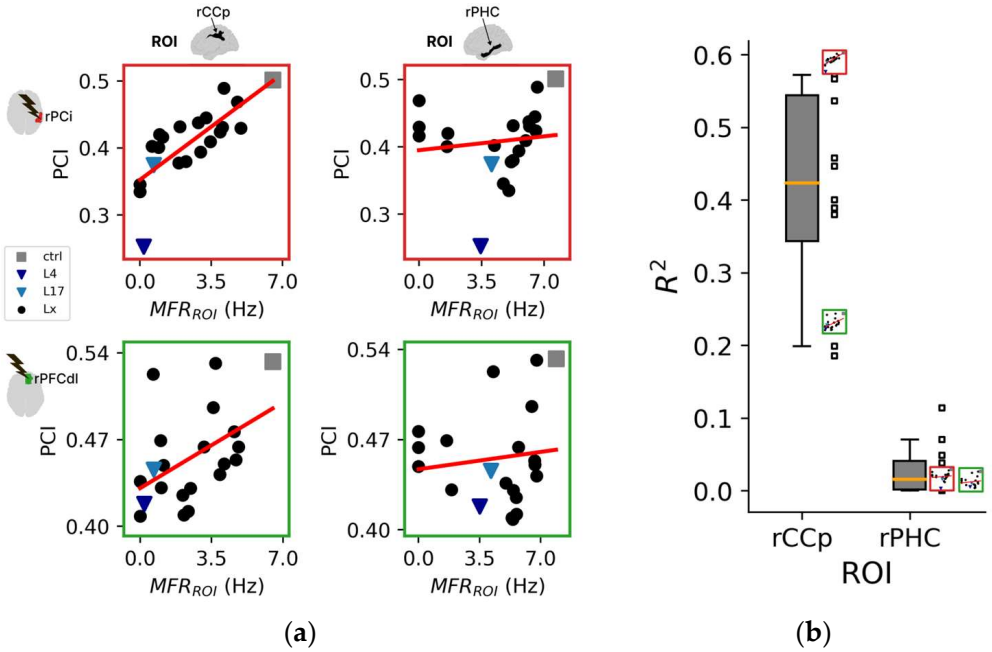

Figure 4. *Cont.*

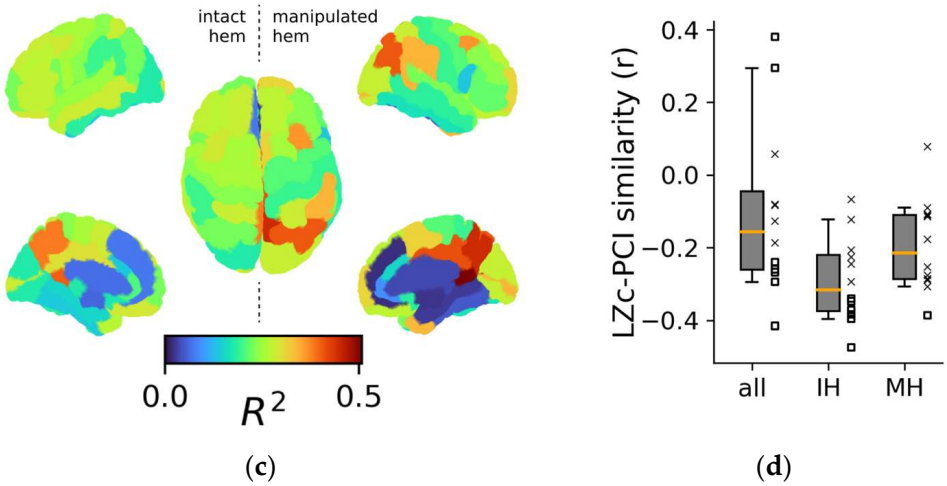

(**c**) (**d**)

Figure 4. Topological aspects of perturbational complexity. (**a**) Linear regressions relating PCI to the spontaneous mean firing rate of the ROIs/nodes rCCp and rPHC for two representative stimulation sites (red boxes: rPCi; green boxes: rPFCdl). (**b**) Boxplot of the R^2 relative to the PCI versus MFR_{ROI} (rCCp) and PCI versus MFR_{ROI} (rPHC) linear regressions for all stimulation sites. Note that the reduced plots of panel A are reported on the right of the boxplot to highlight the corresponding R^2 value. (**c**) Brain topography of the average R^2 across stimulation sites ($<R^2>$). For each ROI in the topography, the corresponding $<R^2>$ is derived as in panel (**b**). (**d**) Distributions of the Pearson correlation coefficients computed across the R^2 topography maps of LZc with PCI and separately for all ROIs (all), intact hemisphere ROIs (IH), and manipulated hemisphere ROIs (MH). Each square and X symbol is relative to a stimulation site, and X markers indicate nonsignificant *p* values (>0.05).

The 12 regional maps of R^2 coefficients for each stimulation are presented topographically in Figure S5A, and the average topography across all stimulations is presented in Figure 4c. Interestingly, the three ROIs with the highest average R^2 across stimulations (i.e., CCr, $<R^2> = 0.51 \pm 0.13$; PCm, $<R^2> = 0.45 \pm 0.14$; CCp, $<R^2> = 0.41 \pm 0.14$) were located in the posterior cortex of the manipulated hemisphere. In addition, the ROIs with the three highest R^2 values across all stimulations were predominantly located in the posterior regions (~89%, Figure S5B,C).

Consistently, we repeated the same analysis for the single stimulation on Hconn and found a similar regional specificity, with the highest R^2 values located in posterior regions of the manipulated hemisphere (Figure S4D).

3.2.3. Assessing Regional Similarity between Spontaneous and Evoked Complexity Metrics

We performed separate linear regressions for MFR_{ROI} versus LZc (Figure S6A,B) and computed the similarity between the R^2 topography maps of these and the 12 R^2 PCI topographies for each stimulation (Figure 4d). We found that the correlations between PCI and LZ topographies were anti-correlated (-0.1 ± 0.23), though many correlations were not significant (5 out of 12). Similar results were obtained when restricting the analysis to either the intact or the manipulated hemisphere (-0.29 ± 0.11 and -0.19 ± 0.12, respectively).

3.3. Assessing the Relationship between Complexity Measures and Graph Properties

We explored the relationship between the R^2-topographies derived from spontaneous (LZc) as well as perturbational complexity (PCI) measures and basic graph properties. To this aim, we correlated the weighted degree (WD) of each node (an index of network centrality calculated both on SC and FC) with the corresponding values of the complexity-R^2 topographies (Figure 5). The WD computed on the SC showed a weak, albeit significant, correlation with the PCI average-R^2 topography across the 12 stimulations ($r = 0.34$, $p = 0.0026$; Figure 5a). Conversely, we did not find a significant correlation with the LZc-R^2 topography ($p = 0.063$, Figure 5b). Similarly, we found a significant correlation between the

WD computed on the SC and the PCI-R^2 topography applied to Hconn (r = 0.44, $p = 2 \cdot 10^{-49}$; Figure S7A). Further, we found even more robust correlations between WD calculated on FC and the average PCI-R^2 topography (r = 0.6, $p = 10^{-8}$, Figure 5c). Again, no significant relationship was found between WD and the LZc-R^2 topography ($p = 0.5$, Figure 5d). Similar results (Figure S7B–E) were obtained when using WD calculated on the FC derived from BOLD signals ($FC_{BOLD;}$ see Section 2).

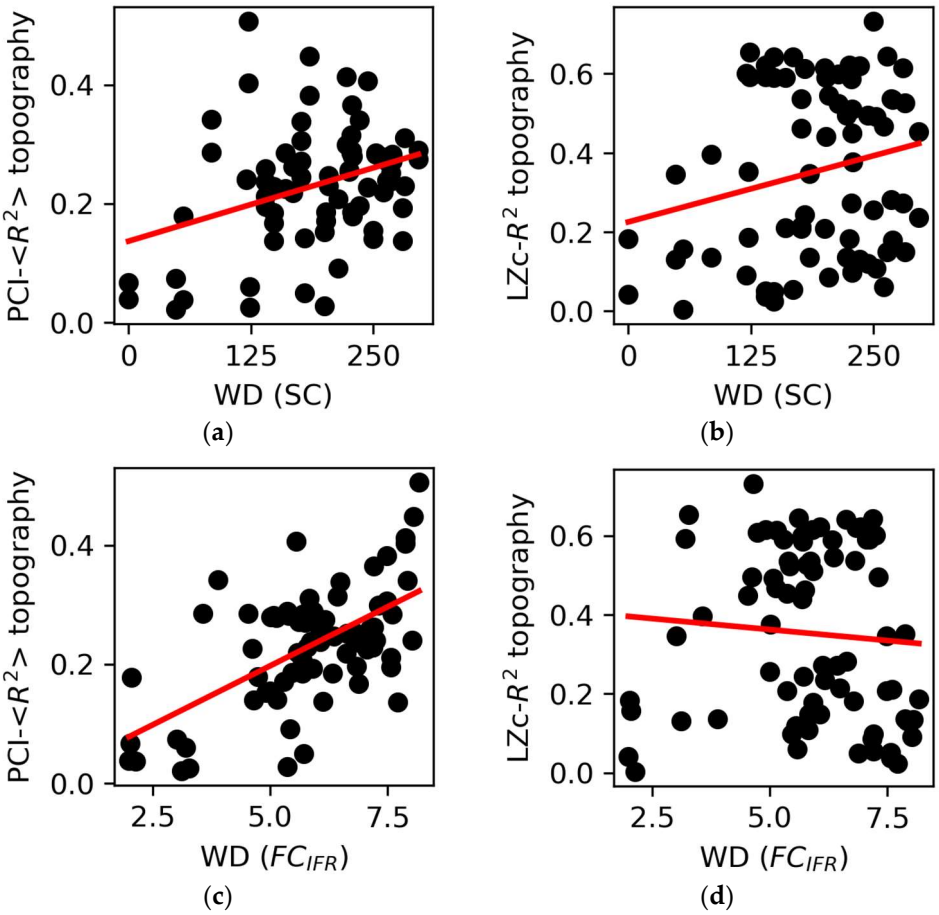

Figure 5. Graph properties and complexity topographies. (**a**) The weighted degree (WD) of structural connectivity (SC) nodes correlated with the PCI-<R^2> topography (r = 0.34, $p = 0.0026$) but (**b**) not with the LZc-R^2 topography ($p = 0.063$). (**c**) The WD of the nodes of the functional connectivity (FC_{IFR}) correlated with the PCI-<R^2> topography (r = 0.6, $p = 10^{-8}$) but (**d**) not with the LZc-R^2 topography ($p = 0.5$). Each point is representative of an ROI/node in the network. The regression lines are reported in red.

4. Discussion

The present study employed whole-brain computer simulations, systematic local manipulations (i.e., node silencing), and perturbations (i.e., brief pulses applied to local nodes) to assess the circuit-level properties underlying estimates of brain complexity. Our model has proved to be particularly suitable for investigating the mechanisms underlying brain complexity using various metrics commonly employed in empirical studies. In the present implementation, we were able to obtain spontaneous network activity as well as complex and enduring cortical interactions upon exogenous perturbations (Figure 1b), reminiscent of empirical observations [17,36]. Unlike in previous simulation works [33] and in line with experimental data, in the present model, brief local pulses were effective in evoking responses that propagated across distant nodes while spanning more prolonged time intervals. The presence of the non-linear NMDA current as implemented in the Larter

and Breakspear model [49] likely explains this important difference. Additionally, the same model has been shown to exhibit complex wave patterns, including traveling waves during spontaneous activity [56], thus arguably making it suitable for investigating complexity metrics that rely on activity propagation evoked by an external stimulus.

4.1. Impact of Local Silencing on Complexity Measures: The Role of Global Activity Levels and Network Dynamics/Interactions

All the local manipulations (i.e., node silencing) explored in this study showed an overall MFR decrease compared to the intact model (MFR_{Δ}), with a large variability depending on the manipulated nodes (Figure 2a). A similar trend was also observed for spontaneous complexity quantified with LZc, indicating a correlation between LZc and the global activity levels (MFR; Figure 2c). However, LZc often remained unchanged or even increased as compared to the control condition (Figure 2b), suggesting that the observed effects of local silencing on LZc were not merely explained by changes in global activity levels. Crucially, local manipulations resulting in a reduction of functional connectivity (i.e., segregation of network interactions) as captured by the correlation of activity across nodes (CC_{IFR}) tended to exhibit higher LZc values (Figure 2d). Thus, we tested the interplay between global activity levels (MFR) and network interactions (CC_{IFR}) in sustaining complex dynamics (LZc) through a 3D linear model (Figure 2e). This model, rooted in simple network activity variables, effectively described LZc, corroborating (1) the role of an optimal global activity level in shaping spontaneous complexity values and (2) the negative relationship of LZc with respect to network interactions. Importantly, this result underscores a significant limitation of various complexity metrics based on spontaneous activity, such as LZc, as they assume a priori network integration [6] and yield high values in systems composed of independent/segregated elements [41]. Here, we confirm, in a whole-brain connectome endowed with neural mass models, previous studies illustrating an imbalance of LZc towards network segregation [44].

A promising method to overcome this limitation and assess brain complexity, defined as the coexistence of integration and differentiation within a system, involves adopting a causal/perturbational approach [6]. This can be achieved empirically by employing local stimulations with TMS and estimating, with PCI, the information content of the causally generated interactions characterizing the integrated EEG response [17]. Unlike LZc, PCI is expected to decrease in systems with a loss of network interactions, given the restricted integrated response. Furthermore, PCI would be equally low in systems where the integrated response is redundant (i.e., undifferentiated), thus capturing an effective balance between functional integration and functional differentiation.

By the same token, in addition to the spontaneous complexity metric discussed above, we simulated this empirical approach by employing local perturbations (i.e., brief local pulses), extensively varying the stimulation site across different conditions (i.e., silencing different nodes). Each local manipulation had a detrimental effect on PCI, albeit with a heterogeneity influenced by the specific stimulus-silencing pair (Figures 3a and S2). An even more substantial impact of local manipulations on PCI was found in Hconn (Figure S4A–C).

A marked difference between spontaneous and perturbational estimates of complexity was further confirmed by the lack of a correlation between LZc and PCI across conditions (Table S4). Such divergence, already observed in experimental studies [65,66], was particularly evident upon local manipulations leading to segregated network dynamics (reduced CC_{IFR}). This resulted in a less complex evoked response (as quantified by PCI; Figure 3b,c) despite increased LZc (Figure 2b). This result is also in line with several empirical findings across a variety of conditions where a disruption of effective connectivity across widespread brain networks results in a spatially constrained, short-lived EEG response to direct cortical stimulations with TMS and, in turn, in a significant reduction of PCI [17,18,25,67,68].

Overall, the comparison between LZc from spontaneous activity and PCI confirms that the latter more coherently hinges on an actual balance between functional integration and

functional differentiation. This intuition is further suggested by the 3D model relating MFR and CC_{IFR} applied to PCI. In this case, compared to LZc, the 3D model does not describe PCI values across conditions resulting in a slope coefficient for CC_{IFR} not significantly different from 0 for most stimulations (8 out of 12; Supplementary Results, Section S3).

4.2. Regional Aspects of Complexity Indices: The Role of Posterior Regions

We observed an association between complexity indices and global activity levels, highlighting the crucial role of suitable network activity in sustaining complex model dynamics (Table S4). However, we found a significant heterogeneity in how various local manipulations affected complexity, and this variation could not be straightforwardly accounted for by the global activity levels. As outlined in previous works [41], local, rather than global, activity features might underlie network complexity. Indeed, experimental EEG and fMRI studies conducted on humans, monkeys, and rats (during sleep, anesthesia, and following severe brain injuries) have linked the loss and recovery of consciousness to brain complexity based on the activity of posterior regions [69–71]. In this regard, a recent whole-brain modeling study [40] identified a few key nodes centered around the 'posterior hot zone' (i.e., precuneus and posterior cingulate cortex) that were pivotal for maintaining the model in an awake-like state. Reducing the activity of these nodes led to a shift in model dynamics, akin to unconscious states.

While LZc was largely explained by the activity of the most firing nodes irrespective of their spatial location (Supplementary Results, Section S4 and Figure S6), our model showed a similar dependency of PCI on the activity of posterior regions (Figures 4 and S5). Specifically, our analysis revealed that the regional spontaneous activity (MFR_{ROI}) displaying the highest correlations with PCI included the retrosplenial cingulate cortex, the medial parietal cortex (precuneus), and the posterior cingulate cortex. Similar findings, encompassing a similar set of posterior regions, were found for the Hconn model (Figure S4D). These results nicely complement recent empirical observations involving rats under ketamine anesthesia [72], which found a strong correlation between PCI and activity in posteromedial regions. This study demonstrated that deactivation of these posteromedial regions was associated with disruptions in long-lasting and widespread cortical interactions following electrical stimulation. Altogether, these findings suggest the central hub role of posterior regions for long-range communications in cortical networks. Consistently, we have observed a positive correlation (Figures 5 and S7) between the weighted degree (a metric quantifying hub centrality), particularly when applied to functional connectivity estimates (Figures 5c,d and S7B,C) and the PCI-R^2 topographies (but not for LZc-R^2).

4.3. Limitations and Future Directions

This work represents a first attempt to characterize the large-scale determinants of brain complexity and to assess the relationship between observational and causal approaches towards its estimation. Given the intrinsic limitation imposed by in silico models of brain dynamics and by the use of surrogate estimates of brain complexity, more biophysically plausible node equations [32,73], as well as simulations including subcortical structures [74], should be considered for future implementations. In addition, the introduction of an appropriate forward model [75] to obtain EEG-level dynamics would allow for a more direct comparison between our findings and those obtained in empirical studies.

Along these lines, our implementation of the Hconn model (Figure S5) represents a proof of concept of the robustness of the observed findings tested on a connectome with a finer parcellation including short-range connections and serves as a promising springboard to expand the investigation to more realistic brain models such as vertex-based simulations [76].

Concerning the local manipulations conducted in this study, forthcoming research could incorporate alterations in local node dynamics that go beyond simply suppressing node activity. This could involve activity-dependent adaptation [34,77]. Indeed, in addition to the direct effect of the local silencing (either performed by activity or connectivity

manipulations), empirical evidence suggests the occurrence of an alteration in the activity of structurally intact cortical regions surrounding [78,79] or remotely connected [80] to the site of structural damage (i.e., regions with suppressed activity). Specifically, the activity of such regions switches to a sleep-like mode characterized by the tendency to display EEG slow waves. This activity is promptly revealed by direct cortical perturbations even when not directly present in the spontaneous EEG, thus confirming its activity-dependent nature [27,81,82]. Using a simple model, Cattani and colleagues [34] recently showed the key role of activity-dependent adaptation mechanisms in shaping the responses to perturbations and affecting the build-up of complex cortical interactions. Embedding such local alterations within a large-scale, connectome-based simulation, such as the one here implemented or similar [33,83], would allow one to more realistically simulate the large-scale network consequences of local node alterations.

4.4. Conclusions

Our work for the first time extensively integrates a perturbational approach with local node manipulations in a whole-brain computational model. This approximation marks an initial step towards a more detailed in silico exploration of the mechanisms behind the loss of brain complexity. Their translation may be relevant in real-world scenarios such as pathological conditions, as well as for therapeutic interventions aimed at recovering brain complexity.

Supplementary Materials: The following supporting information can be downloaded at: https://www.mdpi.com/article/10.3390/app14020890/s1, Supplementary material; Results S1: Pre-silencing activity and connectivity is predictive of the outcome of node manipulation; Results S2: Relation between PCI and the source entropy; Results S3: Comparing spontaneous and perturbational metrics; Results S4: LZc topography; Table S1: Labels of the cortical nodes and their description in Hconn; Table S2: Larter & Breakspear parameters; Table S3: Local manipulation labels in the Hconn connectome; Table S4: Pearson correlation between spontaneous and evoked metrics; Figure S1: Pre-silencing activity and connectivity correlated with the outcome of node manipulation; Figure S2: PCI decreased significantly in most local manipulations; Figure S3: Non-trivial relation between PCI and Hsrc; Figure S4: Impact of local manipulations on perturbational complexity in Hconn; Figure S5: The PCI-R^2 topographies for each stimulation site confirm the importance of the posterior regions; Figure S6: Characterization of the LZc-R^2 topography; Figure S7: Network metrics of centrality correlate with complexity topographies.

Author Contributions: Conceptualization, G.G., T.R.N., S.S. and M.M.; methodology, G.G. and T.R.N.; software, G.G. and T.R.N.; validation, G.G. and T.R.N.; formal analysis, G.G. and T.R.N.; investigation, G.G.; resources, T.R.N.; data curation, G.G.; writing—original draft preparation, G.G., T.R.N. and S.S.; writing—review and editing, G.G., T.R.N., S.S. and M.M.; supervision, S.S.; funding acquisition, M.M. and S.S. All authors have read and agreed to the published version of the manuscript.

Funding: This work was supported by the European Union's Horizon 2020 Framework Program for Research and Innovation under the Specific Grant Agreement No. 945539 (Human Brain Project SGA3), by the Tiny Blue Dot Foundation, by the European Research Council (ERC-2022-SYG–101071900–NEMESIS), by the Ministero dell'Università e della Ricerca (PRIN 2022), by a grant from the Italian Ministry of Foreign Affairs and International Cooperation, MultiScale Brain Function (MS-BFIINE) India-Italy Network of Excellence (DST-MAE), the BigMath Project (H2020-MSCA-ITN-2018, grant agreement no. 812912), and from Core Facility INDACO-Università degli Studi di Milano.

Institutional Review Board Statement: Not applicable.

Informed Consent Statement: Not applicable.

Data Availability Statement: The data and code to reproduce the results and main figures of this work are publicly available at https://github.com/gianlucagag/TVB-LB_complexity (accessed on date: 18 January 2024).

Acknowledgments: The authors acknowledge the computational resources provided by the Core Facility INDACO, which is a project of High-Performance Computing at the Università degli Studi di Milano (http://www.unimi.it, accessed on 18 January 2024).

Conflicts of Interest: The authors declare that they have no known competing financial interests or personal relationships that could have appeared to influence the work reported in this paper. Author Simone Sarasso is an advisor to Intrinsic Powers. Author Marcello Massimini is co-founder of Intrinsic Powers, a spin-off of the University of Milan, who provided funding and technical support for the work.

References

1. Tononi, G.; Sporns, O.; Edelman, G.M. A Measure for Brain Complexity: Relating Functional Segregation and Integration in the Nervous System. *Proc. Natl. Acad. Sci. USA* **1994**, *91*, 5033–5037. [CrossRef] [PubMed]
2. Deco, G.; Tononi, G.; Boly, M.; Kringelbach, M.L. Rethinking Segregation and Integration: Contributions of Whole-Brain Modelling. *Nat. Rev. Neurosci.* **2015**, *16*, 430–439. [CrossRef]
3. Bullmore, E.; Sporns, O. The Economy of Brain Network Organization. *Nat. Rev. Neurosci.* **2012**, *13*, 336–349. [CrossRef] [PubMed]
4. Sporns, O.; Tononi, G.; Edelman, G.M. Connectivity and Complexity: The Relationship between Neuroanatomy and Brain Dynamics. *Neural Netw.* **2000**, *13*, 909–922. [CrossRef] [PubMed]
5. Sporns, O. The Complex Brain: Connectivity, Dynamics, Information. *Trends Cogn. Sci.* **2022**, *26*, 1066–1067. [CrossRef] [PubMed]
6. Sarasso, S.; Casali, A.G.; Casarotto, S.; Rosanova, M.; Sinigaglia, C.; Massimini, M. Consciousness and Complexity: A Consilience of Evidence. *Neurosci. Conscious.* **2021**, *7*, niab023. [CrossRef]
7. Tononi, G.; Edelman, G.M. Consciousness and Complexity. *Science* **1998**, *282*, 1846–1851. [CrossRef]
8. Hagmann, P. *From Diffusion MRI to Brain Connectomics*; EPFL: Lausanne, Switzerland, 2005.
9. Sporns, O.; Tononi, G.; Kötter, R. The Human Connectome: A Structural Description of the Human Brain. *PLoS Comput. Biol.* **2005**, *1*, e42. [CrossRef]
10. Van Essen, D.C.; Smith, S.M.; Barch, D.M.; Behrens, T.E.J.; Yacoub, E.; Ugurbil, K. The WU-Minn Human Connectome Project: An Overview. *NeuroImage* **2013**, *80*, 62–79. [CrossRef]
11. Miller, K.L.; Alfaro-Almagro, F.; Bangerter, N.K.; Thomas, D.L.; Yacoub, E.; Xu, J.; Bartsch, A.J.; Jbabdi, S.; Sotiropoulos, S.N.; Andersson, J.L.R.; et al. Multimodal Population Brain Imaging in the UK Biobank Prospective Epidemiological Study. *Nat. Neurosci.* **2016**, *19*, 1523–1536. [CrossRef]
12. Kaiser, M. Connectomes: From a Sparsity of Networks to Large-Scale Databases. *Front. Neuroinformatics* **2023**, *17*, 1170337. [CrossRef] [PubMed]
13. Sanz Leon, P.; Knock, S.; Woodman, M.; Domide, L.; Mersmann, J.; McIntosh, A.; Jirsa, V. The Virtual Brain: A Simulator of Primate Brain Network Dynamics. *Front. Neuroinform.* **2013**, *7*, 10. [CrossRef]
14. Breakspear, M. Dynamic Models of Large-Scale Brain Activity. *Nat. Neurosci.* **2017**, *20*, 340–352. [CrossRef] [PubMed]
15. Cakan, C.; Jajcay, N.; Obermayer, K. Neurolib: A Simulation Framework for Whole-Brain Neural Mass Modeling. *Cogn. Comput.* **2021**, *15*, 1132–1152. [CrossRef]
16. Lord, L.-D.; Stevner, A.B.; Deco, G.; Kringelbach, M.L. Understanding Principles of Integration and Segregation Using Whole-Brain Computational Connectomics: Implications for Neuropsychiatric Disorders. *Philos. Trans. R. Soc. A Math. Phys. Eng. Sci.* **2017**, *375*, 20160283. [CrossRef]
17. Casali, A.G.; Gosseries, O.; Rosanova, M.; Boly, M.; Sarasso, S.; Casali, K.R.; Casarotto, S.; Bruno, M.-A.; Laureys, S.; Tononi, G.; et al. A Theoretically Based Index of Consciousness Independent of Sensory Processing and Behavior. *Sci. Transl. Med.* **2013**, *5*, 198ra105. [CrossRef]
18. Casarotto, S.; Comanducci, A.; Rosanova, M.; Sarasso, S.; Fecchio, M.; Napolitani, M.; Pigorini, A.G.; Casali, A.; Trimarchi, P.D.; Boly, M.; et al. Stratification of Unresponsive Patients by an Independently Validated Index of Brain Complexity. *Ann. Neurol.* **2016**, *80*, 718–729. [CrossRef]
19. Timme, N.M.; Marshall, N.J.; Bennett, N.; Ripp, M.; Lautzenhiser, E.; Beggs, J.M. Criticality Maximizes Complexity in Neural Tissue. *Front. Physiol.* **2016**, *7*, 425. [CrossRef]
20. Colombi, I.; Nieus, T.; Massimini, M.; Chiappalone, M. Spontaneous and Perturbational Complexity in Cortical Cultures. *Brain Sci.* **2021**, *11*, 1453. [CrossRef]
21. Barbero-Castillo, A.; Mateos-Aparicio, P.; Porta, L.D.; Camassa, A.; Perez-Mendez, L.; Sanchez-Vives, M.V. Impact of GABAA and GABAB Inhibition on Cortical Dynamics and Perturbational Complexity during Synchronous and Desynchronized States. *J. Neurosci.* **2021**, *41*, 5029–5044. [CrossRef]
22. Arena, A.; Comolatti, R.; Thon, S.; Casali, A.G.; Storm, J.F. General Anesthesia Disrupts Complex Cortical Dynamics in Response to Intracranial Electrical Stimulation in Rats. *eNeuro* **2021**, *8*. [CrossRef] [PubMed]
23. Dasilva, M.; Camassa, A.; Navarro-Guzman, A.; Pazienti, A.; Perez-Mendez, L.; Zamora-López, G.; Mattia, M.; Sanchez-Vives, M.V. Modulation of Cortical Slow Oscillations and Complexity across Anesthesia Levels. *NeuroImage* **2021**, *224*, 117415. [CrossRef] [PubMed]

24. Cavelli, M.L.; Mao, R.; Findlay, G.; Driessen, K.; Bugnon, T.; Tononi, G.; Cirelli, C. Sleep/Wake Changes in Perturbational Complexity in Rats and Mice. *iScience* **2023**, *26*, 106186. [CrossRef] [PubMed]
25. Massimini, M.; Ferrarelli, F.; Huber, R.; Esser, S.K.; Singh, H.; Tononi, G. Breakdown of Cortical Effective Connectivity During Sleep. *Science* **2005**, *309*, 2228–2232. [CrossRef] [PubMed]
26. Ragazzoni, A.; Pirulli, C.; Veniero, D.; Feurra, M.; Cincotta, M.; Giovannelli, F.; Chiaramonti, R.; Lino, M.; Rossi, S.; Miniussi, C. Vegetative versus Minimally Conscious States: A Study Using TMS-EEG, Sensory and Event-Related Potentials. *PLoS ONE* **2013**, *8*, e57069. [CrossRef] [PubMed]
27. Sarasso, S.; D'Ambrosio, S.; Fecchio, M.; Casarotto, S.; Viganò, A.; Landi, C.; Mattavelli, G.; Gosseries, O.; Quarenghi, M.; Laureys, S.; et al. Local Sleep-like Cortical Reactivity in the Awake Brain after Focal Injury. *Brain* **2020**, *143*, 3672–3684. [CrossRef] [PubMed]
28. Sinitsyn, D.O.; Poydasheva, A.G.; Bakulin, I.S.; Legostaeva, L.A.; Iazeva, E.G.; Sergeev, D.V.; Sergeeva, A.N.; Kremneva, E.I.; Morozova, S.N.; Lagoda, D.Y.; et al. Detecting the Potential for Consciousness in Unresponsive Patients Using the Perturbational Complexity Index. *Brain Sci.* **2020**, *10*, 917. [CrossRef]
29. Usami, K.; Korzeniewska, A.; Matsumoto, R.; Kobayashi, K.; Hitomi, T.; Matsuhashi, M.; Kunieda, T.; Mikuni, N.; Kikuchi, T.; Yoshida, K.; et al. The Neural Tides of Sleep and Consciousness Revealed by Single-Pulse Electrical Brain Stimulation. *Sleep* **2019**, *42*, zsz050. [CrossRef]
30. Spiegler, A.; Hansen, E.C.A.; Bernard, C.; McIntosh, A.R.; Jirsa, V.K. Selective Activation of Resting-State Networks Following Focal Stimulation in a Connectome-Based Network Model of the Human Brain. *eNeuro* **2016**, *3*. [CrossRef]
31. Spiegler, A.; Abadchi, J.K.; Mohajerani, M.; Jirsa, V.K. In Silico Exploration of Mouse Brain Dynamics by Focal Stimulation Reflects the Organization of Functional Networks and Sensory Processing. *Netw. Neurosci.* **2020**, *4*, 807–851. [CrossRef]
32. Momi, D.; Wang, Z.; Griffiths, J.D. TMS-Evoked Responses Are Driven by Recurrent Large-Scale Network Dynamics. *Elife* **2023**, *12*, e83232. [CrossRef] [PubMed]
33. Goldman, J.S.; Kusch, L.; Aquilue, D.; Yalçınkaya, B.H.; Depannemaecker, D.; Ancourt, K.; Nghiem, T.-A.E.; Jirsa, V.; Destexhe, A. A Comprehensive Neural Simulation of Slow-Wave Sleep and Highly Responsive Wakefulness Dynamics. *Front. Comput. Neurosci.* **2023**, *16*, 1058957. [CrossRef] [PubMed]
34. Cattani, A.; Galluzzi, A.; Fecchio, M.; Pigorini, A.; Mattia, M.; Massimini, M. Adaptation Shapes Local Cortical Reactivity: From Bifurcation Diagram and Simulations to Human Physiological and Pathological Responses. *eNeuro* **2023**, *10*. [CrossRef] [PubMed]
35. Albert, R.; Jeong, H.; Barabási, A.-L. Error and Attack Tolerance of Complex Networks. *Nature* **2000**, *406*, 378–382. [CrossRef] [PubMed]
36. Seguin, C.; Sporns, O.; Zalesky, A. Brain Network Communication: Concepts, Models and Applications. *Nat. Rev. Neurosci.* **2023**, *24*, 557–574. [CrossRef] [PubMed]
37. Aerts, H.; Fias, W.; Caeyenberghs, K.; Marinazzo, D. Brain Networks under Attack: Robustness Properties and the Impact of Lesions. *Brain* **2016**, *139*, 3063–3083. [CrossRef]
38. Rabuffo, G.; Lokossou, H.-A.; Li, Z.; Ziaee-Mehr, A.; Hashemi, M.; Quilichini, P.P.; Ghestem, A.; Arab, O.; Esclapez, M.; Verma, P.; et al. Probing the Mechanisms of Global Brain Reconfiguration after Local Manipulations. *bioRxiv* **2023**, *2023*, 2023-09.
39. Alstott, J.; Breakspear, M.; Hagmann, P.; Cammoun, L.; Sporns, O. Modeling the Impact of Lesions in the Human Brain. *PLOS Comput. Biol.* **2009**, *5*, e1000408. [CrossRef]
40. Hahn, G.; Zamora-López, G.; Uhrig, L.; Tagliazucchi, E.; Laufs, H.; Mantini, D.; Kringelbach, M.L.; Jarraya, B.; Deco, G. Signature of Consciousness in Brain-Wide Synchronization Patterns of Monkey and Human fMRI Signals. *Neuroimage* **2021**, *226*, 117470. [CrossRef]
41. Koch, C.; Massimini, M.; Boly, M.; Tononi, G. Neural Correlates of Consciousness: Progress and Problems. *Nat. Rev. Neurosci.* **2016**, *17*, 307–321. [CrossRef]
42. Sanders, R.D.; Mostert, N.; Lindroth, H.; Tononi, G.; Sleigh, J. Is Consciousness Frontal? Two Perioperative Case Reports That Challenge That Concept. *Br. J. Anaesth.* **2018**, *121*, 330–332. [CrossRef] [PubMed]
43. Sanz-Leon, P.; Knock, S.A.; Spiegler, A.; Jirsa, V.K. Mathematical Framework for Large-Scale Brain Network Modeling in The Virtual Brain. *NeuroImage* **2015**, *111*, 385–430. [CrossRef] [PubMed]
44. Schartner, M.; Seth, A.; Noirhomme, Q.; Boly, M.; Bruno, M.-A.; Laureys, S.; Barrett, A. Complexity of Multi-Dimensional Spontaneous EEG Decreases during Propofol Induced General Anaesthesia. *PLoS ONE* **2015**, *10*, e0133532. [CrossRef] [PubMed]
45. Bullmore, E.; Sporns, O. Complex Brain Networks: Graph Theoretical Analysis of Structural and Functional Systems. *Nat. Rev. Neurosci.* **2009**, *10*, 186–198. [CrossRef]
46. Woodman, M.M.; Pezard, L.; Domide, L.; Knock, S.A.; Sanz-Leon, P.; Mersmann, J.; McIntosh, A.R.; Jirsa, V. Integrating Neuroinformatics Tools in TheVirtualBrain. *Front. Neuroinform.* **2014**, *8*, 36. [CrossRef]
47. Kunze, T.; Hunold, A.; Haueisen, J.; Jirsa, V.; Spiegler, A. Transcranial Direct Current Stimulation Changes Resting State Functional Connectivity: A Large-Scale Brain Network Modeling Study. *NeuroImage* **2016**, *140*, 174–187. [CrossRef]
48. Hagmann, P.; Cammoun, L.; Gigandet, X.; Meuli, R.; Honey, C.J.; Wedeen, V.J.; Sporns, O. Mapping the Structural Core of Human Cerebral Cortex. *PLOS Biol.* **2008**, *6*, e159. [CrossRef]
49. Breakspear, M.; Terry, J.R.; Friston, K.J. Modulation of Excitatory Synaptic Coupling Facilitates Synchronization and Complex Dynamics in a Biophysical Model of Neuronal Dynamics. *Network* **2003**, *14*, 703–732. [CrossRef]
50. Honey, C.J.; Kötter, R.; Breakspear, M.; Sporns, O. Network Structure of Cerebral Cortex Shapes Functional Connectivity on Multiple Time Scales. *Proc. Natl. Acad. Sci. USA* **2007**, *104*, 10240–10245. [CrossRef]

51. Honey, C.J.; Sporns, O.; Cammoun, L.; Gigandet, X.; Thiran, J.P.; Meuli, R.; Hagmann, P. Predicting Human Resting-State Functional Connectivity from Structural Connectivity. *Proc. Natl. Acad. Sci. USA* **2009**, *106*, 2035–2040. [CrossRef]
52. Gollo, L.L.; Breakspear, M. The Frustrated Brain: From Dynamics on Motifs to Communities and Networks. *Philos. Trans. R. Soc. B Biol. Sci.* **2014**, *369*, 20130532. [CrossRef] [PubMed]
53. Gollo, L.L.; Mirasso, C.; Sporns, O.; Breakspear, M. Mechanisms of Zero-Lag Synchronization in Cortical Motifs. *PLoS Comput. Biol.* **2014**, *10*, e1003548. [CrossRef] [PubMed]
54. Gollo, L.L.; Zalesky, A.; Hutchison, R.M.; van den Heuvel, M.; Breakspear, M. Dwelling Quietly in the Rich Club: Brain Network Determinants of Slow Cortical Fluctuations. *Philos. Trans. R. Soc. B Biol. Sci.* **2015**, *370*, 20140165. [CrossRef] [PubMed]
55. Roberts, J.A.; Friston, K.J.; Breakspear, M. Clinical Applications of Stochastic Dynamic Models of the Brain, Part I: A Primer. *Biol. Psychiatry Cogn. Neurosci. Neuroimaging* **2017**, *2*, 216–224. [CrossRef] [PubMed]
56. Roberts, J.A.; Gollo, L.L.; Abeysuriya, R.G.; Roberts, G.; Mitchell, P.B.; Woolrich, M.W.; Breakspear, M. Metastable Brain Waves. *Nat. Commun.* **2019**, *10*, 1056. [CrossRef] [PubMed]
57. Endo, H.; Hiroe, N.; Yamashita, O. Evaluation of Resting Spatio-Temporal Dynamics of a Neural Mass Model Using Resting fMRI Connectivity and EEG Microstates. *Front. Comput. Neurosci.* **2020**, *13*, 91. [CrossRef] [PubMed]
58. Aquino, K.M.; Fulcher, B.; Oldham, S.; Parkes, L.; Gollo, L.; Deco, G.; Fornito, A. On the Intersection between Data Quality and Dynamical Modelling of Large-Scale fMRI Signals. *NeuroImage* **2022**, *256*, 119051. [CrossRef]
59. Honey, C.J.; Sporns, O. Dynamical Consequences of Lesions in Cortical Networks. *Hum. Brain Mapp.* **2008**, *29*, 802–809. [CrossRef]
60. Deco, G.; McIntosh, A.R.; Shen, K.; Hutchison, R.M.; Menon, R.S.; Everling, S.; Hagmann, P.; Jirsa, V.K. Identification of Optimal Structural Connectivity Using Functional Connectivity and Neural Modeling. *J. Neurosci.* **2014**, *34*, 7910–7916. [CrossRef]
61. Adhikari, M.H.; Raja Beharelle, A.; Griffa, A.; Hagmann, P.; Solodkin, A.; McIntosh, A.R.; Small, S.L.; Deco, G. Computational Modeling of Resting-State Activity Demonstrates Markers of Normalcy in Children with Prenatal or Perinatal Stroke. *J. Neurosci.* **2015**, *35*, 8914–8924. [CrossRef]
62. Tagliazucchi, E. The Signatures of Conscious Access and Its Phenomenology Are Consistent with Large-Scale Brain Communication at Criticality. *Conscious. Cogn.* **2017**, *55*, 136–147. [CrossRef] [PubMed]
63. Eryilmaz, H.; Pax, M.; O'Neill, A.G.; Vangel, M.; Diez, I.; Holt, D.J.; Camprodon, J.A.; Sepulcre, J.; Roffman, J.L. Network Hub Centrality and Working Memory Performance in Schizophrenia. *Schizophrenia* **2022**, *8*, 76. [CrossRef] [PubMed]
64. Friston, K.J.; Harrison, L.; Penny, W. Dynamic Causal Modelling. *NeuroImage* **2003**, *19*, 1273–1302. [CrossRef] [PubMed]
65. Farnes, N.; Juel, B.E.; Nilsen, A.S.; Romundstad, L.G.; Storm, J.F. Increased Signal Diversity/Complexity of Spontaneous EEG, but Not Evoked EEG Responses, in Ketamine-Induced Psychedelic State in Humans. *PLoS ONE* **2020**, *15*, e0242056. [CrossRef] [PubMed]
66. Ort, A.; Smallridge, J.W.; Sarasso, S.; Casarotto, S.; von Rotz, R.; Casanova, A.; Seifritz, E.; Preller, K.H.; Tononi, G.; Vollenweider, F.X. TMS-EEG and Resting-State EEG Applied to Altered States of Consciousness: Oscillations, Complexity, and Phenomenology. *iScience* **2023**, *26*. [CrossRef] [PubMed]
67. Ferrarelli, F.; Massimini, M.; Sarasso, S.; Casali, A.; Riedner, B.A.; Angelini, G.; Tononi, G.; Pearce, R.A. Breakdown in Cortical Effective Connectivity during Midazolam-Induced Loss of Consciousness. *Proc. Natl. Acad. Sci. USA* **2010**, *107*, 2681–2686. [CrossRef] [PubMed]
68. Bai, Y.; Xia, X.; Kang, J.; Yin, X.; Yang, Y.; He, J.; Li, X. Evaluating the Effect of Repetitive Transcranial Magnetic Stimulation on Disorders of Consciousness by Using TMS-EEG. *Front. Neurosci.* **2016**, *10*, 473. [CrossRef]
69. King, J.-R.; Sitt, J.D.; Faugeras, F.; Rohaut, B.; El Karoui, I.; Cohen, L.; Naccache, L.; Dehaene, S. Information Sharing in the Brain Indexes Consciousness in Noncommunicative Patients. *Curr. Biol.* **2013**, *23*, 1914–1919. [CrossRef]
70. Sitt, J.D.; King, J.-R.; El Karoui, I.; Rohaut, B.; Faugeras, F.; Gramfort, A.; Cohen, L.; Sigman, M.; Dehaene, S.; Naccache, L. Large Scale Screening of Neural Signatures of Consciousness in Patients in a Vegetative or Minimally Conscious State. *Brain* **2014**, *137*, 2258–2270. [CrossRef]
71. Luppi, A.I.; Craig, M.M.; Pappas, I.; Finoia, P.; Williams, G.B.; Allanson, J.; Pickard, J.D.; Owen, A.M.; Naci, L.; Menon, D.K.; et al. Consciousness-Specific Dynamic Interactions of Brain Integration and Functional Diversity. *Nat. Commun.* **2019**, *10*, 4616. [CrossRef]
72. Arena, A.; Juel, B.E.; Comolatti, R.; Thon, S.; Storm, J.F. Capacity for Consciousness under Ketamine Anaesthesia Is Selectively Associated with Activity in Posteromedial Cortex in Rats. *Neurosci. Conscious.* **2022**, *2022*, niac004. [CrossRef] [PubMed]
73. Bensaid, S.; Modolo, J.; Merlet, I.; Wendling, F.; Benquet, P. COALIA: A Computational Model of Human EEG for Consciousness Research. *Front. Syst. Neurosci.* **2019**, *13*, 59. [CrossRef] [PubMed]
74. Cabrera-Álvarez, J.; Doorn, N.; Maestú, F.; Susi, G. Modeling the Role of the Thalamus in Resting-State Functional Connectivity: Nature or Structure. *PLoS Comput. Biol.* **2023**, *19*, e1011007. [CrossRef] [PubMed]
75. Næss, S.; Halnes, G.; Hagen, E.; Hagler, D.J.; Dale, A.M.; Einevoll, G.T.; Ness, T.V. Biophysically Detailed Forward Modeling of the Neural Origin of EEG and MEG Signals. *NeuroImage* **2021**, *225*, 117467. [CrossRef]
76. Spiegler, A.; Jirsa, V. Systematic Approximations of Neural Fields through Networks of Neural Masses in the Virtual Brain. *NeuroImage* **2013**, *83*, 704–725. [CrossRef] [PubMed]
77. Cakan, C.; Obermayer, K. Biophysically Grounded Mean-Field Models of Neural Populations under Electrical Stimulation. *PLoS Comput. Biol.* **2020**, *16*, e1007822. [CrossRef]
78. Walter, W.G. The Electro-Encephalogram in Cases of Cerebral Tumour. *Proc. R. Soc. Med.* **1937**, *30*, 579–598. [CrossRef]

79. Nuwer, M.R.; Jordan, S.E.; Ahn, S.S. Evaluation of Stroke Using EEG Frequency Analysis and Topographic Mapping. *Neurology* **1987**, *37*, 1153–1159. [CrossRef] [PubMed]
80. Russo, S.; Pigorini, A.; Mikulan, E.; Sarasso, S.; Rubino, A.; Zauli, F.M.; Parmigiani, S.; d'Orio, P.; Cattani, A.; Francione, S.; et al. Focal Lesions Induce Large-Scale Percolation of Sleep-like Intracerebral Activity in Awake Humans. *NeuroImage* **2021**, *234*, 117964. [CrossRef]
81. Tscherpel, C.; Dern, S.; Hensel, L.; Ziemann, U.; Fink, G.R.; Grefkes, C. Brain Responsivity Provides an Individual Readout for Motor Recovery after Stroke. *Brain* **2020**, *143*, 1873–1888. [CrossRef]
82. D'Ambrosio, S.; Certo, F.; Bernardelli, L.; Pini, L.; Corbetta, M.; Pantoni, L.; Massimini, M.; Sarasso, S. Detecting Cortical Reactivity Alterations Induced by Structural Disconnection in Subcortical Stroke. *Clin. Neurophysiol.* **2023**, *156*, 1–3. [CrossRef] [PubMed]
83. Cakan, C.; Dimulescu, C.; Khakimova, L.; Obst, D.; Flöel, A.; Obermayer, K. Spatiotemporal Patterns of Adaptation-Induced Slow Oscillations in a Whole-Brain Model of Slow-Wave Sleep. *Front. Comput. Neurosci.* **2022**, *15*, 800101. [CrossRef] [PubMed]

Supplementary information

Supplementary material

The maximum firing rate of the three nodes prior to the *silencing* (*PS*-MFR_{max}) was monitored to quantify the potential impact of a local manipulation. With regard to the manipulated nodes, we also defined the local manipulation weighted degree (LWD) as the sum of weighted incoming and outgoing connections of the manipulated nodes in the structural connectivity (SC). To compute the MFR of the most active nodes we first ranked the nodes based on their firing rate and then averaged the MFR over groups of consecutive 4 to 7 'ranked' nodes. Since the results were quite comparable irrespective of the size of the groups we report the results only for 5 nodes.

Supplementary results

S1. Pre-silencing activity and connectivity is predictive of the outcome of node manipulation

Further exploring the determinants of the impact of local node manipulations, we investigated whether structural and functional properties prior to silencing could be predictive of the observed impact on both model activity and complexity metrics. First, we implemented a linear model (Fig. S1A) describing the MFR_{Δ} of all nodes as a function of the *PS*-MFR_{max} and found a significant negative relationship ($r=-0.8$, $p=2\cdot10^{-5}$). Next, we computed the linear correlation between *PS*-MFR_{max} and LZc (Fig. S1B) and once again observed a significant negative correlation ($r=-0.64$, $p=0.002$). Then, similar to previous studies (Aerts et al. 2016) showing that silencing of central nodes had a greater impact on network activity, we related the weighted degree of the manipulated nodes (LWD, see Supplementary material) to the same metrics (Fig S1C, D). While the correlation was non-significant for all variables ($p>0.05$), including LWD as a regressor alongside *PS*-MFR_{max} (Fig. S1E, F) resulted in an improved description of the MFR_{Δ} ($R^2=0.75$, $R^2_{adjusted}=0.72$, $p=7\cdot10^{-6}$; $\beta_{PS\text{-}MFRmax}= -0.266$, 95% CI [-0.345, -0.187]; $\beta_{LWD}= -0.0033$, 95% CI [-0.0058, -0.0008]) and LZc ($R^2=0.62$, $R^2_{adjusted}=0.58$, $p=0.0002$; $\beta_{PS\text{-}MFRmax}= -0.0023$, 95% CI [-0.0033, -0.0014]; $\beta_{LWD}=-0.000043$, 95% CI [-0.000072, -0.000014]).

S2. Relation between PCI and the source entropy

In order to exclude the presence of a trivial relationship between the source entropy (Hsrc) and the perturbational complexity index (PCI) we performed additional analysis. Importantly, we found that for a given stimulus there was no clear relation between Hsrc and PCI (Fig S3A, B, C). Instead, only when all stimuli, local manipulations and averages across resamples (i.e. mean across PCI, mean across Hsrc) were reported together a significant linear trend in the data was found (Fig S3D, $r=-0.29$, $p=4\cdot10^{-6}$). The latter shows that complex patterns do not necessarily increase with a larger amount of significant activations of the post-stimulus response. Note that, while PCI decreased significantly with respect to control across resamples (190 out of 240 configurations – 12 stimuli x 20 local manipulations – $p<0.05$; corresponding to the amount of significant cases of Fig. S2), Hsrc instead, either increased or decreased with respect to control condition.

S3. Comparing spontaneous and perturbational metrics

To compare the outcome of spontaneous and perturbational complexity analysis, we summarized the relationship between the various metrics by the Pearson correlation coefficient (Table S4). MFR correlated significantly with all complexity indices, albeit more strongly with LZc, highlighting the important role of suitable network activity in expressing complex cortical dynamics. Notably, PCI and LZc did not correlate (for 11 out of 12 stimulations, $p>0.05$). In addition, as with LZc, we performed multivariate regressions to relate the spontaneous metrics to PCI. Specifically, we modelled PCI as a function of MFR and the activity correlation CC_{IFR}, and we found that the slope

coefficient of CC_{IFR} (β_{CC}) was not significantly different from zero across stimulations (8 out of 12 had CI falling around the zero value), suggesting that PCI is not much sensitive to synchronous activity. Additionally, unlike LZc, PCI was not simply described by the functional (*PS*-MFR_{max}) attributes of the silenced nodes (for 10 out of 12 stimulations, $p>0.05$).

S4. LZc topography

Interestingly, the LZc topography (Fig. S6B) was characterized by higher R^2 values in the intact hemisphere (IH) instead of the manipulated one (MH) as it occurred for PCI. We hypothesized that this result was not correlated to the activity of the intact hemisphere (IH) and, in order to verify this, we restricted the computation of LZc to the manipulated hemisphere (MH) which resulted in a strong correlation with LZc ($r=0.97$, $p=8\cdot10^{-13}$; Fig S6C left panel). Thus the MH alone follows the same trend of the whole brain LZc when silencing the different nodes of the connectome. Subsequently, to exclude the contribution of activities bouncing from one hemisphere to the other we calculated LZc on a truncated connectome, where connections from IH to MH were removed (IMH_{cut}). Again we found that LZc computed on the truncated connectome correlated with LZc computed on the entire connectome ($r=0.88$, $p=2\cdot10^{-7}$; Fig. S6C right panel). Next, to clarify the reasons of the correlation between IH and LZc, we examined how the MH manipulations affected IH. This analysis yielded two key observations: 1) the nodes of the IH covaried across local manipulations (average Pearson correlation coefficient across nodes $\langle r\rangle=0.9$, Fig. S6D), indicating that the latter had a non-specific impact on IH, 2) the activity in the intact hemisphere (MFR_{IH}) correlated strongly ($r=0.98$, $p=4\cdot10^{-15}$) with the activity of the most firing nodes of MH ($MFR_{MH(most\ active)}$; Fig. S6E top panel). Interestingly, the correlation of LZc with MFR_{MH} also increased with the most active nodes ($r=0.81$, $p=8\cdot10^{-6}$; Fig. S6E bottom panel).

Finally, we conclude that: 1) LZc can be largely explained by the manipulated hemisphere, and 2) $MFR_{MH(most\ active)}$ drive the covariation between LZc and MFR_{IH}.

Supplementary tables

Table S1. Labels of the cortical nodes and their description in Hconn. The stimulated region is reported in bold (14 adjacent nodes within this region are stimulated simultaneously in all conditions).

Label	Description
BSTS	Bank of the superior temporal sulcus
CAC	Caudal anterior cingulate cortex
CMF	caudal middle frontal cortex
CUN	Cuneus
ENT	Entorhinal cortex
FP	Frontal pole
FUS	Fusiform gyrus
IP	Inferior parietal cortex
IT	Inferior temporal cortex
ISTC	Isthmus of the cingulate cortex
LOCC	Lateral occipital cortex
LOF	Lateral orbitofrontal cortex
LIN	Lingual gyrus
MOF	Medial orbitofrontal cortex
MT	Middle temporal cortex
PARC	Paracentral lobule
PARH	Parahippocampal cortex
POPE	Pars opercularis
PORB	Pars orbitalis
PTRI	Pars triangularis
PCAL	Pericalcarine cortex
PSTC	Postcentral gyrus
PC	Posterior cingulate cortex
PREC	Precentral gyrus
PCUN	Precuneus
RAC	Rostral anterior cingulate cortex
RMF	Rostral middle frontal cortex
SF	Superior frontal cortex
SP	**Superior parietal cortex**
ST	Superior temporal cortex
SMAR	Supramarginal gyrus
TP	Temporal pole
TT	Transverse temporal cortex

Table S2. Larter & Breakspear parameters. The parameters changed from Alstott et al. 2009 are indicated in bold.

Parameter	Description	Value in Dconn	Value in Hconn
g_{Ca}	Conductance of population of Ca channels	1.1	1.1
V_{Ca}	Ca Nernst potential	1	**1.1**
r_{NMDA}	Ratio of NMDA to AMPA receptors	0.25	0.25
g_{Na}	Conductance of population of Na channels	6.7	6.7
V_{Na}	Na Nernst potential	0.53	0.53
a_{ee}	Excitatory-to-excitatory synaptic strength	**0.35**	**0.5**
g_K	Conductance of population of K channels	**2.5**	**2.5**
V_K	K Nernst potential	-0.7	-0.7
g_L	Conductance of population of leak channels	**0.7**	**1.1**
V_L	Nernst potential of leak channels	-0.5	-0.5
a_{ie}	Inhibitory-to-excitatory synaptic strength	2	2
a_{ne}	Non-specific-to-excitatory synaptic strength	1	1
I	Subcortical input strength	0.3	0.3
b	Time constant scaling factor	0.1	0.1
a_{ni}	Non-specific-to-inhibitory synaptic strength	**0.42**	0.4 (**0.4023** in the left hem)
a_{ei}	Excitatory-to-inhibitory synaptic strength	2	1
T_{Ca}	Threshold potential for Ca channels	-0.01	-0.01
T_{Na}	Threshold potential for Na channels	**0.26**	**0.26**
T_K	Threshold potential for K channels	0	0
δ_{Ca}	Variance of Ca channels threshold	0.15	0.15
δ_{Na}	Variance of Na channels threshold	0.15	0.15
δ_K	Variance of K channels threshold	**0.4**	**0.4**
φ	Temperature scaling factor	0.7	0.7
τ_K	Time constant for K relaxation time	1	1
QV_{max}	Maximal firing rate for excitatory populations	1	1
V_T	Threshold potential for excitatory neurons	**-0.1**	**-0.1**
δ_V	Variance of excitatory threshold	0.65	0.65
QZ_{max}	Maximal firing rate inhibitory populations	1	1
Z_T	Threshold potential for inhibitory neurons	0	0
δ_Z	Variance of inhibitory threshold	**0.6**	**0.6**
C	Strength of excitatory coupling and balance between internal and global dynamics	0.1	0.1

Table S3. Local manipulation labels in the Hconn connectome. The labels of the local manipulation and the corresponding nodes silenced in the Hconn connectome. The number of silenced nodes within the specified region is given in brackets (e.g., in HL1: nodes CUN1, CUN2, ..., CUN7; ISTC1,…, ISTC4; etc.).

Local manipulation label	Nodes
HL1	CUN (7), ISTC (4), LING (3), PCAL (5), PCUN (19), SP (2)
HL2	CMF (5), POPE (1), PREC (16), PSTC (16), SMAR (2)
HL3	FP (2), LOF (15), MOF (11), PORB (1), RAC (4), RMF (4), SF (3)
HL4	ENT (2), FUS (5), IT (9), LOF (2) MT (6), PARH (1), ST (12), TP (3)
HL5	BSTS (7), MT (4), PSTC (5), SMAR (6), ST (15), TT (3)
HL6	BSTS (5), IP (8), MT (2), PSTC (3), SMAR (14), ST (8)
HL7	POPE (4), PREC (11), PSTC (11), SMAR (2), ST (11), TT (1)
HL8	FUS (3), IP (18), IT (1), LOCC (10), MT (2), PCAL (1), PCUN (1), SP (4)
HL9	CUN (1), FUS (5), IP (5), ISTC (3), IT (1), LING (12), LOCC (1), MT (1), PARH (1), PCAL (3), PCUN (5), SP (2)
HL10	CUN (2), FUS (6), LING (11), LOCC (13), PCAL (8)
HL11	FUS (10), IP (4), IT (2), LING (4), LOCC (16), MT (2), PCAL (2)
HL12	LOF (15), POPE (2), PORB (5), PTRI (8), RMF (4), ST (4), TP (2)
HL13	BSTS (5), FUS (6), IP (13), ISTC (1), IT (5), LING (2), LOCC (3), MT (5)
HL14	BSTS (4), FUS (12), ISTC (2), IT (5), LING (7), MT (1), PARH (6), ST (2), TT (1)
HL15	CUN (4), FUS (3), LING (8), LOCC (15), PCAL (9), SP (1)
HL16	CMF (2), LOF (4), POPE (10), PREC (5), PTRI (7), RMF (12)
HL17	LOF (10), POPE (2), PORB (6), PTRI (8), RMF (7), ST (6), TP (1)
HL18	LOF (5), POPE (10), PORB (4), PREC (1), PTRI (8), RMF (12)
HL19	CMF (5), POPE (9), PTRI (8), RMF (16), SF (2)
HL20	CUN (2), IP (14), ISTC (1), LING (1), LOCC (3), PCAL (4), PCUN (7), SP (8)

Table S4. Pearson correlation between spontaneous and evoked metrics. The Pearson correlation coefficients between different metrics are computed across local manipulations. The correlation values between PCI and the other metrics are reported as mean ± SD computed over the 12 Pearson correlation coefficients (1 per stimulus). Asterisks indicate level of statistical significance: *p<0.05, **p<0.01, ***p<0.001; ns: non-significant.

	PCI	**LZc**	**MFR**	**CC_{IFR}**
PCI	1.000			
LZc	0.23 ± 0.12 (* in 1 case)	1.00		
MFR	0.56 ± 0.09 (* in 11 cases)	0.69***	1.00	
CC_{IFR}	0.39 ± 0.13 (* in 4 cases)	-0.55**	0.21^{ns}	1.00

Supplementary figures

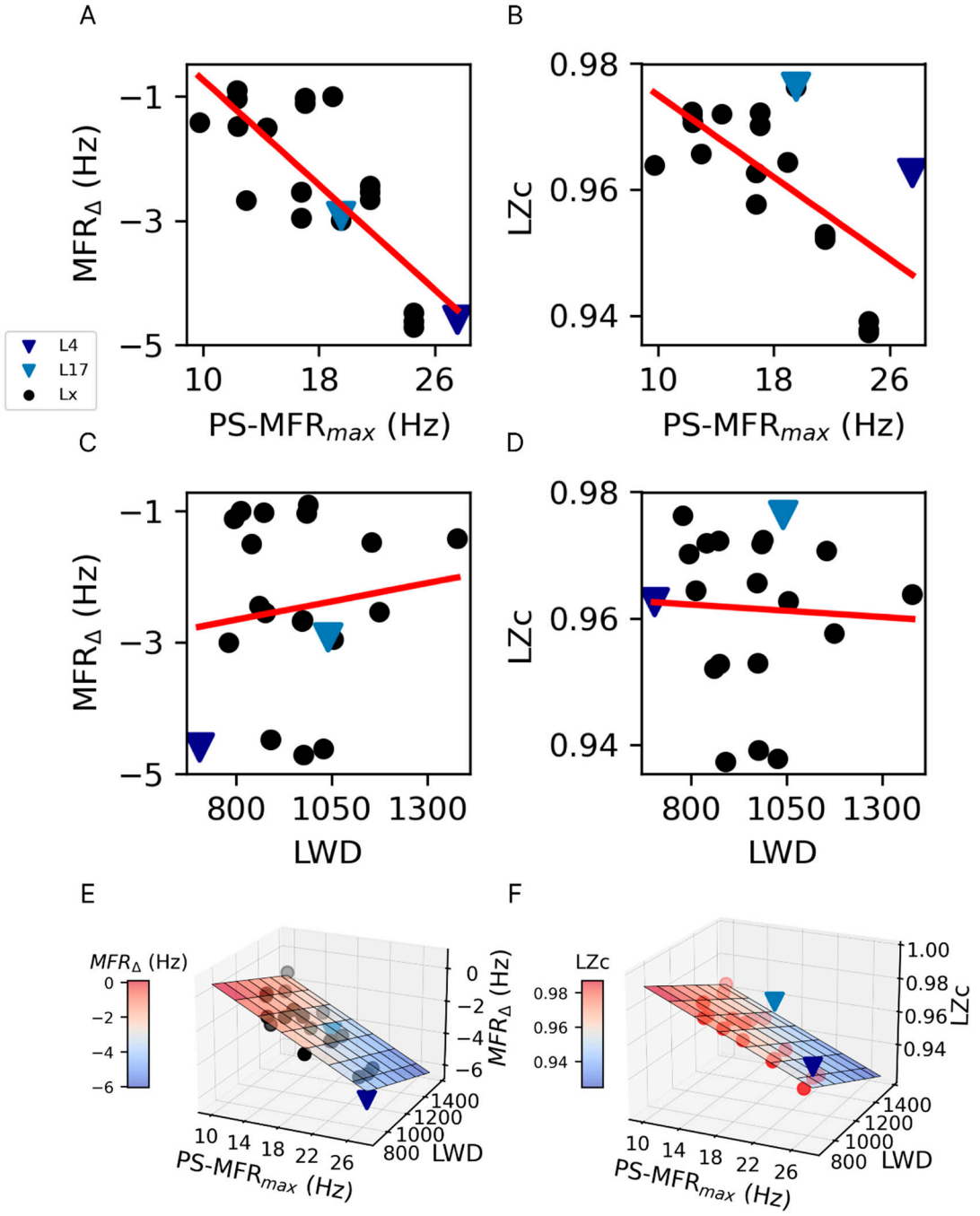

Figure S1. Pre-silencing activity and connectivity correlated with the outcome of node manipulation A) Linear regression of the MFR$_\Delta$ in all nodes with respect to *PS*-MFRmax (r=-0.8, p=2·10^{-5}). B) Linear regression of LZc with respect to *PS*-MFRmax (r=-0.64, p=0.002). C) Linear regression of the MFR$_\Delta$ in all nodes with respect to LWD (p=0.57). D) Linear regression of LZc with respect to LWD (p=0.83). E) Linear regression of the MFR$_\Delta$ in all nodes with respect to the independent *PS*-MFRmax and the weight degree of the locally manipulated nodes (LWD) (R^2=0.75, $R^2_{adjusted}$=0.72, 7·10^{-6}). F) Linear regression of LZc with respect to the independent *PS*-MFRmax and LWD (R^2=0.62, $R^2_{adjusted}$=0.58, p=0.0002).

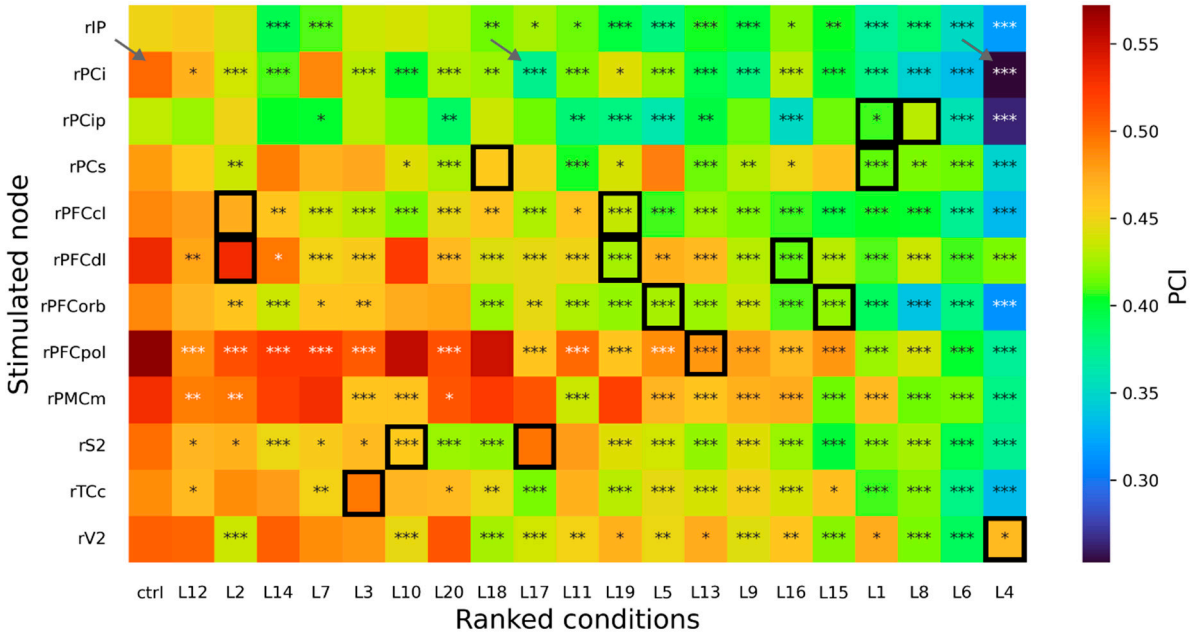

Figure S2. PCI decreased significantly in most local manipulations. PCI values are given for each combination of stimulus (rows) and local manipulation/control (columns). The conditions (control and local manipulations) are sorted in descending order according to the average PCI value computed across stimulation sites. The grey arrows indicate the ctrl, L4 and L17 conditions analysed in the main text (section 3.2.1) and black boxes mark local manipulations that were changed as they included the stimulated node (see methods, section 2.1.4). Asterisks mark significant differences of each local manipulation compared to the control with the same stimulated node (*p<0.05, **p<0.01, ***p<0.001; ANOVA and post hoc pairwise T test with Benjamini-Hochberg correction).

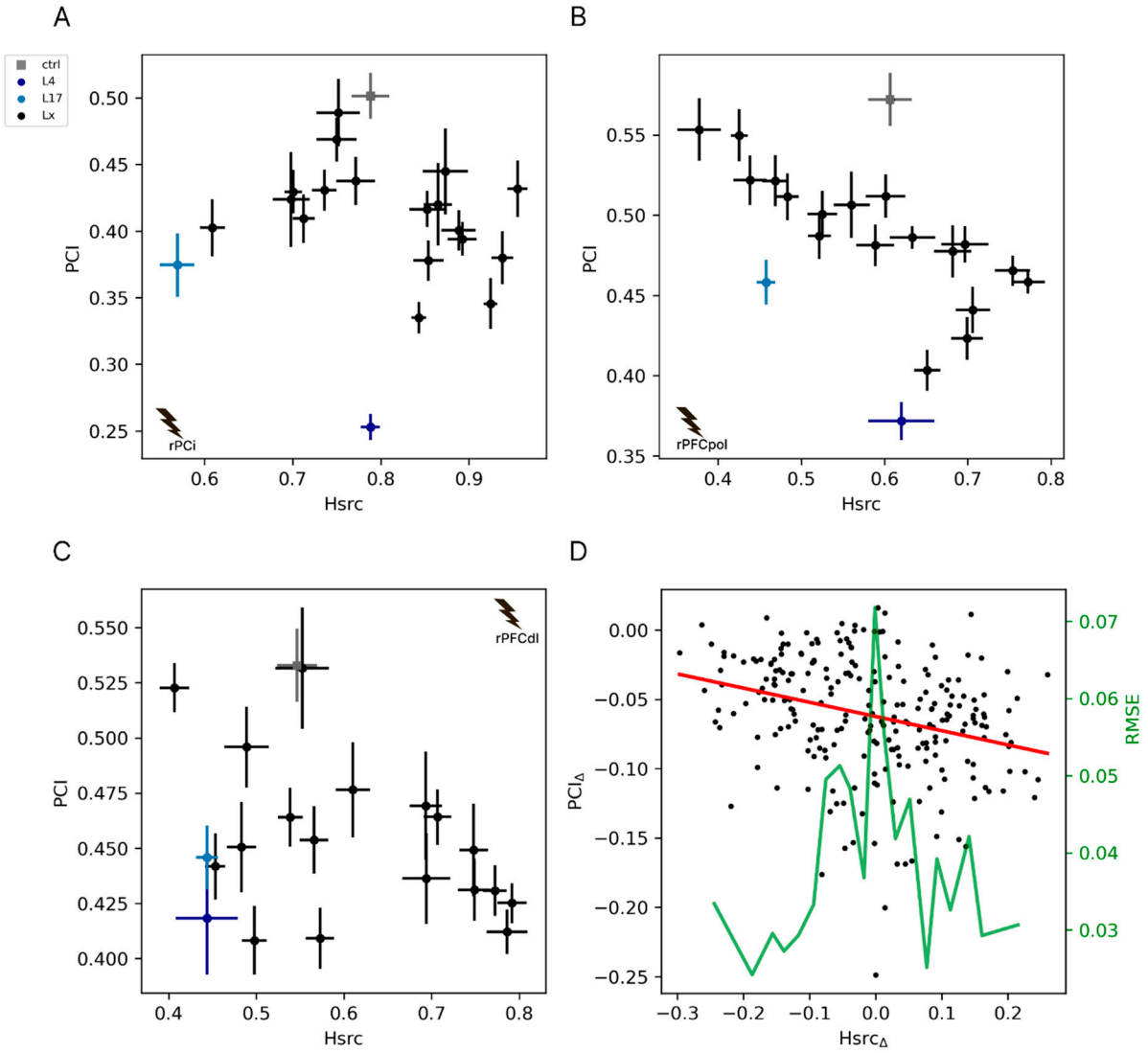

Figure S3. Non-trivial relation between PCI and Hsrc. Relation between PCI and Hsrc, for each local manipulation, in the stimulation of rPCi (A), rPFCpol (B) and rPFCdl (C). The error bars represent 2 SEM computed over resamples of the trials (10 resamples of 300 trials each). D) Summary plot for all stimulation sites and silencing conditions. A significant negative correlation between $Hsrc_{\Delta}$ and PCI_{Δ} is found in the linear regression ($r=-0.29$, $p<0.001$). The green curve represents the root mean squared error (RMSE) from the fit line. The $Hsrc_{\Delta}$ distribution was subdivided in 20 equi-populated bins. The x-values of the curve are the central value of each bin and the y-values are the corresponding RMSEs. PCI_{Δ} and $Hsrc_{\Delta}$ are differences with respect to control condition for a given stimulation site (e.g. stimulation of rPCi: $PCI_{\Delta(\text{local manipulation})} = \langle PCI_{\text{local manipulation}} \rangle - \langle PCI_{ctrl} \rangle$ and $Hsrc_{(\text{local manipulation})} = \langle Hsrc_{\text{local manipulation}} \rangle - \langle Hsrc_{ctrl} \rangle$, where $\langle \ldots \rangle$ indicates mean across resamples).

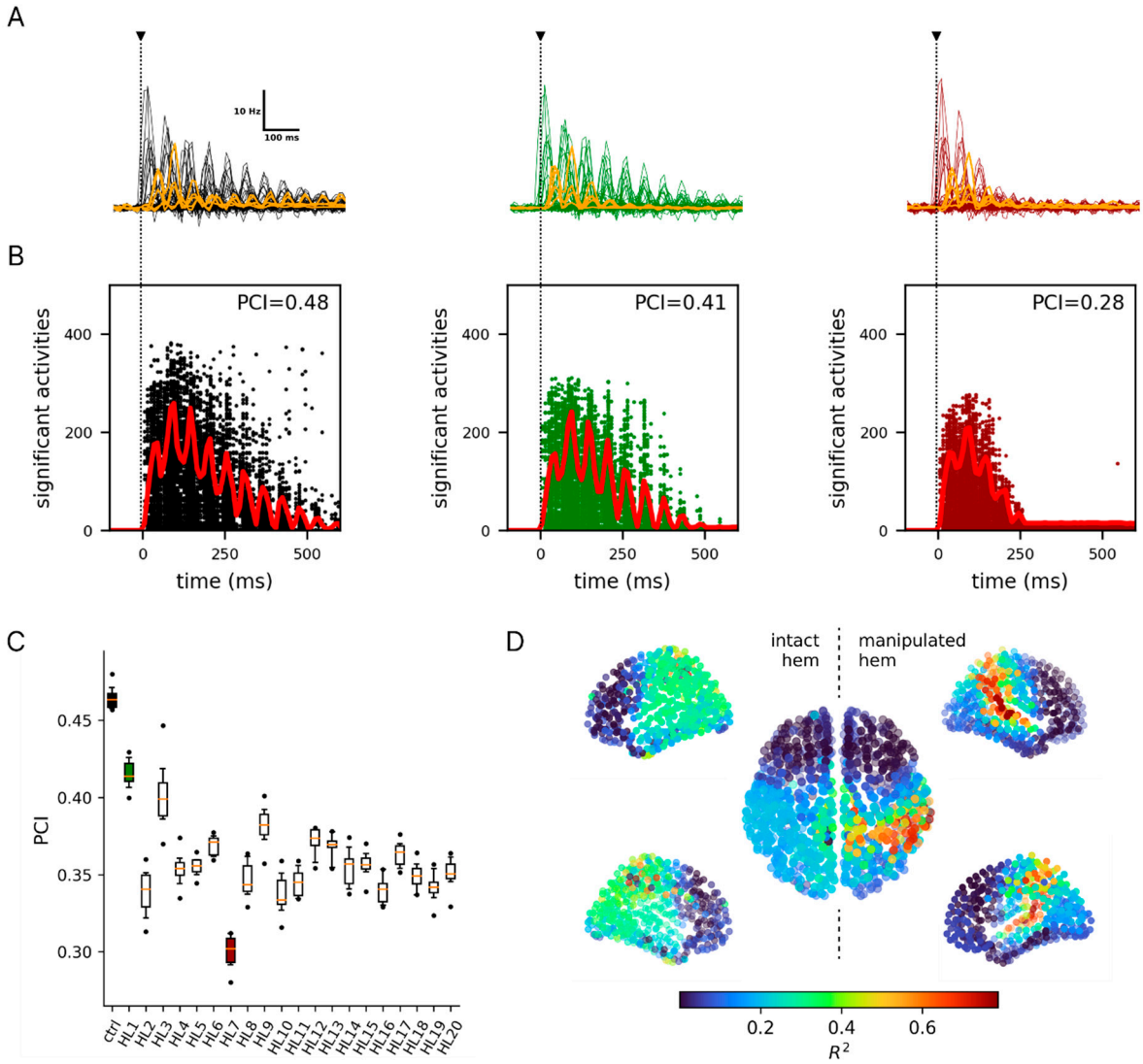

Figure S4. Impact of local manipulations on perturbational complexity in Hconn. A) The temporal courses of the instantaneous firing rate with respect to baseline (averaged across trials, <ΔIFR>) are reported for all regions of the stimulated hemisphere and separately for the representative conditions: ctrl (black), HL1 (green) and HL7 (dark red). For each condition, the highest five <ΔIFRs> (quantified as the total activity in the interval [0,500] ms) of the non-stimulated hemisphere (orange traces) are also reported. The vertical dotted black line marks the time of the stimulus. The IFR traces of the 66 cortical regions are obtained by averaging the IFR of the nodes belonging to the respective region. B) The corresponding sorted binary spatiotemporal matrices of significant activities highlight the impact of the local manipulations with respect to the ctrl condition (the red line is the sum of significant activity over time). C) The Perturbational complexity index (PCI) decreases significantly in all silencing conditions (for each $p<0.000001$, ANOVA and post hoc pairwise T test with Benjamini-Hochberg correction). D) Topography of the R^2 values over the brain map showing the prevalence of higher values at posterior nodes. R^2 values are obtained as in Fig. 4 (main figure), performing a linear regression, for each node, fitting PCI versus the node's pre-stimulus MFR.

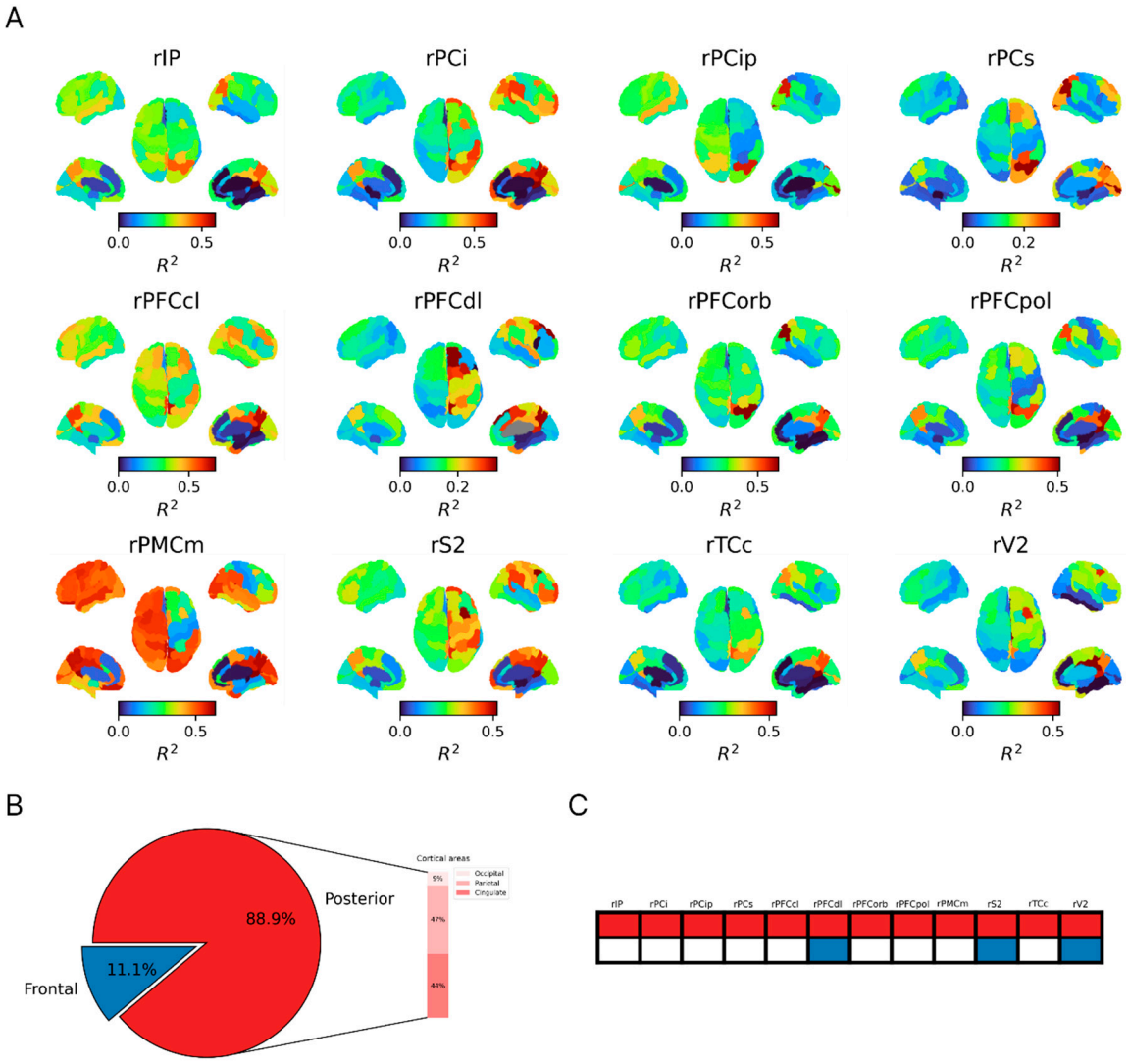

Figure S5. The PCI-R² topographies for each stimulation site confirm the importance of the posterior regions A) R² values over the brain map for each stimulation site (reported above the brain maps). For each node, the R² values are relative to the linear regressions of PCI versus spontaneous MFR across conditions (control and local manipulations). B) Occurrence of the posterior and frontal regions. For each stimulus the highest three R² values are considered (for a total of 3x12 R²-ROIs). C) For each stimulation site (rIP, …, rV2) the presence of the three highest R² values is monitored. Whenever a posterior and/or a frontal node is part of the three highest R² values the corresponding box is coloured in red and/or blue. The nodes belonging to the parietal, occipital, temporal, posterior cingulate (posterior and retrosplenial) cortices in Dconn were considered posterior, for a total of 39 nodes. The remaining 37 nodes were considered frontal.

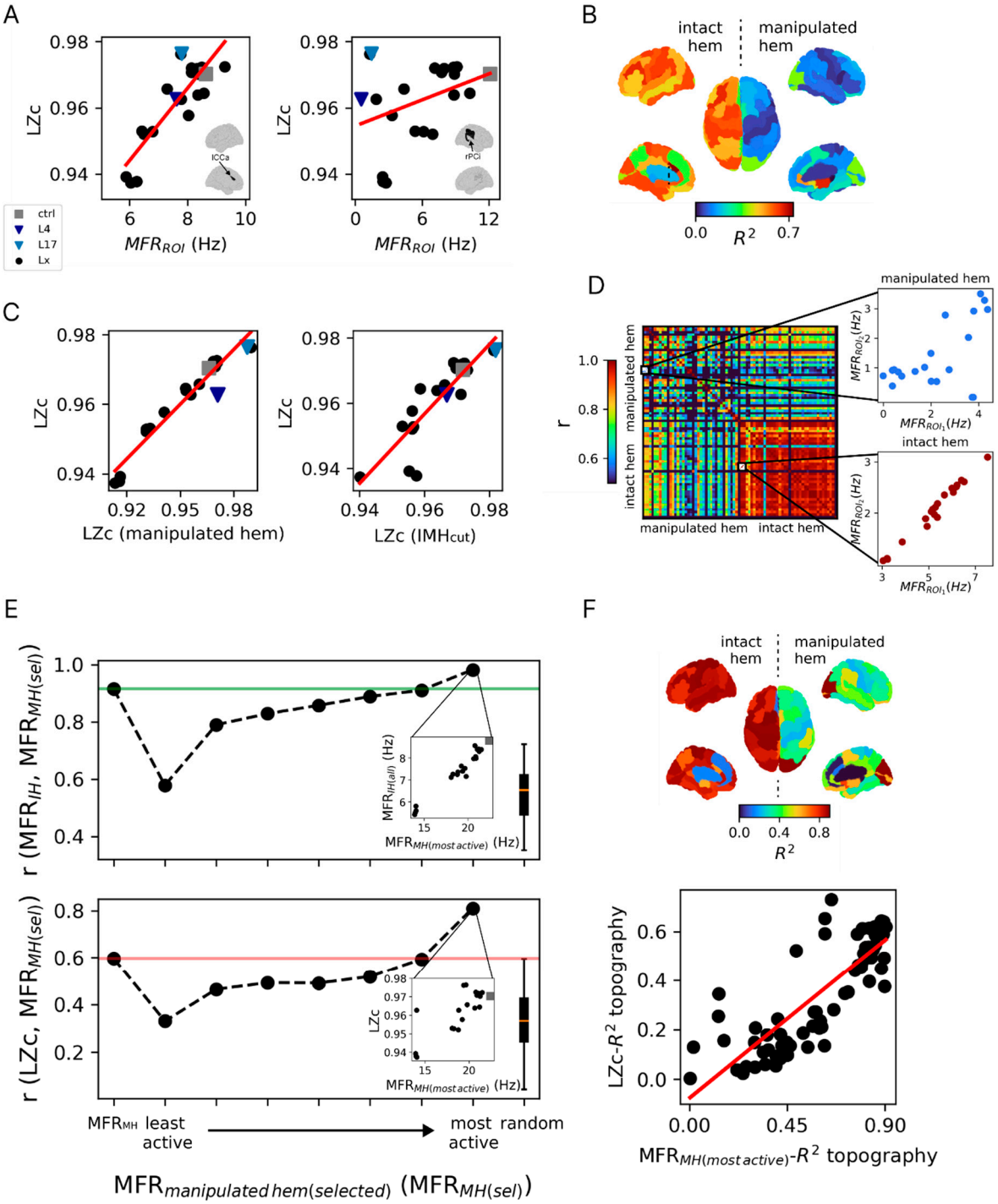

Figure S6. Characterization of the LZc-R² topography. A) Linear regression of LZc (NC) versus MFR for the example ROIs lCCa and rPCi (LZc: lCCa-R^2=0.732, p=10^{-6}, rPCi-R^2=0.131, p=0.11. B) Topographies of the coefficient of determination (R^2) of the linear regressions for LZc. C) Left panel: correlation (r=0.97, p=$8{\cdot}10^{-13}$) between LZc (all nodes) and LZc computed only over the manipulated hemisphere (MH). Right panel: correlation (r=0.88, p=$2{\cdot}10^{-7}$) between LZc (all nodes) and LZc with connections from the Intact to the manipulated hemisphere removed (IMH_{cut}). D) Correlation matrix of node activity (MFR) across local manipulations. The intact and the manipulated hemispheres are specified in the figure. MFR scatter plots for two exemplary nodes (ROI_1 and ROI_2) across local manipulations for the intact and the manipulated hemispheres. E) Top panel: Pearson correlation coefficient (r) calculated between the MFR of selected nodes in the manipulated hemisphere

($MFR_{MH(sel)}$) and the MFR of the intact hemisphere (MFR_{IH}). 'Random' denotes a random sampling of 5 nodes (without replacement, 100 repetitions) and the boxplot of the corresponding correlation values between $MFR_{MH(random)}$ and MFR_{IH} are reported. The inset is relative to the scatter plot with the highest correlation between $MFR_{MH(most\ active)}$ and MFR_{IH} ($r=0.98$, $p=4\cdot10^{-15}$). The horizontal green line marks the value of r ($=0.93$, $p=2\cdot10^{-9}$) when all nodes of the manipulated hemisphere are selected (MFR_{MH}). Bottom panel: the same procedure is repeated with LZc instead of MFR_{IH}. The inset is relative to the scatter plot with the highest correlation between $MFR_{MH(most\ active)}$ and LZc ($r=0.81$, $p=8\cdot10^{-6}$). The horizontal red line indicates the value of r ($=0.61$, $p=0.003$) when all nodes of the manipulated hemisphere are selected (MFR_{MH}). F) Top panel: the coefficients of determination of the linear regressions $MFR_{MH(most\ active)}$ (panel E) vs MFR_{ROI} are reported in the topographic map. Bottom panel: the R^2 values of the linear regressions $MFR_{MH(most\ active)}$ vs MFR_{ROI} ($MFR_{MH(most\ active)}$-R^2 topography, x-axis) and LZc vs MFR_{ROI} (LZc-R^2 topography, y-axis) correlated well ($r=0.83$, $p=10^{-19}$).

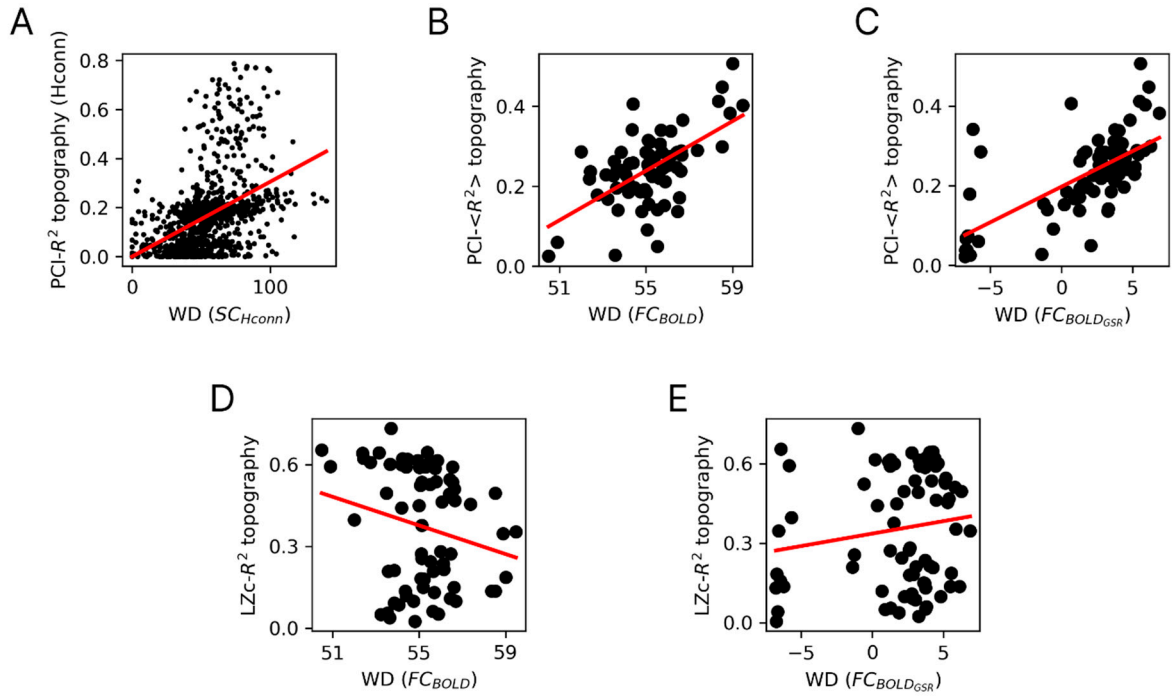

Figure S7 Network metrics of centrality correlate with complexity topographies. A) The weighted degree (WD) of structural connectivity (SC) nodes in Hconn correlated with the PCI-R^2 topography (Pearson correlation: r=0.44 p=$2 \cdot 10^{-49}$; spearman correlation: rho=0.51, p= $4 \cdot 10^{-68}$). B) and C) The WD of the nodes of the functional connectivity extracted from the BOLD signal without or with global signal regression (GSR; FC_{BOLD}, $FC_{BOLDGSR}$, respectively) displayed a significant correlation with the PCI-<R^2> topography (FC_{BOLD}: r=0.6, p= $6 \cdot 10^{-8}$, $FC_{BOLDGSR}$: r=0.65, p=10^{-10}). D) and E) The same analysis showed a nonsignificant correlation between the WD and LZc-R^2 topography (p=0.074 and p=0.17, respectively). Each point is representative of a node in the network. In the panels B and D points with WD<50 (of the FC_{BOLD}) were considered outliers and excluded from the analysis. When all points are considered, comparable results are observed (r=0.51, p=$2 \cdot 10^{-6}$; p=0.081 for panels B and D, respectively).

2.4 Article 4

Title: *Slow Wave Generation and Propagation in a Model of Brain Lesion*

Authors: ***Gianluca Gaglioti****, ***Leonardo Dalla Porta****, *Michele Colombo, Simone Russo, Thierry Nieus, Gustavo Deco, Maurizio Corbetta, Simone Sarasso, Maria V. Sanchez-Vives, Marcello Massimini*

Abstract: *Slow waves (SWs), the hallmark of non-rapid eye movement (NREM) sleep, reflect the periodic occurrence of transient silent periods in cortical neurons (Down states). During NREM, SWs and Down states physiologically disrupt large-scale network interactions. Since early EEG studies, SWs have also been observed in awake patients after brain injury. Emerging evidence indicates that these intrusions of sleep-like activity interfere with ongoing network activity and contribute to motor and cognitive deficits; yet, the mechanisms governing the generation and spread of post-lesional SWs remain unclear. Here, we extend a neural mass model of EEG to capture transitions between wake-like and sleep-like dynamics and embed it in connectome-based networks with virtual lesions. This model supports that local disfacilitation, topology-dependent propagation, and synchrony-dependent amplification throughout the connectome are sufficient to produce post-lesional SWs. These mechanisms reproduce the spatial gradients of post-lesional SWs previously reported in patient studies, and identify actionable targets for neuromodulation and rehabilitation.*

DOI: *https://doi.org/10.1016/j.neuroimage.2026.121817*

**These authors contributed equally*

NeuroImage 329 (2026) 121817

Contents lists available at ScienceDirect

NeuroImage

journal homepage: www.elsevier.com/locate/ynimg

Slow wave generation and propagation in a model of brain lesions

Gianluca Gaglioti [a,b,*,#], Leonardo Dalla Porta [c,*], Michele Angelo Colombo [a], Simone Russo [d], Thierry Nieus [e], Gustavo Deco [f,g], Maurizio Corbetta [h,i], Simone Sarasso [a], Maria V. Sanchez-Vives [c,f], Marcello Massimini [a,j,#]

[a] Department of Biomedical and Clinical Sciences, University of Milan, Milan, Italy
[b] Department of Philosophy "Piero Martinetti", University of Milan, Milan, Italy
[c] Institute of Biomedical Research August Pi Sunyer (IDIBAPS), Barcelona, Spain
[d] Wallace H Coulter Department of Biomedical Engineering, Georgia Institute of Technology and Emory University, Atlanta, GA, USA
[e] Department of Environmental Science and Policy, University of Milan, Milan, Italy
[f] ICREA, Barcelona, Spain
[g] Department of Information and Communication Technologies, Universitat Pompeu Fabra, Center for Brain and Cognition, Barcelona, Spain
[h] Department of Neuroscience and Padova Neuroscience Center (PNC), University of Padova, Padova, Italy
[i] Veneto Institute of Molecular Medicine (VIMM), Padova, Italy
[j] IRCCS Fondazione Don Carlo Gnocchi ONLUS, Milan, Italy

ARTICLE INFO

KeyWords:
Cortical bistability
Slow waves
Computational modeling
Network synchronization
Stroke

ABSTRACT

Slow waves (SWs), the hallmark of non-rapid eye movement (NREM) sleep, reflect the periodic occurrence of transient silent periods in cortical neurons (Down states). During NREM, SWs and Down states physiologically disrupt large-scale network interactions. Since early EEG studies, SWs have also been observed in awake patients after brain injury. Emerging evidence indicates that these intrusions of sleep-like activity interfere with ongoing network activity and contribute to motor and cognitive deficits; yet, the mechanisms governing the generation and spread of post-lesional SWs remain unclear. Here, we extend a neural mass model of EEG to capture transitions between wake-like and sleep-like dynamics and embed it in connectome-based networks with virtual lesions. This model supports that local disfacilitation, topology-dependent propagation, and synchrony-dependent amplification throughout the connectome are sufficient to produce post-lesional SWs. These mechanisms reproduce the spatial gradients of post-lesional SWs previously reported in patient studies, and identify actionable targets for neuromodulation and rehabilitation.

1. Introduction

Brain lesions can affect remote areas beyond the site of structural injury (Carrera and Tononi, 2014, Fornito et al., 2015, Baldassarre et al., 2016), disrupting network-level communication and impairing cognitive and behavioral function (Grefkes et al., 2008, Siegel et al., 2016, Bottom-Tanzer et al., 2024, Latifi and Carmichael, 2024), a phenomenon known as diaschisis (von Monakow, 1914). Understanding the neuronal mechanisms underlying these network-wide effects remains a fundamental challenge in neurology, carrying important implications for rehabilitation and treatment (Carrera and Tononi, 2014). In 1937, Grey Walter first described the appearance of slow waves (SWs) similar to those observed during NREM sleep in the brains of patients with brain lesions (Walter, 1937). Recent evidence suggests that these SWs may play a crucial role in mediating the large-scale functional network alterations following focal brain injury (Massimini et al., 2024).

SWs emerge when a large neuronal population alternates synchronized periods of neuronal firing (Up states) and neuronal silence (Down states) (Steriade et al., 1993, Sanchez-Vives and McCormick, 2000, Luczak et al., 2007, Chauvette et al., 2010), a phenomenon also referred to as cortical bistability (Nir et al., 2011). This dynamics can be described as a slow oscillation (SO), emphasizing the ongoing rhythmic alternation between Up and Down states, while individual cycles or large-amplitude deflections are commonly referred to as SWs. Mechanistically, Down states occur because of neuronal adaptation mediated by activity-dependent K^+ currents (Compte et al., 2003), as well as

Corresponding authors.
E-mail addresses: gianluca.gaglioti@unimi.it (G. Gaglioti), marcello.massimini@unimi.it (M. Massimini).
* These authors contributed equally to this work

https://doi.org/10.1016/j.neuroimage.2026.121817
Received 4 December 2025; Received in revised form 2 February 2026; Accepted 16 February 2026
Available online 21 February 2026

because of reductions in excitatory drive (disfacilitation) (Timofeev et al., 2001) and/or inhibitory activity (Zucca et al., 2017, Perez-Zabalza et al., 2020). Although SWs are most prominent during NREM sleep, they can also occur locally during physiological wakefulness, especially after sleep deprivation (Vyazovskiy et al., 2011, Bernardi et al., 2015, Nir et al., 2017, Andrillon et al., 2021, Marmelshtein et al., 2023). SWs have also been observed in awake subjects following brain lesions, where they are most pronounced around the site of injury but can also extend to distant foci (Walter, 1937, Gloor et al., 1977, Nuwer et al., 1987).

The mechanisms of post lesional SWs are still elusive, and multiple factors may be at play (Massimini et al., 2024). Depending on lesion extent and location, disconnection may locally disrupt ascending activating inputs, enhancing activity-dependent adaptation mechanisms (Meythaler et al., 2001, Schiff, 2008, D'Ambrosio et al., 2023), and/or disrupt lateral excitatory connections, causing disfacilitation and excitation/inhibition unbalance (Zucca et al., 2017, Imbrosci and Mittmann, 2011, Kim et al., 2014, Funk et al., 2017, Santos et al., 2023). Once generated, SWs can then propagate across connected regions (D'Ambrosio et al., 2023, Russo et al., 2021), thus interfering with the functional dynamics of large-scale networks. SWs are known to disrupt network interactions and their intrusion in the brain of awake patients is clinically relevant (Vyazovskiy et al., 2011, Nir et al., 2017, Andrillon et al., 2021). Hence, understanding the mechanisms responsible for the generation and propagation of post-lesional SWs during wakefulness is essential to explain—and ultimately re-normalize—the functional consequences of brain injury.

In the present study, we tackle this question by adopting a multiscale computational approach. Large-scale computational models combine biologically informed network architecture from neuroimaging with node-level neural dynamics (Deco et al., 2008, Breakspear, 2017), allowing us to examine how local interactions scale up to complex systems behavior in health and disease. This framework has already proven useful in epilepsy research (Traub and Wong, 1982), where it is extensively used to study seizure initiation and propagation (Jirsa et al., 2017, Proix et al., 2017, Rigney et al., 2021).

Here, we develop a novel computational approach to study generation and propagation of SWs in cortical networks following brain injury. We adopt a Jansen-Rit (JR) model (Jansen and Rit, 1995), which has been extensively used to simulate spontaneous and evoked electroencephalography (EEG) and local field potential (LFP) oscillatory dynamics in awake-like conditions (David and Friston, 2003, Coronel-Oliveros et al., 2023, Sanchez-Todo et al., 2023, Momi et al., 2023, Momi et al., 2025, Koller et al., 2024). Since the original formulation lacks the adaptation dynamics required to reproduce SWs (Camassa et al., 2022), we extended the JR model by introducing an activity-dependent adaptation mechanism (Fig. 1A–C) (Moran et al., 2007), enabling the model to capture the transition between wake-like and sleep-like states. Finally, by embedding this extended model into simplified motifs, topologically organized networks, and whole-brain connectomes, we systematically examined whether and how virtual lesions—mimicking either disconnection from ascending inputs or disruption of lateral cortico-cortical connectivity—give rise to perilesional SW generation and large-scale propagation (Fig. 1D).

2. Methods

2.1. Jansen-Rit model with spike-frequency adaptation

The Jansen-Rit (JR) model (Jansen and Rit, 1995) describes the temporal evolution of postsynaptic membrane potentials and firing rates of interconnected neuronal pools, representing pyramidal neurons (pyr), excitatory interneurons (IN_e), and inhibitory interneurons (IN_i) (Fig. 1A). In this study, we used the implementation of the JR model available in The Virtual Brain (TVB) simulator and extended it by introducing a spike-frequency adaptation mechanism (Moran et al., 2007). The dynamics of the neuronal pools evolve according to the following set of differential equations:

$$\frac{dy_0}{dt} = y_3 \tag{1}$$

$$\frac{dy_1}{dt} = y_4 \tag{2}$$

$$\frac{dy_2}{dt} = y_5 \tag{3}$$

$$\frac{dy_3}{dt} = Aa\,Sigm(y_1 - y_2) - 2ay_3 - a^2 y_0 \tag{4}$$

$$\frac{dy_4}{dt} = Aa\left[\mu + a_2 J\,Sigm\left(a_1 J\left[y_0 - g\omega\right]\right) + E\right] - 2ay_4 - a^2 y_4 \tag{5}$$

$$\frac{dy_5}{dt} = Bb\left[a_4 J\,Sigm\left(a_3 J y_0\right)\right] - 2by_5 - b^2 y_2 \tag{6}$$

where y_0, y_1, and y_2 represent the average postsynaptic membrane potentials (PSP) of pyr, IN_e, and IN_i, respectively. y_3, y_4, and y_5 represent the PSP time derivatives. The parameters A and B represent the maximum amplitudes of excitatory and inhibitory postsynaptic potentials (EPSP and IPSP), while a and b are the inverse time constants governing synaptic dynamics. μ is the mean firing rate input to IN_e pool, J represents the average number of synapses between neuronal pools, and a_1, a_2, a_3, a_4 are weight coefficients determining the strength of synaptic connections.

Neuronal pools convert input membrane potentials into output firing rates through a sigmoidal activation function (Voltage-to-Firing, Fig. 1A):

$$Sigm(v) = \frac{2\nu_{max}}{1 + e^{r(v_0 - v)}} \tag{7}$$

where ν_{max} is the maximum firing rate, v_0 is the PSP threshold for which 50% firing rate is achieved and r determines the steepness of the sigmoidal function.

In Eq. 5, E represents the excitatory network input. The input to a given node *i* at time *t* is defined as the sum of the contributions from all nodes projecting to node *i*, expressed as:

$$E_i(t) = c\sum_{j=1}^{n} w_{ij} \cdot Sigm\left(y_{1j}\left[t - \tau_{ij}\right] - y_{2j}\left[t - \tau_{ij}\right]\right) \tag{8}$$

where w_{ij} is the connection weight from presynaptic node *j* to postsynaptic node *i*, and τ_{ij} represents the time delay between *i* and *j*. The term c is the global coupling factor that scales all the connection weights. Thus, the effective excitatory coupling strength between *j* and *i* is given by the product of w_{ij} and c, and we denote it by C_{ij}.

Spike-frequency adaptation (ω) is included as a slow dynamic process affecting the excitatory feedback loop:

$$\frac{d\omega}{dt} = k_\omega\left[Sigm\left(a_1 J\left[y_0 - g\omega\right]\right) - \omega\right] \tag{9}$$

where k_ω is the adaptation rate constant and *Sigm* is the sigmoidal input-output function of IN_e (Eqs. 5, 7; Fig. 1A-C). This formulation, proposed by Moran and collaborators, extends the classical Jansen-Rit model by incorporating an adaptation mechanism that reflects the activity-dependent reduction in neuronal excitability observed experimentally (Moran et al., 2007). This equation conforms to a universal phenomenological model (Benda and Herz, 2003), which captures the essential dynamics of activity-dependent adaptation across a wide range of mechanisms and cell type: higher activity leads to a subsequent, relatively slow increase of the adaptation current. Increased adaptation shifts the system's input-output (Voltage-to-Firing) curve to the right

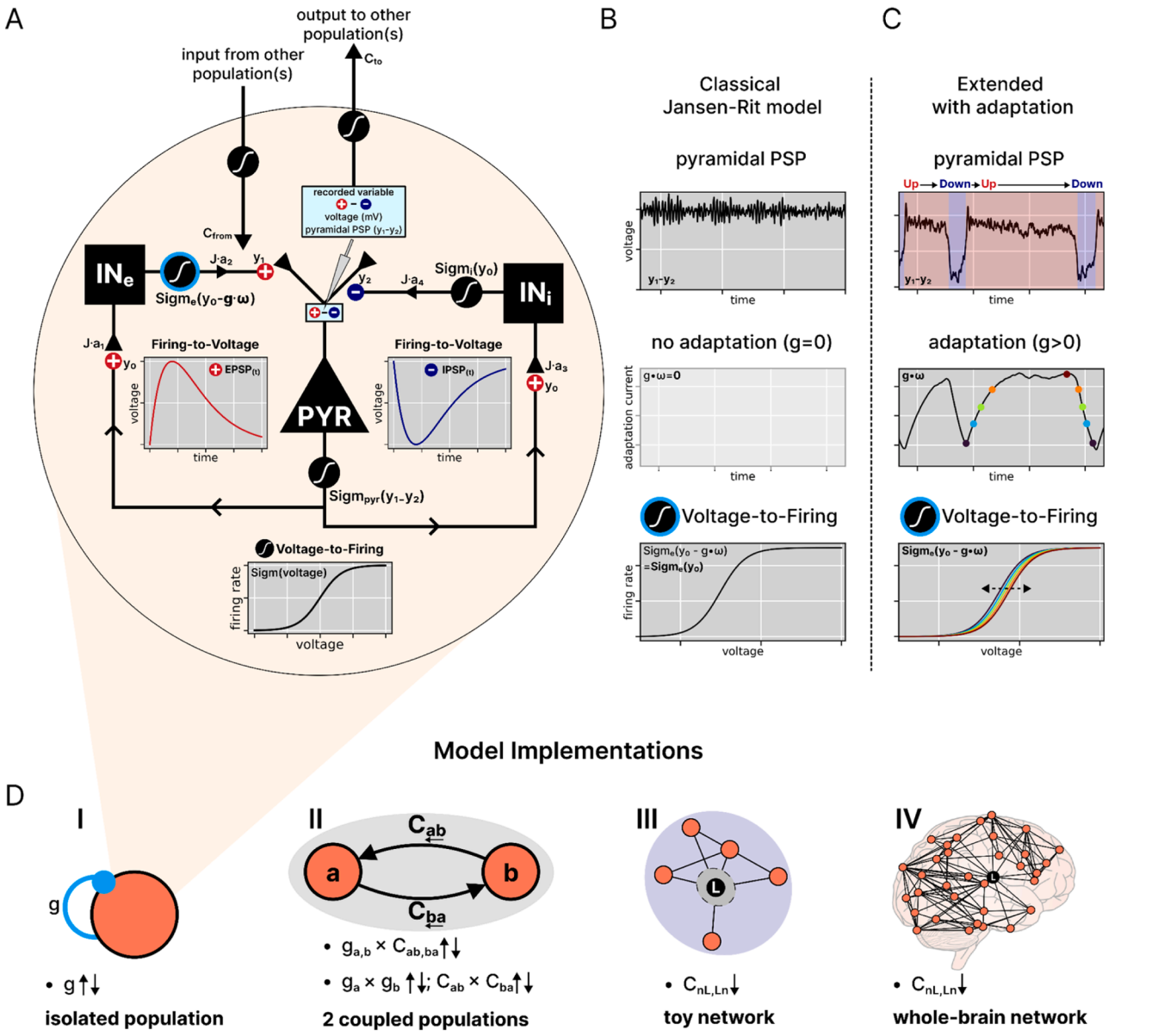

Figure 1. Extension of the neural mass model with spike-frequency adaptation mechanism across different scales: from a single-population to whole-brain network. (A) Representation of the Jansen-Rit (JR) model loop (Gast et al., 2019), consisting of interconnected neuronal pools: pyramidal neurons (PYR), excitatory interneurons (IN_e), and inhibitory interneurons (IN_i). The model converts postsynaptic potentials back to firing rates via Voltage-to-Firing sigmoidal functions (Sigm) and transforms firing rates into postsynaptic potentials through Firing-to-Voltage operators. These Firing-to-Voltage operators differed for excitatory and inhibitory synapses (⊕ and ⊖, respectively). Excitatory postsynaptic potential (EPSP) generating functions are shown in red, while inhibitory postsynaptic potential (IPSP) generating functions are shown in blue. The IPSP is represented as negative for illustrative purposes to highlight its inhibitory effect on the pyramidal population. The recorded variable represents the pyramidal postsynaptic potential (PSP = y_1 - y_2), reflecting the net average postsynaptic potential from both excitatory and inhibitory inputs impinging on pyramidal neurons. This PSP is conventionally used as a proxy for EEG or LFP activity and its voltage-to-firing transformation establishes the communication among populations. Parameter definitions: J represents the average number of synapses between neuronal pools; a_1, a_2, a_3, a_4 are weight coefficients determining synaptic connection strength; y_0, y_1, y_2 denote average postsynaptic membrane potentials of pyramidal, excitatory interneuron, and inhibitory interneuron populations, respectively. Notably, two parameters define the spike frequency adaptation, thereby extending the classical Rit-Jensen model: g is the constant that controls adaptation strength; ω represents the adaptation state-variable over time. Comparison between classical Jansen-Rit model (B) and extended version with adaptation (C). (B) The classical model generates standard pyramidal PSP oscillations without adaptation (coinciding with g=0). (C) Extended model with adaptation (g>0) exhibits Up and Down dynamics. The adaptation mechanism shifts the sigmoidal Voltage-to-Firing curve rightward during periods of high activity, reducing neuronal responsiveness and creating characteristic Up-to-Down state transitions observed in neural recordings; vice versa a leftward shift of the sigmoid increase sensitivity to input voltage during quiet periods, leading to Down-to-Up state transitions. (D) Schematic representations of the network scales explored in the study. I. *Isolated population*: single JR population model with variations in synaptic adaptation strength. II. *Two-coupled populations*: two coupled JR populations with symmetric and asymmetric variations in adaptation g and excitatory coupling C. In the symmetric case, the parameters were varied equally in a and b (i.e., $g_{a,b} \times C_{ab,ba}$). In the asymmetric case, the parameters were varied independently in the two populations (i.e., $g_a \times g_b$, and $C_{ab} \times C_{ba}$). III. *Toy network*: simplified network exploring lesion effects. The lesion was implemented by disconnecting the lesion node (L) (i.e., setting to 0 all the incoming connections C_{Ln}, and outgoing connections C_{nL}). IV. *Whole-brain network*: large-scale model based on human structural connectivity data, investigating the effects of lesions on brain-wide dynamics. Lesions were implemented as in the toy network. Adaptation is implemented at all scales (I–IV). It is depicted as a self-loop (light blue circle) only in the isolated population panel for clarity, to highlight its activity-dependent nature.

(Fig. 1C), requiring stronger depolarizing input to achieve the same firing rate in output. Due to the nonlinear sigmoidal shape, adaptation reduces the system's responsiveness by decreasing the local gain (slope). Compared to the original formulation (Moran et al., 2007) using only the adaptation variable ω, we introduced a scaling factor g that modulates its influence on the input–output function, thereby explicitly controlling the adaptation strength. When g=0, there is no adaptation, and the system reduces to the classical JR formulation (Fig. 1B).

Following the TVB convention, external noise is defined within the stochastic integration scheme and, in our case, it enters as an additive term in Eq. 5, simulating the spontaneous background activity at each node (Jansen and Rit, 1995). Noise was modelled as a white noise process with a standard deviation $sd_{noise}=10^{-4}$. The system was solved using the Heun stochastic method with a time step of 1 ms (Jansen and Rit, 1995), starting from random initial conditions and discarding the first 5 seconds of transient activity. The model parameters are listed in

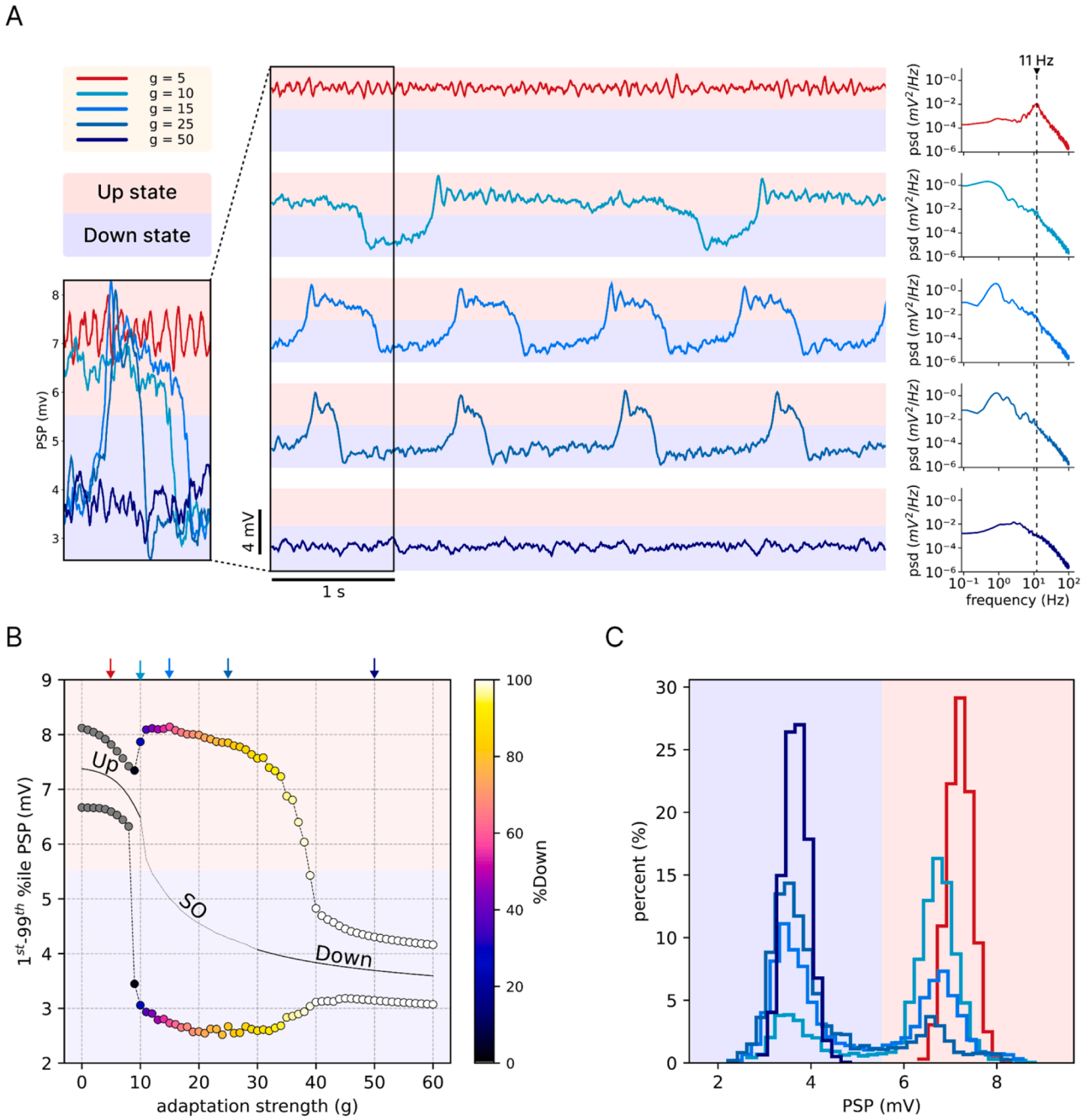

Figure 2. Adaptation induces Up and Down dynamics in an isolated cortical population model. (A) Postsynaptic potential (PSP) traces for different adaptation strength values (g). Low g (top) leads to persistent Up state, while increasing g induces slow oscillations (SO), characterized by alternating Up and Down states. For high g (bottom), the system remains in a persistent Down state. Right panels show the power spectral density (psd) for each case. (B) Bifurcation diagram showing the 1st and 99th percentiles of PSP as a function of g. Three distinct dynamical regimes are observed: persistent Up state (gray dots, left), SO (colored region, middle), and persistent Down state (white dots, right). The color scale indicates the percentage of time spent in the Down state (%Down). The solid black line indicates the presence of a stable fixed-point attractor, corresponding to a high-voltage Up state for low values of g (left) and a low-voltage Down state for sufficiently high g (right). The vertical arrows above the plot denote the cases illustrated in panel (A), with colors matching the corresponding adaptation strength g. (C) Distribution of PSP values for the five cases shown in (A). At low and high g, the distribution is unimodal, reflecting stable Up and Down states, respectively. At intermediate g, a bimodal distribution emerges, corresponding to SO dynamics.

Supplementary Table S1.

The recorded variable in this study was the pyramidal postsynaptic potential (Fig. 1A), representing the net average postsynaptic potential, considering both excitatory and inhibitory input voltages impinging on pyramidal neurons (PSP = y_1 - y_2), which is conventionally used as a proxy for EEG or LFP activity in the source space (David and Friston, 2003, Momi et al., 2023, Momi et al., 2025).

2.2. Isolated population model

A single JR population model (Fig. 1D-I) was implemented as a system of seven first-order ordinary differential equations (ODEs) as described by Eqs. 1-9 (excluding the network input). Bifurcation and fixed-point analyses of the deterministic JR model were performed using XPPAUT (Ermentrout, 2012). The bifurcation parameters were the average number of synapses between neuronal pools (J) and the adaptation strength (g), which were varied independently to assess changes in the qualitative behavior of the system. Local stability of fixed points was determined by XPPAUT via linearization around equilibria and computation of the eigenvalues of the Jacobian matrix. The stochastic version of the model was implemented in TVB and was used for all subsequent simulations of the study. The bifurcation diagram was constructed by collecting the 1st and 99th percentiles of PSP activity as a function of g. For each value of g, an independent simulation of 30s was performed, with g varied in steps of 1. The code used to run these analyses (in XPPAUT and TVB) is available on GitHub at https://github.

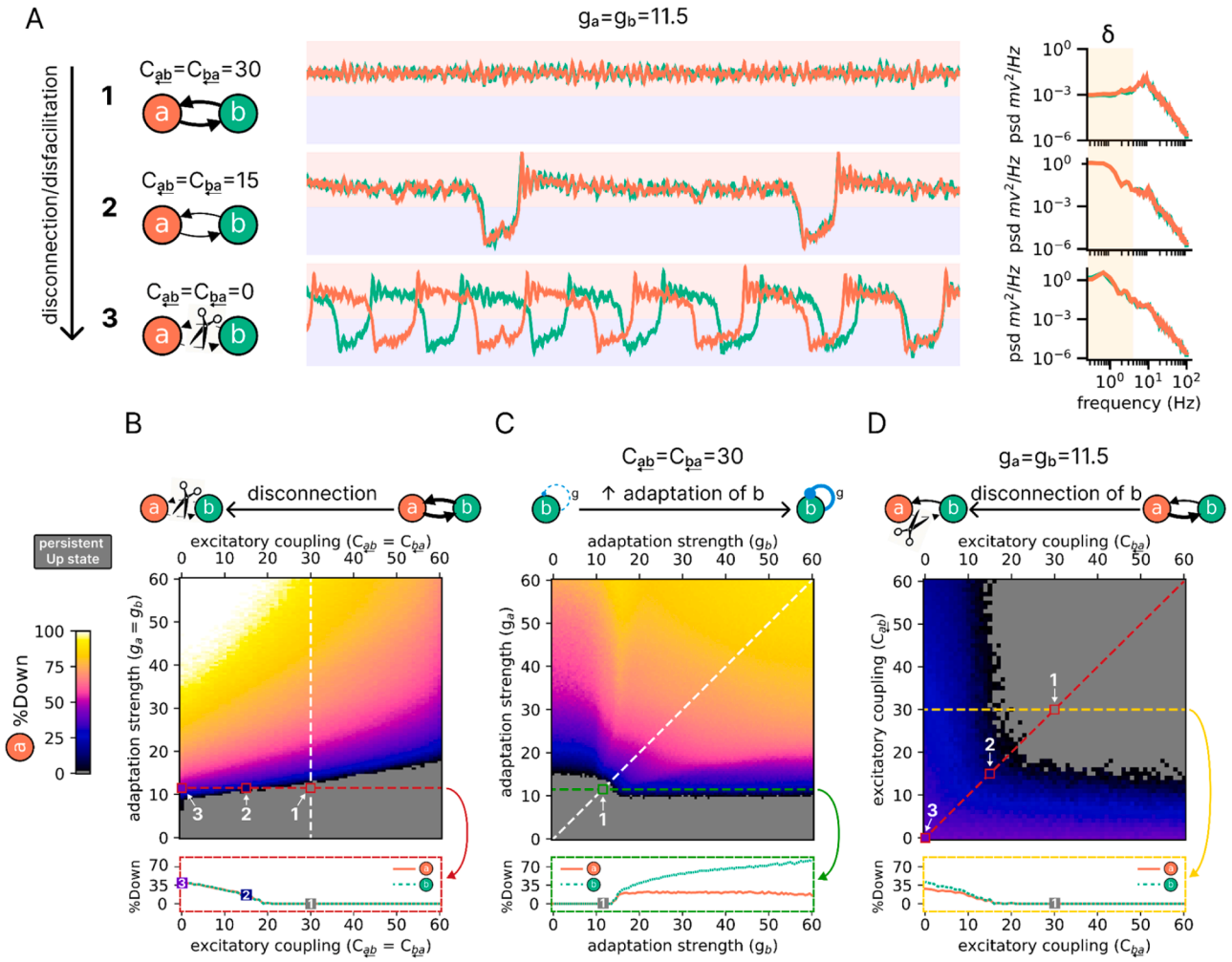

Figure 3. Effects of adaptation strength and excitatory coupling on slow wave emergence in two coupled populations. (A) Example dynamics of two symmetrically coupled populations (JR_a in orange, JR_b in cyan) for three levels of excitatory coupling (C_{ab}=C_{ba}). With C=30 and g=11.5 (top, #1), both populations show alpha oscillations in a persistent Up state. Reducing coupling to C=15 (middle, #2) induces a transition to slow oscillations (SO), reflected in an increase in δ power. Complete disconnection (C=0, bottom, #3) further enhances SO activity. Right panels show the corresponding power spectral densities (psd), with the δ band highlighted by the yellow span. (B) Heatmap showing the percentage of time spent in the Down state (%Down) in JR_a as a function of adaptation strength (g, y-axis) and symmetric excitatory coupling (C, x-axis). The red horizontal dashed line highlights the effect of reducing C at g=11.5, revealing a transition from a persistent Up state (gray region) to SO (colored region). Bottom panel: %Down along the red horizontal dashed line, illustrating the progressive reduction of SO with increasing C. (C) Effect of asymmetric adaptation. Heatmap shows %Down in JR_a as a function of g_b (x-axis) and g_a (y-axis), with symmetric coupling fixed at C=30. The white diagonal dashed line corresponds to the vertical white dashed line in panel A. The green horizontal dashed line indicates that varying g_b alone can induce a transition from a persistent Up state to SO in JR_a, despite g_a being constant. Bottom panel: %Down along the green dashed line, showing that in JR_b (where g varies) the time in the Down state increases continuously, whereas in JR_a (where g is fixed) it increases but quickly reaches a plateau. (D) Effect of asymmetric coupling. Heatmap shows %Down in JR_a as a function of C_{ba} (x-axis) and C_{ab} (y-axis), with g fixed at 11.5. The diagonal red dashed line corresponds to the horizontal red dashed line in panel B. The yellow dashed line illustrates that reducing C_{ba} (i.e., disconnecting JR_b) alone is sufficient to induce a transition from a persistent Up state to SO in JR_a, even when C_{ab} remains constant. Bottom panel: %Down along the yellow dashed line, emphasizing the dependence of the transition on directional disconnection. Numbers 1, 2, and 3 in all panels correspond to identical parameter configurations across plots. The corresponding heatmaps for population JR_b is shown in Supplementary Fig. S2.

com/gianlucagag/SWs-lesion_model

2.3. Two-population model

To assess the effects of cortical disconnection on the emergence of SWs, a two-population model was implemented (Fig. 1D-II). The model consisted of two JR populations, labeled JR_a and JR_b, which were coupled by bidirectional excitatory connections with no time delays. The system behavior was explored parametrically as a function of both symmetric and asymmetric variations of the adaptation strength (g) and the excitatory coupling strength (C) in the two populations, constructing 2D bifurcation diagrams in the parameter space. In the symmetric case, the parameters were varied equally in JR_a and JR_b (i.e., g vs C, where $g_a=g_b$, and $C_{ab}=C_{ba}$) (Fig. 3 A). In the asymmetric case, the parameters were varied independently in the two populations (i.e., g_a vs g_b, in Fig. 3B and C_{ab} vs C_{ba}, where $g_a \neq g_b$ and $C_{ab} \neq C_{ba}$ in Fig. 3D). Each simulation corresponding to a specific parameter configuration was run independently and lasted 30s. In these analyses, g was varied from 0 to 60 in steps of 0.5, while C was varied from 0 to 60 in steps of 1.

2.4. Toy network model

To relate the generation and propagation of SWs to simplified network motifs, a toy network model was implemented (Fig. 1D-III), incorporating delays, with physical distances and signal propagation velocity (v = 4 m/s) consistent with cortico-cortical connections (Lemaréchal et al., 2021). The network consisted of a perilesional sub-network of five nodes (denoted L_k nodes, k=1..5) and a distant chain of three nodes (denoted D_k nodes, k=1..3). The connection weights w_{ij} were normalized such that the sum of the in-degree weights of each node was equal to 1. With this normalization, the total excitatory input coupling to each node is determined by the global coupling factor c. To maintain the same level of excitability at each node, c was set to 30, as explored in the two-population model. The effective excitatory coupling between a presynaptic node *j* and a postsynaptic node *i* is therefore $C_{ij} = Cw_{ij}$ (Eq. 8). In the perilesional network, each node had two afferent nodes, such that lesioning (disconnecting) any node resulted in a 50% reduction in the excitatory input to the connected L_k nodes. Lesions were simulated by setting all in- and out-degree weights of the lesioned node to zero. Twenty simulations were performed for each lesion condition and compared to a control condition (no lesion). Each simulation lasted 100s.

2.5. Human whole-brain network model

For the human brain network simulations, the model was implemented using structural brain connectivity data (Fig. 1D-IV). An open dataset was utilized, which provides brain structural connectivity matrices ready for modeling (Škoch et al., 2022). The dataset contains structural connectivity matrices from 88 healthy subjects. The matrices represent the connectivity among 90 cortical regions of interest (ROIs) as defined by Automatic Anatomical Labeling (AAL) (Tzourio-Mazoyer et al., 2002) (Supplementary Fig. S4). The 10 non-cortical regions were excluded since the JR model is designed for cortical networks only. Connectivity matrices were averaged across subjects, and only connections present in more than 50% of the subjects were retained, to obtain a sparse matrix retaining the typical within-subject density (de Reus and van den Heuvel, 2013). Subsequently, the weighted in-degree normalization was applied, and c=30 was set, as performed in the toy network. This normalization serves as a form of homeostatic regulation, equalizing the excitatory inputs received by the nodes while preserving the structural topology (Coronel-Oliveros et al., 2023). A control simulation was first run, followed by simulations in which each of the 80 nodes was lesioned (as in the toy network), and the effects on the remaining 79 nodes were analyzed. Each simulation lasted 100s.

2.6. Down state statistics

To detect *Down states* in the PSP, a fixed threshold (*th*) was used based on a model parameter representing the firing threshold (v_0). v_0 =5.52 mV corresponds to the PSP value for which a 50% firing rate is achieved (Jansen and Rit, 1995). In other words, it is the input value in mV at the inflection point of the sigmoidal input-output function. The system was considered to be in a *Down state* whenever the PSP fell below v_0 (i.e. PSP<*th*), and in an *Up state* when the PSP exceeded it (i.e. PSP≥*th*). This simple threshold was chosen to effectively distinguish between low and high activity states in the simulation.

The %Down variable quantifies the percentage of time a node spends in the Down state. For a given node *i*, it was computed as the ratio of time spent in the *Down state* to the total simulation time, expressed as a percentage

$$\%\text{Down}_i = \frac{\sum_t (PSP_i(t) < th)}{T} \times 100 \tag{10}$$

where $PSP_i(t)$ is the PSP of node *i* at time t, and T is the total simulation time.

The DownOverlap was computed as the percentage of time during which the PSP signals of two nodes simultaneously fell below the Down state threshold (*th*, Fig. 5C). For example, given nodes *i* and *j*, with corresponding signals PSP_i and PSP_j, the DownOverlap for node *i* relative to node *j* is defined as

$$\text{DownOverlap}_{i|j} = \frac{\sum_t \left(PSP_i(t) < th \wedge PSP_j(t) < th\right)}{\sum_t (PSP_i(t) < th)} \times 100 \tag{11}$$

This measure quantifies the fraction of time points where both node *i* and node *j* are in the Down state, relative to the total *Down state* time of node *i*. Thus, the DownOverlap is directional: $\text{DownOverlap}_{i|j}$ is computed with the denominator depending only on node *i*, while $\text{DownOverlap}_{j|i}$ uses the same numerator but normalizes by the *Down states* of node *j*. The DownOverlap reflects the coherence of the SWs processes between the two nodes, with higher values indicating stronger synchronization of their Down *state* transitions.

The Neighborhood %Down (NBR %Down) was calculated in each node to quantify the amount of SW activity arriving from afferent nodes in a given neighborhood of interest. For a given node *i*, it was computed as the average time spent in down states (%Down, Eq. 10) of the nodes directly connected to *i*:

$$\text{NBR\%Down}_i = \frac{1}{|\mathcal{N}_i|} \sum_{j \in \mathcal{N}_i} \%\text{Down}_j \tag{12}$$

where N_i denotes a neighborhood of interest for node *i* (specified differently for the toy network and for the whole brain, see below), that is, a set of nodes projecting to node *i*; $|N_i|$ denotes its cardinality (i.e., the number of such nodes).

The *Neighborhood* DownOverlap (NBR DownOverlap) was computed in each node to quantify the temporal overlap of SW activity arriving from afferent nodes in the given neighborhood of interest (see below), thus reflecting the coherence of the SWs processes impinging on a node. For a given node *i*, it was calculated as the average DownOverlap across all ordered node pairs in the given neighborhood of interest N_i excluding self-connections:

$$\text{NBR DownOverlap}_i = \frac{1}{|\mathcal{N}_i|(|\mathcal{N}_i| - 1)} \sum_{(j,k) \in \mathcal{N}_i \times \mathcal{N}_i, j \neq k} \text{DownOverlap}_{j|k} \tag{13}$$

where $\text{DownOverlap}_{j|k}$ denotes the DownOverlap of node *j* relative to node *k*, computed over all ordered pairs of afferent nodes to *i*.

The neighborhood of interest differed for the toy network and for the whole-brain model. In the toy network simulations, the neighborhood of the nodes in the distant network was defined by including only afferent

connections originating from the perilesional network, thereby focusing only on the impact of perilesional activity on the distant network.

For the whole-brain model, the *N* was computed by thresholding the structural connectivity matrix and retaining only the top 5% of the strongest connections across the network (while the simulation itself used the full, unthresholded connectome). This threshold highlighted a connected subset of the network that included all network nodes, and was chosen to focus on the most influential connections, given the high number of weak connections in the structural connectivity that are unlikely to strongly affect the dynamics. Control analyses varying this threshold showed that results remained stable when retaining between the top 25% and top 1% of the strongest connections.

2.7. Structural connectivity metrics

Structural connectivity metrics were used to quantify the effects of the lesion on the spared nodes. The distance from the lesion was computed as the Euclidean distance between each node and the lesion node(s). The position of each node is represented in 3D space, with coordinates corresponding to the center of the AAL-defined parcel to which it belongs. Euclidean distance provides a simple geometric metric to characterize the spatial extent of lesion impact on nearby versus distant nodes, and has been used in a previous intracranial electrophysiology study (Russo et al., 2021) to quantify distance from recorded electrode sites to lesion locations. We adopt this metric here to enable direct comparison with those empirical observations. However, in the present neural mass model approach, the effective spread of lesion effects is governed by network connectivity weights and transmission delays rather than geometric distance per se. Since structural connectivity covaries with Euclidean distance due to wiring cost constraints (i.e., nearby regions tend to be more strongly connected), we employed the connection loss metric. This metric was used to directly quantify the amount of disconnection that each node suffered following the lesion. It is defined as the percentage of the incoming weights that is lost post-lesion relative to the pre-lesion network. This metric reflects the reduction in excitatory coupling and serves to characterize the degree of disfacilitation caused by the lesion.

2.8. Spectral analysis

The power spectral density (psd) of the PSP was computed using the Welch method with time segments of 3 seconds and 50% overlap. From the resulting psd, *δ power* was extracted by summing the power values of frequencies below 4 Hz. To assess the relative change in delta (δ) band between conditions, the *δ ratio* was calculated by dividing the *δ power* in the condition of interest by the *δ power* in the control condition. This ratio provides a normalized measure of the shift in SW activity after the lesion.

2.9. Statistical analysis

The bar graphs in this study display the mean values of the reported variables across multiple simulation runs, with error bars representing the corresponding standard deviation.

Exponential fit was performed to model the relationship between *distance from the lesion* and the %Down variable following (Russo et al., 2021). The optimal parameters for the exponential decay function were obtained using the *curve_fit* function from the SciPy Python library (Virtanen et al., 2020). To stabilize variance and enable better linear correlation analysis, the %Down variable was square root–transformed (%$Down_{sqrt}$). Pearson's correlation coefficient (*r*) was then computed to assess linear relationships between %$Down_{sqrt}$ and each predictor variable separately: connection loss, NBR %Down, and NBR DownOverlap. To validate these associations and address potential violations of independence in the pooled data, we performed linear mixed-effects regression models with random intercepts for lesion and target node using the lme4 package in R. The same three predictor variables were modeled against %$Down_{sqrt}$, and results were examined under both raw and rank-transformed data to assess robustness to zero inflation and non-linear relationships.

Partial Least Squares (PLS) regression (Wold et al., 1993, Wold et al., 2001) was used to combine the predictor variables (connection loss, NBR %Down, NBR DownOverlap) into the first PLS latent component (PLS_1) to predict %$Down_{sqrt}$. This predictive model effectively reduces the dimensionality of the three considered predictors into a single component that is the most linearly related to the outcome variable, and has been used elsewhere in the study of neurophysiology to deal with correlated variables(Colombo et al., 2023). PLS regression was implemented using the *PLSRegression* function from the scikit-learn Python library (Pedregosa et al., 2011). The R^2 value was computed for both the full model and under 10-fold cross-validation to evaluate generalization performance. The relative importance and contribution of each predictor variable to the prediction of %$Down_{sqrt}$ were quantified using the Variable Importance in Projection (VIP) scores for the PLS_1 component. Variables with VIP scores > 1 are generally considered significant contributors (Mehmood et al., 2012), and the value of 0.8 is often used as a limit below which variables are considered unimportant (Wold et al., 1993). Finally, to assess distance-dependent contributions, nodes were divided into quartiles based on their distance from the lesion, and PLS regression was applied separately to each group.

3. Results

In this work, we explored two mechanisms proposed to modulate the generation of SWs, namely activity-dependent adaptation and structural disfacilitation. In the context of brain lesions, these mechanisms can be interpreted as proxies for vertical disconnection (e.g., disruption of the ascending activation fibers) and lateral disconnection (e.g., impaired cortico-cortical connectivity). We began by describing how adaptation shapes the dynamics of an isolated cortical population, then examined how SWs emerge through the interaction between adaptation and disfacilitation in coupled populations. Building on this mechanistic foundation, we investigated how lesion-induced disfacilitation and, consequently, functional network-mediated effects drive SW propagation in simplified network motifs. Finally, in a whole-brain model, we quantified the relative contribution of disfacilitation, network hierarchy, and temporal coherence to post-lesional SWs dynamics.

3.1. Adaptation induces Up and Down dynamics in an isolated model of the cortical population

The JR model has been extensively used to simulate spontaneous and evoked cortical activity at a mesoscale level (EEG and LFP-like signals) (Jansen and Rit, 1995, David and Friston, 2003). However, it has mostly been applied without considering activity-dependent adaptation dynamics (Moran et al., 2007). Here, we characterized the JR model in the presence of adaptation and investigated its relationship with Up and Down dynamics. As a function of the adaptation strength (g), the model qualitatively reproduced distinct dynamical regimes ranging from wake-like states (Up or active state) to those observed during SWS (i.e., SO, slow intermittent Up and Down dynamics). Specifically, for low values of adaptation strength (g=5; Fig. 2A, top-trace), the average postsynaptic membrane potential (PSP) was characterized by an Up (active) state with oscillatory activity at ~10Hz with an amplitude of ~7mV, resembling wake-like cortical dynamics (Linkenkaer-Hansen et al., 2001, Destexhe et al., 2007, Compte et al., 2008). By increasing g (Fig. 2A middle traces), we observed a transition to a bistable regime of SO, where periods of Up states were interspersed by Down states (PSP ~4mV) together with an increment in the δ power (see psd in Fig. 2A), a fingerprint of SWS dynamics (Massimini et al., 2004, Torao-Angosto et al., 2021). As g further increased, Down states became more frequent and regular (Mattia and Sanchez-Vives, 2012, Cattani et al., 2023). At

sufficiently high g values, Down states dominated the dynamics over the regular presence of Up states (g=50, Fig. 2A, bottom trace). Notice that a persistent Up state (high-voltage; top trace in Fig. 2A) led to rapid oscillatory patterns, in sharp contrast with a persistent Down state (low-voltage; bottom trace in Fig. 2A).

Then, we explored the model's dynamical landscape by systematically varying g from 0 to 60 and quantified the amplitude of oscillations as 1st and 99th percentiles of the PSP (Fig. 2B). The Up state (high-voltage/active state) regime corresponded to a stable fixed-point (Fig. 2B solid line), which, when subjected to stochastic noise, exhibited low-amplitude alpha oscillations (from ~6.5 mV to ~8.2mV; Fig. 2B gray dots; Supplementary Fig. S1). For instance, when g=0, the system was in a subcritical regime near a supercritical Hopf bifurcation (Supplementary Fig. S1) and acted as a damped oscillator, decaying towards the fixed-point attractor. This behavior persisted for small increases in g (g<9; Fig. 2 and Fig. S1). However, for larger values of g (g>9 up to 39), the model exhibited large oscillations between high- and low-voltage states, driven by the slow negative feedback effect of adaptation (Fig. 1C). As firing activity continues, the adaptation gradually builds up, lowering sensitivity to input potentials, until the Up state loses stability, triggering a transition to the Down state. In this low-activity regime, adaptation slowly decays until it reaches its minimum, enhancing sensitivity to input potentials, allowing the system to spontaneously generate a new Up state, thus re-initiating the Up/Down cycle. For high values of g (>39), the system fell in a persistent Down state, due to a stable low-voltage fixed point attractor (Fig. 2B and Supplementary Fig. S1B). Notably, near the transition, from a persistent Up to SO (g~10) or from SO to persistent Down (g~40), the system remains at a stable-fixed point (solid line in Fig. 2B), however, due to the stochastic noise, transitions were still observed (Supplementary Fig. S1B).

Finally, in Fig. 2C, we report the PSP for the five cases illustrated in Fig. 2A. At the two extremes (g=5 and g=50), the PSP exhibited a unimodal distribution, corresponding to the high-voltage attractor of the Up state and the low-voltage attractor of the Down state, respectively (Fig. 2C). Conversely, for intermediate values of g, the PSP followed a bimodal distribution, reflecting the alternation of Up and Down states typical of SO. Altogether, our results demonstrate that, in a local circuit (Fig. 1D, I), represented by the JR model, manipulating the strength of adaptation induces a phase transition from a persistent Up state to a bistable SO regime, resembling a transition from wakefulness to sleep-like states.

3.2. *Effects of adaptation strength and excitatory coupling on slow oscillations in two connected populations*

The cerebral cortex relies on recurrent excitatory connectivity to sustain stable activity, and its disruption profoundly alters neuronal dynamics. Consistent with empirical evidence showing SO after cortical deafferentation and brain injury (Russo et al., 2021, Timofeev et al., 2000, Sarasso et al., 2020, Tscherpel et al., 2024, Massimini et al., 2024), we hypothesized that in our model sleep-like dynamics may arise from two complementary mechanisms: (i) *structural disfacilitation*, reflecting reduced cortico-cortical afferent excitatory input (Imbrosci and Mittmann, 2011, Kim et al., 2014, Santos et al., 2023), and (ii) *loss of ascending neuromodulatory drive*, which reduces acetylcholine and norepinephrine release, thereby enhancing neuronal adaptation and favoring SO emergence (McCormick et al., 2020; Dalla Porta et al., 2025). To test this, we coupled two JR neural populations (JR_a, JR_b) through bidirectional excitatory connections without delays (Fig. 1D II) and systematically varied the adaptation strength (g) and excitatory coupling (C) (Fig. 3).

We first examined the dynamics of two symmetrically coupled populations, JR_a and JR_b, with excitatory coupling strength fixed at 30 (C_{ab}=C_{ba}=30) and g=11.5. Under these conditions, both populations exhibited alpha oscillations in a persistent Up state (Fig. 3A, top trace and PSD; #1). Reducing C induced a transition from the persistent Up state to SO, characterized by an increase in δ power (Fig. 3A, middle trace; #2). This effect can be interpreted as an increase in the "level of structural disfacilitation" (Schwindt et al., 1989, McCormick and Williamson, 1989). When these populations were fully disconnected (C=0), SO activity became more frequent and regular (Fig. 3A, bottom trace; #3). We then systematically investigated the impact of disconnection across different levels of adaptation strength (Fig. 3B). As highlighted by the red horizontal dashed line, decreasing C (x-axis) while keeping g (y-axis) fixed revealed a phase transition from SO (colored region) to a persistent Up state (gray region). For example, when uncoupled (C=0), both populations displayed SO, spending approximately 35% of the time in the Down state (%Down) (Fig. 3B, bottom). With increasing coupling strength, the %Down progressively decreased, disappearing around C≈20, beyond which the system settled into a stable persistent Up state (Fig. 3B, bottom).

Next, we explored the case of asymmetrical variations of g, i.e., whether manipulating g in only one population could induce a change in the dynamics of the other population, while keeping C=30 fixed (Fig. 3C). The bifurcation diagram for population JR_a, as a function of g_a and g_b, revealed that a transition from persistent Up state (gray area) to SO (colored area) could occur by simply manipulating the adaptation in the other population, JR_b. For instance, when g_a=11.5 and g_b was varied, population JR_a transitioned from a persistent Up state to SO (Fig. 3C, green horizontal dashed line). Importantly, the %Down in JR_b, increased as a function of g_b while, in the connected population JR_a (where g was fixed), the %Down reached a plateau (Fig. 3C, bottom).

Finally, we evaluated the case of asymmetrical variations of C. We showed that for fixed values of g in both populations JR_a and JR_b (g_a=g_b=11.5), population JR_a can transition from a persistent Up state to SO as a function of C_{ba} (the coupling strength from JR_a to JR_b) even if C_{ab} (the coupling strength from JR_b to JR_a) remains unchanged (Fig. 3D). In other words, the disconnection of population JR_b induces a transition from a persistent Up state to SO in JR_a. Moreover, we replicated these results in the Wilson-Cowan rate model, demonstrating that the observed dynamics are consistent across different models (Supplementary Fig. S3).

Thus, local manipulations in a two-population model point to two complementary routes to post-lesional SWs: (i) a primary structural disconnection of ascending and/or cortico-cortical afferents, that directly increase adaptation and/or disfacilitation, leading to the generation of local SWs; (ii) secondary, functional network-mediated effects whereby the silent periods generated by the primary disconnection reshape the dynamical landscape of distant nodes.

3.3. *Slow wave propagation in a toy-network model*

In the previous section, we demonstrated that the transition from a persistent Up state to SO depends on local ascending (e.g., adaptation level) and cortico-cortical (e.g., coupling strength) connections in a simple bidirectionally coupled system. To further explore these aspects, we extended the model to include the interaction with other regions (nodes), incorporating a distance-dependent connectivity pattern to mimic both local and long-range connections (Fig. 4). In this context, we focused primarily on the functional impact of cortico-cortical disconnections for two reasons. First, the consequences of disrupting lateral excitation (i.e., disfacilitation) for SWs are less well understood than those of altering ascending neuromodulation (Steriade et al., 1993, Timofeev et al., 2000, Dalla Porta et al., 2023). Second, focal cortical and subcortical lesions are more likely to compromise cortico-cortical pathways, which vastly outnumber ascending projections (Douglas and Martin, 2004).

This toy network was composed of two sub-networks, referred to as the perilesional network and the distant network, in accordance with where the lesion was applied (Fig. 4A). The control pre-lesion case (Fig. 4B) represents the intact network (i.e., before any disconnection was applied) in the wake-like (active) regime, where all the nodes

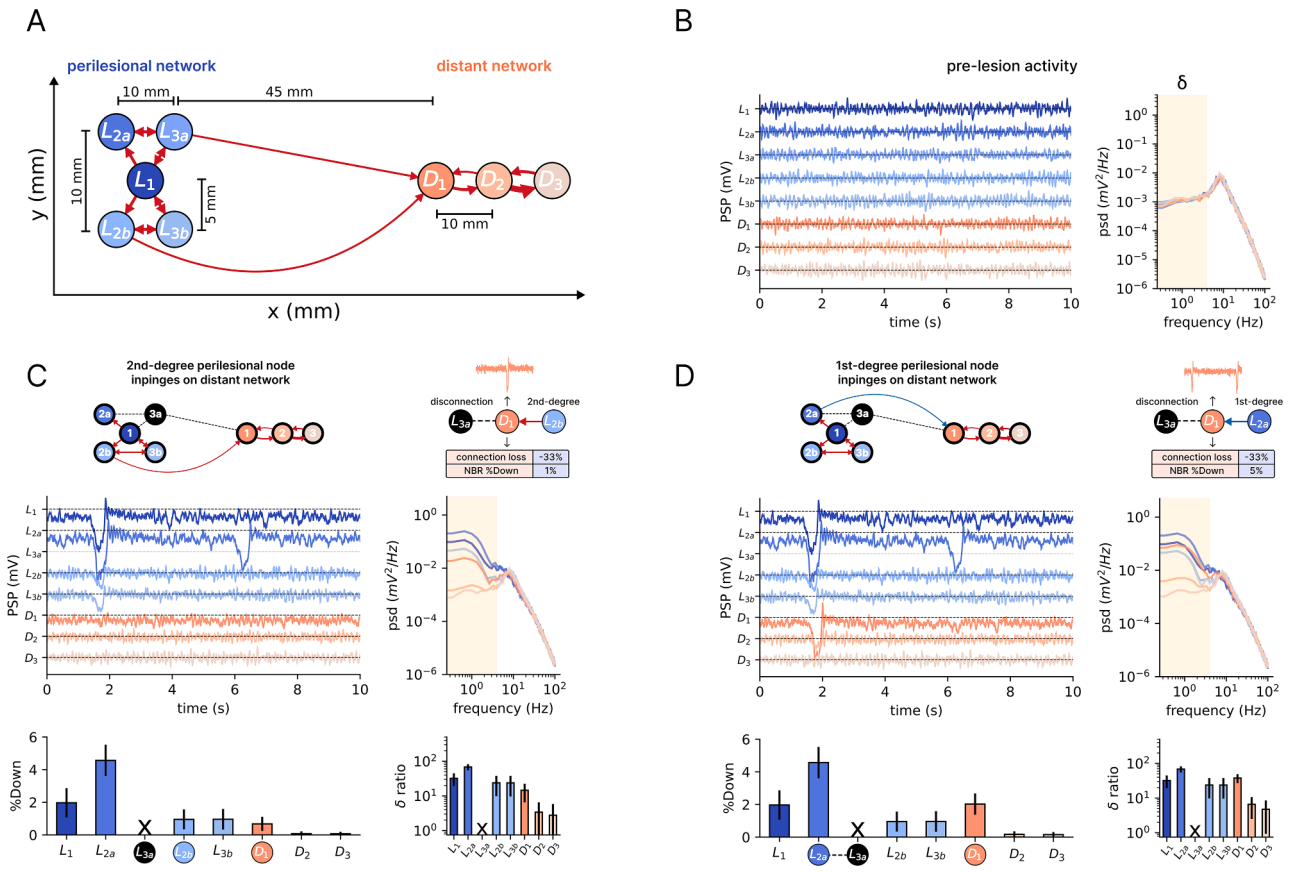

Figure 4. Impact of disconnection and disfacilitation on slow wave propagation in a toy network. (A) Schematic representation of the toy network model, composed of a perilesional network (blue) and a distant network (red), here shown in the pre-lesion control condition (i.e., before performing any disconnection). Nodes are connected with a distance-dependent connectivity pattern, with the thickness of the arrows indicating coupling strength. The perilesional network projects to the distant network via node D1. Delays between nodes are determined by inter-node distances and a fixed propagation velocity of 4 m/s. (B) Activity and spectrum of the control condition: all nodes oscillate in the alpha band in a persistent Up state (awake-like regime). Left panel shows postsynaptic potential (PSP) traces recorded from perilesional (blue) and distant (red) nodes. The right panel displays the corresponding power spectral density (psd), highlighting the dominant alpha activity. The δ band is highlighted by the yellow span. (C) Effect of disfacilitation following the lesion of node L3a (black node), which projected both locally and to the distant network in the control condition. The loss of L3a primarily affects its first-degree nodes L1 and L2a, with L2a exhibiting the strongest impact due to additional inputs from its first-degree node L1. The distant node D1 also shows signs of slow wave propagation, since now it receives inputs from node L2B (a second-degree node relative to the lesioned node L3a). The bottom panels quantify the percentage of time spent in the Down state (%Down) and the δ ratio for each node. The δ ratio was calculated by dividing the δ power in the network after the lesion by the δ power in the control condition. The percentage of time neighboring nodes (presynaptic nodes) spend in Down states (here, 1% for D1) is referred to as NBR %Down (see Methods 2.6). (D) Effect of modifying connectivity so that D1 receives input from node L2a rather than node L2b, thus from a first-degree node relative to the lesioned node (NBR %Down=5%) instead of a second-degree node, as in (C) (NBR %Down=1%). This change amplifies SW propagation, leading to a greater impact on distant nodes (D2 and D3), as reflected by increased time spent in the Down state and a higher δ ratio.

oscillated at ~10Hz. In this toy network, adaptation was kept fixed (g=11.5) and the total excitatory input coupling was equalized across nodes (c=30; see Methods 2.4) corresponding to configuration 1 in Fig. 3A.

Within this framework, we explored the impact of disfacilitation over the perilesional network and its influence on the distant network, by simulating a virtual local lesion, removing a node and all of its connections. Specifically, the lesion was simulated by disconnecting a node (L3a) that projected to both local nodes (i.e., perilesional network) and distant nodes (i.e., distant network) (see Fig. 4C). The impact of disfacilitation was quantified by the amount of time spent in the Down state and by the δ ratio (Fig. 4C-D).

Within the perilesional network, the nodes most affected were those directly connected to the lesioned node (L2a and L1, hereafter referred to as first-degree neighbors), though to different extents. Node L2a was the most impacted, as it not only lost its direct connection to the lesioned node but also received input from L1, which itself was directly connected to the lesion (i.e., a first-degree neighbor; see Fig. 4C). In contrast, node L1 was less affected, suggesting that its stability depended less on the lesioned node. This reduced impact may be explained by the small recurrent circuit involving L1, L2b, and L3b, which received only indirect (second-degree) input from the lesion.

Next, we examined the impact of disfacilitation on the distant network. The perilesional network projects only to node D1 in the distant network (Fig. 4A). In the paradigm depicted in Fig. 4C, D1 lost its connection to the lesioned node and received inputs from node L2b, a second-degree neighbor of the lesion (less affected). To characterize these two aspects, we computed the connection loss, which represents the percentage of lost connections (coupling strength) relative to the control condition for each node (-33% for D1), and the NBR %Down, which quantifies the time neighboring nodes spend in Down states (1% for D1) indicating the extent to which inputs come from affected regions. Although less pronounced, the effect on the D1 dynamics resembled that observed in L1, characterized by a small amount of time spent in the Down state and increased δ ratio. Interestingly, we observed signs of SW propagation in the distant network, as indicated by time spent in the Down state and δ ratio of D2 and D3, which received progressively indirect inputs from the lesion, specifically the second- and third-degree

neighbors of the lesion, respectively (Fig. 4C).

Finally, we examined the effect on D1 when it received input from a first-degree neighbor of the lesion (NBR %Down=5%, Fig. 4D), rather than from a second-degree neighbor of the lesioned node (as in Fig. 4C). As shown in Fig. 4D, this configuration resulted in a greater impact on the distant nodes and enhanced SW propagation to nodes D2 and D3. These findings suggest that the spread of SWs to distant nodes depends not only on the presence of SWs in the perilesional network but also on the hierarchical position of the affected nodes relative to the lesion, which is mirrored in their level of SW activity or δ power.

3.4. Slow wave coherence drives propagation in a toy-network model

To further investigate the impact of lesion-induced SWs, we examined how their temporal organization influences propagation to the distant network. Specifically, we compared two conditions following the lesion of the L1 node: two uncorrelated SW-generating nodes (Fig. 5A) and two correlated SW-generating nodes (Fig. 5B). Even though the amount of SW activity conveyed to the D1 node was identical between conditions (NBR %Down=14%), the coherence of SW activity across nodes led to remarkably different effects. When SW activity was coherent (Fig. 5B), the distant nodes (D1, D2, D3) were significantly more impacted, as reflected in the increased time spent in the Down state (%Down) and a higher δ ratio. These observations suggest that the propagation of SW activity into intact nodes depends not only on the amount of SWs (NBR %Down) but also on the coherence of these oscillations, highlighting a dependence on the temporal dynamics of the perilesional network.

To quantify the impact of coherent SWs on distant nodes, we computed the percentage of Down state overlap (DownOverlap) between pairs of perilesional nodes (see Methods 2.6; Fig. 5C,D). Focusing on the coherence among nodes projecting to D1, we first calculated the DownOverlap between neighboring pairs (L2b–L3a and L2a–L3a), corresponding to the two scenarios illustrated in Fig. 5A,B. We then averaged the DownOverlap across all neighbors of D1 to obtain the NBR DownOverlap measure. As expected, L2a and L3a exhibited markedly higher Down state overlap (NBR DownOverlap = 94.2% ± 1.2%) than L2b and L3a (NBR DownOverlap = 11.7% ± 4.6%; Fig. 5E), resulting in a stronger impact on D1 and consequently on D2 and D3.

Finally, to assess the causal role of SW activity coherence in modulating SW propagation in the distant network, we altered the propagation delay from L2a to D1 (as in the scenario depicted in Fig. 5B),

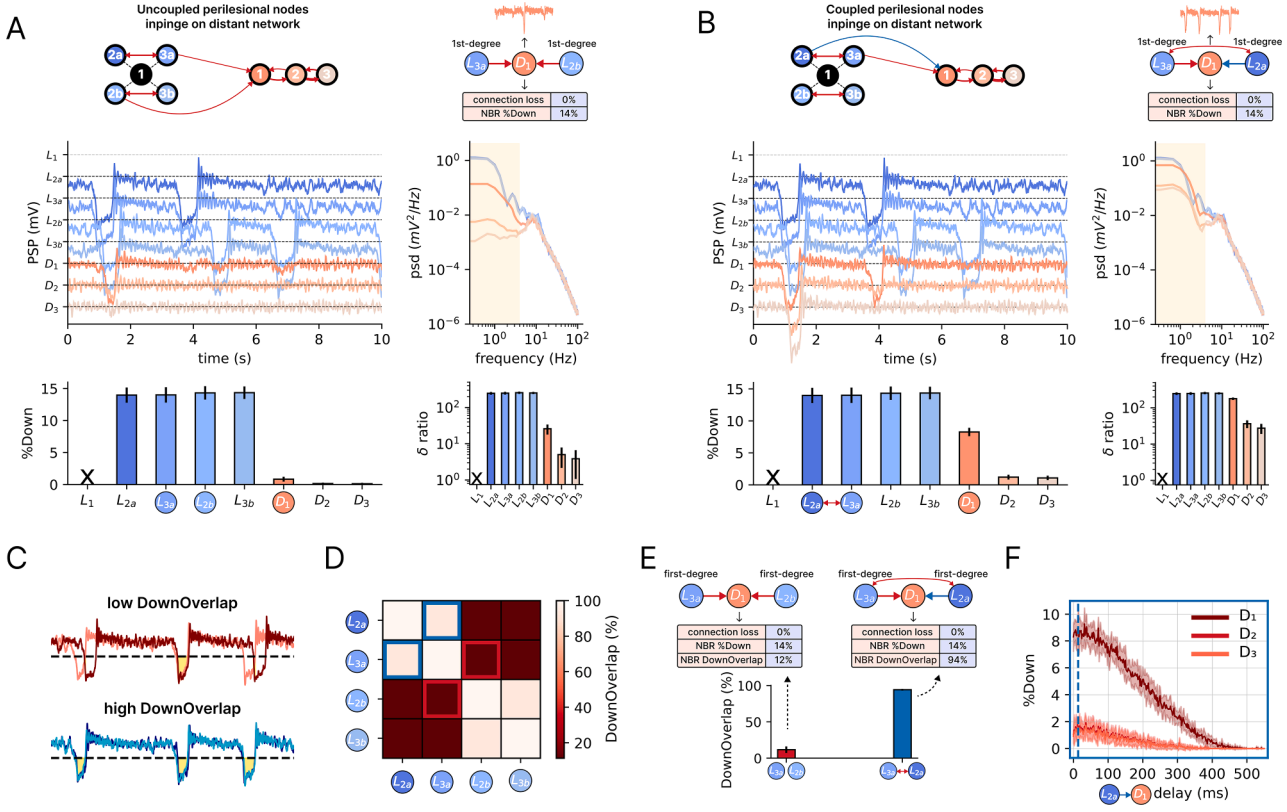

Figure 5. Impact of coherent and uncoherent slow wave inputs on the propagation of activity in a distant network. (A) Schematic representation of the network model where uncoupled perilesional nodes impinge on the distant network, resulting in uncoherent slow wave (SW) inputs. Below, postsynaptic potential (PSP) traces of the network, with the perilesional nodes (blue) and distant nodes (red). Right, corresponding power spectral density (psd) and δ ratio. The δ band is highlighted by the yellow span in the psd. (B) Same as in (A), but the perilesional nodes that impinge on the distant network are coupled, resulting in coherent SW inputs. For the same amount of SW input (i.e., same NBR %Down for D1 in both scenarios), coherent inputs lead to a greater impact on the distant network, as reflected by the increased time spent in the Down state (%Down) and higher δratio. The δ ratio was calculated by dividing the δ power in the network after the lesion by the δ power in the control condition. (C) Illustration of DownOverlap calculation. Given a pair of PSP traces, the *DownOverlap* computes for each trace the fraction of its total Down state duration during which both traces simultaneously fall below the Down state threshold (black dashed horizontal line). (D) Heatmap representing the *DownOverlap* between pairs of perilesional nodes. Lighter colors indicate higher overlap, showing that specific node pairs exhibit stronger coherence (blue and red squares). (E) The L2a–L3a node pair (corresponding to the coupled perilesional nodes scenario in B) shows significantly higher overlap than the L2b–L3a node pair (the uncoupled perilesional nodes scenario in A). The average DownOverlap of presynaptic nodes projecting to a given postsynaptic node (here, D1) is referred to as NBR DownOverlap (see Methods 2.6). Given that DownOverlap is not necessarily symmetric (i.e., the overlap from node *i* to node *j* may differ from *j* to *i*), we reported the average of the two directions. (F) Effect of propagation delay on Down state occurrence in the distant network. Delay was progressively increased between L2a and D1 (the coupled perilesional nodes scenario in B), reducing the overlap of the two SW activity inputs arriving at D1. Traces represent the mean over 10 runs, and the shaded area indicates the standard deviation. The blue vertical line marks the actual delay in (B).

thereby reducing the overlap of the two SW inputs arriving at D1 (see Fig. 5F). As the delay increased (less overlapping of the SW activity impinging to D1), we observed a progressive decrease in the time spent in the Down states in the distant network, suggesting that SW coherence plays a key role in network-wide SW activity propagation.

Together, these results identify a third mechanism by which lesions influence neuronal activity beyond directly deafferented nodes. The emergence of SWs in distant regions depends on the synchrony of inputs from nodes closer to the lesion, and this timing-dependent effect persists even when total SW input is held constant. Coherent activity within a tightly connected perilesional focus promotes further percolation of SWs to nodes several steps away. Thus, a node's vulnerability to SW intrusion scales with both the strength and the coherence of SW activity in its presynaptic neighborhood.

3.5. Slow wave propagation in a whole-brain network model

Overall, analysis of a topologically organized cortical motifs revealed

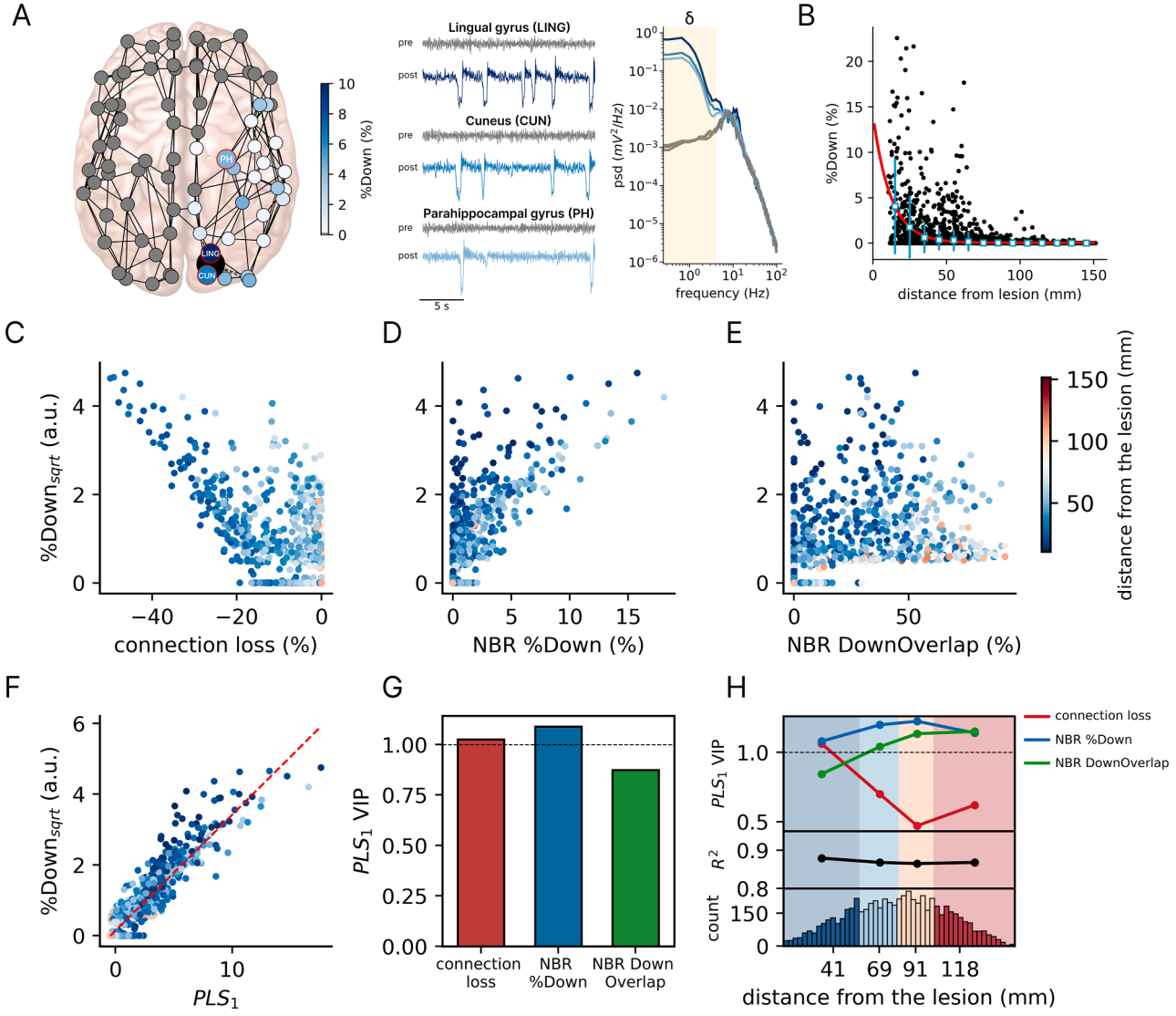

Figure 6. Whole-brain modeling of slow wave generation and propagation following lesion. (A) Whole-brain network model with nodes defined by the Automatic Anatomical Labeling (AAL) atlas (Tzourio-Mazoyer et al., 2002). The lesion of a node (here, the right calcarine cortex) is represented as a black circle, with the impact on the spared nodes quantified as the time spent in the Down state (%Down). The node colors indicate %Down, as shown in the accompanying color bar, with gray nodes representing regions where no Down states were detected. Traces illustrate simulated PSP activity from three representative regions in the pre-lesion (control; gray) and post-lesion (blue hues) conditions. In the control condition, the nodes oscillate in the alpha band in a persistent Up state (awake-like regime). After the lesion, Down states emerge along with an increase in δ power in power spectral density (psd). The δ band is highlighted by the yellow span in the psd. (B) Percentage of time spent in the Down state (%Down) as a function of the Euclidean distance from the lesion. The red curve represents an exponential fit (R^2=0.21), indicating a distance-dependent decay in SW propagation, consistent with experimental results (Russo et al., 2021). Cyan squares represent binned means (10 mm intervals) with error bars indicating the standard deviation within each bin. (C) Relationship between connection loss (percentage of lost coupling strength due to the lesion relative to control) and the square root of %Down (%$Down_{sqrt}$). A negative relationship is observed (r=-0.76). (D) Relationship between the time spent in the Down state of neighboring nodes (NBR %Down) and %$Down_{sqrt}$. A positive relationship is observed (r=0.81). (E) Relationship between the DownOverlap of neighboring nodes (NBR DownOverlap) and %$Down_{sqrt}$. The variables show a positive relationship (r=0.65). (F) Partial least squares regression (PLS) of %$Down_{sqrt}$ and the score of the first PLS component (PLS_1) derived from the three predictor variables (connection loss, NBR %Down, and NBR DownOverlap). The model explained ~90% of the variance (R^2=0.89; after cross-validation R^2=0.88). (G) PLS_1 weights for the three predictor variables, indicating their relative contributions. (H) Distance-dependent contributions of the three predictor variables to %$Down_{sqrt}$. Nodes were divided into quartiles based on their distance from the lesion, and PLS regression was performed for each subset. For each quartile, the model's R^2 and the VIP scores of each variable are reported.

three concurrent mechanisms governing the generation and propagation of post-lesional SWs: first, primary structural disconnection; second, network-mediated effects that scale with the input received from the perilesional SW focus; and third, a timing-dependent effect governed by the synchrony of those inputs. To examine how these mechanisms interact under more realistic conditions, we applied the same manipulations (i.e., node lesions) to a human whole-brain connectome.

We implemented the JR model in a whole-brain composed of 80 nodes (Škoch et al., 2022) (Fig. 6 and Supplementary Fig. S4). Similar to our control toy network, the whole-brain network dynamics in the control condition were characterized by alpha oscillations (Fig. 6A, gray traces). To assess the impact of lesions, we systematically disconnected each node and examined its effects on both perilesional and distant nodes. As shown in Fig. 6A for a representative lesion (black circle), the most affected nodes were the perilesional ones, where Down states emerged along with an increase in δ power (Fig. 6A). Moreover, we showed that SW propagation decayed exponentially (R^2=0.21, $p<0.001$) with the distance from the lesion, i.e., closer nodes were more affected than distant ones, consistent with empirical observations (Fig. 6B) (Russo et al., 2021).

Given the limited explanatory power of this geometric relationship, we aimed to investigate the mechanisms underlying post-lesional SW beyond simple distance from the lesion. Since anatomical distance covaries with structural weights and the lesion is modeled as a reduction of connection weights, we first used the percentage of connection loss to mechanistically explain SW emergence and propagation, as demonstrated in the toy network. We observed that the square root of the time spent in the Down state ($\%Down_{sqrt}$; see Methods 2.9) followed a negative relationship ($r=-0.76$, $p<0.001$) with the percentage of connection loss, i.e., nodes more connected to the lesion site were impacted the most (Fig. 6C). Next, we assessed the dependence of SW propagation on the hierarchical node position relative to the lesion. Specifically, we explored whether the time spent in the Down states could be explained by the time spent in the Down states by neighboring nodes (NBR %Down). We observed a positive relationship ($r=0.81$, $p<0.001$), suggesting that recurrent connectivity, i.e., the influence of neighboring nodes, can explain, to some extent, the impact on a given node (Fig. 6D).

Finally, we assessed whether the amount of SW overlap in presynaptic nodes could account for the time spent in the Down state of the postsynaptic nodes (NBR DownOverlap). Albeit more dispersed, we also observed a positive relationship ($r=0.65$, $p<0.001$) between the amount of SW overlap and the $\%Down_{sqrt}$ (Fig. 6E). To ensure robustness of our findings, we performed complementary analyses addressing violations of independence and zero inflation. We calculated per-lesion correlations (Supplementary Fig. S5A) and applied mixed-effects regression models with random intercepts for lesion and target node, confirming our main findings (Supplementary Tables S3-S4). Additionally, we performed rank-based Spearman correlations (Supplementary Fig. S5B) and mixed-effects modeling on ranked variables (Supplementary Tables S5–S6) to account for zero-inflated outcomes, which yielded concordant results.

However, it is important to note that, while each of the three explored mechanisms (connection loss, NBR %Down, and NBR *DownOverlap*) were significantly correlated with $\%Down_{sqrt}$ (Fig. 6C-E), each predictor exhibited a clear dispersion around zero on the x-axis, suggesting that neither predictor alone fully accounts for the variability in the time spent in the Down states. Further, in a complex brain network with a hierarchical, recurrent, and modular architecture (Boucsein et al., 2011, Ercsey-Ravasz et al., 2013), these mechanisms are likely to be strongly interdependent. For example, nodes disconnected by a lesion are typically embedded within neighborhoods that are likewise compromised, where prominent SWs may be further amplified by synchrony. To disentangle their individual contributions in explaining the time spent in the Down state and SW activity propagation, and also to address multicollinearity (Supplementary Fig. S5C), we employed partial least squares regression (PLS). Specifically, we aggregated the three factors into the first PLS latent component (PLS_1) and subsequently related its score to $\%Down_{sqrt}$. We observed a strong linear relationship (R^2=0.89, $p<0.001$) between the PLS_1 and $\%Down_{sqrt}$ (Fig. 6F), with all factors robustly explained the variance of the outcome, as indicated by their VIP scores (Fig. 6G; all variables have scores around 1; see Methods 2.9). Finally, we found that these predictors exert distance-dependent effects: connection loss had higher VIP scores for nodes closer to the lesion (stronger predictive power for $\%Down_{sqrt}$), NBR DownOverlap had higher VIP scores for more distant nodes, and NBR %Down showed VIP scores largely independent of distance from the lesion (Fig. 6H). These findings were also consistent with the Wilson-Cowan rate model (Supplementary Fig. S6).

4. Discussion

In this study, we employed a population model of cortical activity and applied a multiscale analytical framework to examine the mechanisms underlying the emergence and propagation of SWs following brain lesions (Fig. 1). Our findings identify three interacting factors: i) the critical role of disconnection, leading to increased adaptation and/or disfacilitation, in SW generation, ii) the hierarchical organization of cortical connectivity as a constraint on SW propagation, and iii) temporal coherence as a recruitment modulator of distant structurally intact nodes. Together, these results reveal that post-lesional SW propagation depends jointly on topological distance from the lesion and dynamic synchrony of SWs, underscoring the interplay between local connectivity disruption and global network organization in shaping cortical dynamics.

SWs are a hallmark of cortical dynamics during NREM sleep. Organized into a slow, quasi-periodic rhythm termed SO, they reflect the alternation between periods of neuronal firing (Up states) and periods of hyperpolarization associated with neuronal silence (Down states, or off-periods). During NREM sleep, SWs and the associated off-periods disrupt network interactions leading to loss of consciousness, while they simultaneously promote restorative and homeostatic processes (Huber et al., 2004, Stickgold, 2005, Tononi and Cirelli, 2006, Marshall et al., 2006, Uji et al., 2025). When SWs intrude into physiological wakefulness, they can impair motor and cognitive functions in a topology-specific manner, as shown in sleep-deprivation studies (Vyazovskiy et al., 2011, Nir et al., 2017, Andrillon et al., 2021). Crucially, SWs have also been observed during wakefulness following brain lesions of varying extent and etiology (Walter, 1937, Butz et al., 2004), where they can produce substantial network and functional impairments (Tscherpel et al., 2024, Sarasso et al., 2025, Sheybani et al., 2023, Lanzone et al., 2022). Hence, characterizing the mechanisms responsible for the generation and propagation of post-lesional SWs are essential for understanding the functional consequences of brain injury and for identifying new therapeutic targets.

Using a multiscale modeling approach (Fig. 1), our results show that disruption of ascending fibers (increasing adaptation, g) and cortico-cortical fibers (causing disfacilitation, C) is sufficient to shift neuronal populations toward bistable dynamics and increase their susceptibility to enter Down states during wakefulness. The effects of these global manipulations across nodes generalized previous single-node bifurcation diagrams (Cattani et al., 2023) and recapitulated the main electrophysiological features found in N3 sleep, as well in conditions of massive deafferentation, such as in cortical slices (Covelo et al., 2025), slabs (Timofeev et al., 2000), hemispherotomy (Colombo et al., 2025) and severe brain injury (Rosanova et al., 2018, Colombo et al., 2023). Importantly, once generated, these sleep-like events do not remain confined to the lesioned site. Instead, their impact spreads through intact structural pathways in a manner constrained by network topology and strongly modulated by the temporal coherence of incoming SW activity. This combination of local vulnerability and network-mediated amplification provides a unifying mechanistic explanation for how focal

lesions can give rise to spatially extended patterns of neuronal silencing.

Across network scales, hierarchical distance from the lesion emerged as a key determinant of SW propagation, with perilesional regions showing the most prominent intrusions and more distant nodes being progressively less affected. However, structural disconnection alone was insufficient to fully explain the observed variability. Temporal coherence among presynaptic SWs played a critical role in determining whether distant, structurally intact nodes were recruited into a sleep-like regime, indicating that timing-dependent interactions act as an additional gating mechanism for SW spread.

To examine how these mechanisms interact under more realistic conditions, we extended our analyses to a whole-brain connectome model. In this context, structural disconnection, network-mediated effects from perilesional regions, and SW coherence were strongly interdependent, reflecting the hierarchical, recurrent, and modular architecture of cortical networks (Boucsein et al., 2011, Ercsey-Ravasz et al., 2013). By integrating these factors using partial least squares regression, we showed that their combined contribution explained the majority of the variance in post-lesional SW activity. Notably, the relative importance of each factor varied with distance from the lesion, with structural disconnection dominating locally and SW coherence playing an increasingly prominent role in shaping propagation to distant regions.

The SW propagation pattern predicted by our computational model not only aligns with classic reports of prominent perilesional EEG slowing (Walter, 1937, Gloor et al., 1977, Nuwer et al., 1987) but also provides a mechanistic account of intracranial recordings of SW dynamics following controlled radiofrequency thermocoagulation (RFTC) lesions (Russo et al., 2021). In those recordings, SW intrusion peaked near the lesion, exhibited long-range propagation to connected sites, and decayed exponentially with anatomical distance, consistent with our modeling results (Fig. 6B). This hierarchical gradient mirrors the exponential distance rule of cortical connectivity (Boucsein et al., 2011, Ercsey-Ravasz et al., 2013) and likely reflects SW spread via cascades of structural and functional effects, whereby upstream Down states induce downstream neuronal silencing, as suggested by our model.

These modeling results position SWs as the potential electrophysiological substrate of diaschisis, the classical concept introduced by von Monakow. (1914). Von Monakow originally described *diaschisis* as a distant effect of focal brain injury, characterized by an "abolition of excitability" and a resulting "functional standstill" in structurally intact but connected regions. This concept resonates closely with the disfacilitation mechanism explored here, where the loss of excitatory input from the lesioned area induces a leftward shift in the bifurcation diagram (Fig. 3), pushing the system toward a regime of SW activity (Rabuffo et al., 2025). In this framework, prolonged neuronal silence associated with SWs emerges around the lesion and propagates along anatomical pathways in a topology- and timing-dependent manner, shaping the spatial extent of remote functional alterations beyond the primary structural damage. These neuronal silences, which transiently interrupt communication within the cortical network—as observed during sleep (Pigorini et al., 2015), anesthesia (Krom et al., 2020), and in awake brain-injured patients (Rosanova et al., 2018)—have been associated with impaired behavioral performance in both rodents and humans (Vyazovskiy et al., 2011, Bernardi et al., 2015, Nir et al., 2017, Andrillon et al., 2021, Marmelshtein et al., 2023, Sheybani et al., 2023), thereby representing a plausible mechanism for the cognitive and behavioral impairments observed following focal brain lesions.

Importantly, this dynamic perspective on diaschisis complements static structural disconnectomics approaches (Thiebaut de Schotten et al., 2020), which map lesion-induced white-matter disconnections to account for deficits extending beyond the visible injury. Functional magnetic resonance imaging (fMRI) studies further show that even small focal lesions can disrupt a substantial proportion of brain connections, resulting in widespread alterations in functional connectivity (Griffis et al., 2019). Building on these findings, our model suggests that post-lesional neuronal silencing, and its propagation throughout the connectome, may underlie these large-scale functional alterations, thereby bridging classical electrophysiological observations with modern fMRI findings. Supporting this view, recent evidence shows that enhanced slow/delta power is associated with the magnitude and spatial profile of fMRI connectivity alterations (Rocchi et al., 2022), linking electrophysiological and hemodynamic markers of diaschisis and recovery.

Our framework can also be extended to other brain pathologies that exhibit pathological EEG slowing and behavioral deficits. Comparable slowing occurs in multiple sclerosis (Kassubek et al., 1999, Van der Meer et al., 2013, Keune et al., 2019, Krupina et al., 2020, Salim et al., 2021, Mórocz et al., 2025), traumatic brain injury (Mofakham et al., 2021, Tewarie et al., 2023), brain tumors (Walter, 1937), and Parkinson's disease (Bernasconi et al., 2025), where inflammation, white-matter lesions, or diffuse network disruption increase delta- and theta-band activity associated with cognitive impairment. Therefore, SW activity may represent a shared neurophysiological marker underlying functional deficits across diverse forms of brain damage.

In light of the results presented here, clear limitations and open avenues emerge. At the microscale, while our population model allowed us to investigate disconnection and spontaneous propagation patterns, it did not account for other mechanisms known to have a local impact on cortical dynamics following brain injury (Massimini et al., 2024). These include GABA-mediated excitation/inhibition imbalance (Imbrosci and Mittmann, 2011, Kim et al., 2014, Santos et al., 2023), cortical hyperexcitability (Schiene et al., 1996, Koch et al., 2008), local temperature increase (Karaszewski et al., 2006), inflammation (Yoshida et al., 2004, Yasuda et al., 2005), and hypoxia (Sun and Feng, 2013). These factors could be addressed in future work and considered as additive contributors to perilesional SW generation, potentially enhancing SW propagation from the initial SW foci alongside the structural disconnection explored in our study. Further, our large-scale model can be tuned to subject-specific dynamics (Capone et al., 2023, Momi et al., 2023, Momi et al., 2025) by incorporating personalized structural and functional connectivity derived from patient lesion data (Idesis et al., 2024). This approach would enable predictions about how specific lesions affect large-scale spontaneous (Idesis et al., 2024) and evoked (Momi et al., 2025) dynamics. Finally, extending the present framework to neural field modeling (Proix et al., 2018, Pang et al., 2023) would enable explicit investigation of slow-wave propagation across cortical space and allow assessment of how focal lesions alter the spatiotemporal organization of these waves.

Extending the factors of SW generation and propagation explored in our study, the model further suggests a potential role for arousal fluctuations (Schiff, 2008, Makeig and Inlow, 1993, Makeig and Jung, 1995, Berridge, 2008, Raut et al., 2021, Raut et al., 2025, Carro-Domínguez et al., 2025), which could be investigated in future work. Arousal, driven by brainstem and thalamic inputs, fluctuates over time and affects adaptation currents via potassium channel modulation (McCormick, 1992, Lee and Dan, 2012). Because disconnected regions lie closer to the bifurcation point for SW generation, the model predicts that fluctuations in adaptation (mimicking physiological arousal dynamics) that would have moderate effects in healthy brains could instead trigger lesion-specific topographical patterns of enhanced SW activity in the damaged brain.

Finally, our results also raise several testable hypotheses regarding intervention strategies aimed at renormalizing the network-level alterations associated with pathological SWs. On one hand, locally confined SW activity around the injured site, identified in our model as first-degree disconnected nodes, may play adaptive or beneficial roles as it does during sleep (Carmichael and Chesselet, 2002, Krone and Vyazovskiy, 2020), and whether its dampening is desirable remains an open question. On the other hand, large-scale propagation of neuronal silence, which disrupts network communication, could potentially be mitigated by dampening or desynchronizing SW sources (i.e., by

reducing SW coherence), as suggested by our modeling results (Fig. 5F). By simulating lesion-specific network dynamics, our model provides a computational framework to generate in silico exploration of how interventions—such as non-invasive brain stimulation techniques including repetitive TMS, transcranial alternating current stimulation, or temporal interference electrical stimulation (Xie and Zhang, 2012, Garside et al., 2015, Grossman et al., 2017, Fehér et al., 2021, Violante et al., 2023, Vieira et al., 2024, Covelo et al., 2025)—might selectively reduce pathological SW propagation while preserving potentially beneficial local activity, thereby providing a conceptual reference of how network-level perturbations shape SW dynamics.

Data and Code Availability Statement

All custom code developed for this study will be made publicly available upon acceptance at https://github.com/gianlucagag/SWs-lesion_model. The structural connectivity data used for the whole-brain model are available from https://www.nature.com/articles/s41597-022-01596-9.

CRediT authorship contribution statement

Gianluca Gaglioti: Writing – review & editing, Writing – original draft, Visualization, Validation, Software, Methodology, Investigation, Formal analysis, Conceptualization. **Leonardo Dalla Porta:** Writing – review & editing, Writing – original draft, Validation, Software, Methodology, Investigation, Formal analysis, Conceptualization. **Michele Angelo Colombo:** Writing – review & editing, Methodology. **Simone Russo:** Writing – review & editing, Conceptualization. **Thierry Nieus:** Writing – review & editing, Methodology. **Gustavo Deco:** Writing – review & editing. **Maurizio Corbetta:** Writing – review & editing. **Simone Sarasso:** Writing – review & editing, Supervision, Conceptualization. **Maria V. Sanchez-Vives:** Writing – review & editing, Supervision, Conceptualization. **Marcello Massimini:** Writing – review & editing, Supervision, Conceptualization.

Declaration of competing interest

The authors declare the following financial interests/personal relationships which may be considered as potential competing interests: Marcello Massimini is co-founder and shareholder of Intrinsic Powers, a spin-off of the University of Milan. Simone Sarasso is advisor of Intrinsic Powers. These affiliations in no way affect the content of this article.

Acknowledgements

The authors thank Daniel Levenstein for support with the Wilson-Cowan model, and Marta Porro, Sasha D'Ambrosio, Ezequiel Mikulan, and Andrea Pigorini for their comments and suggestions on the manuscript. This work was financially supported by the following entities: ERC-2022-SYG Grant number 101071900 neurological mechanisms of injury and sleep-like cellular dynamics (NEMESIS); Italian National Recovery and Resilience Plan (NRRP), M4C2, funded by the European Union - NextGenerationEU (Project IR0000011, CUP B51E22000150006, "EBRAINS-Italy"); European Union's Horizon 2020 Framework Program for Research and Innovation under the Specific Grant Agreement No.945539 (Human Brain Project SGA3); Tiny Blue Dot Foundation; Canadian Institute for Advanced Research (CIFAR), Canada; Italian Ministry for Universities and Research (PRIN 2022); Fondazione Regionale per la Ricerca Biomedica (Regione Lombardia), Project ERAPERMED2019–101, GA 779282; Project INFRASLOW PID2023-152918OB-I00 financed by MICIU / AEI / 10.13039/501100011033/FEDER, UE; Departament de Recerca i Universitats de la Generalitat de Catalunya (AGAUR 2021-SGR-01165 - NEURO-VIRTUAL), supported by FEDER; Fondazione Cassa di Risparmio di Padova e Rovigo (CARIPARO) Grant Agreement number 55403; Ministry of Health, Italy (RF-2008 −12366899) Brain connectivity measured with high-density electroencephalography: a novel neurodiagnostic tool for stroke- NEUROCONN; BIAL foundation grant (Grant Agreement number 361/18); H2020 European School of Network Neuroscience (euSNN); H2020 Visionary Nature Based Actions For Heath, Wellbeing & Resilience in Cities (VARCITIES); Ministry of Health Italy (RF-2019-12369300): Eye-movement dynamics during free viewing as biomarker for assessment of visuospatial functions and for closed-loop rehabilitation in stroke (EYEMOVINSTROKE); Brazilian agency CNPQ (Grant Agreement number 444500/2024-3).

Supplementary materials

Supplementary material associated with this article can be found, in the online version, at doi:10.1016/j.neuroimage.2026.121817.

References

Andrillon, T., Burns, A., Mackay, T., Windt, J., Tsuchiya, N., 2021. Predicting lapses of attention with sleep-like slow waves. Nat Commun 12, 3657.
Baldassarre, A., Ramsey, L.E., Siegel, J.S., Shulman, G.L., Corbetta, M., 2016. Brain connectivity and neurological disorders after stroke. Curr Opin Neurol 29, 706–713.
Benda, J., Herz, A.V.M., 2003. A universal model for spike-frequency adaptation. Neural Comput 15, 2523–2564.
Bernardi, G., et al., 2015. Neural and Behavioral Correlates of Extended Training during Sleep Deprivation in Humans: Evidence for Local, Task-Specific Effects. J. Neurosci. 35, 4487–4500.
Bernasconi, F. et al. Sleep-like slow waves during wakefulness uncover a malignant form of Parkinson's disease. 2025.08.29.25334276 Preprint at https://doi.org/10.1101/2025.08.29.25334276 (2025).
Berridge, C.W., 2008. Noradrenergic modulation of arousal. Brain Research Reviews 58, 1–17.
Bottom-Tanzer, S., et al., 2024. Traumatic brain injury disrupts state-dependent functional cortical connectivity in a mouse model. Cereb Cortex 34, bhae038.
Boucsein, C., Nawrot, M., Schnepel, P., Aertsen, A., 2011. Beyond the Cortical Column: Abundance and Physiology of Horizontal Connections Imply a Strong Role for Inputs from the Surround. Front. Neurosci. 5.
Breakspear, M., 2017. Dynamic models of large-scale brain activity. Nat Neurosci 20, 340–352.
Butz, M., et al., 2004. Perilesional pathological oscillatory activity in the magnetoencephalogram of patients with cortical brain lesions. Neuroscience Letters 355, 93–96.
Camassa, A., Galluzzi, A., Mattia, M., Sanchez-Vives, M.V., 2022. Deterministic and Stochastic Components of Cortical Down States: Dynamics and Modulation. J. Neurosci. 42, 9387–9400.
Capone, C., et al., 2023. Simulations approaching data: cortical slow waves in inferred models of the whole hemisphere of mouse. Commun Biol 6, 1–14.
Carmichael, S.T., Chesselet, M.-F., 2002. Synchronous Neuronal Activity Is a Signal for Axonal Sprouting after Cortical Lesions in the Adult. J. Neurosci. 22, 6062–6070.
Carrera, E., Tononi, G., 2014. Diaschisis: past, present, future. Brain 137, 2408–2422.
Carrera, E., Tononi, G., 2014. Diaschisis: past, present, future. Brain 137, 2408–2422.
Carro-Domínguez, M., et al., 2025. Pupil size reveals arousal level fluctuations in human sleep. Nat Commun 16, 2070.
Cattani, A., et al., 2023. Adaptation Shapes Local Cortical Reactivity: From Bifurcation Diagram and Simulations to Human Physiological and Pathological Responses. eNeuro 10.
Chauvette, S., Volgushev, M., Timofeev, I., 2010. Origin of Active States in Local Neocortical Networks during Slow Sleep Oscillation. Cerebral Cortex 20, 2660–2674.
Colombo, M.A., et al., 2023. Beyond alpha power: EEG spatial and spectral gradients robustly stratify disorders of consciousness. Cereb Cortex 33, 7193–7210.
Colombo, M.A., et al., 2025. Hemispherotomy leads to persistent sleep-like slow waves in the isolated cortex of awake humans. PLOS Biology 23, e3003060.
Compte, A., Sanchez-Vives, M.V., McCormick, D.A., Wang, X.-J., 2003. Cellular and Network Mechanisms of Slow Oscillatory Activity (<1 Hz) and Wave Propagations in a Cortical Network Model. Journal of Neurophysiology 89, 2707–2725.
Compte, A., et al., 2008. Spontaneous High-Frequency (10–80 Hz) Oscillations during Up States in the Cerebral Cortex In Vitro. J. Neurosci. 28, 13828–13844.
Coronel-Oliveros, C., Gießing, C., Medel, V., Cofré, R., Orio, P., 2023. Whole-brain modeling explains the context-dependent effects of cholinergic neuromodulation. NeuroImage 265, 119782.
Covelo, J., et al., 2025. Spatiotemporal network dynamics and structural correlates in the human cerebral cortex *in vitro*. Progress in Neurobiology 246, 102719.
Covelo, J., Cortada, M., Vinci, G.V., Mattia, M., Sanchez-Vives, M.V., 2025. Network Desynchronization with Sine Waves: from Synchrony to Asynchrony by Periodic Stimulation. Advanced Science 12, e14602.
D'Ambrosio, S., et al., 2023. Detecting cortical reactivity alterations induced by structural disconnection in subcortical stroke. Clinical Neurophysiology 156, 1–3.
Dalla Porta, L., Barbero-Castillo, A., Sanchez-Sanchez, J.M., Sanchez-Vives, M.V., 2023. M-current modulation of cortical slow oscillations: Network dynamics and computational modeling. PLOS Computational Biology 19, e1011246.

Dalla Porta, L., Fousek, J., Destexhe, A., Sanchez-Vives, M.V., 2025. Cholinergic heterogeneity facilitates synchronization and information flow in a whole-brain model. bioRxiv, 10.28.685048, p. 2025.
David, O., Friston, K.J., 2003. A neural mass model for MEG/EEG:: coupling and neuronal dynamics. NeuroImage 20, 1743–1755.
de Reus, M.A., van den Heuvel, M.P, 2013. Estimating false positives and negatives in brain networks. NeuroImage 70, 402–409.
Deco, G., Jirsa, V.K., Robinson, P.A., Breakspear, M., Friston, K., 2008. The Dynamic Brain: From Spiking Neurons to Neural Masses and Cortical Fields. PLOS Computational Biology 4, e1000092.
Destexhe, A., Hughes, S.W., Rudolph, M., Crunelli, V., 2007. Are corticothalamic 'up' states fragments of wakefulness? Trends Neurosci 30, 334–342.
Douglas, R.J., Martin, K.A.C., 2004. Neuronal circuits of the neocortex. Annu Rev Neurosci 27, 419–451.
Ercsey-Ravasz, M., et al., 2013. A Predictive Network Model of Cerebral Cortical Connectivity Based on a Distance Rule. Neuron 80, 184–197.
Ermentrout, B.XPPAUT.in, 2012. *Computational Systems Neurobiology* (ed. Le Novère, N.). Springer, Netherlands, Dordrecht, pp. 519–531. https://doi.org/10.1007/978-94-007-3858-4_17.
Fehér, K.D., et al., 2021. Shaping the slow waves of sleep: A systematic and integrative review of sleep slow wave modulation in humans using non-invasive brain stimulation. Sleep Medicine Reviews 58, 101438.
Fornito, A., Zalesky, A., Breakspear, M., 2015. The connectomics of brain disorders. Nat Rev Neurosci 16, 159–172.
Funk, C.M., et al., 2017. Role of Somatostatin-Positive Cortical Interneurons in the Generation of Sleep Slow Waves. J. Neurosci. 37, 9132–9148.
Garside, P., Arizpe, J., Lau, C.-I., Goh, C., Walsh, V., 2015. Cross-hemispheric Alternating Current Stimulation During a Nap Disrupts Slow Wave Activity and Associated Memory Consolidation. Brain Stimul 8, 520–527.
Gast, R., et al., 2019. PyRates—A Python framework for rate-based neural simulations. PLOS ONE 14, e0225900.
Gloor, P., Ball, G., Schaul, N., 1977. Brain lesions that produce delta waves in the EEG. Neurology 27, 326–333.
Grefkes, C., Eickhoff, S.B., Nowak, D.A., Dafotakis, M., Fink, G.R., 2008. Dynamic intra- and interhemispheric interactions during unilateral and bilateral hand movements assessed with fMRI and DCM. NeuroImage 41, 1382–1394.
Griffis, J.C., Metcalf, N.V., Corbetta, M., Shulman, G.L., 2019. Structural Disconnections Explain Brain Network Dysfunction after Stroke. Cell Reports 28, 2527-2540.e9.
Grossman, N., et al., 2017. Noninvasive Deep Brain Stimulation via Temporally Interfering Electric Fields. Cell 169, 1029–1041 e16.
Huber, R., Felice Ghilardi, M., Massimini, M., Tononi, G., 2004. Local sleep and learning. Nature 430, 78–81.
Idesis, S., et al., 2024. Generative whole-brain dynamics models from healthy subjects predict functional alterations in stroke at the level of individual patients. Brain Communications 6, fcae237.
Idesis, S., et al., 2024. Whole-brain model replicates sleep-like slow-wave dynamics generated by stroke lesions. Neurobiology of Disease 200, 106613.
Imbrosci, B., Mittmann, T., 2011. Functional Consequences of the Disturbances in the GABA-Mediated Inhibition Induced by Injuriesin the Cerebral Cortex. Neural Plast 2011, 614329.
Jansen, B.H., Rit, V.G., 1995. Electroencephalogram and visual evoked potential generation in a mathematical model of coupled cortical columns. Biol Cybern 73, 357–366.
Jirsa, V.K., et al., 2017. The Virtual Epileptic Patient: Individualized whole-brain models of epilepsy spread. NeuroImage 145, 377–388.
Karaszewski, B., et al., 2006. Measurement of brain temperature with magnetic resonance spectroscopy in acute ischemic stroke. Annals of Neurology 60, 438–446.
Kassubek, J., Sörös, P., Kober, H., Stippich, C., Vieth, J.B., 1999. Focal slow and beta brain activity in patients with multiple sclerosis revealed by magnetoencephalography. Brain Topogr 11, 193–200.
Keune, P.M., et al., 2019. Frontal brain activity and cognitive processing speed in multiple sclerosis: An exploration of EEG neurofeedback training. NeuroImage: Clinical 22, 101716.
Kim, Y.K., Yang, E.J., Cho, K., Lim, J.Y., Paik, N.-J., 2014. Functional Recovery After Ischemic Stroke Is Associated With Reduced GABAergic Inhibition in the Cerebral Cortex: A GABA PET Study. Neurorehabil Neural Repair 28, 576–583.
Koch, G., et al., 2008. Hyperexcitability of parietal-motor functional connections for the intact left-hemisphere in neglect patients. Brain 131, 3147–3155.
Koller, D.P., Schirner, M., Ritter, P., 2024. Human connectome topology directs cortical traveling waves and shapes frequency gradients. Nat Commun 15, 3570.
Krom, A.J., et al., 2020. Anesthesia-induced loss of consciousness disrupts auditory responses beyond primary cortex. Proceedings of the National Academy of Sciences 117, 11770–11780.
Krone, L.B., Vyazovskiy, V.V, 2020. Unresponsive or just asleep? Do local slow waves in the perilesional cortex have a function? Brain 143, 3513–3515.
Krupina, N.A., Churyukanov, M.V., Kukushkin, M.L., Yakhno, N.N., 2020. Central Neuropathic Pain and Profiles of Quantitative Electroencephalography in Multiple Sclerosis Patients. Front Neurol 10, 1380.
Lanzone, J., et al., 2022. EEG spectral exponent as a synthetic index for the longitudinal assessment of stroke recovery. Clin Neurophysiol 137, 92–101.
Latifi, S., Carmichael, S.T., 2024. The emergence of multiscale connectomics-based approaches in stroke recovery. Trends in Neurosciences 47, 303–318.
Lee, S.-H., Dan, Y., 2012. Neuromodulation of Brain States. Neuron 76, 209–222.
Lemaréchal, J.-D., et al., 2021. A brain atlas of axonal and synaptic delays based on modelling of cortico-cortical evoked potentials. Brain 145, 1653–1667.
Linkenkaer-Hansen, K., Nikouline, V.V., Palva, J.M., Ilmoniemi, R.J., 2001. Long-Range Temporal Correlations and Scaling Behavior in Human Brain Oscillations. J. Neurosci. 21, 1370–1377.
Luczak, A., Barthó, P., Marguet, S.L., Buzsáki, G., Harris, K.D., 2007. Sequential structure of neocortical spontaneous activity in vivo. Proceedings of the National Academy of Sciences 104, 347–352.
Mórocz, I. et al. Brain states analysis of EEG predicts multiple sclerosis and mirrors disease duration and burden. Preprint at https://doi.org/10.48550/arXiv.2406.15665 (2025).
Makeig, S., Inlow, M., 1993. Lapse in alertness: coherence of fluctuations in performance and EEG spectrum. Electroencephalography and Clinical Neurophysiology 86, 23–35.
Makeig, S., Jung, T.P., 1995. Changes in alertness are a principal component of variance in the EEG spectrum. Neuroreport 7, 213–216.
Marmelshtein, A., Eckerling, A., Hadad, B., Ben-Eliyahu, S., Nir, Y., 2023. Sleep-like changes in neural processing emerge during sleep deprivation in early auditory cortex. Current Biology 33, 2925–2940 e6.
Marshall, L., Helgadóttir, H., Mölle, M., Born, J., 2006. Boosting slow oscillations during sleep potentiates memory. Nature 444, 610–613.
Massimini, M., Huber, R., Ferrarelli, F., Hill, S., Tononi, G., 2004. The Sleep Slow Oscillation as a Traveling Wave. J. Neurosci. 24, 6862–6870.
Massimini, M., et al., 2024. Sleep-like cortical dynamics during wakefulness and their network effects following brain injury. Nat Commun 15, 7207.
Mattia, M., Sanchez-Vives, M.V., 2012. Exploring the spectrum of dynamical regimes and timescales in spontaneous cortical activity. Cogn Neurodyn 6, 239–250.
McCormick, D.A., Williamson, A., 1989. Convergence and divergence of neurotransmitter action in human cerebral cortex. Proceedings of the National Academy of Sciences 86, 8098–8102.
McCormick, D.A., Nestvogel, D., He, B.J., 2020. Neuromodulation of Brain State and Behavior. Annu Rev Neurosci 43, 391–415.
McCormick, D.A., 1992. Neurotransmitter actions in the thalamus and cerebral cortex and their role in neuromodulation of thalamocortical activity. Prog Neurobiol 39, 337–388.
Mehmood, T., Liland, K.H., Snipen, L., Sæbø, S., 2012. A review of variable selection methods in Partial Least Squares Regression. Chemometrics and Intelligent Laboratory Systems 118, 62–69.
Meythaler, J.M., Peduzzi, J.D., Eleftheriou, E., Novack, T.A., 2001. Current concepts: Diffuse axonal injury–associated traumatic brain injury. Archives of Physical Medicine and Rehabilitation 82, 1461–1471.
Mofakham, S., et al., 2021. Electrocorticography reveals thalamic control of cortical dynamics following traumatic brain injury. Commun Biol 4, 1210.
Momi, D., Wang, Z., Griffiths, J.D., 2023. TMS-evoked responses are driven by recurrent large-scale network dynamics. Elife 12, e83232.
Momi, D., et al., 2025. Stimulation mapping and whole-brain modeling reveal gradients of excitability and recurrence in cortical networks. Nat Commun 16, 3222.
Moran, R.J., et al., 2007. A neural mass model of spectral responses in electrophysiology. Neuroimage 37, 706–720.
Nir, Y., et al., 2011. Regional Slow Waves and Spindles in Human Sleep. Neuron 70, 153–169.
Nir, Y., et al., 2017. Selective neuronal lapses precede human cognitive lapses following sleep deprivation. Nat Med 23, 1474–1480.
Nuwer, M.R., Jordan, S.E., Ahn, S.S., 1987. Evaluation of stroke using EEG frequency analysis and topographic mapping. Neurology 37, 1153–1159.
Pang, J.C., et al., 2023. Geometric constraints on human brain function. Nature 618, 566–574.
Pedregosa, F., et al., 2011. Scikit-learn: Machine Learning in Python. J. Mach. Learn. Res. 12, 2825–2830.
Perez-Zabalza, M., et al., 2020. Modulation of cortical slow oscillatory rhythm by GABAB receptors: an in vitro experimental and computational study. J Physiol 598, 3439–3457.
Pigorini, A., et al., 2015. Bistability breaks-off deterministic responses to intracortical stimulation during non-REM sleep. Neuroimage 112, 105–113.
Proix, T., Bartolomei, F., Guye, M., Jirsa, V.K., 2017. Individual brain structure and modelling predict seizure propagation. Brain 140, 641–654.
Proix, T., Jirsa, V.K., Bartolomei, F., Guye, M., Truccolo, W., 2018. Predicting the spatiotemporal diversity of seizure propagation and termination in human focal epilepsy. Nat Commun 9, 1088.
Rabuffo, G., et al., 2025. Mapping global brain reconfigurations following local targeted manipulations. Proceedings of the National Academy of Sciences 122, e2405706122.
Raut, R.V., et al., 2021. Global waves synchronize the brain's functional systems with fluctuating arousal. Science Advances 7, eabf2709.
Raut, R.V., et al., 2025. Arousal as a universal embedding for spatiotemporal brain dynamics. Nature 1–8. https://doi.org/10.1038/s41586-025-09544-4.
Rigney, G., Lennon, M., Holderrieth, P., 2021. The use of computational models in the management and prognosis of refractory epilepsy: A critical evaluation. Seizure 91, 132–140.
Rocchi, F., et al., 2022. Increased fMRI connectivity upon chemogenetic inhibition of the mouse prefrontal cortex. Nat Commun 13, 1056.
Rosanova, M., et al., 2018. Sleep-like cortical OFF-periods disrupt causality and complexity in the brain of unresponsive wakefulness syndrome patients. Nat Commun 9, 4427.
Russo, S., et al., 2021. Focal lesions induce large-scale percolation of sleep-like intracerebral activity in awake humans. NeuroImage 234, 117964.
Škoch, A., et al., 2022. Human brain structural connectivity matrices–ready for modelling. Sci Data 9, 486.

Salim, A.A., Ali, S.H., Hussain, A.M., Ibrahim, W.N., 2021. Electroencephalographic evidence of gray matter lesions among multiple sclerosis patients. Medicine (Baltimore) 100, e27001.
Sanchez-Todo, R., et al., 2023. A physical neural mass model framework for the analysis of oscillatory generators from laminar electrophysiological recordings. NeuroImage 270, 119938.
Sanchez-Vives, M.V., McCormick, D.A., 2000. Cellular and network mechanisms of rhythmic recurrent activity in neocortex. Nat Neurosci 3, 1027–1034.
Santos, F.P.dos, Vohryzek, J., Verschure, P.F.M.J, 2023. Multiscale effects of excitatory-inhibitory homeostasis in lesioned cortical networks: A computational study. PLOS Computational Biology 19, e1011279.
Sarasso, S., et al., 2020. Local sleep-like cortical reactivity in the awake brain after focal injury. Brain 143, 3672–3684.
Sarasso, S., et al., 2025. Reduction of sleep-like perilesional slow waves and clinical evolution after stroke: A TMS-EEG study. Clinical Neurophysiology 175, 2110746.
Schiene, K., et al., 1996. Neuronal Hyperexcitability and Reduction of GABAA-Receptor Expression in the Surround of Cerebral Photothrombosis. J Cereb Blood Flow Metab 16, 906–914.
Schiff, N.D., 2008. Central Thalamic Contributions to Arousal Regulation and Neurological Disorders of Consciousness. Annals of the New York Academy of Sciences 1129, 105–118.
Schwindt, P.C., Spain, W.J., Crill, W.E., 1989. Long-lasting reduction of excitability by a sodium-dependent potassium current in cat neocortical neurons. J Neurophysiol 61, 233–244.
Sheybani, L., et al., 2023. Wake slow waves in focal human epilepsy impact network activity and cognition. Nat Commun 14, 7397.
Siegel, J.S., et al., 2016. Disruptions of network connectivity predict impairment in multiple behavioral domains after stroke. Proceedings of the National Academy of Sciences 113, E4367–E4376.
Steriade, M., Nunez, A., Amzica, F., 1993. A novel slow (< 1 Hz) oscillation of neocortical neurons in vivo: depolarizing and hyperpolarizing components. J. Neurosci. 13, 3252–3265.
Stickgold, R., 2005. Sleep-dependent memory consolidation. Nature 437, 1272–1278.
Sun, H., Feng, Z., 2013. Neuroprotective role of ATP-sensitive potassium channels in cerebral ischemia. Acta Pharmacol Sin 34, 24–32.
Tewarie, P.K.B., et al., 2023. Early EEG monitoring predicts clinical outcome in patients with moderate to severe traumatic brain injury. Neuroimage Clin 37, 103350.
Thiebaut de Schotten, M., Foulon, C., Nachev, P., 2020. Brain disconnections link structural connectivity with function and behaviour. Nat Commun 11, 5094.
Timofeev, I., Grenier, F., Bazhenov, M., Sejnowski, T.J., Steriade, M., 2000. Origin of slow cortical oscillations in deafferented cortical slabs. Cereb Cortex 10, 1185–1199.
Timofeev, I., Grenier, F., Steriade, M., 2001. Disfacilitation and active inhibition in the neocortex during the natural sleep-wake cycle: An intracellular study. Proceedings of the National Academy of Sciences 98, 1924–1929.
Tononi, G., Cirelli, C., 2006. Sleep function and synaptic homeostasis. Sleep Med Rev 10, 49–62.
Torao-Angosto, M., Manasanch, A., Mattia, M., Sanchez-Vives, M.V., 2021. Up and Down States During Slow Oscillations in Slow-Wave Sleep and Different Levels of Anesthesia. Front. Syst. Neurosci. 15.
Traub, R.D., Wong, R.K., 1982. Cellular mechanism of neuronal synchronization in epilepsy. Science 216, 745–747.
Tscherpel, C., et al., 2024. Local neuronal sleep after stroke: The role of cortical bistability in brain reorganization. Brain Stimulation: Basic, Translational, and Clinical Research in Neuromodulation 17, 836–846.
Tzourio-Mazoyer, N., et al., 2002. Automated Anatomical Labeling of Activations in SPM Using a Macroscopic Anatomical Parcellation of the MNI MRI Single-Subject Brain. NeuroImage 15, 273–289.
Uji, M., et al., 2025. Human deep sleep facilitates cerebrospinal fluid dynamics linked to spontaneous brain oscillations and neural events. Proceedings of the National Academy of Sciences 122, e2509626122.
Van der Meer, M.L., et al., 2013. Cognition in MS correlates with resting-state oscillatory brain activity: An explorative MEG source-space study. Neuroimage Clin 2, 727–734.
Vieira, P.G., Krause, M.R., Pack, C.C., 2024. Temporal interference stimulation disrupts spike timing in the primate brain. Nat Commun 15, 4558.
Violante, I.R., et al., 2023. Non-invasive temporal interference electrical stimulation of the human hippocampus. Nat Neurosci 26, 1994–2004.
Virtanen, P., et al., 2020. SciPy 1.0: fundamental algorithms for scientific computing in Python. Nat Methods 17, 261–272.
von Monakow, C., 1914. Die Lokalisation im Grosshirn und der Abbau der Funktion durch Kortikale Herde. JAMA LXIII, 797.
Vyazovskiy, V.V., et al., 2011. Local sleep in awake rats. Nature 472, 443–447.
Walter, W.G., 1937. The Electro-encephalogram in Cases of Cerebral Tumour. Proc R Soc Med 30, 579–598.
Wold, S., Johansson, E., Cocchi, M., 1993. PLS: partial least squares projections to latent structures. 3D QSAR in Drug Design: Theory, Methods and Applications. Kluwer ESCOM Science Publisher, pp. 523–550.
Wold, S., Sjöström, M., Eriksson, L., 2001. PLS-regression: a basic tool of chemometrics, 58. Chemometrics and Intelligent Laboratory Systems, pp. 109–130.
Xie, Y., Zhang, T., 2012. Repetitive transcranial magnetic stimulation improves consciousness disturbance in stroke patients: A quantitative electroencephalography spectral power analysis. Neural Regen Res 7, 2465–2472.
Yasuda, T., Yoshida, H., Garcia-Garcia, F., Kay, D., Krueger, J.M., 2005. Interleukin-1β has a Role in Cerebral Cortical State-Dependent Electroencephalographic Slow-Wave Activity. Sleep 28, 177–186.
Yoshida, H., et al., 2004. State-specific asymmetries in EEG slow wave activity induced by local application of TNFα. Brain Research 1009, 129–136.
Zucca, S., et al., 2017. An inhibitory gate for state transition in cortex. eLife 6, e26177.

Supplementary Information

Table of Contents

1. Supplementary Methods

1.1 Wilson-Cowan rate model with Spike-frequency adaptation

We implemented in The Virtual Brain (TVB) a Wilson-Cowan (WC) rate model with spike frequency adaptation current (Fig. S3A), as in Levenstein et al[1]. This model reproduces key features of Up and Down state transitions arising from the interplay between adaptation, recurrent excitation, external inputs, and noise. We used it to validate our main findings with a simplified rate-based model. The WC comprises three state variables representing the excitatory firing rate r_e, inhibitory firing rate r_i, and adaptation current *a*. Two independent Ornstein-Uhlenbeck (OU) noise processes, u_e and u_i, act on the excitatory and inhibitory populations, respectively. The population firing rates evolve according to:

$$\tau_e \frac{dr_e}{dt} = -r_e + R_e(w_{ee}r_e - w_{ie}r_i + c\sum_k W_{jk}r_e^k[t-\tau_{jk}] + I_e - a + u_e), \quad (1)$$

$$\tau_i \frac{dr_i}{dt} = -r_i + R_i(w_{ei}r_e - w_{ii}r_i + I_i + u_i), \quad (2)$$

where R_e and R_i are power-law input-output functions[2] defined as:

$$R_{e/i,\infty}(x) = k_{e/i}\,[x - h_{e/i}]_+^n, \quad (3)$$

with scaling factors k_e and k_i, thresholds h_e and h_i, and exponent n. The internal coupling terms include recurrent weights w_{ee} (excitatory-to-excitatory), w_{ei} (excitatory-to-inhibitory), w_{ie} (inhibitory-to-excitatory), and w_{ii} (inhibitory-to-inhibitory neurons); the network coupling, which targets the excitatory population, is given by $c\sum_k W_{jk}r_e^k[t-\tau_{jk}]$, where W_{jk} is the connection weight from presynaptic node k to postsynaptic node j, and τ_{jk} represents the time delay between j and k. The term c is the global coupling factor that scales all the connection weights. Thus, the effective excitatory coupling strength between j and k is given by the product of W_{jk} and c, and we denote it by C_{jk}. r_e^k is the firing rate of node k, and I_e and I_i are external inputs to excitatory and inhibitory populations, respectively. The slow adaptation current *a* implements spike-frequency adaptation through:

$$\tau_a \frac{da}{dt} = -a + A_\infty(r_e), \quad (4)$$

where

$$A_\infty(r_e) = \frac{g}{1 + e^{-a_a(r_e - \mu_a)}}, \quad (5)$$

is a sigmoid function of the excitatory firing rate with gain a_a, threshold μ_a, and strength g (denoted as b in the original article). τ_a is the time constant of the adaptation dynamics. The noise processes follow the OU dynamics:

$$\tau_{ou} \frac{du_{e/i}}{dt} = -u_{e/i} + \sigma_{ou}\xi_{e/i}(t), \quad (6)$$

where $\xi_{e\backslash i}(t)$ are independent Wiener processes with amplitude σ_{ou} and time constant τ_{ou}. The parameters used for the WC simulations are listed in Table S2. Equations were integrated using the Heun stochastic method in TVB with a time step of 0.5 ms.

1.2 Simulation and analysis of coupled WC models: from two nodes to whole-brain networks

Two-population model. To assess the effects of disconnectivity on the emergence of slow wave (SW) activity, a two-node model was implemented, consisting of two bidirectionally connected WC nodes (denoted WC_a and WC_b) as in Section 2.3 of the main Methods. The nodes were coupled symmetrically or asymmetrically through excitatory-to-excitatory connections. The system behavior was explored parametrically as a function of the adaptation strength (g) and the excitatory coupling strength (C). In the symmetric configuration, g and C were varied equally in both populations, while in the asymmetric configuration, they were varied independently. For each parameter configuration, an independent 25s simulation was performed, with g varying from 0 to 4 in increments of 0.4, and C varying from 0 to 1 in increments of 0.05.

Whole-brain network model. The human whole-brain simulations were implemented using the same structural connectivity dataset described in the main Methods (Section 2.5). The connectivity matrix comprised 80 cortical regions from the Automatic Anatomical Labeling (AAL) atlas, averaged across subjects and thresholded to retain only connections present in more than 50% of individuals. The weights were normalized by in-degree to equalize excitatory input across nodes while preserving the structural topology. The model was first simulated in a control configuration, followed by lesion simulations in which each node was disconnected sequentially by setting its incoming and outgoing weights to zero. Each simulation lasted 100s, with a global coupling factor c=0.45 and g=1.8.

Spectral analysis. The power spectral density (psd) of the excitatory firing rate r_e was computed using Welch's method with 3-s segments and 50% overlap. δ power (<4 Hz) was extracted from the psd and used as an index of SW activity. To characterize the SW activity impinging on a given node, two neighborhood-level measures were computed: i) Neighborhood δ power (NBR δ power): the average δ power across the afferent nodes projecting to a given node, ii) Neighborhood δ coherence (NBR δ coherence): the average pairwise spectral coherence in the δ band among afferent nodes of each target node. These measures are in accordance with the NBR %Down and NBR DownOverlap metrics described for the Jansen–Rit model (Section 2.6), but are computed in the spectral domain. The definition of the neighborhood was the same as that described in Section 2.6 of the main Methods.

Statistical analysis. Statistical analyses were performed as described in the main Methods (Section 2.9). The relationships between δ power (and its square root), connection loss, NBR δ power, and NBR δ coherence were assessed using Pearson's correlation and Partial Least Squares (PLS) regression. As in the main analyses, the % variance explained (R^2) was computed under both full and 10-fold cross-validation to evaluate model generalization. The contribution of each predictor to the first PLS component (PLS1) was quantified using Variable Importance in Projection (VIP) scores.

2. Supplementary Figures

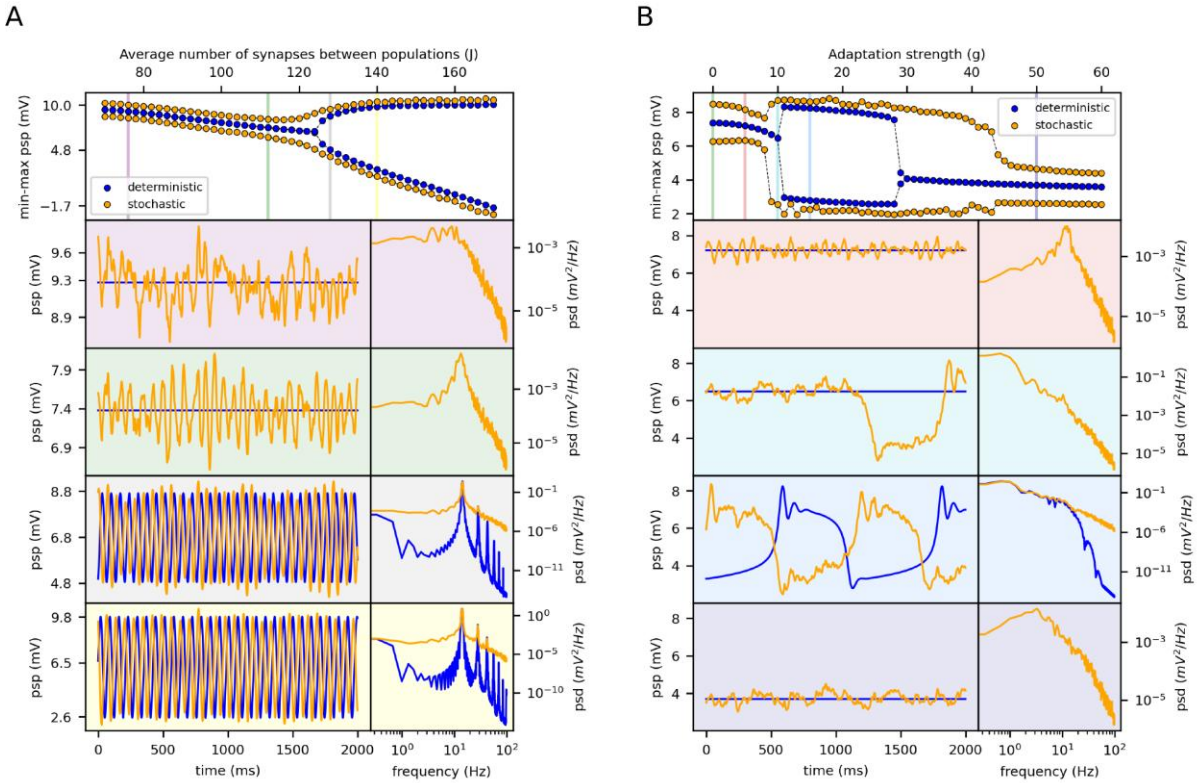

Figure S1 Bifurcation diagrams and oscillatory dynamics in deterministic and stochastic JR model. (A) Bifurcation diagram showing the min-max range of postsynaptic potential (PSP) as a function of J, for the deterministic (blue) and stochastic (yellow) models. Vertical bars mark specific values of J, for which representative psp traces (left) and their power spectral densities (psd, right) are shown. The background color of each panel corresponds to the respective vertical colored bar in the bifurcation diagram. The model was run without adaptation (g=0). A supercritical Hopf bifurcation occurs around J=128. (B) Bifurcation diagram as a function of adaptation strength (g), with the same conventions as in (A). The synaptic strength J is set to 112 (matching the green vertical bar in panel A). When g=0 the system corresponds to the same configuration of panel (A) for J=112. For low g, the system is near a supercritical Hopf bifurcation and exhibits damped oscillations. For g>9, Up/Down oscillations emerge. At g=9 and g=10, stochastic fluctuations drive transient transitions to the Down state. For g>39, the system stabilizes in a persistent Down state, with occasional Up state excursions for 30<g<39. Vertical bars indicate specific values of g (i.e., g=0, g=5, g=10, g=15, g=50), for which corresponding PSP traces and psd are shown in the lower panels, color-coded accordingly. Stability analysis of the deterministic model was performed in XPPAUT.

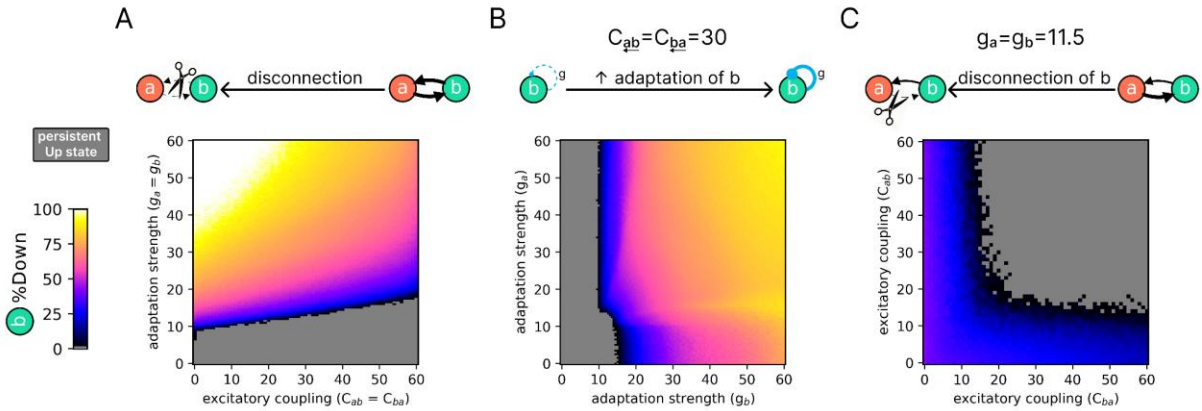

Figure S2 Effects of adaptation strength and excitatory coupling on slow wave emergence in population JR_b. Each heatmap shows the percentage of time spent in the Down state (%Down) in JR_b as a function of (A) symmetric excitatory coupling ($C_{ab} = C_{ba}$) and adaptation strength ($g_a = g_b$), (B) asymmetric adaptation (g_a, g_b) with fixed symmetric coupling ($C_{ab} = C_{ba} = 30$), and (C) asymmetric coupling (C_{ab}, C_{ba}) with fixed adaptation strength ($g_a = g_b = 11.5$). The color scale indicates the proportion of time spent in the Down state, from persistent Up state (gray) to predominant Down state (white).

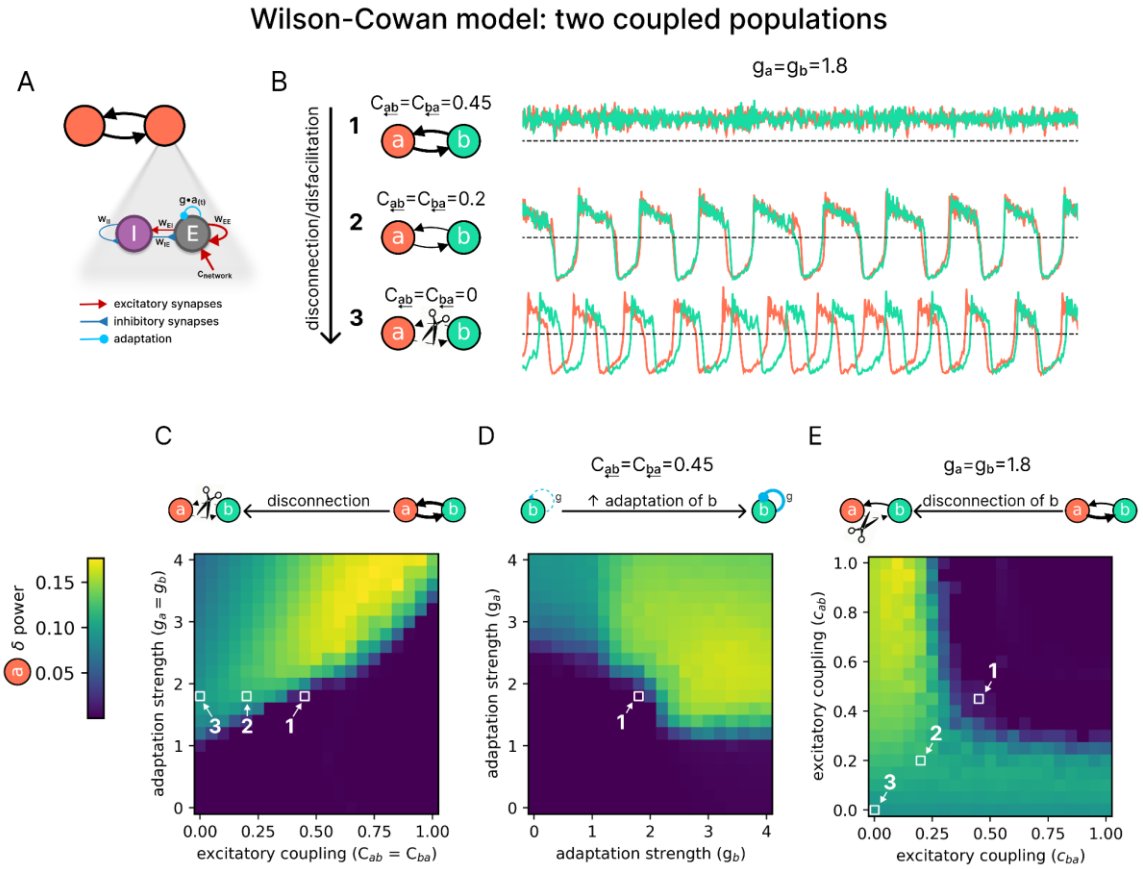

Figure S3 Effects of adaptation strength and excitatory coupling on slow wave emergence in two coupled WC nodes. (A) Representation of the Wilson-Cowan (WC) model with spike-frequency adaptation, consisting of interconnected excitatory (E) and inhibitory (I) neuronal pools. (B) Example dynamics of two symmetrically coupled populations (WC_a in orange, WC_b in cyan) for three levels of excitatory coupling ($C_{ab}=C_{ba}$). With C=0.45 and g=1.8 (top, #1), both populations show fast oscillations in a persistent Up state. Reducing coupling to C=0.2 (middle, #2) induces a transition to slow oscillations (SO). Complete disconnection (C=0, bottom, #3) further enhances SO activity.. (C) Heatmap showing the δ power of node WC_a as a function of adaptation strength (g, y-axis) and symmetric excitatory coupling (C, x-axis). The three squares with numbers correspond to the configuration of panel B, highlighting the effect of reducing C with g=0.45 kept fixed. Notice how the δ power increases through the transition from a persistent Up state (δ power) to SO (high δ power). (D) Effect of asymmetric adaptation. Heatmap shows δ power in WC_a as a function of g_b (x-axis) and g_a (y-axis), with symmetric coupling fixed at C=0.45. From the square #1, varying g_b (i.e., changing the adaptation of WC_b) alone can induce a transition from a persistent Up state to SO (high δ power) in WC_a, despite g_a being kept constant. (E) Effect of asymmetric coupling. Heatmap shows δ power in WC_a as a function of C_{ba} (x-axis) and C_{ab} (y-axis), with g=1.8 kept fixed. From the square #1, reducing C_{ba} (i.e., disconnecting WC_b) alone is sufficient to induce a transition from a persistent Up state to SO (high δ power) in WC_a, even when C_{ab} remains constant. Numbers 1, 2, and 3 in all panels correspond to identical parameter configurations across plots.

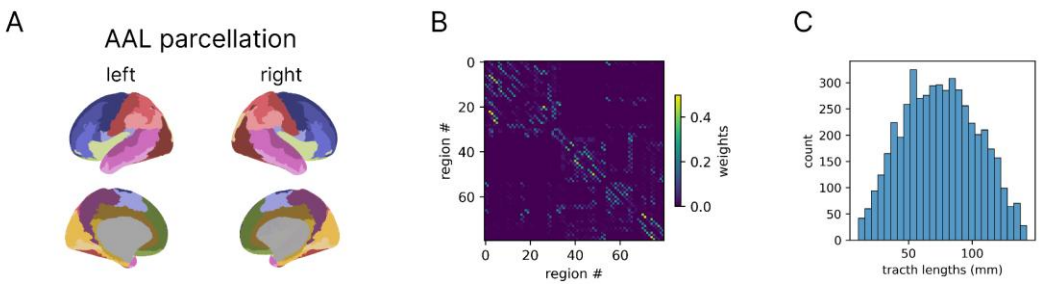

Figure S4 Whole-brain structural network parcellation and connectivity statistics. (A) Anatomical Automatic Labeling (AAL) parcellation scheme displaying bilateral regional divisions across cortical structures. (B) Connectivity weight matrix derived from diffusion tensor imaging (DTI) tractography, showing inter-regional connection strengths between all 80 AAL cortical regions. (C) Histogram of white matter tract lengths across all streamlines in the network.

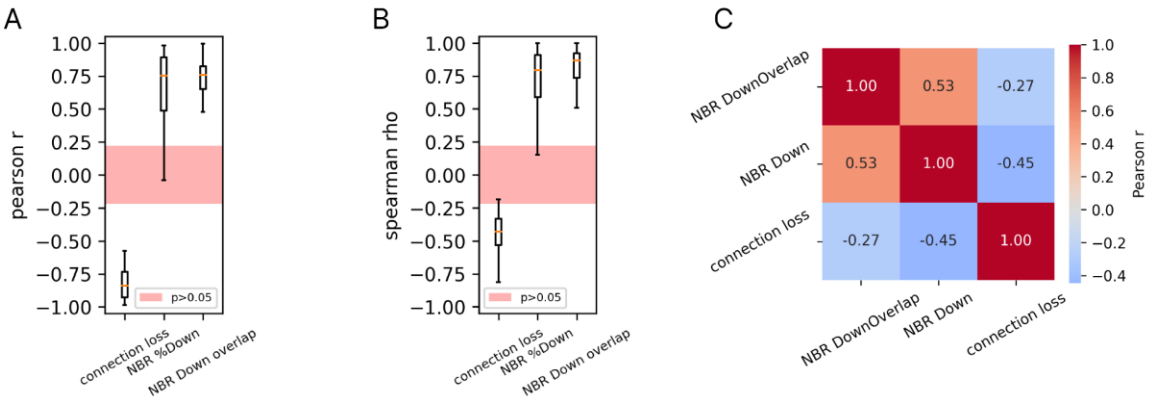

Figure S5 Per-lesion correlation analyses and predictor collinearity. (A-B) Pearson (A) and Spearman rank-order (B) correlation coefficients between each predictor and $\%Down_{sqrt}$, computed independently for each of the 80 lesioned nodes. Boxplots display the median (orange line), interquartile range (box), and whiskers extending to 1.5 × the interquartile range. The shaded pink band shows the significance threshold ($p = 0.05$) for each per-lesion sample size ($n = 79$ targets), determined by two-tailed t-test. Across all three predictors, at least 83% of per-lesion correlations exceeded the significance threshold. Median values align with pooled-data correlations from the main analysis of Fig. 6. (C) Correlation matrix of predictor variables (connection loss, NBR %Down, NBR DownOverlap). All predictor-predictor correlations are statistically significant ($p < 0.05$), indicating collinearity.

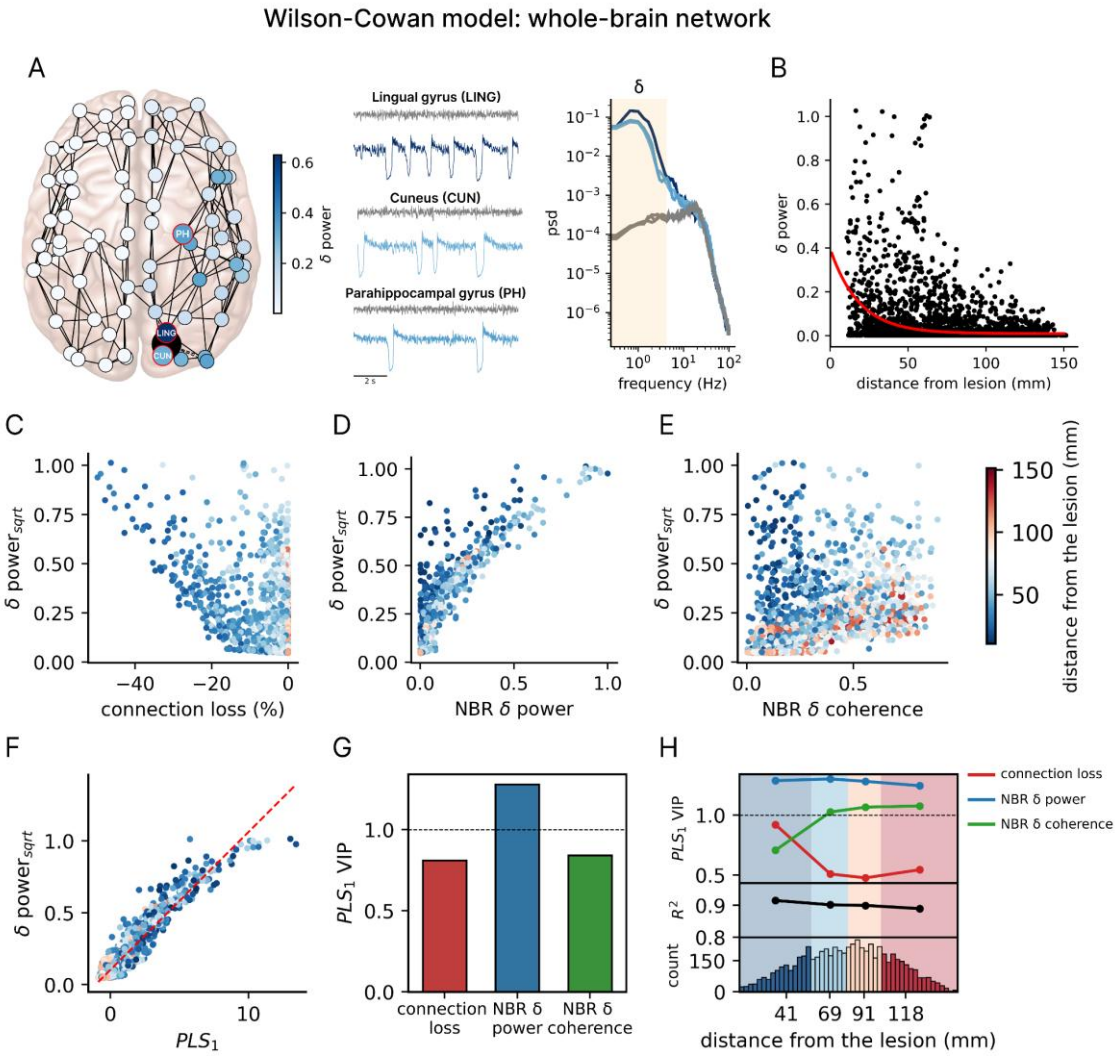

Figure S6 Slow wave generation and propagation following lesion in a whole-brain network of WC nodes. (A) Whole-brain network model with nodes defined by the Automatic Anatomical Labeling (AAL) atlas. The lesion of a node (here, the right calcarine cortex) is represented as a black dot, with the impact on the intact nodes quantified with δ power. The node colors indicate δ power, as shown in the accompanying color bar. Traces illustrate simulated activity from three representative regions in the pre-lesion (control; gray) and post-lesion (blue hues) conditions. In the control condition, the nodes display low-amplitude and fast oscillations in a persistent Up state (awake-like regime). After the lesion, SWs emerge along with an increase in δ power in the power spectral density (psd). The δ band is highlighted by the yellow span in the psd. (B) δ power as a function of the Euclidean distance from the lesion. The red curve represents an exponential fit (R^2=0.11), indicating a distance-dependent decay in SW propagation. (C) Relationship between connection loss (percentage of lost coupling strength due to the lesion relative to control) and the square root of δ power (δ $power_{sqrt}$). A negative relationship is observed (r=-0.57). (D) Relationship between the δ power of neighboring nodes (NBR δ power) and δ $power_{sqrt}$. A positive relationship is observed (r=0.89). (E) Relationship between the coherence of SW activity of neighboring nodes (NBR δ coherence) and δ $power_{sqrt}$. The variables show a positive relationship (r=0.59). (F) Partial least squares regression (PLS) of δ $power_{sqrt}$ and the score of the first PLS component (PLS_1) derived from the three independent variables (connection loss, NBR δ power, and NBR δ coherence). The model explained ~90% of the variance (R^2=0.92; after cross-validation R^2=0.91). (G) PLS_1 weights for the three independent variables, indicating their relative contributions. (H) Distance-dependent contributions of the three independent variables to δ $power_{sqrt}$. Nodes were divided into quartiles based on their distance from the lesion, and PLS regression was performed for each subset. For each quartile, the model's R^2 and the VIP scores of each variable are reported.

3. Supplementary Tables

Table S1 Parameters of the Jansen-Rit model used in the simulations. The table lists the parameters used in The Virtual Brain (TVB) implementation of the Jansen-Rit (JR) model with spike-frequency adaptation. All values lie within physiological ranges and have been previously explored in the literature (e.g., J and V_0[3]; A, B, a, and b[4]; k_{ad}[5]). The excitatory coupling strength factor c and the adaptation strength g were varied in the study and were set to c=30 and g=11.5 for both the toy and whole-brain networks. The parameter J was explored within the range used in[3] and was set to produce subcritical dynamics just before a supercritical Hopf bifurcation, resulting in a peak in the power spectrum in the alpha band (J=121 for the whole-brain network model and J=112 for all other models).

Parameter	Description	Value
A	Maximum amplitude of EPSP. Also called average synaptic gain	3.25 mV
B	Maximum amplitude of IPSP. Also called average synaptic gain	36.67 mV
a	Reciprocal of the time constant of the passive membrane and all other spatially distributed delays in the dendritic network. Also called average synaptic time constant	0.1 ms^{-1} (=10 ms)
b	Reciprocal of the time constant of the passive membrane and all other spatially distributed delays in the dendritic network. Also called average synaptic time constant	0.083 ms^{-1} (=12 ms)
v_0	Firing threshold (PSP) for which a 50% firing rate is achieved	5.52 mV
v_{max}	Determines the maximum firing rate of the neuronal pools	0.0025 ms^{-1}
r	Steepness of the sigmoidal transformation	0.56 mV^{-1}
J	Average number of synapses between the neuronal pools	varied
a_1	Average probability of synaptic contacts in the feedback excitatory loop	1
a_2	Average probability of synaptic contacts in the slow feedback excitatory loop	0.8
a_3	Average probability of synaptic contacts in the feedback inhibitory loop	0.25
a_4	Average probability of synaptic contacts in the slow feedback inhibitory loop	0.25
μ	Mean input firing rate	0.22
k_{ad}	Adaptation rate constant	0.001 ms^{-1}
g	Adaptation strength	varied
σ_{noise}	Noise strength. Standard deviation of the Gaussian distribution used to generate the additive white noise	10^{-4}
c	Factor scaling the excitatory coupling strength between nodes	varied
v	Signal propagation velocity	4 m/s

Table S2 Parameters of the Wilson-Cowan model used in the simulations. The table lists the parameters used in The Virtual Brain (TVB) implementation of the rate model with spike-frequency adaptation. All parameter values were taken from the original publication[1], except for the time constant of the adaptation dynamics (tau_a, changed here from 200 to 500 ms to better align with the JR model while remaining consistent with adaptation kinetics[6]) and the threshold of the inhibitory input-output function (h_i changed from 12 to 9 to increase the contribution of the inhibitory population). In the two-coupled-population model, the adaptation strength (g; denoted as b in the original article) and the excitatory coupling strength (c) were varied, whereas in the whole-brain model, these were fixed to 1.8 and 0.45, respectively, to produce an awake-like regime in the intact model (pre-lesion).

Parameter	Description	Value
$\tau_{e/i}$	Time constant of the excitatory/inhibitory population	5 ms
τ_a	Time constant of the adaptation dynamics	500 ms
w_{ee}	Internal coupling from excitatory to excitatory neurons	4
w_{ei}	Internal coupling from excitatory to inhibitory neurons	4
w_{ie}	Internal coupling from inhibitory to excitatory neurons	3
w_{ii}	Internal coupling from inhibitory to inhibitory neurons	0
$k_{e/i}$	Amplitude or scaling factor for the excitatory/inhibitory input-output function	0.02/0.05
$h_{e/i}$	Threshold of excitatory/inhibitory input-output function	0/9
n	Power law exponent of input-output functions; determines the sharpness of the population response	2
a_a	Gain of the adaptation dynamics	5
mu_a	Firing threshold of the adaptation	1.5
g	Adaptation strength	varied
$I_{e/i}$	External input to excitatory/inhibitory population	3.6
σ_{ou}	Noise strength. Standard deviation of the Ornstein-Uhlenbeck process	0.002
τ_{ou}	Correlation time of the Ornstein-Uhlenbeck process	5 ms
c	Factor scaling the excitatory coupling strength between nodes	varied
v	Signal propagation velocity	4 m/s

Table S3 Ordinary least squares regression of $\%Down_{sqrt}$ on predictors.

$\%Down_{sqrt} \sim x$				
predictor (x)	**t-value**	**p-value**	**β**	**C.I. [0.025 0.975]**
connection loss	−92.600	<0.001	−0.077	−0.079 −0.076
NBR %Down	108.120	<0.001	0.384	0.378 0.389
NBR DownOvelap	67.360	<0.001	0.023	0.022 0.023

Table S4 Linear mixed-effects regression of $\%Down_{sqrt}$ on predictors with random intercepts.

$\%Down_{sqrt} \sim x + (1\|lesion\_node) + (1\|target\_node)$				
predictor (x)	**t-value**	**p-value**	**β**	**C.I. [0.025 0.975]**
connection loss	−98.489	<0.001	−0.076	−0.077 −0.075
NBR %Down	104.386	<0.001	0.382	0.376 0.388
NBR DownOvelap	64.696	<0.001	0.022	0.022 0.023

Table S5 Ordinary least squares regression of rank-transformed $\%Down_{sqrt}$ on rank-transformed predictors.

$\%Down_{sqrt}\_ranked \sim x\_ranked$				
predictor (x_ranked)	**t-value**	**p-value**	**β**	**C.I. [0.025 0.975]**
connection loss	−40.080	<0.001	−0.254	−0.264 −0.243
NBR %Down	107.900	<0.001	0.704	0.693 0.715
NBR DownOvelap	138.120	<0.001	0.924	0.913 0.935

Table S6 Linear mixed-effects regression of rank-transformed $\%Down_{sqrt}$ on rank-transformed predictors with random intercepts.

$\%Down_{sqrt}\_ranked \sim x\_ranked + (1\|lesion\_node) + (1\|target\_node)$				
predictor (x_ranked)	**t-value**	**p-value**	**β**	**C.I. [0.025 0.975]**
connection loss	−42.640	<0.001	−0.271	−0.282 −0.261
NBR %Down	106.460	<0.001	0.703	0.691 0.714
NBR DownOvelap	137.850	<0.001	0.927	0.915 0.938

4. Supplementary References

1. Levenstein, D., Buzsáki, G. & Rinzel, J. NREM sleep in the rodent neocortex and hippocampus reflects excitable dynamics. *Nat Commun* **10**, 2478 (2019).

2. Ahmadian, Y., Rubin, D. B. & Miller, K. D. Analysis of the stabilized supralinear network. *Neural Comput* **25**, 1994–2037 (2013).

3. Jansen, B. H. & Rit, V. G. Electroencephalogram and visual evoked potential generation in a mathematical model of coupled cortical columns. *Biol Cybern* **73**, 357–366 (1995).

4. David, O. & Friston, K. J. A neural mass model for MEG/EEG:: coupling and neuronal dynamics. *NeuroImage* **20**, 1743–1755 (2003).

5. Moran, R. J. *et al.* A neural mass model of spectral responses in electrophysiology. *Neuroimage* **37**, 706–720 (2007).

6. Benda, J. & Herz, A. V. M. A universal model for spike-frequency adaptation. *Neural Comput* **15**, 2523–2564 (2003).

2.5 Article 5

Title: *Different Sensitivity of Complexity Measures to Network Integration and Segregation*

Authors: ***Gianluca Gaglioti***, *Anna Cattani, Thierry Nieus, Leonardo Dalla Porta, Renzo Comolatti, Davide Momi, Simone Sarasso, Marcello Massimini*

Abstract: *Brain complexity measures, capturing the critical balance between integration and segregation in neuronal circuits, are increasingly recognized as promising markers of consciousness. Various metrics have been proposed to estimate brain complexity, from entropy-based measures to network-theoretic approaches, and can be applied either observationally, by analysing spontaneous activity patterns, or through perturbation, by examining responses evoked by direct brain stimulation. Despite their widespread use, the relationships between these metrics and the specific aspects of brain structure they capture are seldom articulated. To address this issue, we employed a mean-field model of excitatory and inhibitory neural populations to simulate activity across networks with diverse architectures. By systematically rewiring network connectivity, we generated varying degrees of integration and segregation, and we applied multiple complexity metrics—observational and perturbational—to assess their sensitivity to these structural modifications. We found that different complexity metrics responded differently to network architecture: observational metrics exhibited biases toward either integration or segregation, or were insensitive to network changes, whereas the Perturbational Complexity Index (PCI) identified a peak in complexity when integration and segregation were optimally balanced, aligning more closely with the theoretical notion of brain complexity. Importantly, we further show that spontaneous measures are vulnerable to spurious correlations, most critically the common driver problem, which can inflate integration between otherwise independent regions, while PCI remained comparatively robust. These findings underscore the importance of selecting appropriate metrics and of considering dynamical confounds when investigating brain dynamics and consciousness.*

DOI: *forthcoming*

Different sensitivity of complexity measures to network integration and segregation

Gianluca Gaglioti, Anna Cattani, Thierry Nieus, Leonardo Dalla Porta, Renzo Comolatti, Davide Momi, Simone Sarasso, Marcello Massimini

Abstract

Brain complexity measures, capturing the critical balance between integration and segregation in neuronal circuits, are increasingly recognized as promising markers of consciousness. Various metrics have been proposed to estimate brain complexity, from entropy-based measures to network-theoretic approaches, and can be applied either observationally, by analysing spontaneous activity patterns, or through perturbation, by examining responses evoked by direct brain stimulation. Despite their widespread use, the relationships between these metrics and the specific aspects of brain structure they capture are seldom articulated. To address this issue, we employed a mean-field model of excitatory and inhibitory neural populations to simulate activity across networks with diverse architectures. By systematically rewiring network connectivity, we generated varying degrees of integration and segregation, and we applied multiple complexity metrics—observational and perturbational—to assess their sensitivity to these structural modifications. We found that different complexity metrics responded differently to network architecture: observational metrics exhibited biases toward either integration or segregation, or were insensitive to network changes, whereas the Perturbational Complexity Index (PCI) identified a peak in complexity when integration and segregation were optimally balanced, aligning more closely with the theoretical notion of brain complexity. Importantly, we further show that spontaneous measures are vulnerable to spurious correlations, most critically the common driver problem, which can inflate integration between otherwise independent regions, while PCI remained comparatively robust. These findings underscore the importance of selecting appropriate metrics and of considering dynamical confounds when investigating brain dynamics and consciousness.

1. Introduction

A central question in neuroscience is how the extraordinarily rich repertoire of large-scale brain dynamics emerges from the underlying structural architecture (Sporns, 2022). These dynamics are characterized not by randomness or trivial regularity, but by a property referred to as complexity (Tononi et al., 1994, 1998; Edelman and Gally, 2001). In neuroscience, brain complexity denotes the coexistence of integration—the ability to coordinate activity across distributed regions—and segregation—the preservation of specialized, differentiated local processes (Bullmore and Sporns, 2009; Sporns, 2013; Cohen and D'Esposito, 2016). Indeed, a system that is too integrated collapses into redundant homogeneity, while one that is too

segregated fragments into disconnected modules; complexity emerges in between this dialectic tension, where global coordination and local specialization are balanced.

This integration–segregation balance has been formalized in information theory and network science and is considered a key signature of conscious brain function (Tononi and Edelman, 1998; Sarasso et al., 2021). Consistent with this view, both theoretical models and empirical studies suggest that brain complexity underlies the richness of conscious experience, while its disruption is linked to the loss of consciousness in physiological (e.g., sleep), pharmacological (e.g., anesthesia), and pathological (e.g., coma, vegetative state) conditions (Sitt et al., 2014; Sarasso et al., 2015; Schartner et al., 2015; Casarotto et al., 2016; Demertzi et al., 2019; Luppi et al., 2019; Hahn et al., 2021; Lord et al., 2023; Jang et al., 2024).

The emergence of complex dynamics is thought to reflect the anatomical arrangement of the underlying neuronal circuitry (Sporns et al., 2000, 2005; Honey et al., 2009; Betzel and Bassett, 2017; Fukushima and Sporns, 2020). A key principle of the brain architecture is the small-world organization (Watts and Strogatz, 1998; Bassett and Bullmore, 2017), characterized by high clustering supporting local specialization together with short path lengths enabling efficient global communication. This balance is further enriched by modularity (Bertolero et al., 2015; Sporns and Betzel, 2016), which provides functional specialization across subnetworks, and by hierarchical organization (Meunier et al., 2010; Hilgetag and Goulas, 2020; Pathak et al., 2024), which enables interactions across multiple scales of processing. Critically, this architectural framework incorporates highly connected hub regions that form a rich-club organization, facilitating global integration by serving as convergence points for distributed information processing (Zamora-López et al., 2010; Heuvel and Sporns, 2011, 2013; Senden et al., 2014; Griffa and Van den Heuvel, 2018). Conversely, connection constraints based on physical distance promote segregation through metabolic efficiency, preferentially favoring local connectivity patterns (Boucsein et al., 2011; Ercsey-Ravasz et al., 2013). Within densely connected clusters, recurrent connections and feedback loops create triangular motifs that sustain and amplify activity through local reverberations (Kaiser et al., 2007; Hilgetag and Hütt, 2014) enabling both criticality and increased responsiveness to external stimuli (Spiegler et al., 2016). This widespread prevalence of recurrence across scales provides the structural basis for re-entrant signaling (Tononi et al., 1992; Edelman and Gally, 2013), where bidirectional, recursive exchanges between distributed regions enable spatiotemporal synchronization.

Because of this organization, the brain seems structurally predisposed to balance segregation and integration, creating the conditions for complex dynamics. To quantify this balance empirically, a wide range of complexity measures has been developed, including entropy-based metrics, algorithmic compressibility, and graph-theoretic approaches. Some measures rely on an observational approach, analyzing fluctuations in ongoing neural signals to infer the repertoire of accessible dynamical states (Sarasso et al., 2021). Others take a perturbational approach, probing how activity causally propagates throughout the system after direct neural stimulation (Massimini et al., 2009; Shew et al., 2011). The Perturbational Complexity Index (PCI) (Casali et al., 2013) is a prominent example of the latter: by

estimating the algorithmic complexity of the spatiotemporal pattern of cortical activity extracted from the electroencephalographic (EEG) response to transcranial magnetic stimulation (TMS), PCI has proven to be a robust and theoretically grounded index of consciousness (Casarotto et al., 2016) capturing the interplay between integration and segregation in brain dynamics.

Yet, despite the widespread use of complexity estimates, important gaps remain. It has not been made explicit which aspects of network structure and dynamics different measures are actually sensitive to, or how they relate to each other. Perturbational indices directly capture integration as expressed in global propagation patterns, whereas entropy-based metrics derived from spontaneous activity may be strongly influenced by local variability, often presupposing integration rather than directly testing it. Moreover, measures based on spontaneous interactions are particularly vulnerable to spurious functional connectivity. The most critical example is the common driver problem, whereby a shared input (e.g., visual inputs, neuromodulatory fluctuations) induces artificial correlations between otherwise independent regions. This issue can inflate apparent integration and thus distort complexity estimates, raising the question of whether observed complexity reflects genuine network interactions or merely shared external drive.

Computational modeling offers a principled approach to address these challenges. By simulating neuronal populations within controlled network architectures, models allow the contributions of structure and dynamics to emergent complexity to be disentangled. Neural mass models are particularly suited for this purpose: they capture the nonlinear excitatory–inhibitory interactions that shape cortical dynamics, yet remain computationally tractable for large-scale simulations. When arranged into networks with systematically varied topology, these models make it possible to examine how architectural features such as small-world organization, efficiency, and modularity influence both spontaneous and evoked activity. Importantly, they also permit the introduction of controlled confounds, such as common drivers or noise, providing a rigorous framework to test the robustness and specificity of different complexity measures.

In this work, we leveraged large-scale network simulations of neural mass models to investigate how different measures of brain complexity relate to the underlying balance of integration and segregation. By systematically varying the network topologies—from ring to random to modular architectures—we examined how spontaneous and evoked dynamics reflect structural organization, and how commonly used complexity indices respond to these variations. We further assessed the robustness of these measures in the presence of controlled confounds such as common drivers, which can artificially inflate integration. Through this approach, we aimed to disentangle the specific structural and dynamical determinants that each measure captures, clarify their differences and complementarities, and provide a principled basis for interpreting complexity estimates as markers of brain function and consciousness.

2. Methods

2.1 Network definition and analysis

Our goal was to isolate the role of connectivity patterns in shaping the balance between integration and segregation, and consequently the complexity of network dynamics as quantified by multiple metrics. To this end, we used binary and undirected graphs with a fixed degree for all nodes. We simulated N=225 nodes with a fixed degree of connections k=24 neighbors per node. This approach ensures that any change in dynamics reflects topology rather than degree or strength. Delays were assigned randomly from an exponential distribution with mean $\lambda = 5$ ms to approximate realistic conduction delay values (Cabral et al., 2022), further ensuring that only changes in connectivity patterns contributed to observed effects and not delay structures.

Two distinct network families were generated (Fig. 1A). The first spanned the continuum from ordered ring lattices to increasingly disordered random graphs (from segregation to integration). The second started from the latter random graphs and introduced progressively stronger modular organization (from integration to segregation). Ten independent realizations were produced for each family.

Ring-to-random randomization. To explore the transition from ordered to disordered architectures, we implemented a rewiring procedure starting from regular ring lattices and progressively randomizing connections. Ten independent ring lattices were generated using the Watts–Strogatz model with N=225 nodes, and k=24 nearest neighbors, implemented in the NetworkX library (Hagberg et al., 2008). Each of the ten ring lattices was then iteratively rewired 20 times according to a degree-preserving randomization procedure based on the link-switching method (Zamora-López et al., 2016), implemented in the pyGAlib library (https://github.com/gorkazl/pyGAlib).

From the ten original ring lattices (rewiring step=0) the subsequent 20 rewiring steps were implemented by changing the rewiring parameter r, distributed in a logarithmic space between 10^{-3} and 3. At each step, the network obtained in the previous step was used as input, so that the applied increment Δr was cumulative across steps. The r parameter controls the number of iterations of the link switching procedure and a given r results in $r \times L$ rewired links, where L is the total number of links in the network. The result was a set of ten networks per step, resulting in 210 networks (10 initial rings × 21 steps each) ranging from ordered ring lattices to disordered random graphs.

Random-to-modular clusterization. From the ten fully randomized graphs obtained in the randomization procedure, we then constructed progressively more modular networks using a novel degree-preserving clusterization algorithm developed for this study, inspired by topological overlap–based approaches to community detection. At each iteration, a node *i* was selected at random, and its neighbors and non-neighbors were compared based on the number of common neighbors (CNs) they shared with *i*. To promote clustering, an existing edge was removed between node *i* and a neighbor *j* with fewer CNs, and a new edge was added between *i* and a non-neighbor *k* with more CNs. To preserve the degree of all nodes, this operation was paired with a compensatory swap: an edge between *k* and one of its neighbors *l* with fewer CNs was removed, and a new edge was created between *j* and *l*. Repeating this procedure progressively increased clustering and modular structure while leaving the connectivity degree distribution unchanged.

From the ten random graphs (rewiring step=0) the subsequent 20 rewiring steps were implemented by incrementing the number of iteration *I* of the clusterization algorithm, with *I* distributed logarithmically between 500 and 15,000. As in the randomization procedure, the algorithm was applied cumulatively: the network obtained at each step was used as input for the following step. The result was a set of ten networks per step, resulting in 210 total networks (10 initial random graphs × 21 steps each) ranging from the random starting point to architectures with progressively higher clustering and stronger modular organization.

Network metrics. To characterize the structural properties of the generated networks, we quantified integration, segregation, and their balance using standard graph-theoretic measures. Segregation was assessed with the average clustering coefficient (Watts and Strogatz, 1998), defined as the mean probability that the neighbors of a node are also connected to each other, thereby quantifying the density of local triangular motifs. This measure was computed using the *average_clustering* function of the NetworkX library. Integration was quantified using global efficiency (Latora and Marchiori, 2001), which captures how efficiently information can be exchanged across the entire network. For a given pair of nodes, efficiency is defined as the reciprocal of their shortest path length. Global efficiency is then obtained by averaging this quantity across all node pairs, thus reflecting the overall capacity of the network to support information transfer through short paths. We computed global efficiency using the implementation available in the NetworkX library (*global_efficiency*), which enumerates all-pairs shortest paths and averages their inverse distances.

To evaluate the balance between segregation and integration, we computed the small-world propensity (Muldoon et al., 2016), which jointly normalizes the observed clustering coefficient and characteristic path length (i.e., the average shortest path length between all pairs of nodes) relative to corresponding lattice and random null models. This index is bounded between 0 (no small-worldness) and 1 (maximal small-worldness) and quantifies the extent to which a network exhibits small-world structure.

2.2 Local node dynamics

Wilson-Cowan neural mass model. The network dynamics were modeled using a system of coupled Wilson–Cowan (WC) equations for excitatory (E) and inhibitory (I) populations at each node, adapted from the *neurolib* (Cakan et al., 2021) implementation. For a given node, the population activities *E(t)* and *I(t)* evolve according to

$$\tau_E \frac{dE(t)}{dt} = -E(t) + \big(1 - E(t)\big)\, S_E\Big(c_{EE}E(t) - c_{IE}I(t) + G\sum_l w_l E(t - d_l) + P_E(t)\Big), \quad (1)$$

$$\tau_I \frac{dI(t)}{dt} = -I(t) + \big(1 - I(t)\big)\, S_I\Big(c_{EI}E(t) - c_{II}I(t) + P_I(t)\Big), \quad (2)$$

where τ_E and τ_I are the excitatory and inhibitory time constants, c_{XY} the synaptic coupling strengths from population X to Y, and G is the global coupling scaling factor for inter-node connectivity. The connectivity weights from other nodes are denoted by w_l with corresponding transmission delays d_l.
The function $S_{E/I}(\cdot)$ is a sigmoidal activation function mapping inputs to firing rates:

$$S_{E/I}(t) = \frac{1}{1 + \exp\big(-a_{E/I}(input - \mu_{E/I})\big)}, \quad (3)$$

where $a_{E/I}$ controls the slope and $\mu_{E/I}$ defines the input at which the function reaches its midpoint. The excitatory drive $P_E(t)$ was defined as:

$$P_E(t) = P_0 + \eta(t) + P_{\mathrm{stim}}(t), \quad (4)$$

where P_0 is a stationary external input, $\eta(t)$ is a stochastic drive, and $P_{stim}(t)$ is a transient input in the stimulation trials. The latter was implemented as a square pulse of amplitude 1 a.u. and duration 5 ms. The inhibitory population received only the stationary input, i.e.

$$P_I(t) = P_0. \quad (5)$$

The stochastic drive $\eta(t)$ was generated as an independent Ornstein–Uhlenbeck (OU) process for each node, according to:

$$d\eta(t) = -\frac{1}{\tau}\big(\eta(t) - \mu\big)\, dt + \sigma\, dW_t \quad (7)$$

where μ is the mean, τ the correlation timescale, σ the noise amplitude, and $dW(t)$ a Wiener increment. This corresponds to the case s=0 in the mixture formulation below, where all nodes receive uncorrelated fluctuations.

Common-driver input. To investigate the role of independent versus shared fluctuations (e.g, common drivers) across neural populations, we extended the model by introducing a common OU process shared across all nodes. The effective stochastic input was defined as a normalized mixture of an *independent* OU process $\eta_I(t)$ (specific to each node) and a *common* OU process $\eta_C(t)$ (shared across all nodes):

$$\eta(t) = \frac{s\,\eta_C(t) + (1-s)\,\eta_I(t)}{\sqrt{s^2 + (1-s)^2}}, \tag{8}$$

where the mixing parameter $s \in [0,1]$ controls the relative contribution of the common driver. For s=0, each node receives only independent fluctuations, while for s=1, all nodes receive the same common input. The denominator acts as a normalization factor, ensuring that the variance of $\eta(t)$ remains constant across values of s, thereby enabling direct comparisons between conditions.

Model parameters. We primarily used the default parameters of the WC model implemented in *neurolib* (see Supplementary Table S1). To study the bifurcation behavior of the whole network (Fig. 1C), we varied the global coupling parameter (G). We then set G=0.1 to all simulations, which corresponds to a subcritical near-bifurcation regime.

2.3 Network simulations

All simulations were performed using the *neurolib* Python library (Cakan et al., 2021) with the Euler–Maruyama integration scheme and a time step of dt=0.1 ms. The output was downsampled to 1 ms using the SciPy (Virtanen et al., 2020) *decimate* function, which downsamples the signal after applying an anti-aliasing filter (an order-8 Chebyshev type I filter). All simulations were initialized with random initial conditions.

Spontaneous activity. Spontaneous activity was simulated for 63,000 ms, with the first 3,000 ms discarded as transient. This resulted in 60,000 ms of spontaneous activity per network.

Evoked activity. Evoked responses were simulated in 100 independent trials, each consisting of a stimulation pulse delivered to a single randomly chosen node. The stimulation consisted of a square pulse with amplitude 1 a.u. and duration of 5 ms. At each trial, the simulation was reinitialized with random initial conditions, and after discarding the first 3,000 ms of transient activity, the pulse was applied within a random time window between 300 and 800 ms. For analysis, the stimulus onset was centered at time 0 ms, with the pre-stimulus window defined from –300 ms to –1 ms and the post-stimulus window from 1ms to 800 ms.

2.4 Spontaneous metrics

Spontaneous metrics were computed from the full spontaneous signals obtained as described in Methods 2.3.

Average excitatory activity. The average excitatory activity $\langle mean\ r_E \rangle$ was computed to characterize the working point of each network. This metric was obtained by averaging the excitatory population activity (r_E) over time ($mean\ r_E$) and then across nodes ($\langle mean\ r_E \rangle$). Since the nodes were designed to operate in a subcritical regime, each node possesses a stable fixed point perturbed by an OU process with zero mean. As a result, the long-term time

average (*mean* r_E) converges to the value of this fixed point in each node. Thus, ⟨*mean* r_E⟩ provides a direct measure of the system's distance to the critical point.

Functional connectivity. Functional connectivity (FC) was estimated to capture the strength of spontaneous nodal interactions. To account for delays, we used the cross-correlation function (CCF) across time lags up to 65 ms. FC was defined as the peak CCF value for each pair of nodes, expressed as a correlation coefficient (r). From the resulting distribution of FC values, we extracted the median and the 5th and 95th percentiles.

Lempel-Ziv complexity. Lempel–Ziv complexity (LZc) was used to quantify the diversity of spatiotemporal patterns and implemented following Schartner et al., 2015. After applying the Hilbert transform, the amplitude signal was binarized using the mean amplitude as threshold. This yielded a binary spatiotemporal activity matrix, to which the LZ76 algorithm (citation to LZ) was applied on the spatially concatenated binary sequence. Normalization was performed by dividing the raw value by the LZc of the same data temporally shuffled.

Amplitude coalition entropy. Similarly to LZc, Amplitude coalition entropy (ACE) was computed as in Schartner et al., 2015 to capture the richness of spatiotemporal patterns. ACE is defined as the entropy, over time, of the set (coalition) of active nodes based on the same binarization procedure used for LZc. As for LZc, ACE values were normalized against shuffled data.

Neural complexity. Neural complexity (NC) (Tononi et al., 1998) was computed by estimating the mutual information (MI) between complementary partitions of the network of increasing size, thereby capturing the degree of shared information between network subsets across scales. For each partition size n (ranging from n=1 to $\lfloor N/2 \rfloor$, where N is the total number of nodes), a subset of n nodes was randomly selected, and their mean activity were compared with the mean activity of the complementary set. The MI between the two signals was then computed. This procedure was repeated 50 times to obtain a representative sample of possible bipartitions. The MI values were averaged across repetitions, and NC was defined as the sum of these averaged MI values across all partition sizes. Mutual information was computed using the *neurokit2* (Makowski et al., 2021) *mutual_information* function, with the number of bins estimated following (Hacine-Gharbi and Ravier, 2018).

Functional complexity. Functional complexity (Fcomp) was computed as described in (Zamora-López et al., 2016). Fcomp quantifies the balance between functional integration and segregation by measuring the richness of interactions in the FC matrix (derived as described above). Low functional complexity corresponds to narrow FC distributions, reflecting either statistical independence (⟨FC⟩ ≈ 0; segregation) or global synchrony (⟨FC⟩ ≈ 1; integration). Higher values arise when intermediate states yield broad FC distributions. Fcomp was quantified as the sum of absolute differences between the FC distribution and a uniform distribution across m bins.

2.5 Evoked metrics

Evoked metrics were computed from the stimulation trials described in Methods 2.3.

Significant activations. Significantly active nodes were identified by applying a non-parametric bootstrap-based maximal statistic procedure (Nichols and Holmes, 2001) to the excitatory activity (r_E) of each node. First, evoked responses were baseline-corrected by subtracting the mean and dividing by the standard deviation of the pre-stimulus period. Next, pre-stimulus activities were bootstrapped across trials and samples. At each node and time point, the mean of the bootstrapped values (Jboot) was computed. Then, for each pre-stimulus time point, the maximum absolute Jboot across nodes was obtained. This procedure (steps 2–4) was repeated 500 times to build a null distribution. The $(1 - \alpha)$ percentile of this distribution, with $\alpha = 0.01$, defined the significance threshold. Finally, a binary spatiotemporal matrix of significant activations was obtained, marking samples exceeding the threshold as significant (Casali et al., 2013).

Active nodes. From the binary spatiotemporal activation matrix, we computed the time course of the percentage of active nodes by summing across nodes and dividing by the total node count. From this time course, we extracted (i) the maximum early activation (max_{EA}), defined as the maximum percentage of active nodes in the [0-20] ms window; (ii) the mean late activation ($mean_{LA}$), defined as the average percentage of active nodes in the [450-800] ms window; and (iii) the ratio $mean_{LA} / max_{EA}$.

Perturbational complexity index. The Perturbational Complexity Index (PCI) was computed as the Lempel–Ziv complexity of the binary spatiotemporal activation matrix, normalized by source entropy, as described in (Casali et al., 2013).

3. Results

3.1 Constructing network families along the segregation–integration continuum

We generated two families of networks using complementary rewiring procedures: a ring-to-random family constructed via randomization and a random-to-modular family constructed via a novel clusterization algorithm. Both processes traversed the continuum between segregation and integration, passing through an intermediate small-world regime where network clustering and efficiency coexisted (see Methods 2.1).

For the ring-to-random transition, we started from a regular ring lattice (C1; Fig. 1A), characterized by a high clustering coefficient (Fig. 1B). Random rewiring progressively disrupted this structure, progressively leading to fully disordered random networks (R), characterized by low clustering coefficient and higher global efficiency (Fig. 1B). Intermediate stages of this process produced small-world architectures (B1), resulting in a balance between clustering and efficiency (Fig. 1B).

For the random-to-modular transition, we began from the random network (R) previously obtained (Fig. 1A) and applied our developed clusterization algorithm, which progressively imposed a modular structure, producing networks with strong clustering (C2; Fig. 1B). Intermediate stages again generated small-world modular configurations (B2) with balanced structural properties.

To simulate neuronal network dynamics, each node was modeled according to the Wilson–Cowan (WC) equations, simulating the interaction between excitatory and inhibitory populations (Fig. 1A). All the nodes were tuned to operate in the same dynamical regime, near a bifurcation point shown to best approximate empirical brain activity. A bifurcation analysis of the deterministic WC model (without noise) was performed by varying the global coupling strength, G. Since all nodes had identical connectivity degree, changes in G uniformly scaled the input to each node, shifting their collective state equally. As shown in Fig. 1C, the fixed point lost stability at $G = 0.1$, where a stable limit cycle emerged via a supercritical Hopf bifurcation. For all subsequent simulations, we set $G = 0.1$, corresponding to this critical point. At this value, the introduction of an Ornstein–Uhlenbeck (OU) noise process elicits noise-driven damped gamma oscillations (see Methods 2.2).

To ensure all simulated network configurations operated at a similar dynamical working point near the critical bifurcation, we simulated the models in the presence of the OU noise process and measured the mean excitatory activity, $\langle \text{mean } r_E \rangle$ (see Methods 2.4). The $\langle \text{mean } r_E \rangle$ did not significantly differ across the rewiring spectrum (repeated-measures ANOVA; randomization: $p = 0.66$, clusterization: $p = 0.61$; Fig. 1D), confirming a comparable distance from the critical point for all networks. This result ensures that any differences in the emergent dynamics can be attributed to differences in the underlying network topology rather than to variations in the local dynamical regime.

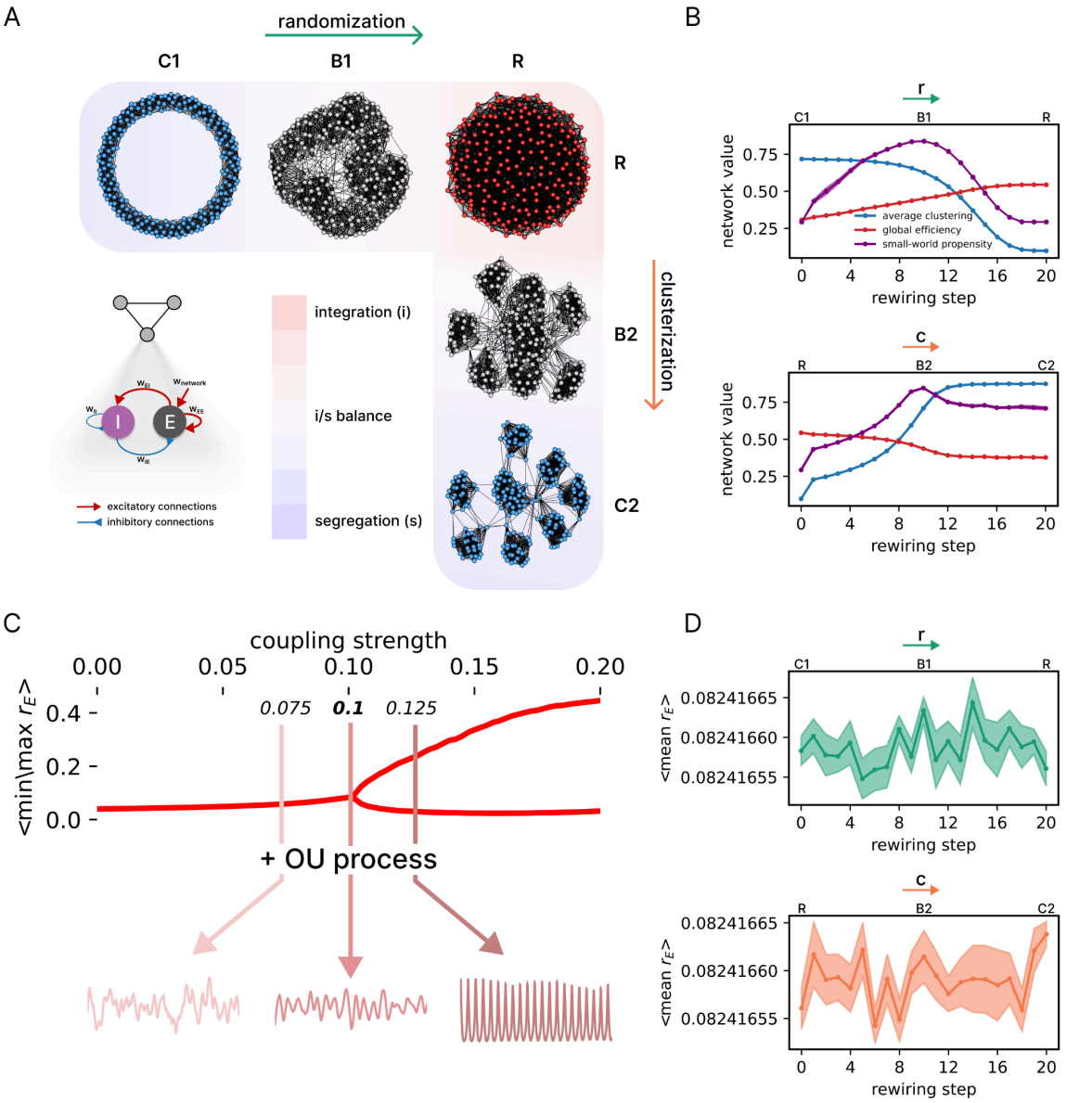

Figure 1. Network topologies and dynamics. (A) Starting from a regular ring lattice (C1, top left), connections were progressively randomized, yielding small-world topologies (B1) and eventually a random network (R, top right). From the random network, a degree-preserving clusterization procedure was applied, progressively increasing network clusterization, yielding balanced modular networks (B2) and finally a strongly segregated network (C2, bottom right). The continuum defined by these two families spans regimes of predominant integration (i), segregation (s), or balanced segregation–integration (i/s balance). Each network node was modeled as Wilson–Cowan (WC) of interactiong excitatory (E) and inhibitory (I) population (inset). **(B)** Network measures across rewiring steps (see Methods 2.1). Randomization (r; top panel) decreased average clustering (blue line) and increased global efficiency (red line), with a peak in small-world propensity (purple line), which occurred at intermediate steps (B1). Clusterization (c; bottom panel) showed the complementary trend, increasing clustering and reducing efficiency, again passing through a balanced regime (B2). **(C)** Bifurcation analysis of the deterministic Wilson–Cowan network. For an exemplary randomized topology (C1), the global coupling G was systematically varied, and for each valu,e the minimum and maximum excitatory activity r_E(t)were computed and then averaged across nodes, yielding ⟨min r_E⟩ ⟨max r_E⟩. The fixed point lost stability at G≈0.1, beyond which a limit cycle emerged via a

supercritical Hopf bifurcation. Throughout the study, we set G=0.1, i.e., at the critical point. When an Ornstein–Uhlenbeck (OU) process is added to the inputs (Methods 2.2), this working point gives rise to noise-driven, damped gamma-frequency oscillations (example traces, bottom). **(D)** Average excitatory activity across the network (⟨mean r_E⟩; see Methods 2.4) for the two families of networks, showing that the overall activity remains stable across rewiring steps, indicating a common working distance from criticality across networks. Panels denoted by a green arrow and 'r' correspond to the randomization process, while those denoted by an orange arrow and 'c' correspond to the clusterization process.

3.2 Spontaneous dynamics reflect structural topological constraints

We next characterized the emergent spontaneous dynamics by analyzing functional connectivity (FC), defined as the matrix of pairwise correlations between nodes' time series (Fig. 2A; see Methods 2.4). The FC matrices for representative networks (C1, B1, R, B2, C2) are shown in Fig. 2A. Segregated networks (C1, C2) exhibited FC patterns that directly reflected their underlying structural connectivity: a ring lattice (C1) showed strong correlations between nearest neighbors (along the matrix diagonal), while a modular network (C2) showed strong within-module correlations. Notably, the balanced networks (B1, B2) preserved these structural segregation signatures. In stark contrast, the random network (R) displayed a diffuse, diluted FC matrix without spatial structure.

These observations were further quantified using the distributions of FC values (Fig. 2B). Clustered and balanced networks exhibited a long-tailed distribution, reflecting a subset of strongly correlated pairs. This tail was absent in the random network, consistent with the loss of local clustered structure (Fig. 2B, e.g., compare C1 and R). To track this trend across all networks, we analyzed the evolution of the 5th percentile, median, and 95th percentile of the FC distributions (Fig. 2C). Across the randomization process, the 95th percentile of FC values decreased progressively, while the median and 5th percentile increased (Fig. 2C). This indicates that randomization promoted more spatially diffuse interactions, narrowing the distribution around a higher median. In contrast, the clusterization process produced the opposite effect, strengthening within-cluster correlations while weakening between-cluster correlations, thereby yielding a broader distribution.

We related these FC features to global topological metrics (Fig. 2D–E). The median FC was strongly correlated with global efficiency, while the 95th percentile FC was strongly correlated with the average clustering coefficient. These relationships held for both the randomization (Fig. 2D) and clusterization processes (Fig. 2E), confirming that recurrent connections within clusters reinforce pairwise interactions, while random architectures promote widespread but diluted coupling across the network.

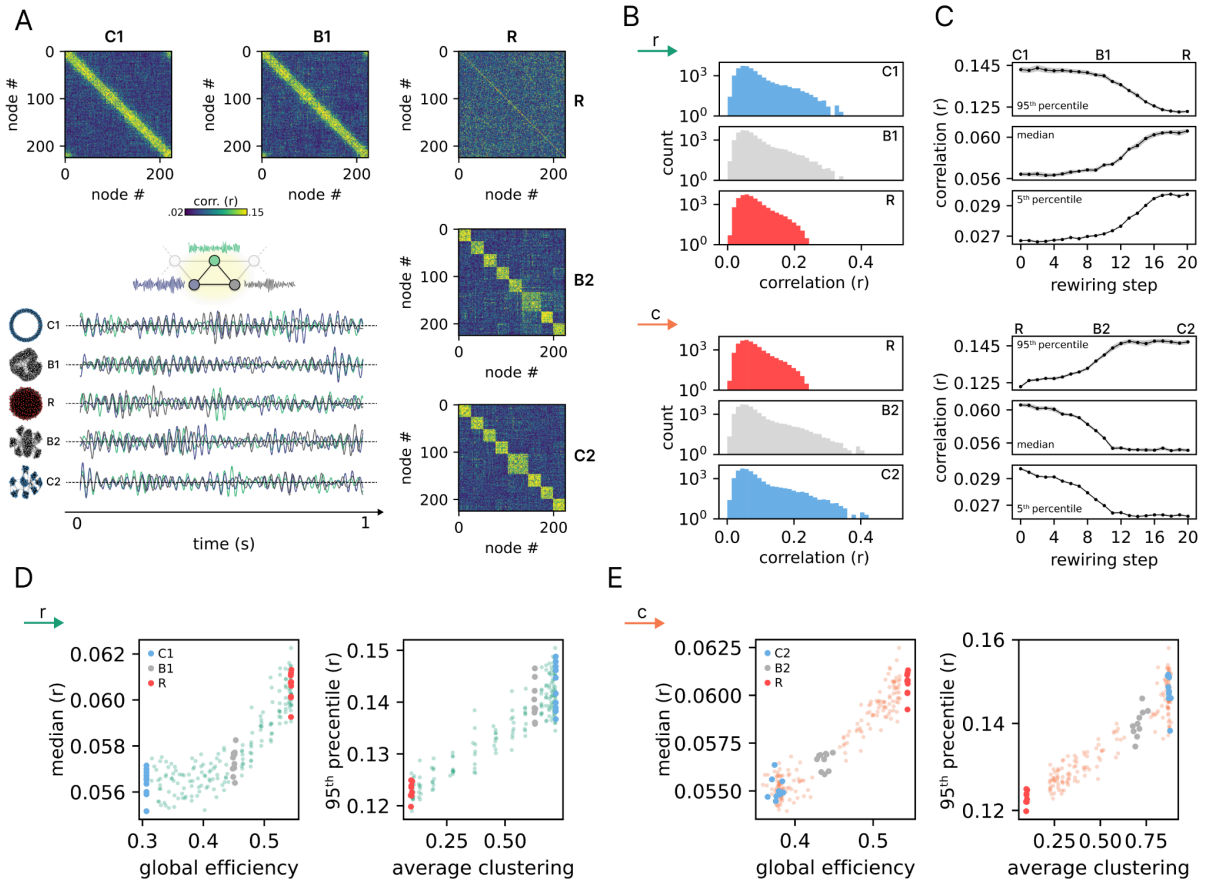

Figure 2. Spontaneous functional connectivity signatures across network families. (A) Functional connectivity (FC) matrices were obtained from spontaneous activity in representative networks (C1, B1, R, B2, C2) along the two rewiring processes. FC was computed using the cross-correlation function, retaining the maximum value across lags for each node pair. The underlying structural motifs are reflected in the spatial organization of strong correlations. For networks B2 and C2, node indices were resorted to group nodes within the same module for visual clarity; modules were identified using the Louvain community detection algorithm on the structural graph. Example traces (bottom) illustrate spontaneous fluctuations in excitatory activity (r_E). **(B)** Distribution of correlation values (r) in the FC matrices for the networks shown in (A). Clustered (C1, C2) and balanced (B1, B2) networks exhibit a long right tail of high correlation values, whereas this feature is absent in the random network. **(C)** Evolution of FC statistics across rewiring steps. For each step, the distribution of correlations was summarized by the 5th, 50th (median), and 95th percentiles. Randomization (top) shifted the FC distribution toward higher median and 5th percentile values, while reducing the 95th percentile, whereas clusterization (bottom) increased the 95th percentile consistently with the emergence of a pronounced right tail. Shaded areas denote SEM across network realizations (10 per step). **(D, E)** Relation of FC statistics to structural measures. The FC median was positively associated with global efficiency, while the upper tail (95th percentile) increased with clustering in both the randomization (D; median vs. global efficiency: $\rho=0.86$, $p=2\times10^{-63}$; 95th percentile vs. average clustering: $\rho=0.86$, $p=2\times10^{-61}$) and the clusterization family (E; median vs. global efficiency: $\rho=0.87$, $p=6\times10^{-65}$; 95th percentile vs. average clustering: $\rho=0.87$, $p=5\times10^{-66}$). Each point corresponds to a network realization (10 per step); colors indicate the realizations corresponding to the representative networks (C1, B1, R, C2, B2).

3.3 Evoked dynamics reveal complementary roles of segregation and integration

We next characterize the network dynamics in response to external stimulation. Following brief stimulation of a single network node, and depending on the network topology, different spatiotemporal dynamics were observed (Fig. 3A; see Methods 2.3 and 2.5). In segregated architectures (C1, C2), evoked responses were sustained and spatially confined, reflecting low network integration capacity (Fig. 3A-B). In the random network (R), stimulation elicited an explosive but less sustained network-wide response, consistent with the absence of recurrent amplification. In turn, in balanced architectures (B1, B2), stimulation revealed both a persistent and network-wide response. For this network topology, activity propagated broadly while remaining sustained, supported by residual clustered motifs.

These differences are summarized in Fig. 3B, where we quantified the percentage of significantly active nodes (Methods 2.5). Balanced networks resembled both random architectures in terms of maximal spatial recruitment and clustered networks in terms of temporal reverberation. To quantify this trade-off, we extracted three measures: maximum early activation (max_{EA}), indexing the extent of initial propagation; mean late activation ($mean_{LA}$), indexing sustained activity; and the ratio $mean_{LA}/max_{EA}$, indexing the proportion of sustained activity relative to initial activation. As shown in Fig. 3C, max_{EA} decreased progressively from random to clustered networks, while the meanLA peaked for balanced configurations, reflecting the coexistence of integration and segregation in balanced configurations. The ratio $mean_{LA}/max_{EA}$ increased through the rewiring process, illustrating how the relation between late and early activity evolved.
As with spontaneous dynamics, these evoked metrics were strongly correlated to the underlying network structure (Fig. 3D-E). max_{EA} correlated strongly with global efficiency, while the ratio $mean_{LA}/max_{EA}$ correlated with average clustering. These relationships held across both network families, confirming that clustered motifs support amplification and temporal reverberation of activity, whereas random architectures support rapid, widespread propagation.

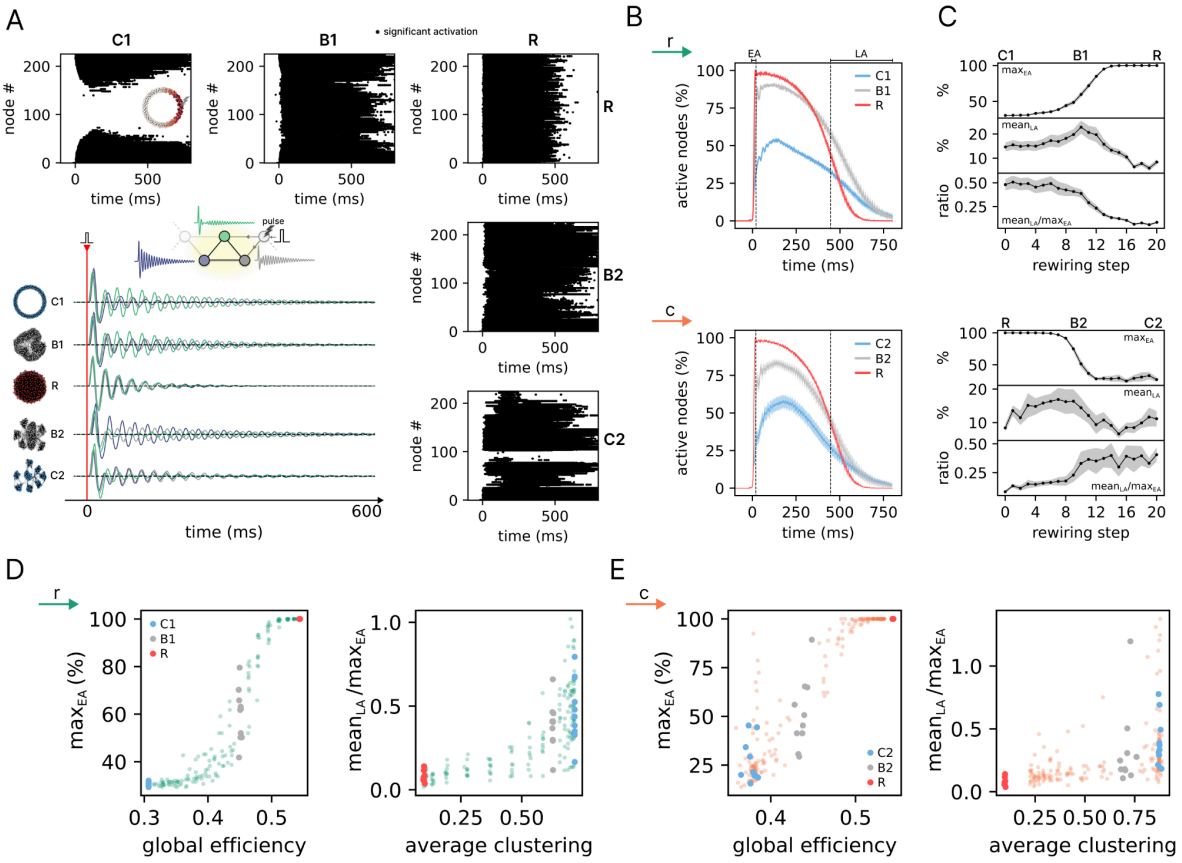

Figure 3. Propagation and reverberation of evoked responses across network families. (A) Spatiotemporal matrix of significant node activations (see Methods 2.5) in representative networks following a brief excitatory pulse applied to a single node (schematized in inset).. Networks along the randomization (C1, B1, R) and clusterization (R, B2, C2) processes displayed distinct propagation patterns. In C1 (inset), activity dissipates before all nodes are engaged. Color scale indicates the number of significant activations, with darker red denoting higher counts and white indicating no activation. The superimposed traces (bottom left) illustrate the evoked responses of three exemplary nodes obtained by averaging the excitatory population activity (r_E) across trials. The average r_E of the three nodes with the largest early response (assessed by the area under the envelope of the average r_E in the first 20 ms) is shown. **(B)** Time courses of the percentage of active nodes (mean ± SEM across network realization) highlight differences in response amplitude and duration. EA and LA denote the windows used to define early activations (0–20 ms after stimulation) and late activations (450–800 ms), respectively. **(C)** Evolution of evoked response metrics across rewiring steps. For each family, the maximum early activation (max_{EA}), the mean late activation ($mean_{LA}$), and their ratio ($mean_{LA}/max_{EA}$) were quantified. **(D, E)** Relation of evoked response metrics to structural measures. The $\max_{EA}$ was positively associated with global efficiency, while the ratio $mean_{LA}/max_{EA}$ increased with clustering in both the randomization (D; $\max_{EA}$ vs. global efficiency: $\rho=0.97$, $p=6\times10^{-126}$; $mean_{LA}/max_{EA}$ vs. average clustering: $\rho=0.8$, $p=2\times10^{-47}$) and the clusterization family (E; $\max_{EA}$ vs. global efficiency: $\rho=0.91$, $p=5\times10^{-80}$; $mean_{LA}/max_{EA}$ vs. average clustering: $\rho=0.67$, $p=2\times10^{-28}$). Each point corresponds to a network realization (10 per step); colors indicate the realizations corresponding to the representative networks (C1, B1, R, C2, B2). Shaded areas (in B and C) denote SEM across network realizations (10 per step).

3.4 Complexity metrics reveal different sensitivities to network segregation and integration

We next quantified the complexity of both spontaneous and evoked activity using observational and perturbational metrics, respectively (see Methods 2.4 and 2.5). For spontaneous activity, we assessed signal diversity through Lempel–Ziv complexity (LZc), amplitude coalition entropy (ACE), and synchrony coalition entropy (SCE); non-linear interactions across network partitions through neural complexity (NC); and the richness of the functional connectivity distribution through functional complexity (Fcomp). For evoked activity, we computed the perturbational complexity index (PCI), which captures the spatiotemporal richness of deterministic responses following stimulation. The evolution of these measures across rewiring steps is shown in Fig. 4.

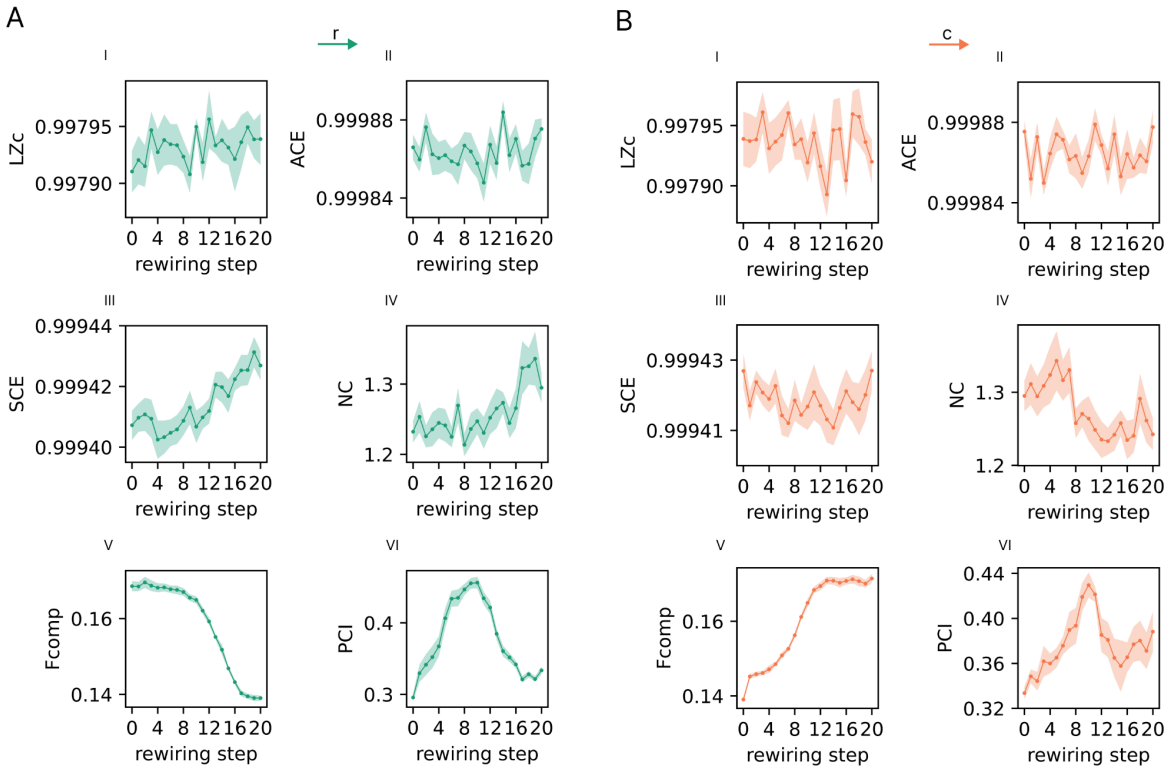

Figure 4. Evolution of complexity metrics across network rewiring. (A) Randomization process. **(B)** Clusterization process. For spontaneous activity, we quantified Lempel–Ziv complexity (LZc, I), amplitude coalition entropy (ACE, II), synchrony coalition entropy (SCE, III), neural complexity (NC, IV), and functional complexity (Fcomp, V). For evoked activity, we computed the perturbational complexity index (PCI, VI). Each panel shows the average metric value across rewiring steps, with shaded areas indicating SEM across network realizations (10 per step).

Overall, observational metrics exhibited biases toward either integration or segregation, or remained largely insensitive to network changes. Conversely, the perturbational metric PCI exhibited a pronounced peak at intermediate rewiring steps, where integration and segregation were balanced. Specifically, LZc and ACE—both derived from a binarization scheme based on signal amplitude—were insensitive to network rewiring in either process (Fig. 4A–B I–II). This likely reflects the fact that, by construction, all networks operated at a comparable distance from the critical point (Fig. 1D), resulting in similar levels of signal diversity. SCE increased along the randomization process but reached a plateau from R to C2 in the clusterization process (Fig. 4A–B III). NC and Fcomp exhibited opposing trends: NC increased with randomization, consistent with its known bias toward integration (Zamora-López et al., 2016), whereas Fcomp grew with stronger clustering, reflecting the broadening of the functional connectivity distribution (Fig. 4A–B IV–V). Despite that, both NC and Fcomp were unable to discriminate between balanced and clustered architectures, which shared similarly heavy-tailed FC distributions (Fig. 2B–C). In contrast, PCI followed an inverted U-shape across both randomization and clusterization processes, peaking around B1 and B2 in both families. These results suggest that PCI is sensitive to the interplay between segregation and integration, effectively capturing the network's balanced state.

Finally, we assessed the interrelationships among structural, dynamical, and complexity measures by computing their Spearman correlations across all networks (Fig. 5A for randomization, Fig. 5B for clusterization). This analysis confirmed a strong association between Fcomp and the clustering coefficient, as well as a tight coupling with the 95th percentile of the FC distribution (FC_{95})—both metrics reflecting the heterogeneity of functional interactions. They also revealed a robust correlation between PCI and the small-world propensity (swp) of the underlying graphs, underscoring the sensitivity of PCI to architectures that optimize the coexistence of integration and segregation.

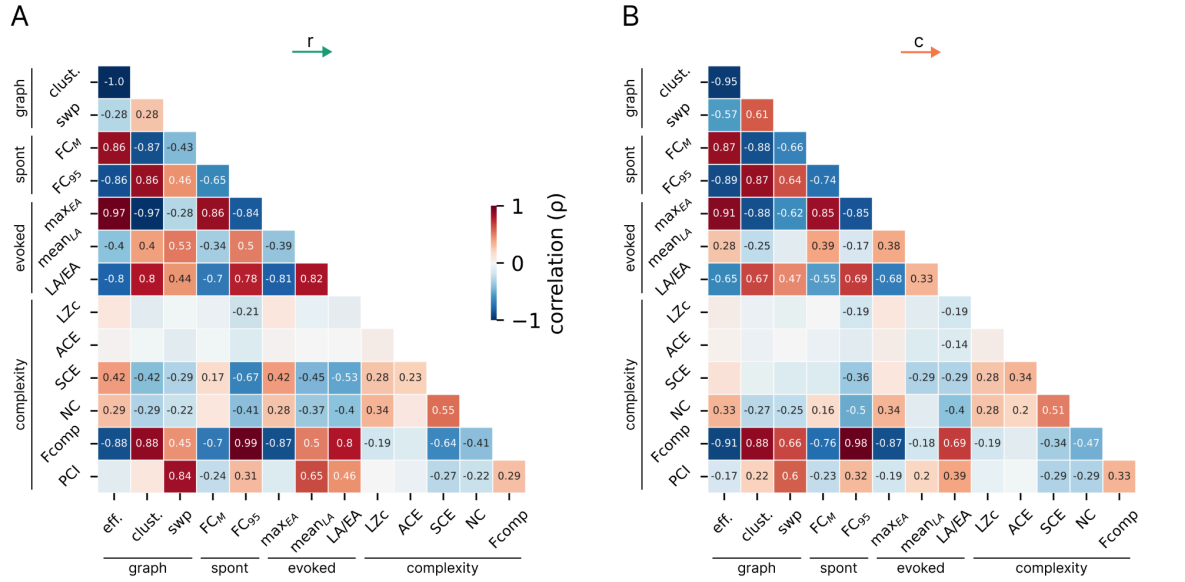

Figure 5. Correlation structure among graph, dynamical, and complexity measures. Pairwise Spearman correlations (ρ) across rewiring steps are shown for **(A)** randomization and **(B)** clusterization processes. Graph-theoretical measures (graph) include global efficiency (eff.), average clustering coefficient (clust.), and small-world propensity (swp). Dynamical measures of spontaneous activity include the median of the FC distribution (FC_M) and its 95th percentile (FC_{95}). Dynamical measures of evoked activity include the maximum early activation (max_{EA}), the mean late activation ($mean_{LA}$), and their ratio (LA/EA). Complexity measures comprise observational metrics (LZc, ACE, SCE, NC, Fcomp) and the perturbational measure PCI. Color indicates correlation strength and direction, with red denoting positive and blue denoting negative values. Only significant correlation ($p<0.05$) values are displayed.

3.5 Perturbational complexity is maximized by the balance of segregation and integration

Given the reversed U-shaped profile of PCI across rewiring steps (Fig. 4), we further examined its sensitivity to the segregation–integration balance. We first assessed PCI as a function of core graph-theoretical properties, namely the average clustering coefficient (Fig. 6A), global efficiency (Fig. 6B), and small-world propensity (Fig. 6C), for both randomization and clusterization processes. PCI consistently decreased at the extremes of high clustering or high efficiency, indicating that only balanced architectures, in which segregation and integration coexist, sustain complex evoked dynamics. Supporting this interpretation, PCI showed a significant positive correlation with small-world propensity.

In the clusterization process, however, we observed a subset of highly clustered networks in which PCI values were markedly dispersed (Fig. 6C, bottom). These networks corresponded to the plateau region of the clustering coefficient (Fig. 1B, bottom), where further clusterization steps no longer increased clustering. To isolate this subgroup, we applied a threshold on clustering values (supplementary Fig. S2). Within this subgroup, PCI remained significantly correlated with small-world propensity (Fig. 6D). Moreover, PCI was also

significantly related to global efficiency (Fig. 6E), suggesting that residual differences in integration continued to shape the complexity of evoked responses.

We next tested whether specific structural features of the stimulated nodes contributed to PCI variability. To this end, we computed the neighborhood efficiency of the stimulated node, defined as the average nodal efficiency of its first-order neighbors. PCI showed an even stronger correlation with this measure (Fig. 6F), highlighting the role of hub-like clusters in supporting rich spatiotemporal response patterns.

Finally, we asked whether PCI merely reflected the duration of the evoked activity, as captured by the mean late activation ($mean_{LA}$). As previously described, both measures exhibited a reversed U-shape across rewiring steps (compare Fig. 3C and Fig. 4A–B VI), and PCI correlated significantly with $mean_{LA}$ (Fig. 5A–B). However, the association was moderate, particularly in the clusterization family. To further disentangle their relationship, we examined the temporal evolution of PCI in representative networks. While a late increase in PCI after ~500 ms distinguished randomized networks from clustered and balanced ones—consistent with differences in sustained activity—we also observed an early rise in PCI that separated randomized from clustered and balanced networks (Fig. 6G). This indicates that PCI captures not only the persistence but also the complexity of the spatiotemporal patterns emerging immediately after stimulation.

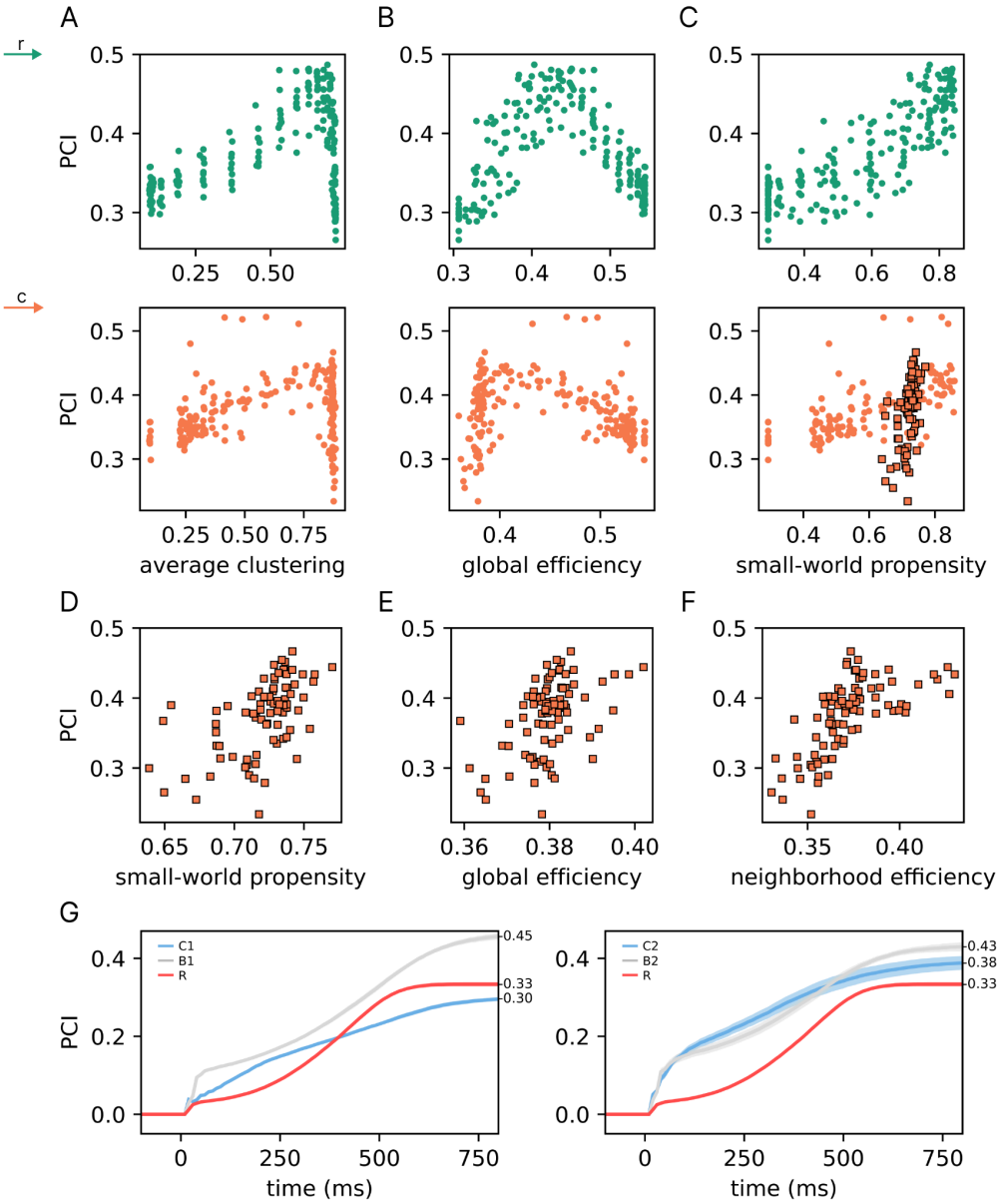

Figure 6. Relation between perturbational complexity and network structural features. (A–C) Scatter plots of PCI as a function of (A) average clustering, (B) global efficiency, and (C) small-world propensity, shown separately for the randomization (top, green) and clusterization (bottom, orange) processes. Orange square markers in panel C indicate the subgroup of highly clustered networks, identified by thresholding clustering values (see Supplementary Fig. S2). Spearman correlations between PCI and small-world propensity were significant in both rewiring processes (randomization: $\rho=0.84$, $p=2\times10^{-57}$; clusterization: $\rho=0.60$, $p=3\times10^{-22}$, and $\rho=0.73$, $p=8\times10^{-22}$ when excluding the highly clustered networks). **(D–F)** Within the highly clustered subgroup, PCI is shown as a function of (D) small-world propensity ($\rho=0.60$, $p=2\times10^{-9}$), (E) global efficiency ($\rho=0.48$, $p=4\times10^{-6}$), and (F) neighborhood efficiency of the stimulated node ($\rho=0.72$, $p=9\times10^{-15}$), defined as the average nodal efficiency of its first-order neighbors. **(G)** Temporal evolution of PCI following stimulation in representative networks (C1, B1, R for randomization; C2, B2, R for clusterization). Curves represent the mean across realizations, with shaded areas denoting SEM. Final PCI values at 800 ms are indicated next to the corresponding traces.

3.6 Divergent sensitivities of complexity metrics to common driver confounds

Having established that complexity metrics display distinct sensitivities to gradients of network integration and segregation (Fig. 4), we next examined their robustness to a major confound in empirical data: the presence of external common drivers.

Shared inputs, such as neuromodulatory fluctuations or sensory stimulation, can induce widespread synchronization across structurally independent nodes. Such effects may artificially inflate functional integration and obscure inferences about the underlying network architecture. To address this, we systematically injected into all nodes an external common driver signal of increasing strength, while maintaining the total variance of the input signals constant (Fig. 7A; see Methods 2.2). Representative network classes were tested (C1, B1, R, B2, C2), allowing us to evaluate the impact of the driver on both spontaneous and evoked complexity.

To quantify the effect of the common driver on ongoing interactions, we examined the median value of the FC matrices as a function of driver strength s (Fig. 7B). As expected, the median monotonically increased with s, confirming the emergence of spurious pairwise correlations.

We then assessed the deviation of each complexity metric from its baseline value ($s = 0$). Spontaneous activity metrics proved highly vulnerable, although with heterogeneous directions of sensitivity. Measures of signal diversity, including LZc, ACE, and SCE, progressively decreased as spurious connectivity increased (Fig. 7C–D I–III). In contrast, NC systematically increased with s (Fig. 7C–D IV), reflecting its bias toward integration and confirming its susceptibility to artifactual coupling. Fcomp exhibited a non-monotonic profile, peaking at intermediate values of s, where independent and shared fluctuations were balanced (Fig. 7C–D V), consistent with its dependence on the integration–segregation balance but also highlighting its sensitivity to the common driver problem.

By contrast, PCI exhibited markedly greater robustness. As a causal measure, PCI preserved its ability to discriminate between network classes despite increasing common-driver strength (Fig. 7C–D VI). Moreover, for different values of s PCI was still able to discriminate among different network structures (C1, B1, and R), thereby ensuring consistent separation between network classes.

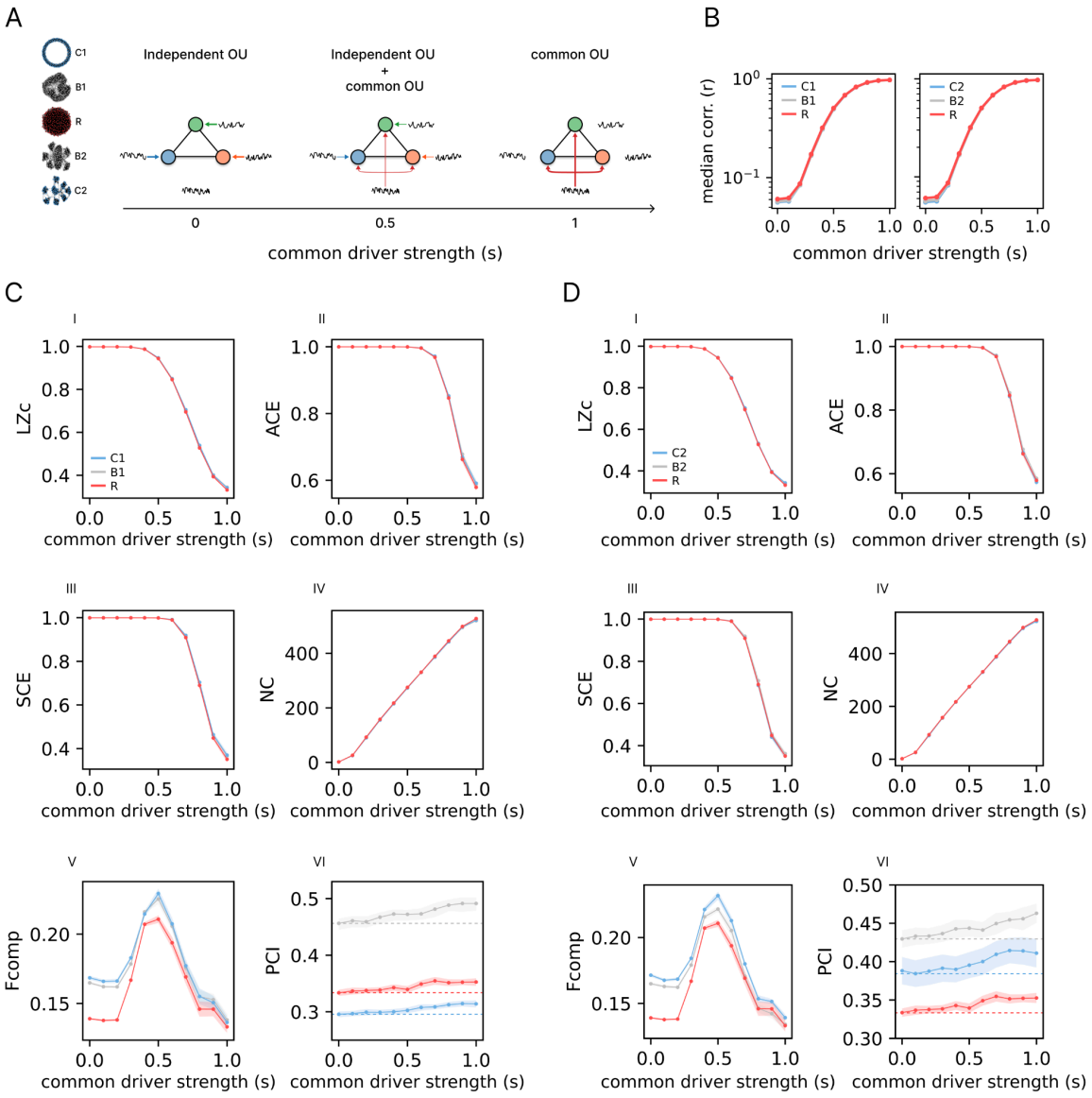

Figure 7. Effect of a common driver on complexity measures. (A) Schematic of the protocol. Independent Ornstein–Uhlenbeck (OU) processes were injected into each node, and a common OU process was added with a mixing strength parameter *s* (see Methods 2.2) ranging from 0 (independent inputs only) to 1 (common input only). The protocol was applied to the representative network classes of the randomization and clusterization families (C1, B1, R, B2, C2). **(B)** Median correlation of the functional connectivity (FC) matrices as a function of common driver strength *s*, shown separately for the representative networks of the randomization family (left) and the clusterization family (right). **(C–D)** Complexity measures as a function of common driver strength *s*. Panels show (I) Lempel–Ziv complexity (LZc), (II) amplitude coalition entropy (ACE), (III) synchrony coalition entropy (SCE), (IV) neural complexity (NC), (V) functional complexity (Fcomp), and (VI) perturbational complexity index (PCI). Curves represent the mean across network realizations (n = 10); shaded areas denote SEM. In panel VI, horizontal dashed lines indicate the minimum PCI observed within each network class, highlighting the absence of overlap between classes across the full range of *s*.

4. Discussion

In this study, we systematically compared a suite of complexity metrics in artificial neuronal networks undergoing controlled topological transformations. By applying randomization and clusterization procedures, we generated families of networks spanning a wide spectrum of integration–segregation balance. We then probed both spontaneous and evoked dynamics, quantifying complexity with observational and perturbational measures, and further tested their robustness under the influence of an external common driver. Across analyses, a taxonomy of complexity metrics emerged.

Signal diversity metrics decreased monotonically under the influence of spurious interactions introduced by a common driver, while remaining largely insensitive to network structure given the comparable local node near-bifurcation regime. Neural complexity (NC) was biased toward structural integration, showing increased values in random networks, but it was also inflated by the artificial correlations induced by common drivers. Functional complexity (Fcomp) was sensitive to the balance between integration and segregation but peaked merely when independent noise and common input were balanced, and failed to distinguish between clustered and balanced topologies.

By contrast, PCI exhibited a distinctive inverted-U profile, peaking only when integration and segregation were simultaneously expressed, and retained its discriminative power across network classes even in the presence of strong common drivers. This sensitivity reflects the regime predicted by theories of consciousness as optimal for information processing: one in which global integration coexists with local differentiation (Tononi and Edelman, 1998; Sarasso et al., 2021). This mechanistic link helps explain why PCI has consistently emerged as a reliable biomarker of conscious states (Casali et al., 2013; Casarotto et al., 2016). Importantly, empirical and modeling works have also demonstrated a dissociation between PCI and spontaneous signal diversity measures (Farnes et al., 2020; Ort et al., 2023; Gaglioti et al., 2024). For example, under eyes-closed conditions, the predominance of alpha rhythms leads to marked reductions in signal diversity, whereas the complexity of the evoked response measured by PCI remains stable (Farnes et al., 2020; Ort et al., 2023). Such evidence highlights that PCI, unlike spontaneous metrics, directly captures, through causal perturbation, the capacity of a network architecture to sustain complex dynamics rather than inferring it indirectly from ongoing fluctuations.

Our findings also resonate with the criticality hypothesis (Beggs and Plenz, 2003; Shew and Plenz, 2013; Cocchi et al., 2017; O'Byrne and Jerbi, 2022). The perturbational complexity peak emerged at the transition between segregated and integrated topologies, consistent with the notion that brains operate near a phase transition to maximize their dynamical repertoire. Importantly, recent empirical work has directly linked PCI to criticality (Maschke et al., 2024). In resting-state EEG under anesthesia, criticality measures were found to reliably predict PCI values, establishing a firm connection between perturbational complexity and

critical dynamics. In this work, rewiring reorganized network topology and thereby shifted the system across dynamical regimes. Although coupling strength and node degree were held constant, the rewiring procedure alone was sufficient to drive transitions between them. Clustered motifs enriched with triangular feedback loops amplified and prolonged responses, leading to longer-lasting reverberations (Spiegler et al., 2016)—an expression of critical slowing down, i.e., the phenomenon whereby recovery from perturbations becomes progressively slower as the system approaches a bifurcation point. In our setting, this was reflected in delayed decay of evoked responses, a hallmark of proximity to criticality. At the same time, the same motifs also boosted correlations in spontaneous functional connectivity, consistent with the idea that recurrent loops sustain local amplification of activity (Kaiser et al., 2007; Hilgetag and Hütt, 2014). Yet in highly segregated regimes, clusters remained isolated, producing local but not global criticality. Balanced architectures reconciled this trade-off: they preserved local motifs that sustain reverberation while providing shortcuts for global broadcast, resulting in both sustained and integrated responses.

This architecture-dependent criticality suggests that heterogeneity across brain networks may support functional specialization. Different regions need not operate at the same point along the criticality continuum: variations in connectivity—for example, between sensory and association cortices—may place regions in distinct dynamical regimes. Recent electrophysiological analyses confirm this view: higher-order regions of the mouse visual cortex were found to be positioned closer to criticality than primary sensory regions, consistent with their longer integration timescales and increased computational demands (Harris et al., 2024). Complementary large-scale neuronal recordings further reveal that signatures of near-critical scaling are not restricted to a subset of regions but are widespread across the brain, with each area operating to a greater or lesser degree near the edge of instability (Morales et al., 2023). Our results emphasize network topology as a determinant of such heterogeneity, but regional variations in receptor distributions are also likely contributors, providing a promising target for future investigation.

Although our model used abstract, undirected, and binary graphs with random delays—where nodes represent mean-field approximations of neural populations—the principles it uncovered can be tested in more biologically realistic architectures. Layered cortical microcircuits with structured excitatory–inhibitory interactions could reveal how local dynamics shape global complexity. Similarly, grid-like topologies reminiscent of posterior cortical motifs (Salin and Bullier, 1995; Haun and Tononi, 2019) would directly connect our results to system and theoretical neuroscience. Such grid-like structures are theoretically intriguing: despite their apparent simplicity, they can support strong integration and high levels of complexity. This connects to a longstanding question in consciousness research—whether posterior cortices constitute “hot spots” for complexity (Koch et al., 2016; Sanders et al., 2018) owing to their wiring patterns or rich-club organization. Indeed, converging EEG and fMRI evidence shows that loss and recovery of consciousness are accompanied by changes in complexity located in posterior cortices (King et al., 2013; Luppi et al., 2019; Sitt et al., 2014). Our modeling framework provides a route to mechanistically test this link between circuit architecture and perturbational complexity.

An important corollary is that PCI depends not only on global architecture but also on the embedding of the stimulated node. In particular, the neighborhood efficiency of the stimulated site correlated strongly with PCI in highly clustered networks. This demonstrates that the capacity to generate complex dynamics is not uniformly distributed across a network but is shaped by nodal roles. Building on this, one could envision an "atlas of complexity," mapping how stimulation of different nodes elicits varying levels of complex network responses. Such predictions can be tested empirically using cortico-cortical evoked potentials (David et al. 2013; Trebaul et al. 2018, Momi et al. 2025), where targeted stimulation and recording across cortical sites could reveal how local embedding determines the richness of both local and global responses.

Finally, our analyses highlight the profound impact of the common driver problem on observational metrics. Common drivers are shared inputs that impinge simultaneously on many nodes, creating correlations that do not reflect genuine network interactions (Blinowska and Kaminski, 2013; Kaminski et al., 2016; Gilpin, 2025). They are a major confound in neuroscience because sensory inputs or neuromodulatory fluctuations can make disconnected areas appear functionally linked. In our simulations, spontaneous metrics were highly susceptible to this effect: depending on the measure, common input either collapsed activity toward minimal diversity or artificially inflated apparent integration. In contrast, PCI maintained a clear separation between network classes across the full range of driver strengths. This robustness stems from the perturbational approach, which forces the system to reveal its causal pathways. The contribution of the common driver—which does not participate in these causal interactions—is effectively averaged out across repeated stimulations, thereby preserving the structural determinants of complexity.

In conclusion, our work provides a principled taxonomy of complexity measures, clarifying how each interacts with network topology and confounds. We identify PCI as uniquely sensitive to the integration–segregation balance that underlies complex dynamics and robust to global confounds. These results bridge levels of analysis, from local motifs to large-scale dynamics, and offer a mechanistic foundation for empirical and computational studies of the neural correlates of consciousness.

References

Bassett, D.S., Bullmore, E.T., 2017. Small-World Brain Networks Revisited. Neuroscientist 23, 499–516. https://doi.org/10.1177/1073858416667720

Beggs, J.M., Plenz, D., 2003. Neuronal avalanches in neocortical circuits. J Neurosci 23, 11167–11177. https://doi.org/10.1523/JNEUROSCI.23-35-11167.2003

Bertolero, M.A., Yeo, B.T.T., D'Esposito, M., 2015. The modular and integrative functional architecture of the human brain. Proceedings of the National Academy of Sciences 112, E6798–E6807. https://doi.org/10.1073/pnas.1510619112

Betzel, R.F., Bassett, D.S., 2017. Multi-scale brain networks. NeuroImage, Functional Architecture of the Brain 160, 73–83. https://doi.org/10.1016/j.neuroimage.2016.11.006

Blinowska, K.J., Kaminski, M., 2013. Functional Brain Networks: Random, "Small World" or Deterministic? PLOS ONE 8, e78763. https://doi.org/10.1371/journal.pone.0078763

Boucsein, C., Nawrot, M., Schnepel, P., Aertsen, A., 2011. Beyond the Cortical Column: Abundance and Physiology of Horizontal Connections Imply a Strong Role for Inputs from the Surround. Front. Neurosci. 5. https://doi.org/10.3389/fnins.2011.00032

Bullmore, E., Sporns, O., 2009. Complex brain networks: graph theoretical analysis of structural and functional systems. Nat Rev Neurosci 10, 186–198. https://doi.org/10.1038/nrn2575

Cabral, J., Castaldo, F., Vohryzek, J., Litvak, V., Bick, C., Lambiotte, R., Friston, K., Kringelbach, M.L., Deco, G., 2022. Metastable oscillatory modes emerge from synchronization in the brain spacetime connectome. Commun Phys 5, 1–13. https://doi.org/10.1038/s42005-022-00950-y

Cakan, C., Jajcay, N., Obermayer, K., 2021. neurolib: A Simulation Framework for Whole-Brain Neural Mass Modeling. Cogn Comput 15, 1132–1152. https://doi.org/10.1007/s12559-021-09931-9

Casali, A.G., Gosseries, O., Rosanova, M., Boly, M., Sarasso, S., Casali, K.R., Casarotto, S., Bruno, M.-A., Laureys, S., Tononi, G., Massimini, M., 2013. A theoretically based index of consciousness independent of sensory processing and behavior. Sci Transl Med 5, 198ra105. https://doi.org/10.1126/scitranslmed.3006294

Casarotto, S., Comanducci, A., Rosanova, M., Sarasso, S., Fecchio, M., Napolitani, M., Pigorini, A., G Casali, A., Trimarchi, P.D., Boly, M., Gosseries, O., Bodart, O., Curto, F., Landi, C., Mariotti, M., Devalle, G., Laureys, S., Tononi, G., Massimini, M., 2016. Stratification of unresponsive patients by an independently validated index of brain complexity. Ann Neurol 80, 718–729. https://doi.org/10.1002/ana.24779

Cocchi, L., Gollo, L.L., Zalesky, A., Breakspear, M., 2017. Criticality in the brain: A synthesis of neurobiology, models and cognition. Prog Neurobiol 158, 132–152. https://doi.org/10.1016/j.pneurobio.2017.07.002

Cohen, J.R., D'Esposito, M., 2016. The Segregation and Integration of Distinct Brain Networks and Their Relationship to Cognition. J Neurosci 36, 12083–12094. https://doi.org/10.1523/JNEUROSCI.2965-15.2016

Demertzi, A., Tagliazucchi, E., Dehaene, S., Deco, G., Barttfeld, P., Raimondo, F., Martial, C., Fernández-Espejo, D., Rohaut, B., Voss, H.U., Schiff, N.D., Owen, A.M., Laureys, S., Naccache, L., Sitt, J.D., 2019. Human consciousness is supported by dynamic complex patterns of brain signal coordination. Sci Adv 5, eaat7603. https://doi.org/10.1126/sciadv.aat7603

Edelman, G.M., Gally, J.A., 2013. Reentry: a key mechanism for integration of brain function. Front Integr Neurosci 7, 63. https://doi.org/10.3389/fnint.2013.00063

Edelman, G.M., Gally, J.A., 2001. Degeneracy and complexity in biological systems. Proceedings of the National Academy of Sciences 98, 13763–13768. https://doi.org/10.1073/pnas.231499798

Ercsey-Ravasz, M., Markov, N.T., Lamy, C., Van Essen, D.C., Knoblauch, K., Toroczkai, Z., Kennedy, H., 2013. A Predictive Network Model of Cerebral Cortical Connectivity Based on a Distance Rule. Neuron 80, 184–197. https://doi.org/10.1016/j.neuron.2013.07.036

Farnes, N., Juel, B.E., Nilsen, A.S., Romundstad, L.G., Storm, J.F., 2020. Increased signal diversity/complexity of spontaneous EEG, but not evoked EEG responses, in ketamine-induced psychedelic state in humans. PLOS ONE 15, e0242056. https://doi.org/10.1371/journal.pone.0242056

Fukushima, M., Sporns, O., 2020. Structural determinants of dynamic fluctuations between segregation and integration on the human connectome. Commun Biol 3, 606. https://doi.org/10.1038/s42003-020-01331-3

Gaglioti, G., Nieus, T.R., Massimini, M., Sarasso, S., 2024. Investigating the Impact of Local Manipulations on Spontaneous and Evoked Brain Complexity Indices: A Large-Scale Computational Model. Applied Sciences 14, 890. https://doi.org/10.3390/app14020890

Gilpin, W., 2025. Recurrences Reveal Shared Causal Drivers of Complex Time Series. Phys. Rev. X 15, 011005. https://doi.org/10.1103/PhysRevX.15.011005

Griffa, A., Van den Heuvel, M.P., 2018. Rich-club neurocircuitry: function, evolution, and vulnerability. Dialogues in Clinical Neuroscience 20, 121–132. https://doi.org/10.31887/DCNS.2018.20.2/agriffa

Hacine-Gharbi, A., Ravier, P., 2018. A binning formula of bi-histogram for joint entropy estimation using mean square error minimization. Pattern Recognition Letters 101, 21–28. https://doi.org/10.1016/j.patrec.2017.11.007

Hagberg, A.A., Schult, D.A., Swart, P.J., 2008. Exploring Network Structure, Dynamics, and Function using NetworkX. scipy. https://doi.org/10.25080/TCWV9851

Hahn, G., Zamora-López, G., Uhrig, L., Tagliazucchi, E., Laufs, H., Mantini, D., Kringelbach, M.L., Jarraya, B., Deco, G., 2021. Signature of consciousness in brain-wide synchronization patterns of monkey and human fMRI signals. Neuroimage 226, 117470. https://doi.org/10.1016/j.neuroimage.2020.117470

Harris, B., Gollo, L.L., Fulcher, B.D., 2024. Tracking the Distance to Criticality in Systems with Unknown Noise. Phys. Rev. X 14, 031021. https://doi.org/10.1103/PhysRevX.14.031021

Haun, A., Tononi, G., 2019. Why Does Space Feel the Way it Does? Towards a Principled Account of Spatial Experience. Entropy 21, 1160. https://doi.org/10.3390/e21121160

Heuvel, M.P. van den, Sporns, O., 2013. Network hubs in the human brain. Trends in Cognitive Sciences 17, 683–696. https://doi.org/10.1016/j.tics.2013.09.012
Heuvel, M.P. van den, Sporns, O., 2011. Rich-Club Organization of the Human Connectome. J. Neurosci. 31, 15775–15786. https://doi.org/10.1523/JNEUROSCI.3539-11.2011
Hilgetag, C.C., Goulas, A., 2020. 'Hierarchy' in the organization of brain networks. Philosophical Transactions of the Royal Society B: Biological Sciences 375, 20190319. https://doi.org/10.1098/rstb.2019.0319
Hilgetag, C.C., Hütt, M.-T., 2014. Hierarchical modular brain connectivity is a stretch for criticality. Trends in Cognitive Sciences 18, 114–115. https://doi.org/10.1016/j.tics.2013.10.016
Honey, C.J., Sporns, O., Cammoun, L., Gigandet, X., Thiran, J.P., Meuli, R., Hagmann, P., 2009. Predicting human resting-state functional connectivity from structural connectivity. Proceedings of the National Academy of Sciences 106, 2035–2040. https://doi.org/10.1073/pnas.0811168106
Jang, H., Mashour, G.A., Hudetz, A.G., Huang, Z., 2024. Measuring the dynamic balance of integration and segregation underlying consciousness, anesthesia, and sleep in humans. Nat Commun 15, 9164. https://doi.org/10.1038/s41467-024-53299-x
Kaiser, M., Görner, M., Hilgetag, C., 2007. Criticality of spreading dynamics in hierarchical cluster networks without inhibition. New Journal of Physics 9. https://doi.org/10.1088/1367-2630/9/5/110
Kaminski, M., Brzezicka, A., Kaminski, J., Blinowska, K.J., 2016. Measures of Coupling between Neural Populations Based on Granger Causality Principle. Front. Comput. Neurosci. 10. https://doi.org/10.3389/fncom.2016.00114
King, J.-R., Sitt, J.D., Faugeras, F., Rohaut, B., El Karoui, I., Cohen, L., Naccache, L., Dehaene, S., 2013. Information Sharing in the Brain Indexes Consciousness in Noncommunicative Patients. Current Biology 23, 1914–1919. https://doi.org/10.1016/j.cub.2013.07.075
Koch, C., Massimini, M., Boly, M., Tononi, G., 2016. Neural correlates of consciousness: progress and problems. Nat Rev Neurosci 17, 307–321. https://doi.org/10.1038/nrn.2016.22
Latora, V., Marchiori, M., 2001. Efficient Behavior of Small-World Networks. Phys. Rev. Lett. 87, 198701. https://doi.org/10.1103/PhysRevLett.87.198701
Lord, L.-D., Carletti, T., Fernandes, H., Turkheimer, F.E., Expert, P., 2023. Altered dynamical integration/segregation balance during anesthesia-induced loss of consciousness. Front. Netw. Physiol. 3. https://doi.org/10.3389/fnetp.2023.1279646
Luppi, A.I., Craig, M.M., Pappas, I., Finoia, P., Williams, G.B., Allanson, J., Pickard, J.D., Owen, A.M., Naci, L., Menon, D.K., Stamatakis, E.A., 2019. Consciousness-specific dynamic interactions of brain integration and functional diversity. Nat Commun 10, 4616. https://doi.org/10.1038/s41467-019-12658-9
Makowski, D., Pham, T., Lau, Z.J., Brammer, J.C., Lespinasse, F., Pham, H., Schölzel, C., Chen, S.H.A., 2021. NeuroKit2: A Python toolbox for neurophysiological signal processing. Behav Res Methods 53, 1689–1696. https://doi.org/10.3758/s13428-020-01516-y
Maschke, C., O'Byrne, J., Colombo, M.A., Boly, M., Gosseries, O., Laureys, S., Rosanova, M., Jerbi, K., Blain-Moraes, S., 2024. Critical dynamics in spontaneous EEG predict anesthetic-induced loss of consciousness and perturbational complexity. Commun Biol 7, 946. https://doi.org/10.1038/s42003-024-06613-8
Massimini, M., Boly, M., Casali, A., Rosanova, M., Tononi, G., 2009. A perturbational approach for evaluating the brain's capacity for consciousness, in: Laureys, S., Schiff, N.D., Owen, A.M. (Eds.), Progress in Brain Research, Coma Science: Clinical and

Ethical Implications. Elsevier, pp. 201–214. https://doi.org/10.1016/S0079-6123(09)17714-2
Meunier, D., Lambiotte, R., Bullmore, E.T., 2010. Modular and Hierarchically Modular Organization of Brain Networks. Front. Neurosci. 4. https://doi.org/10.3389/fnins.2010.00200
Morales, G.B., di Santo, S., Muñoz, M.A., 2023. Quasiuniversal scaling in mouse-brain neuronal activity stems from edge-of-instability critical dynamics. Proceedings of the National Academy of Sciences 120, e2208998120. https://doi.org/10.1073/pnas.2208998120
Muldoon, S.F., Bridgeford, E.W., Bassett, D.S., 2016. Small-World Propensity and Weighted Brain Networks. Sci Rep 6, 22057. https://doi.org/10.1038/srep22057
Nichols, T.E., Holmes, A.P., 2001. Nonparametric permutation tests for functional neuroimaging: A primer with examples. Hum Brain Mapp 15, 1–25. https://doi.org/10.1002/hbm.1058
O'Byrne, J., Jerbi, K., 2022. How critical is brain criticality? Trends Neurosci 45, 820–837. https://doi.org/10.1016/j.tins.2022.08.007
Ort, A., Smallridge, J.W., Sarasso, S., Casarotto, S., Rotz, R. von, Casanova, A., Seifritz, E., Preller, K.H., Tononi, G., Vollenweider, F.X., 2023. TMS-EEG and resting-state EEG applied to altered states of consciousness: oscillations, complexity, and phenomenology. iScience 26. https://doi.org/10.1016/j.isci.2023.106589
Pathak, A., Menon, S.N., Sinha, S., 2024. A hierarchy index for networks in the brain reveals a complex entangled organizational structure. Proceedings of the National Academy of Sciences 121, e2314291121. https://doi.org/10.1073/pnas.2314291121
Salin, P.A., Bullier, J., 1995. Corticocortical connections in the visual system: structure and function. Physiological Reviews 75, 107–154. https://doi.org/10.1152/physrev.1995.75.1.107
Sanders, R.D., Mostert, N., Lindroth, H., Tononi, G., Sleigh, J., 2018. Is consciousness frontal? Two perioperative case reports that challenge that concept. British Journal of Anaesthesia 121, 330–332. https://doi.org/10.1016/j.bja.2018.01.010
Sarasso, S., Boly, M., Napolitani, M., Gosseries, O., Charland-Verville, V., Casarotto, S., Rosanova, M., Casali, A.G., Brichant, J.-F., Boveroux, P., Rex, S., Tononi, G., Laureys, S., Massimini, M., 2015. Consciousness and Complexity during Unresponsiveness Induced by Propofol, Xenon, and Ketamine. Current Biology 25, 3099–3105. https://doi.org/10.1016/j.cub.2015.10.014
Sarasso, S., Casali, A.G., Casarotto, S., Rosanova, M., Sinigaglia, C., Massimini, M., 2021. Consciousness and complexity: a consilience of evidence. Neuroscience of Consciousness niab023. https://doi.org/10.1093/nc/niab023
Schartner, M., Seth, A., Noirhomme, Q., Boly, M., Bruno, M.-A., Laureys, S., Barrett, A., 2015. Complexity of Multi-Dimensional Spontaneous EEG Decreases during Propofol Induced General Anaesthesia. PLOS ONE 10, e0133532. https://doi.org/10.1371/journal.pone.0133532
Senden, M., Deco, G., de Reus, M.A., Goebel, R., van den Heuvel, M.P., 2014. Rich club organization supports a diverse set of functional network configurations. NeuroImage 96, 174–182. https://doi.org/10.1016/j.neuroimage.2014.03.066
Shew, W.L., Plenz, D., 2013. The Functional Benefits of Criticality in the Cortex. Neuroscientist 19, 88–100. https://doi.org/10.1177/1073858412445487
Shew, W.L., Yang, H., Yu, S., Roy, R., Plenz, D., 2011. Information Capacity and Transmission Are Maximized in Balanced Cortical Networks with Neuronal Avalanches. J. Neurosci. 31, 55–63. https://doi.org/10.1523/JNEUROSCI.4637-10.2011

Sitt, J.D., King, J.-R., El Karoui, I., Rohaut, B., Faugeras, F., Gramfort, A., Cohen, L., Sigman, M., Dehaene, S., Naccache, L., 2014. Large scale screening of neural signatures of consciousness in patients in a vegetative or minimally conscious state. Brain 137, 2258–2270. https://doi.org/10.1093/brain/awu141

Spiegler, A., Hansen, E.C.A., Bernard, C., McIntosh, A.R., Jirsa, V.K., 2016. Selective Activation of Resting-State Networks following Focal Stimulation in a Connectome-Based Network Model of the Human Brain. eNeuro 3. https://doi.org/10.1523/ENEURO.0068-16.2016

Sporns, O., 2022. The complex brain: connectivity, dynamics, information. Trends in Cognitive Sciences 26, 1066–1067. https://doi.org/10.1016/j.tics.2022.08.002

Sporns, O., 2013. Network attributes for segregation and integration in the human brain. Current Opinion in Neurobiology, Macrocircuits 23, 162–171. https://doi.org/10.1016/j.conb.2012.11.015

Sporns, O., Betzel, R.F., 2016. Modular Brain Networks. Annu Rev Psychol 67, 613–640. https://doi.org/10.1146/annurev-psych-122414-033634

Sporns, O., Tononi, G., Edelman, G.M., 2000. Connectivity and complexity: the relationship between neuroanatomy and brain dynamics. Neural Netw 13, 909–922. https://doi.org/10.1016/s0893-6080(00)00053-8

Sporns, O., Tononi, G., Kötter, R., 2005. The Human Connectome: A Structural Description of the Human Brain. PLoS Comput Biol 1, e42. https://doi.org/10.1371/journal.pcbi.0010042

Tononi, G., Edelman, G.M., 1998. Consciousness and Complexity. Science 282, 1846–1851. https://doi.org/10.1126/science.282.5395.1846

Tononi, G., Edelman, G.M., Sporns, O., 1998. Complexity and coherency: integrating information in the brain. Trends Cogn Sci 2, 474–484. https://doi.org/10.1016/s1364-6613(98)01259-5

Tononi, G., Sporns, O., Edelman, G.M., 1994. A measure for brain complexity: relating functional segregation and integration in the nervous system. Proc Natl Acad Sci U S A 91, 5033–5037.

Tononi, G., Sporns, O., Edelman, G.M., 1992. Reentry and the problem of integrating multiple cortical areas: simulation of dynamic integration in the visual system. Cereb Cortex 2, 310–335. https://doi.org/10.1093/cercor/2.4.310

Virtanen, P., Gommers, R., Oliphant, T.E., Haberland, M., Reddy, T., Cournapeau, D., Burovski, E., Peterson, P., Weckesser, W., Bright, J., van der Walt, S.J., Brett, M., Wilson, J., Millman, K.J., Mayorov, N., Nelson, A.R.J., Jones, E., Kern, R., Larson, E., Carey, C.J., Polat, İ., Feng, Y., Moore, E.W., VanderPlas, J., Laxalde, D., Perktold, J., Cimrman, R., Henriksen, I., Quintero, E.A., Harris, C.R., Archibald, A.M., Ribeiro, A.H., Pedregosa, F., van Mulbregt, P., 2020. SciPy 1.0: fundamental algorithms for scientific computing in Python. Nat Methods 17, 261–272. https://doi.org/10.1038/s41592-019-0686-2

Watts, D.J., Strogatz, S.H., 1998. Collective dynamics of ‘small-world’ networks. Nature 393, 440–442. https://doi.org/10.1038/30918

Zamora-López, G., Chen, Y., Deco, G., Kringelbach, M.L., Zhou, C., 2016. Functional complexity emerging from anatomical constraints in the brain: the significance of network modularity and rich-clubs. Sci Rep 6, 38424. https://doi.org/10.1038/srep38424

Zamora-López, G., Zhou, C., Kurths, J., 2010. Cortical hubs form a module for multisensory integration on top of the hierarchy of cortical networks. Front. Neuroinform. 4. https://doi.org/10.3389/neuro.11.001.2010

Supplementary material

Table S1. Model parameters.

Figure S1. Bifurcation diagram for the representative networks.

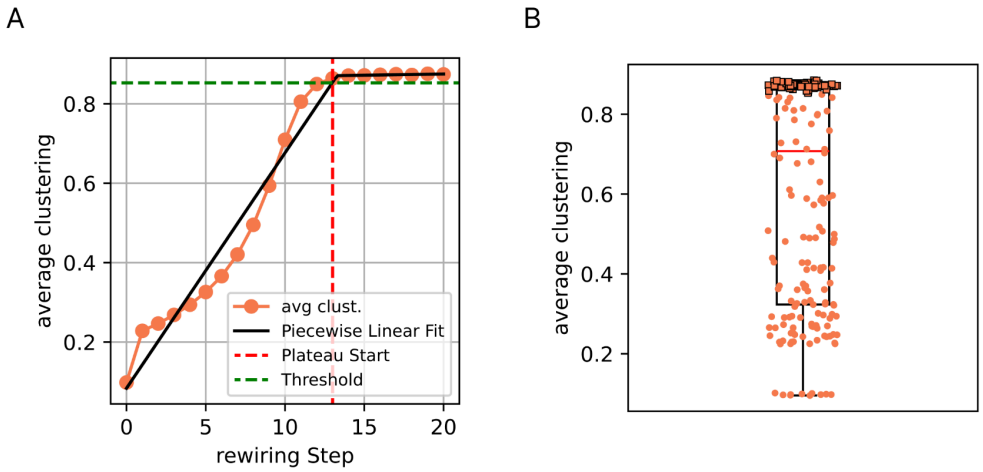

Figure S2. Identification of highly clustered networks in the clusterization process. (A) The threshold for identifying the subgroup of highly clustered networks was derived from the evolution of average clustering during the clusterization process. The mean clustering trajectory across rewiring steps (orange circles) was fitted with a two-segment piecewise linear model (black line), capturing the initial rise and the subsequent plateau. The breakpoint of this fit (red dashed line) marked the onset of the plateau, and all networks sampled at steps beyond this point were considered part of the plateau regime. To define a permissive threshold within this regime, we computed the mean clustering value across plateau networks and subtracted three standard deviations (green dashed line). **(B)** Distribution of clustering values across all networks (10 realizations for each of the 21 rewiring steps). Networks exceeding the threshold are highlighted with orange square markers and were classified as highly clustered.

3

Discussion

This thesis has pursued a multifaceted investigation into the mechanisms underlying brain complexity, conceptualized as the dynamic balance between functional integration and differentiation. By combining empirical tools, computational modeling, and systematic theoretical validation, the five articles presented herein provide a cohesive and mechanistic account of how the brain generates and sustains complex dynamics, how this complexity breaks down in pathology, and how it can be reliably measured. This chapter synthesizes these contributions, discusses their theoretical and clinical implications, acknowledges their limitations, and outlines promising avenues for future research.

3.1 Synthesis of Main Findings

The articles in this thesis collectively advance the understanding of brain complexity by addressing the problem across multiple scales and through a tight dialectic between empirical observation and computational simulation.

3.1.1 Collective Advancement

The journey begins with Article 1, which provides a standardized empirical tool (TEPpy) to quantify differentiation—the specialized, local response properties of cortical circuits. By demonstrating robust gradients in natural frequencies and response latencies across the cortex, it operationalizes the concept of local functional specialization. Article 2 then establishes the computational foundation, demonstrating that whole-brain models can be tuned to a critical-like regime that simultaneously captures key features of spontaneous activity (e.g., alpha rhythms, infra-slow fluctuations, spatio-temporal heterogeneity) and evokes complex, widespread responses to perturbation, as quantified by PCI. Article 3 leverages this model to demonstrate a direct causal link between structure and function, showing that targeted silencing of highly connected posterior hubs induces the most severe

reductions in perturbational complexity, while often sparing or even increasing measures of local signal diversity (LZc). This dissociation not only underscores a significant limitation of various complexity metrics based on spontaneous activity, such as LZc, as they assume a priori network integration and yield high values in systems composed of independent/segregated elements, but also highlights the superior sensitivity of perturbational approaches like PCI to the genuine integration-differentiation balance. Article 4 delves into the primary mechanism of complexity disruption (section 1.3.2.2), revealing that structural disconnection is a sufficient driver for the generation of slow waves through a mechanism of disfacilitation, providing a computational foundation for empirical evidence on the emergence of sleep-like dynamics after brain injury. Crucially, it shows that these slow waves are not merely local epiphenomena but propagate through the network's topological architecture, driven by temporal coherence, thereby explaining how a focal lesion can generate widespread functional impairment. Finally, Article 5 provides the crucial theoretical validation for the entire endeavor, proving that PCI is an empirical measure that peaks uniquely at the optimal integration-differentiation balance, is robust to common confounds like shared inputs, and is inherently linked to the network's critical dynamical regime.

3.1.2 Integration of Approaches

The power of this work lies in the recursive loop between method development, empirical observation, and computational testing. TEPpy (Article 1) provides empirical measures to constrain and validate models. The modeling framework (Articles 2-5) allows for controlled causal experiments (e.g., virtual lesions, network rewiring) that are impossible in vivo, generating predictions about mechanisms and metrics. The results of these simulations, such as the pivotal role of posterior hubs (Article 3) or the mechanism of slow wave propagation (Article 4), in turn, provide deeper explanations for empirical observations in patients and healthy subjects.

3.2 Methodological Contributions

A significant output of this thesis is the development and dissemination of standardized methodologies.

3.2.1 Standardized Pipelines: TEPpy

Article 1 addresses a critical lack of standardization in TMS-EEG analysis. The TEPpy package provides an open-source, automated framework for extracting reproducible features—peak latencies, amplitudes, interpeak intervals, and natural frequencies—from TEPs. Its agnosticism to acquisition hardware and preprocessing pipelines ensures high reproducibility and comparability across labs. This tool transforms subjective, "first-glance" assessments of TEPs into quantitative, data-driven metrics of local circuit differentiation, paving the way for large-scale normative mapping and robust clinical biomarker extraction.

3.2.2 Computational Frameworks: TVB-Cobrawap

Article 2 showcases an integrated workflow for whole-brain modeling that is a crucial tool for the field. By combining The Virtual Brain (TVB) simulator with the Collaborative Brain Wave Analysis Pipeline (Cobrawap), it establishes a reproducible framework for simulating, analyzing, and tuning whole-brain models against a battery of biologically relevant observables (e.g., spectral content, functional connectivity, evoked complexity). This integration, delivered via the EBRAINS infrastructure, moves the field beyond ad-hoc model fitting and lays the groundwork for direct, quantitative comparison between simulated and empirical data, setting a new standard for rigor and reproducibility in computational neuroscience.

3.3 Theoretical Implications

3.3.1 Integration-Differentiation Balance and Criticality

The findings across the articles provide direct support for the notion that realistic brain dynamics emerge from a balance between integration and differentiation, which is mechanistically linked to critical dynamics. In whole-brain simulations (article 2; section 2.2), parameter tuning shifts models toward critical-like regimes exhibiting scale-free spectral scaling, infra-slow fluctuations, long-range temporal correlations, and heightened sensitivity to perturbations, as evidenced by prolonged and complex evoked responses quantified with PCI. Similarly, artificial network studies (article 5; section 2.5) reveal that PCI displays a distinctive inverted-U profile, peaking precisely when integration and segregation coexist, consistent with theoretical predictions of optimal information processing in systems balancing global coordination and local specialization. This regime aligns with the criticality hypothesis, where networks near phase transitions maximize their dynamical repertoire through features like critical slowing down and efficient signal propagation.

3.3.2 Network Connectivity and Phase Transitions

The computational analysis in Article 5 reveals that network topology fundamentally determines dynamical regimes. Rewiring reorganizes network topology and thereby shifts the system across dynamical regimes. Although coupling strength and node degree were held constant, the rewiring procedure alone was sufficient to drive transitions between them. Clustered motifs enriched with triangular feedback loops amplified and prolonged responses, leading to longer-lasting reverberations, an expression of critical slowing down.

However, in highly segregated regimes, clusters remained isolated, producing local but not global criticality. Balanced architectures reconciled this trade-off: they preserved local motifs that sustain reverberation while providing shortcuts for global broadcast, resulting in both

sustained and integrated responses. This architecture-dependent criticality suggests that heterogeneity across brain networks may support functional specialization

3.3.3 Insights into Pathological Dynamics

The work provides a mechanistic account for the breakdown of complexity. Article 4 provides mechanistic insights into pathological brain states following injury. Three factors govern post-lesional dynamics: (i) disconnection-induced disfacilitation shifts local circuits toward slow-wave generation, (ii) hierarchical network organization with respect to the lesion determines distance-dependent propagation, and (iii) temporal coherence of Down-states amplifies remote network disruption. This framework explains empirical observations of perilesional slowing and provides mechanistic support for the hypothesis that focal lesions induce sleep-like dynamics in structurally intact but functionally disconnected regions. These results are consistent with empirical findings (Massimini et al., 2024) and potentially link the concept of diaschisis to a specific electrophysiological mechanism.

3.4 Clinical Relevance

The translational potential of this work is significant, offering new pathways for diagnosis and therapeutic intervention.

3.4.1 Applications to Brain Injury: Modeling

The computational framework developed in Article 4 (section 2.4) provides a testbed for simulating patient-specific lesions. By incorporating individual structural connectomes and calibrating against empirical dynamics, it offers a pathway to predict the functional impact of brain injury, identifying lesions most likely to induce widespread network dysfunction through slow-wave propagation. Such predictions could inform rehabilitation strategies and guide neuromodulation interventions aimed at desynchronizing pathological slow-wave activity and restoring healthy dynamics.

3.4.2 Applications to Brain Injury: TEPpy

Section 2.1 (Article 1) provides the empirical foundation for clinical applications through TEPpy's standardized natural frequency measurements. Systematic slowing of TMS-EEG responses has been consistently reported in stroke patients when stimulating perilesional sites (Sarasso et al., 2020) or structurally disconnected regions (D'Ambrosio et al., 2023), with renormalization tracking recovery. The standardized framework enables establishment of normative cortical fingerprints and detection of pathological deviations in patient populations, offering a quantitative biomarker for network integrity.

3.5 Limitations and Future Directions

While comprehensive, this work naturally has limitations that chart a course for future research.

3.5.1 Current Modeling Constraints

Several limitations constrain the current modeling approaches. The neural mass models used in this thesis rely on coarse-grained population dynamics without explicit representation of finer-scale biophysical mechanisms. Subcortical structures, known to orchestrate brain rhythms and propagate neural activity, are not included in current implementations. The artificial network studies (section 2.5), while mechanistically informative, employ abstract binary graphs with random delays rather than biologically realistic architectures. The slow-wave generation and propagation model (section 2.4), though validated at multiple scales, does not incorporate additional factors known to influence post-lesional dynamics, including GABA-mediated excitation–inhibition imbalance, cortical hyperexcitability, inflammation, and hypoxia

3.5.2 Opportunities for Empirical Validation

Future work should directly compare model outputs to empirical data rather than relying solely on qualitative feature matching. The introduction of appropriate forward models would enable EEG-level simulations for direct comparison with experimental findings. Subject-specific model tuning using personalized structural and functional connectivity from patient data could enable predictions about lesion-specific effects on spontaneous and evoked dynamics.

3.5.3 Model Extensions

The framework's generalizability beyond stroke and focal lesions remains to be established. Extensions to neurodegenerative conditions, epilepsy, and psychiatric disorders would test the broader applicability of the modeling framework. The slow-wave generation and propagation model (section 2.4) could be adapted to investigate arousal fluctuations and their interactions with lesion-induced slow waves. The artificial network approach (section 2.5) provides a foundation for testing more biologically realistic architectures, including layered cortical microcircuits with structured excitatory–inhibitory interactions and grid-like topologies reminiscent of posterior cortical organization. Such extensions would directly test hypotheses about posterior cortices as "hot zones" for consciousness and complexity

3.6 Concluding Remarks

In conclusion, this thesis makes a contribution to computational neuroscience and our understanding of brain function. It provides a mechanistic, multi-scale account of brain complexity, from the local circuit properties that enable differentiation to the large-scale network architecture that enables integration.

The broader implications are twofold. First, it demonstrates the indispensable power of a cohesive theory-computation-experiment cycle, where computational models are not just used to simulate data but to conduct causal experiments that deepen our explanatory understanding of empirical phenomena. Second, it bridges a fundamental gap between abstract information-theory (integration/differentiation) and concrete neurobiology (network structure/dynamics), showing how the former emerges from the latter.

By providing standardized tools, validated metrics, and a unified theoretical framework, this work lays a foundation for a more rigorous, reproducible, and mechanistic neuroscience, with clear pathways to improving the diagnosis and treatment of brain disorders.

Bibliography

Achard, S., Bullmore, E., 2007. Efficiency and Cost of Economical Brain Functional Networks. PLOS Computational Biology 3, e17. https://doi.org/10.1371/journal.pcbi.0030017

Albert, R., Jeong, H., Barabási, A.-L., 2000. Error and attack tolerance of complex networks. Nature 406, 378–382. https://doi.org/10.1038/35019019

Alstott, J., Breakspear, M., Hagmann, P., Cammoun, L., Sporns, O., 2009. Modeling the Impact of Lesions in the Human Brain. PLOS Computational Biology 5, e1000408. https://doi.org/10.1371/journal.pcbi.1000408

Andrillon, T., Poulsen, A.T., Hansen, L.K., Léger, D., Kouider, S., 2016. Neural Markers of Responsiveness to the Environment in Human Sleep. J Neurosci 36, 6583–6596. https://doi.org/10.1523/JNEUROSCI.0902-16.2016

Aru, J., Suzuki, M., Larkum, M.E., 2020. Cellular Mechanisms of Conscious Processing. Trends Cogn Sci 24, 814–825. https://doi.org/10.1016/j.tics.2020.07.006

Atalay, A.S., Fecchio, M., Edlow, B.L., 2025. Visualizing Effective Connectivity in the Human Brain. bioRxiv 2025.03.06.641642. https://doi.org/10.1101/2025.03.06.641642

Bassett, D.S., Bullmore, E.T., 2017. Small-World Brain Networks Revisited. Neuroscientist 23, 499–516. https://doi.org/10.1177/1073858416667720

Beggs, J.M., Plenz, D., 2003. Neuronal avalanches in neocortical circuits. J Neurosci 23, 11167–11177. https://doi.org/10.1523/JNEUROSCI.23-35-11167.2003

Bertazzoli, G., Esposito, R., Mutanen, T.P., Ferrari, C., Ilmoniemi, R.J., Miniussi, C., Bortoletto, M., 2021. The impact of artifact removal approaches on TMS–EEG signal. NeuroImage 239, 118272. https://doi.org/10.1016/j.neuroimage.2021.118272

Bertolero, M.A., Yeo, B.T.T., D'Esposito, M., 2015. The modular and integrative functional architecture of the human brain. Proceedings of the National Academy of Sciences 112, E6798–E6807. https://doi.org/10.1073/pnas.1510619112

Betzel, R.F., Bassett, D.S., 2017. Multi-scale brain networks. NeuroImage, Functional Architecture of the Brain 160, 73–83. https://doi.org/10.1016/j.neuroimage.2016.11.006

Bharioke, A., Munz, M., Brignall, A., Kosche, G., Eizinger, M.F., Ledergerber, N., Hillier, D., Gross-Scherf, B., Conzelmann, K.-K., Macé, E., Roska, B., 2022. General anesthesia globally synchronizes activity selectively in layer 5 cortical pyramidal neurons. Neuron 110, 2024-2040.e10. https://doi.org/10.1016/j.neuron.2022.03.032

Boucsein, C., Nawrot, M., Schnepel, P., Aertsen, A., 2011. Beyond the Cortical Column: Abundance and Physiology of Horizontal Connections Imply a Strong Role for Inputs from the Surround. Front. Neurosci. 5. https://doi.org/10.3389/fnins.2011.00032

Breakspear, M., 2017. Dynamic models of large-scale brain activity. Nat Neurosci 20, 340–352. https://doi.org/10.1038/nn.4497

Brette, R., Gerstner, W., 2005. Adaptive exponential integrate-and-fire model as an effective description of neuronal activity. J Neurophysiol 94, 3637–3642. https://doi.org/10.1152/jn.00686.2005

Brunel, N., 2000. Dynamics of sparsely connected networks of excitatory and inhibitory spiking neurons. J Comput Neurosci 8, 183–208. https://doi.org/10.1023/a:1008925309027

Bullmore, E., Sporns, O., 2012. The economy of brain network organization. Nat Rev Neurosci 13, 336–349. https://doi.org/10.1038/nrn3214

Bullmore, E., Sporns, O., 2009. Complex brain networks: graph theoretical analysis of structural and functional systems. Nat Rev Neurosci 10, 186–198. https://doi.org/10.1038/nrn2575

Burt, J.B., Demirtaş, M., Eckner, W.J., Navejar, N.M., Ji, J.L., Martin, W.J., Bernacchia, A., Anticevic, A., Murray, J.D., 2018. Hierarchy of transcriptomic specialization across human cortex captured by structural neuroimaging topography. Nat Neurosci 21, 1251–1259. https://doi.org/10.1038/s41593-018-0195-0

Buzsáki, G., Draguhn, A., 2004. Neuronal oscillations in cortical networks. Science 304, 1926–1929. https://doi.org/10.1126/science.1099745

Cakan, C., Jajcay, N., Obermayer, K., 2021. neurolib: A Simulation Framework for Whole-Brain Neural Mass Modeling. Cognitive Computation 15, 1132–1152. https://doi.org/10.1007/s12559-021-09931-9

Casali, A.G., Casarotto, S., Rosanova, M., Mariotti, M., Massimini, M., 2010. General indices to characterize the electrical response of the cerebral cortex to TMS. NeuroImage 49, 1459–1468. https://doi.org/10.1016/j.neuroimage.2009.09.026

Casali, A.G., Gosseries, O., Rosanova, M., Boly, M., Sarasso, S., Casali, K.R., Casarotto, S., Bruno, M.-A., Laureys, S., Tononi, G., Massimini, M., 2013. A theoretically based index of consciousness independent of sensory processing and behavior. Sci Transl Med 5, 198ra105. https://doi.org/10.1126/scitranslmed.3006294

Casarotto, S., Comanducci, A., Rosanova, M., Sarasso, S., Fecchio, M., Napolitani, M., Pigorini, A., G. Casali, A., Trimarchi, P.D., Boly, M., Gosseries, O., Bodart, O., Curto, F., Landi, C., Mariotti, M., Devalle, G., Laureys, S., Tononi, G., Massimini, M., 2016. Stratification of unresponsive patients by an independently validated index of brain complexity. Ann Neurol 80, 718–729. https://doi.org/10.1002/ana.24779

Casarotto, S., Fecchio, M., Rosanova, M., Varone, G., D'Ambrosio, S., Sarasso, S., Pigorini, A., Russo, S., Comanducci, A., Ilmoniemi, R.J., Massimini, M., 2022. The rt-TEP tool: real-time visualization of TMS-Evoked Potentials to maximize cortical activation and minimize artifacts. Journal of Neuroscience Methods 370, 109486. https://doi.org/10.1016/j.jneumeth.2022.109486

Casarotto, S., Hassan, G., Rosanova, M., Sarasso, S., Derchi, C.-C., Trimarchi, P.D., Viganò, A., Russo, S., Fecchio, M., Devalle, G., Navarro, J., Massimini, M., Comanducci, A., 2024. Dissociations between spontaneous electroencephalographic features and the perturbational complexity index in the minimally conscious state. Eur J Neurosci 59, 934–947. https://doi.org/10.1111/ejn.16299

Casarotto, S., Romero Lauro, L.J., Bellina, V., Casali, A.G., Rosanova, M., Pigorini, A., Defendi, S., Mariotti, M., Massimini, M., 2010. EEG responses to TMS are sensitive to changes in the perturbation parameters and repeatable over time. PLoS One 5, e10281. https://doi.org/10.1371/journal.pone.0010281

Cattani, A., Galluzzi, A., Fecchio, M., Pigorini, A., Mattia, M., Massimini, M., 2023. Adaptation Shapes Local Cortical Reactivity: From Bifurcation Diagram and Simulations to Human Physiological and Pathological Responses. eNeuro 10. https://doi.org/10.1523/ENEURO.0435-22.2023

Chialvo, D.R., 2010. Emergent complex neural dynamics. Nature Phys 6, 744–750. https://doi.org/10.1038/nphys1803

Cohen, J.R., D'Esposito, M., 2016. The Segregation and Integration of Distinct Brain Networks and Their Relationship to Cognition. J Neurosci 36, 12083–12094. https://doi.org/10.1523/JNEUROSCI.2965-15.2016

Colombo, M.A., Napolitani, M., Boly, M., Gosseries, O., Casarotto, S., Rosanova, M., Brichant, J.-F., Boveroux, P., Rex, S., Laureys, S., Massimini, M., Chieregato, A., Sarasso, S., 2019. The spectral exponent of the resting EEG indexes the presence of consciousness during unresponsiveness induced by propofol, xenon, and ketamine. NeuroImage 189, 631–644. https://doi.org/10.1016/j.neuroimage.2019.01.024

Crossley, N.A., Mechelli, A., Scott, J., Carletti, F., Fox, P.T., McGuire, P., Bullmore, E.T., 2014. The hubs of the human connectome are generally implicated in the anatomy of brain disorders. Brain 137, 2382–2395. https://doi.org/10.1093/brain/awu132

Crucitti, P., 2004. Model for cascading failures in complex networks. Phys. Rev. E 69. https://doi.org/10.1103/PhysRevE.69.045104

D'Ambrosio, S., Certo, F., Bernardelli, L., Pini, L., Corbetta, M., Pantoni, L., Massimini, M., Sarasso, S., 2023. Detecting cortical reactivity alterations induced by structural disconnection in subcortical stroke. Clinical Neurophysiology 156, 1–3. https://doi.org/10.1016/j.clinph.2023.09.007

David, O., Harrison, L., Friston, K.J., 2005. Modelling event-related responses in the brain. Neuroimage 25, 756–770. https://doi.org/10.1016/j.neuroimage.2004.12.030

Deco, G., Jirsa, V.K., Robinson, P.A., Breakspear, M., Friston, K., 2008. The Dynamic Brain: From Spiking Neurons to Neural Masses and Cortical Fields. PLOS Computational Biology 4, e1000092. https://doi.org/10.1371/journal.pcbi.1000092

Deco, G., Kringelbach, M.L., Jirsa, V.K., Ritter, P., 2017. The dynamics of resting fluctuations in the brain: metastability and its dynamical cortical core. Sci Rep 7, 3095. https://doi.org/10.1038/s41598-017-03073-5

Deco, G., Tononi, G., Boly, M., Kringelbach, M.L., 2015. Rethinking segregation and integration: contributions of whole-brain modelling. Nat Rev Neurosci 16, 430–439. https://doi.org/10.1038/nrn3963

Destexhe, A., 2009. Self-sustained asynchronous irregular states and Up–Down states in thalamic, cortical and thalamocortical networks of nonlinear integrate-and-fire neurons. J Comput Neurosci 27, 493–506. https://doi.org/10.1007/s10827-009-0164-4

Economo, C., Koskinas, G., Triarhou, L., 2008. Atlas of Cytoarchitectonics of the Adult Human Cerebral Cortex.

Edelman, G.M., Gally, J.A., 2013. Reentry: a key mechanism for integration of brain function. Front Integr Neurosci 7, 63. https://doi.org/10.3389/fnint.2013.00063

Edelman, G.M., Tononi, G., 2000. Reentry and the Dynamic Core: Neural Correlates of Conscious Experience. https://doi.org/10.7551/mitpress/4928.003.0012

Ercsey-Ravasz, M., Markov, N.T., Lamy, C., Van Essen, D.C., Knoblauch, K., Toroczkai, Z., Kennedy, H., 2013. A Predictive Network Model of Cerebral Cortical Connectivity Based on a Distance Rule. Neuron 80, 184–197. https://doi.org/10.1016/j.neuron.2013.07.036

Ferrarelli, F., Massimini, M., Peterson, M.J., Riedner, B.A., Lazar, M., Murphy, M.J., Huber, R., Rosanova, M., Alexander, A.L., Kalin, N., Tononi, G., 2008. Reduced evoked gamma oscillations in the frontal cortex in schizophrenia patients: a TMS/EEG study. Am J Psychiatry 165, 996–1005. https://doi.org/10.1176/appi.ajp.2008.07111733

Ferrarelli, F., Massimini, M., Sarasso, S., Casali, A., Riedner, B.A., Angelini, G., Tononi, G., Pearce, R.A., 2010. Breakdown in cortical effective connectivity during midazolam-induced loss of consciousness. Proc Natl Acad Sci U S A 107, 2681–2686. https://doi.org/10.1073/pnas.0913008107

Fukushima, M., Sporns, O., 2020. Structural determinants of dynamic fluctuations between segregation and integration on the human connectome. Commun Biol 3, 606. https://doi.org/10.1038/s42003-020-01331-3

Gaglioti, G., Cardinale, A., Lupo, C., Nieus, T., Marmoreo, F., Gutzen, R., Denker, M., Pigorini, A., Massimini, M., Sarasso, S., Paolucci, P.S., Bonis, G.D., 2025. Emergent complexity and rhythms in evoked and spontaneous dynamics of human whole-brain models after tuning through analysis tools. https://doi.org/10.48550/arXiv.2509.12873

Gaglioti, G., Nieus, T.R., Massimini, M., Sarasso, S., 2024. Investigating the Impact of Local Manipulations on Spontaneous and Evoked Brain Complexity Indices: A Large-Scale Computational Model. Applied Sciences 14, 890. https://doi.org/10.3390/app14020890

Gollo, L.L., Zalesky, A., Hutchison, R.M., van den Heuvel, M., Breakspear, M., 2015. Dwelling quietly in the rich club: brain network determinants of slow cortical fluctuations. Philosophical Transactions of the Royal Society B: Biological Sciences 370, 20140165. https://doi.org/10.1098/rstb.2014.0165

Gramfort, A., Luessi, M., Larson, E., Engemann, D.A., Strohmeier, D., Brodbeck, C., Parkkonen, L., Hämäläinen, M.S., 2014. MNE software for processing MEG and EEG data. NeuroImage 86, 446–460. https://doi.org/10.1016/j.neuroimage.2013.10.027

Griffa, A., Van den Heuvel, M.P., 2018. Rich-club neurocircuitry: function, evolution, and vulnerability. Dialogues in Clinical Neuroscience 20, 121–132. https://doi.org/10.31887/DCNS.2018.20.2/agriffa

Griffiths, J.D., Bastiaens, S.P., Kaboodvand, N., 2022. Whole-Brain Modelling: Past, Present, and Future. Adv Exp Med Biol 1359, 313–355. https://doi.org/10.1007/978-3-030-89439-9_13

Gutzen, R., De Bonis, G., De Luca, C., Pastorelli, E., Capone, C., Allegra Mascaro, A.L., Resta, F., Manasanch, A., Pavone, F.S., Sanchez-Vives, M.V., Mattia, M., Grün, S., Paolucci, P.S., Denker, M., 2024. A modular and adaptable analysis pipeline to compare slow cerebral rhythms across heterogeneous datasets. Cell Reports Methods 4, 100681. https://doi.org/10.1016/j.crmeth.2023.100681

Gutzen, R., von Papen, M., Trensch, G., Quaglio, P., Grün, S., Denker, M., 2018. Reproducible Neural Network Simulations: Statistical Methods for Model Validation on the Level of Network Activity Data. Front Neuroinform 12, 90. https://doi.org/10.3389/fninf.2018.00090

Hagmann, P., Cammoun, L., Gigandet, X., Meuli, R., Honey, C.J., Wedeen, V.J., Sporns, O., 2008. Mapping the Structural Core of Human Cerebral Cortex. PLOS Biology 6, e159. https://doi.org/10.1371/journal.pbio.0060159

Haldeman, C., Beggs, J., 2005. Critical Branching Captures Activity in Living Neural Networks and Maximizes the Number of Metastable States. Physical review letters 94, 058101. https://doi.org/10.1103/PhysRevLett.94.058101

Hansen, J.Y., Shafiei, G., Markello, R.D., Smart, K., Cox, S.M.L., Nørgaard, M., Beliveau, V., Wu, Y., Gallezot, J.-D., Aumont, É., Servaes, S., Scala, S.G., DuBois, J.M., Wainstein, G., Bezgin, G., Funck, T., Schmitz, T.W., Spreng, R.N., Galovic, M., Koepp, M.J., Duncan, J.S., Coles, J.P., Fryer, T.D., Aigbirhio, F.I., McGinnity, C.J., Hammers, A., Soucy, J.-P., Baillet, S., Guimond, S., Hietala, J., Bedard, M.-A., Leyton, M., Kobayashi, E., Rosa-Neto, P., Ganz, M., Knudsen, G.M., Palomero-Gallagher, N., Shine, J.M., Carson, R.E., Tuominen, L., Dagher, A., Misic, B., 2022. Mapping neurotransmitter systems to the structural and functional organization of the human neocortex. Nat Neurosci 25, 1569–1581. https://doi.org/10.1038/s41593-022-01186-3

Harris, B., Gollo, L.L., Fulcher, B.D., 2024. Tracking the Distance to Criticality in Systems with Unknown Noise. Phys. Rev. X 14, 031021. https://doi.org/10.1103/PhysRevX.14.031021
Harris, J.D., Ermentrout, B., 2018. Traveling waves in a spatially-distributed Wilson–Cowan model of cortex: From fronts to pulses. Physica D: Nonlinear Phenomena 369, 30–46. https://doi.org/10.1016/j.physd.2017.12.011
Hassan, G., De Cuntis, I., Blasi, V., Baglio, F., Rosanova, M., Bottari, D., Ricciardi, E., Bernardi, G., Pietrini, P., Massimini, M., 2025. Reactivity Changes in the Occipital Cortex of Blind Individuals: a TMS-EEG study. Brain Stimulation: Basic, Translational, and Clinical Research in Neuromodulation 18, 551.
Haun, A., Tononi, G., 2019. Why Does Space Feel the Way it Does? Towards a Principled Account of Spatial Experience. Entropy 21, 1160. https://doi.org/10.3390/e21121160
Hernandez-Pavon, J.C., Veniero, D., Bergmann, T.O., Belardinelli, P., Bortoletto, M., Casarotto, S., Casula, E.P., Farzan, F., Fecchio, M., Julkunen, P., Kallioniemi, E., Lioumis, P., Metsomaa, J., Miniussi, C., Mutanen, T.P., Rocchi, L., Rogasch, N.C., Shafi, M.M., Siebner, H.R., Thut, G., Zrenner, C., Ziemann, U., Ilmoniemi, R.J., 2023. TMS combined with EEG: Recommendations and open issues for data collection and analysis. Brain Stimul 16, 567–593. https://doi.org/10.1016/j.brs.2023.02.009
Herz, A.V.M., Gollisch, T., Machens, C.K., Jaeger, D., 2006. Modeling single-neuron dynamics and computations: a balance of detail and abstraction. Science 314, 80–85. https://doi.org/10.1126/science.1127240
Heuvel, M.P. van den, Sporns, O., 2013. Network hubs in the human brain. Trends in Cognitive Sciences 17, 683–696. https://doi.org/10.1016/j.tics.2013.09.012
Heuvel, M.P. van den, Sporns, O., 2011. Rich-Club Organization of the Human Connectome. J. Neurosci. 31, 15775–15786. https://doi.org/10.1523/JNEUROSCI.3539-11.2011
Hilgetag, C.C., Goulas, A., 2020. 'Hierarchy' in the organization of brain networks. Philosophical Transactions of the Royal Society B: Biological Sciences 375, 20190319. https://doi.org/10.1098/rstb.2019.0319
Hilgetag, C.C., Hütt, M.-T., 2014. Hierarchical modular brain connectivity is a stretch for criticality. Trends in Cognitive Sciences 18, 114–115. https://doi.org/10.1016/j.tics.2013.10.016
Hodgkin, A.L., Huxley, A.F., 1952. A quantitative description of membrane current and its application to conduction and excitation in nerve. J Physiol 117, 500–544. https://doi.org/10.1113/jphysiol.1952.sp004764
Honey, C.J., Sporns, O., Cammoun, L., Gigandet, X., Thiran, J.P., Meuli, R., Hagmann, P., 2009. Predicting human resting-state functional connectivity from structural connectivity. Proceedings of the National Academy of Sciences 106, 2035–2040. https://doi.org/10.1073/pnas.0811168106
Horvát, S., Gămănuț, R., Ercsey-Ravasz, M., Magrou, L., Gămănuț, B., Essen, D.C.V., Burkhalter, A., Knoblauch, K., Toroczkai, Z., Kennedy, H., 2016. Spatial Embedding and Wiring Cost Constrain the Functional Layout of the Cortical Network of Rodents and Primates. PLOS Biology 14, e1002512. https://doi.org/10.1371/journal.pbio.1002512
Ilmoniemi, R.J., Virtanen, J., Ruohonen, J., Karhu, J., Aronen, H.J., Näätänen, R., Katila, T., 1997. Neuronal responses to magnetic stimulation reveal cortical reactivity and connectivity. Neuroreport 8, 3537–3540. https://doi.org/10.1097/00001756-199711100-00024
Jansen, B.H., Rit, V.G., 1995. Electroencephalogram and visual evoked potential generation in a mathematical model of coupled cortical columns. Biol Cybern 73, 357–366. https://doi.org/10.1007/BF00199471

Kaiser, M., Görner, M., Hilgetag, C., 2007. Criticality of spreading dynamics in hierarchical cluster networks without inhibition. New Journal of Physics 9. https://doi.org/10.1088/1367-2630/9/5/110
King, J.-R., Sitt, J.D., Faugeras, F., Rohaut, B., El Karoui, I., Cohen, L., Naccache, L., Dehaene, S., 2013. Information Sharing in the Brain Indexes Consciousness in Noncommunicative Patients. Current Biology 23, 1914–1919. https://doi.org/10.1016/j.cub.2013.07.075
Kinouchi, O., Copelli, M., 2006. Optimal dynamical range of excitable networks at criticality. Nature Phys 2, 348–351. https://doi.org/10.1038/nphys289
Komssi, S., Kähkönen, S., 2006. The novelty value of the combined use of electroencephalography and transcranial magnetic stimulation for neuroscience research. Brain Res Rev 52, 183–192. https://doi.org/10.1016/j.brainresrev.2006.01.008
Larkum, M., 2013. A cellular mechanism for cortical associations: an organizing principle for the cerebral cortex. Trends in Neurosciences 36, 141–151. https://doi.org/10.1016/j.tins.2012.11.006
Larkum, M.E., Senn, W., Lüscher, H.-R., 2004. Top-down dendritic input increases the gain of layer 5 pyramidal neurons. Cereb Cortex 14, 1059–1070. https://doi.org/10.1093/cercor/bhh065
Lau, P.-M., Bi, G.-Q., 2005. Synaptic mechanisms of persistent reverberatory activity in neuronal networks. Proc Natl Acad Sci U S A 102, 10333–10338. https://doi.org/10.1073/pnas.0500717102
Llinás, R., Ribary, U., Contreras, D., Pedroarena, C., 1998. The neuronal basis for consciousness. Philos Trans R Soc Lond B Biol Sci 353, 1841–1849. https://doi.org/10.1098/rstb.1998.0336
López-González, A., Panda, R., Ponce-Alvarez, A., Zamora-López, G., Escrichs, A., Martial, C., Thibaut, A., Gosseries, O., Kringelbach, M.L., Annen, J., Laureys, S., Deco, G., 2021. Loss of consciousness reduces the stability of brain hubs and the heterogeneity of brain dynamics. Commun Biol 4, 1037. https://doi.org/10.1038/s42003-021-02537-9
Luppi, A.I., Craig, M.M., Pappas, I., Finoia, P., Williams, G.B., Allanson, J., Pickard, J.D., Owen, A.M., Naci, L., Menon, D.K., Stamatakis, E.A., 2019. Consciousness-specific dynamic interactions of brain integration and functional diversity. Nat Commun 10, 4616. https://doi.org/10.1038/s41467-019-12658-9
Maschke, C., O'Byrne, J., Colombo, M.A., Boly, M., Gosseries, O., Laureys, S., Rosanova, M., Jerbi, K., Blain-Moraes, S., 2024. Critical dynamics in spontaneous EEG predict anesthetic-induced loss of consciousness and perturbational complexity. Commun Biol 7, 946. https://doi.org/10.1038/s42003-024-06613-8
Massimini, M., Corbetta, M., Sanchez-Vives, M.V., Andrillon, T., Deco, G., Rosanova, M., Sarasso, S., 2024. Sleep-like cortical dynamics during wakefulness and their network effects following brain injury. Nat Commun 15, 7207. https://doi.org/10.1038/s41467-024-51586-1
Massimini, M., Ferrarelli, F., Huber, R., Esser, S.K., Singh, H., Tononi, G., 2005. Breakdown of Cortical Effective Connectivity During Sleep. Science 309, 2228–2232. https://doi.org/10.1126/science.1117256
Mateos, D.M., Guevara Erra, R., Wennberg, R., Perez Velazquez, J.L., 2018. Measures of entropy and complexity in altered states of consciousness. Cogn Neurodyn 12, 73–84. https://doi.org/10.1007/s11571-017-9459-8

Mediano, P.A.M., Rosas, F.E., Bor, D., Seth, A.K., Barrett, A.B., 2022. The strength of weak integrated information theory. Trends Cogn Sci 26, 646–655. https://doi.org/10.1016/j.tics.2022.04.008
Meisel, C., Klaus, A., Kuehn, C., Plenz, D., 2015. Critical Slowing Down Governs the Transition to Neuron Spiking. PLOS Computational Biology 11, e1004097. https://doi.org/10.1371/journal.pcbi.1004097
Meunier, D., Lambiotte, R., Bullmore, E.T., 2010. Modular and Hierarchically Modular Organization of Brain Networks. Front. Neurosci. 4. https://doi.org/10.3389/fnins.2010.00200
Momi, D., Wang, Z., Griffiths, J.D., 2023. TMS-evoked responses are driven by recurrent large-scale network dynamics. Elife 12, e83232. https://doi.org/10.7554/eLife.83232
Momi, D., Wang, Z., Parmigiani, S., Mikulan, E., Bastiaens, S.P., Oveisi, M.P., Kadak, K., Gaglioti, G., Waters, A.C., Hill, S., Pigorini, A., Keller, C.J., Griffiths, J.D., 2025. Stimulation mapping and whole-brain modeling reveal gradients of excitability and recurrence in cortical networks. Nat Commun 16, 3222. https://doi.org/10.1038/s41467-025-58187-6
Morales, G.B., di Santo, S., Muñoz, M.A., 2023. Quasiuniversal scaling in mouse-brain neuronal activity stems from edge-of-instability critical dynamics. Proceedings of the National Academy of Sciences 120, e2208998120. https://doi.org/10.1073/pnas.2208998120
Mountcastle, V.B., 1997. The columnar organization of the neocortex. Brain 120 (Pt 4), 701–722. https://doi.org/10.1093/brain/120.4.701
Mukovski, M., Chauvette, S., Timofeev, I., Volgushev, M., 2007. Detection of Active and Silent States in Neocortical Neurons from the Field Potential Signal during Slow-Wave Sleep. Cereb Cortex 17, 400–414. https://doi.org/10.1093/cercor/bhj157
Mutanen, T.P., Kukkonen, M., Nieminen, J.O., Stenroos, M., Sarvas, J., Ilmoniemi, R.J., 2016. Recovering TMS-evoked EEG responses masked by muscle artifacts. Neuroimage 139, 157–166. https://doi.org/10.1016/j.neuroimage.2016.05.028
Nilsen, A.S., Arena, A., Storm, J.F., 2024. Exploring effects of anesthesia on complexity, differentiation, and integrated information in rat EEG. Neurosci Conscious 2024, niae021. https://doi.org/10.1093/nc/niae021
Nunez, P.L., Srinivasan, R., Nunez, P.L., Srinivasan, R., 2006. Electric Fields of the Brain: The neurophysics of EEG, Second Edition, Second Edition. ed. Oxford University Press, Oxford, New York.
O'Byrne, J., Jerbi, K., 2022. How critical is brain criticality? Trends Neurosci 45, 820–837. https://doi.org/10.1016/j.tins.2022.08.007
Oizumi, M., Albantakis, L., Tononi, G., 2014. From the phenomenology to the mechanisms of consciousness: Integrated Information Theory 3.0. PLoS Comput Biol 10, e1003588. https://doi.org/10.1371/journal.pcbi.1003588
Palva, J.M., Palva, S., 2012. Infra-slow fluctuations in electrophysiological recordings, blood-oxygenation-level-dependent signals, and psychophysical time series. NeuroImage, Connectivity 62, 2201–2211. https://doi.org/10.1016/j.neuroimage.2012.02.060
Pathak, A., Menon, S.N., Sinha, S., 2024. A hierarchy index for networks in the brain reveals a complex entangled organizational structure. Proceedings of the National Academy of Sciences 121, e2314291121. https://doi.org/10.1073/pnas.2314291121
Premoli, I., Castellanos, N., Rivolta, D., Belardinelli, P., Bajo, R., Zipser, C., Espenhahn, S., Heidegger, T., Müller-Dahlhaus, F., Ziemann, U., 2014. TMS-EEG signatures of GABAergic neurotransmission in the human cortex. J Neurosci 34, 5603–5612. https://doi.org/10.1523/JNEUROSCI.5089-13.2014

Rosanova, M., Casali, A., Bellina, V., Resta, F., Mariotti, M., Massimini, M., 2009. Natural Frequencies of Human Corticothalamic Circuits. J. Neurosci. 29, 7679–7685. https://doi.org/10.1523/JNEUROSCI.0445-09.2009
Rosanova, M., Gosseries, O., Casarotto, S., Boly, M., Casali, A.G., Bruno, M.-A., Mariotti, M., Boveroux, P., Tononi, G., Laureys, S., Massimini, M., 2012. Recovery of cortical effective connectivity and recovery of consciousness in vegetative patients. Brain: a Journal of Neurology 135. https://doi.org/10.1093/brain/awr340
Rubinov, M., Sporns, O., 2010. Complex network measures of brain connectivity: uses and interpretations. Neuroimage 52, 1059–1069. https://doi.org/10.1016/j.neuroimage.2009.10.003
Ruohonen, J., Karhu, J., 2010. Navigated transcranial magnetic stimulation. Neurophysiol Clin 40, 7–17. https://doi.org/10.1016/j.neucli.2010.01.006
Russo, S., Claar, L.D., Furregoni, G., Marks, L.C., Krishnan, G., Zauli, F.M., Hassan, G., Solbiati, M., d'Orio, P., Mikulan, E., Sarasso, S., Rosanova, M., Sartori, I., Bazhenov, M., Pigorini, A., Massimini, M., Koch, C., Rembado, I., 2025. Thalamic feedback shapes brain responses evoked by cortical stimulation in mice and humans. Nat Commun 16, 3627. https://doi.org/10.1038/s41467-025-58717-2
Russo, S., Pigorini, A., Mikulan, E., Sarasso, S., Rubino, A., Zauli, F.M., Parmigiani, S., d'Orio, P., Cattani, A., Francione, S., Tassi, L., Bassetti, C.L.A., Lo Russo, G., Nobili, L., Sartori, I., Massimini, M., 2021. Focal lesions induce large-scale percolation of sleep-like intracerebral activity in awake humans. NeuroImage 234, 117964. https://doi.org/10.1016/j.neuroimage.2021.117964
Sacha, M., Tesler, F., Cofre, R., Destexhe, A., 2025. A computational approach to evaluate how molecular mechanisms impact large-scale brain activity. Nat Comput Sci 5, 405–417. https://doi.org/10.1038/s43588-025-00796-8
Salin, P.A., Bullier, J., 1995. Corticocortical connections in the visual system: structure and function. Physiological Reviews 75, 107–154. https://doi.org/10.1152/physrev.1995.75.1.107
Sanchez-Vives, M.V., Massimini, M., Mattia, M., 2017. Shaping the Default Activity Pattern of the Cortical Network. Neuron 94, 993–1001. https://doi.org/10.1016/j.neuron.2017.05.015
Sanz Leon, P., Knock, S.A., Woodman, M.M., Domide, L., Mersmann, J., McIntosh, A.R., Jirsa, V., 2013. The Virtual Brain: a simulator of primate brain network dynamics. Front Neuroinform 7, 10. https://doi.org/10.3389/fninf.2013.00010
Sarasso, S., Boly, M., Napolitani, M., Gosseries, O., Charland-Verville, V., Casarotto, S., Rosanova, M., Casali, A.G., Brichant, J.-F., Boveroux, P., Rex, S., Tononi, G., Laureys, S., Massimini, M., 2015. Consciousness and Complexity during Unresponsiveness Induced by Propofol, Xenon, and Ketamine. Current Biology 25, 3099–3105. https://doi.org/10.1016/j.cub.2015.10.014
Sarasso, S., Casali, A.G., Casarotto, S., Rosanova, M., Sinigaglia, C., Massimini, M., 2021. Consciousness and complexity: a consilience of evidence. Neuroscience of Consciousness niab023. https://doi.org/10.1093/nc/niab023
Sarasso, S., D'Ambrosio, S., Fecchio, M., Casarotto, S., Viganò, A., Landi, C., Mattavelli, G., Gosseries, O., Quarenghi, M., Laureys, S., Devalle, G., Rosanova, M., Massimini, M., 2020. Local sleep-like cortical reactivity in the awake brain after focal injury. Brain 143, 3672–3684. https://doi.org/10.1093/brain/awaa338
Schartner, M., Seth, A., Noirhomme, Q., Boly, M., Bruno, M.-A., Laureys, S., Barrett, A., 2015. Complexity of Multi-Dimensional Spontaneous EEG Decreases during Propofol

Induced General Anaesthesia. PLOS ONE 10, e0133532. https://doi.org/10.1371/journal.pone.0133532
Senden, M., Deco, G., de Reus, M.A., Goebel, R., van den Heuvel, M.P., 2014. Rich club organization supports a diverse set of functional network configurations. NeuroImage 96, 174–182. https://doi.org/10.1016/j.neuroimage.2014.03.066
Shew, W.L., Plenz, D., 2013. The functional benefits of criticality in the cortex. Neuroscientist 19, 88–100. https://doi.org/10.1177/1073858412445487
Shew, W.L., Yang, H., Petermann, T., Roy, R., Plenz, D., 2009. Neuronal avalanches imply maximum dynamic range in cortical networks at criticality. J Neurosci 29, 15595–15600. https://doi.org/10.1523/JNEUROSCI.3864-09.2009
Sitt, J.D., King, J.-R., El Karoui, I., Rohaut, B., Faugeras, F., Gramfort, A., Cohen, L., Sigman, M., Dehaene, S., Naccache, L., 2014. Large scale screening of neural signatures of consciousness in patients in a vegetative or minimally conscious state. Brain 137, 2258–2270. https://doi.org/10.1093/brain/awu141
Spiegler, A., Hansen, E.C.A., Bernard, C., McIntosh, A.R., Jirsa, V.K., 2016. Selective Activation of Resting-State Networks following Focal Stimulation in a Connectome-Based Network Model of the Human Brain. eNeuro 3. https://doi.org/10.1523/ENEURO.0068-16.2016
Sporns, O., 2013. Network attributes for segregation and integration in the human brain. Current Opinion in Neurobiology, Macrocircuits 23, 162–171. https://doi.org/10.1016/j.conb.2012.11.015
Sporns, O., Betzel, R.F., 2016. Modular Brain Networks. Annu Rev Psychol 67, 613–640. https://doi.org/10.1146/annurev-psych-122414-033634
Sporns, O., Tononi, G., Edelman, G.M., 2000. Connectivity and complexity: the relationship between neuroanatomy and brain dynamics. Neural Netw 13, 909–922. https://doi.org/10.1016/s0893-6080(00)00053-8
Sporns, O., Tononi, G., Kötter, R., 2005. The Human Connectome: A Structural Description of the Human Brain. PLoS Comput Biol 1, e42. https://doi.org/10.1371/journal.pcbi.0010042
Steriade, M., Nunez, A., Amzica, F., 1993. A novel slow (< 1 Hz) oscillation of neocortical neurons in vivo: depolarizing and hyperpolarizing components. J. Neurosci. 13, 3252–3265. https://doi.org/10.1523/JNEUROSCI.13-08-03252.1993
Suzuki, M., Larkum, M.E., 2020. General Anesthesia Decouples Cortical Pyramidal Neurons. Cell 180, 666-676.e13. https://doi.org/10.1016/j.cell.2020.01.024
Takahashi, N., Oertner, T.G., Hegemann, P., Larkum, M.E., 2016. Active cortical dendrites modulate perception. Science 354, 1587–1590. https://doi.org/10.1126/science.aah6066
Timme, N.M., Marshall, N.J., Bennett, N., Ripp, M., Lautzenhiser, E., Beggs, J.M., 2016. Criticality Maximizes Complexity in Neural Tissue. Front Physiol 7, 425. https://doi.org/10.3389/fphys.2016.00425
Tononi, G., 2004. An information integration theory of consciousness. BMC Neurosci 5, 42. https://doi.org/10.1186/1471-2202-5-42
Tononi, G., Boly, M., Massimini, M., Koch, C., 2016. Integrated information theory: from consciousness to its physical substrate. Nat Rev Neurosci 17, 450–461. https://doi.org/10.1038/nrn.2016.44
Tononi, G., Edelman, G.M., 1998. Consciousness and Complexity. Science 282, 1846–1851. https://doi.org/10.1126/science.282.5395.1846

Tononi, G., Sporns, O., Edelman, G.M., 1994. A measure for brain complexity: relating functional segregation and integration in the nervous system. Proc Natl Acad Sci U S A 91, 5033–5037.
Tononi, G., Sporns, O., Edelman, G.M., 1992. Reentry and the problem of integrating multiple cortical areas: simulation of dynamic integration in the visual system. Cereb Cortex 2, 310–335. https://doi.org/10.1093/cercor/2.4.310
Trensch, G., Gutzen, R., Blundell, I., Denker, M., Morrison, A., 2018. Rigorous Neural Network Simulations: A Model Substantiation Methodology for Increasing the Correctness of Simulation Results in the Absence of Experimental Validation Data. Front. Neuroinform. 12. https://doi.org/10.3389/fninf.2018.00081
van Vreeswijk, C., Sompolinsky, H., 1996. Chaos in neuronal networks with balanced excitatory and inhibitory activity. Science 274, 1724–1726. https://doi.org/10.1126/science.274.5293.1724
Watts, D.J., Strogatz, S.H., 1998. Collective dynamics of 'small-world' networks. Nature 393, 440–442. https://doi.org/10.1038/30918
Wilson, H.R., Cowan, J.D., 1973. A mathematical theory of the functional dynamics of cortical and thalamic nervous tissue. Kybernetik 13, 55–80. https://doi.org/10.1007/BF00288786
Wilson, H.R., Cowan, J.D., 1972. Excitatory and inhibitory interactions in localized populations of model neurons. Biophys J 12, 1–24. https://doi.org/10.1016/S0006-3495(72)86068-5
Wischnewski, M., Shirinpour, S., Alekseichuk, I., Lapid, M.I., Nahas, Z., Lim, K.O., Croarkin, P.E., Opitz, A., 2024. Real-time TMS-EEG for brain state-controlled research and precision treatment: a narrative review and guide. J Neural Eng 21, 061001. https://doi.org/10.1088/1741-2552/ad8a8e
Yegenoglu, A., Subramoney, A., Hater, T., Jimenez-Romero, C., Klijn, W., Pérez Martín, A., van der Vlag, M., Herty, M., Morrison, A., Diaz-Pier, S., 2022. Exploring Parameter and Hyper-Parameter Spaces of Neuroscience Models on High Performance Computers With Learning to Learn. Front. Comput. Neurosci. 16. https://doi.org/10.3389/fncom.2022.885207
Zamora-López, G., Chen, Y., Deco, G., Kringelbach, M.L., Zhou, C., 2016. Functional complexity emerging from anatomical constraints in the brain: the significance of network modularity and rich-clubs. Sci Rep 6, 38424. https://doi.org/10.1038/srep38424
Zerlaut, Y., Chemla, S., Chavane, F., Destexhe, A., 2018. Modeling mesoscopic cortical dynamics using a mean-field model of conductance-based networks of adaptive exponential integrate-and-fire neurons. J Comput Neurosci 44, 45–61. https://doi.org/10.1007/s10827-017-0668-2
Zrenner, C., Desideri, D., Belardinelli, P., Ziemann, U., 2018. Real-time EEG-defined excitability states determine efficacy of TMS-induced plasticity in human motor cortex. Brain Stimul 11, 374–389. https://doi.org/10.1016/j.brs.2017.11.016

List of Abbreviations

EEG — Electroencephalography

TMS — Transcranial Magnetic Stimulation

TEP — TMS-EEG evoked potential

MRI — Magnetic resonance imaging

PCI — Perturbational Complexity Index

LZc — Lempel-Ziv Complexity

LIF — Leaky integrate-and-fire

AdEx — Adaptive exponential integrate-and-fire

WC — Wilson-Cowan

JR — Jansen-Rit

LB — Larter-Breakspear

List of Publications

Gaglioti, G., Nieus, T. R., Massimini, M., & Sarasso, S. (2024). Investigating the Impact of Local Manipulations on Spontaneous and Evoked Brain Complexity Indices: A Large-Scale Computational Model. Applied Sciences, 14(2), 890. https://doi.org/10.3390/app14020890

Momi, D., Wang, Z., Parmigiani, S., Mikulan, E., Bastiaens, S. P., Oveisi, M. P., Kadak, K., **Gaglioti, G.,** Waters, A. C., Hill, S., Pigorini, A., Keller, C. J., & Griffiths, J. D. (2025). Stimulation mapping and whole-brain modeling reveal gradients of excitability and recurrence in cortical networks. Nature communications, 16(1), 3222. https://doi.org/10.1038/s41467-025-58187-6

Berjaga-Buisan, T., Monti. J. M., Cortada, M., Colombo, M. A., Geli, S. M., **Gaglioti, G.**, Sarasso, S., Kringelbach, M. L., Corbetta, M., Sanchez-Vives, M. V., Massimini, M., Sanz Perl, Y., Deco, G. (2025). Thermodynamics of consciousness: A non-invasive perturbational framework. bioRxiv 2025.12.09.691422. https://doi.org/10.64898/2025.12.09.691422

Gaglioti, G., Cardinale, A,. Lupo, C., Nieus, T., Marmoreo, F., Gutzen, R., Denker, M., Pigorini, A., Massimini, M., Sarasso, S., Paolucci, P.S. & De Bonis, G. (2026). Emergent complexity and rhythms in evoked and spontaneous dynamics of human whole-brain models after tuning through analysis tools. Neurocomputing, 132735. https://doi.org/10.1016/j.neucom.2026.132735

Gaglioti, G., Dalla Porta, L., Colombo, M. A., Russo, S., Nieus, T., Deco, G., Corbetta, M., Sarasso, S., Sanchez-Vives, M. V., & Massimini, M. (2026). Slow wave generation and propagation in a model of brain lesions. NeuroImage, 329, 121817. https://doi.org/10.1016/j.neuroimage.2026.121817

Acknowledgments

This thesis would never have taken shape without the people who surrounded me, and who made this journey feel at once simple and fleeting, as if these years had passed in the blink of an eye.

My gratitude goes to my advisors, Marcello and Simone, who entrusted me with the opportunity to undertake this PhD. Their sharp scientific insight animated our discussions, while their confidence in me allowed my independence of thought to flourish. It is a gift beyond measure, because autonomy is the lifeblood of science. The rigor I have absorbed from them is a lesson I will carry with me always, a compass for the rest of my career.

I am equally indebted to Silvia, Mario, Andrea, and Ezequiel, whose devotion to science and to teaching has been for me both a source of trust and a model to aspire to. Their example stands as a reminder of what it means to practice science with both skill and generosity.

To Thierry, who has guided me from my Master's degree to this day with care and precision, and who has given me invaluable advice for life beyond academia. Much of my enthusiasm and curiosity comes from the patience with which he supported me in those formative years: without it, I would not be the researcher I am today.

To Michele, my lab "benchmate" and friend in life, for the stimulating conversations that spanned the whole spectrum of human knowledge. They made this PhD journey not only scientifically enriching, but also profoundly human.

To Marta, Gabriel, Giulia, and Elisabetta, who started this road alongside me: it seems like only yesterday that we first gathered in the lab, yet these three years have flown by, leaving behind countless shared moments—scientific debates, life discussions, laughter and doubts—that have woven a bond I will carry forever. I hope every PhD student is as lucky as I have been in finding such colleagues and friends.

To Simone and Renzo, who walked the path before me: their example and support have been invaluable. I know you would never hesitate to help me if I were in need.

To those who joined later, Letizia, Elena, Serena, Francesca, and Lucas, thank you for making the lab a serene and vibrant place, where science and life could flow together easily.

To the group in Rome, Pier, Giulia, Cosimo, and Alessandra, thank you for our stimulating collaborations, which have helped me grow as a scientist. And to the group in Barcelona, Mavi, and especially Leonardo, collaborator and friend, thank you for the science and the friendship shared.

Finally, to my family, my mother, my father, and my brother, my deepest gratitude. Your support has always been quiet yet steadfast, an inexhaustible presence that I know I can rely

on. My autonomy and my critical spirit were born from your trust and your respect, which gave me the freedom to make choices with the right lightness of heart.

To all of you, and to the friends I have not named, thank you. You have made this journey possible. More than that, you have made it a path I would choose a thousand times over.